FINITE ELEMENT MODELING OF PILE–SOIL INTERACTION: EFFECTS OF INSTALLATION AND RESPONSE IN SLOPING GROUND

By

© Ripon Karmaker

A Thesis Submitted to the

School of Graduate Studies

in partial fulfillment of the requirements for the degree of

Doctor of Philosophy

Faculty of Engineering and Applied Science

Memorial University of Newfoundland

May 2022

St. John's   Newfoundland   Canada

ABSTRACT

Piles are installed in many civil engineering projects on the level ground and near the slopes in vertical and inclined directions. While axial capacity is the primary concern in foundation design, the effects of lateral load due to ground movement are equally important in many cases, such as slope stabilization by piles and the impact of lateral spreading.

Displacement piles are generally installed by jacking or diving. During installation, a large volume of soil displaces around the pile, which could cause soil disturbance and thus affect the subsequent load-carrying capacity. Modeling the pile installation is a challenging task, especially when installed in sensitive clays. The contractive response and structural breakdown during shearing cause strain softening and develop a significant excess pore water pressure that could reduce the effective stress of the soil around the pile close to zero for high sensitive clays. The soil disturbance and penetration resistance, especially the skin friction, highly depend on softening and excess pore water pressure. The rate of shearing could also affect the soil strength and penetration behaviour. In the present study, the installation of the pile in sensitive clays are simulated for undrained condition. Mathematical models for strain-softening and strain-rate effects on the undrained shear strength are implemented using user subroutines. A comparison with the results of a field test conducted previously in Québec, Canada, shows that the present numerical technique can successfully simulate the installation process. The simulation results also show that the simplified approaches (e.g., cavity expansion or strain path methods) cannot model some key aspects of pile installation in highly sensitive clay. For jacking, the shear strength of soil in a small zone around the pile reduces to a small value due to strain softening, and the disturbed soil flows primarily through this narrow zone when the penetration is continued to a larger depth. The plastic

shear strain develops over a larger area for low sensitive clays, but its magnitude near the pile is higher in high sensitive clays.

The penetration due to impact driving is different from that in jacking. Near the ground surface, each blow results in continuous penetration, although the rate of penetration is negligible at the end. However, at a deeper condition, the hammer impact results in penetration first, and then the pile rebounds some distance. The strain rate effects on undrained shear strength play a significant role in impact driving, as compared to jacking because the rate of penetration is higher during impact, which increases the mobilized shear strength near the pile surface, and therefore soil flow occurs through a relatively larger area. For a given depth of penetration at the end of a blow, the stress distribution around the pile in driving and jacking is comparable.

For a sloping ground, the installation of a pile could cause the retrogressive failure of the slope, as reported in some studies. It is extremely difficult to conclude whether such failure was occurred only due to pile driving or a combination of other factors. Two retrogressive landslide cases studies are presented, where, in the first one, the failure of a sensitive clay slope was triggered by pile driving and, in the second one, landslide might have been triggered by toe erosion. However, the post-slide investigations show similar failure patterns, which implies that, although the soil type and triggering mechanisms are different, simulations can be performed using the same numerical technique.

In the sloping ground, piles might be located at different locations of the slope—for example, near the toe/crest or on the slope. When slope failure occurs, the upper part of the pile in the sliding mass experience lateral load. Similar loading occurs in lateral spreading. Large deformation FE analyses are performed to calculate the force acting on the pile due to ground movement. The effects of arching on the lateral force in relation to soil behaviour and pile spacing are examined.

This thesis is dedicated to my parents

for their endless love, support and encouragement

ACKNOWLEDGMENTS

TABLE OF CONTENTS

LIST OF FIGURES

LIST OF TABLES

LIST OF SYMBOLS

As the thesis is written in manuscript format, symbols used in this study are listed at the end of each chapter (Chapters 3–6).

Chapter 1

Introduction

1.1 Background

Piles are used in many civil engineering projects for a wide range of problems, such as transferring load from a superstructure to a stronger soil in a deeper layer and slope stabilization. Displacement piles are commonly used piles that are generally installed by jacking or impact driving using a hammer. The installation process displaces a large volume of soil, which could cause the disturbance of adjacent soil within several diameters. For sensitive clays, the main adverse effect of pile installation is the development of large strains, which generates excess pore water pressure and causes structural breakdown, thereby reduction of the undrained shear strength (Flaate, 1972; Bozozuk et al., 1978; Blanchet et al., 1980; Roy et al., 1981; Azzouz & Lutz, 1986; Azzouz & Morrisson, 1988). The sensitivity of soil is defined as the ratio of the undrained shear strength of the intact clay over fully remoulded clay at the same water content. The excess pore water pressure dissipation after consolidation may not bring the soil to its initial conditions because of the soil structure change. Therefore, the modeling of the pile installation process could provide the soil conditions that control the subsequent load-carrying capacity. Several analytical solutions have been developed to model the pile installation processes. Among them, the drivability of the pile is commonly estimated using the wave equation considering a one-dimensional hammer-pile-soil system, where the soil is modelled as a spring (Smith, 1960). The change in stresses and strains during installation can be modelled using cavity expansion theory and strain path methods (Butterfield & Banerjee, 1971; Vesić, 1972; Baligh, 1976; Baligh, 1985; Sagaseta, 1987; Chow &

Teh, 1990; Teh & Houlsby, 1991; Sagaseta & Whittle, 2001). These analytical solutions have some limitations because the solutions are developed based on simplified assumptions (De Chaunac & Holeyman, 2018). For example, the cavity expansion theory cannot correctly model the strain paths followed by soil elements. The strain path methods are primarily applicable to the deep penetration in undrained conditions. Randolph (2003) stated that the pile design methods rely primarily on empirical correlations, which sometimes overlook the changes in stresses and fabric surrounding the pile.

When the pile is installed in sensitive clays, the observed ground responses are significantly different as compared to those found in the non-sensitive clay (Koizumi & Ito, 1967; Flaate, 1972; Bozozuk et al., 1978; Blanchet et al., 1980; Roy et al., 1981; Azzouz & Lutz, 1986; Azzouz & Morrisson, 1988). While physical modeling of pile installation into non- to low-sensitive clays is available, modeling of pile installation in sensitive clays is limited. Sensitive clay exhibits strain-softening and strain rate-dependent behaviours, which change the soil flow mechanisms during the installation. Koizumi and Ito (1967) mounted measuring cells (earth pressure cells, pore water pressure cells, wire strain gages) on the pile surfaces and found almost zero effective stress in the soil elements near the pile. Measuring the tip and shaft resistances, Roy et al. (1981) showed a negligible contribution of shaft friction to the total penetration resistance during continuous penetration of a pile into highly sensitive clay. A comparison of responses during installation of the pile in low- and high-sensitive clays shows that the effective stress of soil near the pile is almost zero for the high sensitive clay, whereas it is considerably high for low sensitive clay. Also, for sand, comparative studies on physical and numerical modeling of pile jacking and impact driving give different responses (Yang et al., 2006; Fan et al., 2021).

Pile installation in sensitive clays causes the increase in radial and vertical stresses of the soils around the pile. The changes in stress state coupled with existing deviatoric stress in the sloping ground could cause the failure of a slope, and, in sensitive clay, it could be a potential cause of the large landslide. Several studies reported small to large slope failure incidents due to pile driving (Bernander, 1978; Carson, 1979a & 1979b; LaGatta & Whiteside, 1984; Shen et al., 2005). For example, Bernander (1978) documented two unfinished landslides in normally consolidated clays in Sweden, where approximately 200 m long cracks of 0.1–0.2 m width were formed during pile driving. The May 1978 Rigaud landslide occurred during pile driving in a sensitive clay (Carson, 1979a & 1979b). A large retrogressive landslide of 300 m long and a retrogression distance of 45–75 m with a backscarp of 7–8 m was found in post-slide investigations (Fig. 1.1).

Fig. 1.1. The May 1978 Rigaud landslide flowbowl (Carson, 1979b)

When a relatively mild slope fails, and the failed soil blocks are displaced downward (e.g., the sliding of clay soil over a liquified layer), the failed soil mass could cause structural damages to the pile. For example, Cubrinovski et al. (2009) reported permanent lateral ground displacements

3

of up to 4 m in some mild-sloped areas after the 1995 Kobe earthquake. The displacement of soil caused significant damage to piles in those areas. The arching effects of the soil between the two piles and the lateral loads acting on the pile due to the sliding clay mass might contribute to the damages.

A successful pile installation in the sloping ground increases the Factor of Safety (*FS*) of the slope. The location of the pile for effective stabilization and the effects of the pile spacing on a clay slope behaviour have been investigated in several studies (Cai & Ugai, 2000; Won et al., 2005; Ho, 2015).

Numerical simulation techniques have been developed to study the pile installation processes; however, most of these studies are limited to non- and low-sensitive clay (Randolph et al., 1979; Smith & Chow, 1982; Borja, 1988; Sheng et al., 2005; Qiu et al., 2011; Tian et al., 2011; Tho et al., 2012; Basu et al., 2014; Karmaker et al., 2019; Zhou et al., 2019). Pile installation processes and associated slope failure analyses are typically large deformation problems that are difficult to model using the Lagrangian-based traditional finite element and limit equilibrium analyses. Hence, advanced large deformation finite element modeling techniques, incorporating appropriate soil models, need to be developed.

1.2 Focus of the research

The present study is primarily focused on pile jacking and impact pile driving in sensitive clays. The currently used simplified approaches (e.g., wave theory, cavity expansion theory, strain path method) cannot model the installation process properly. Moreover, the potential causes of slope failure due to the installation of a pile in the sloping ground cannot be explained using the above-simplified approaches or limit equilibrium methods. Therefore, numerical modeling, such as large deformation FE modeling, would provide a better understanding.

4

The Coupled Eulerian-Lagrangian (CEL) approach in Abaqus FE software can handle large deformation. However, the software does not have any built-in model that can be directly used to model the undrained behaviour of sensitive clay. Also, CEL can model only single-phase materials; that means the excess pore water pressure generation during installation cannot be modelled. Moreover, the simplified cavity expansion and strain path methods cannot model the triggering of a slope failure and subsequent landslides. Therefore, for successful simulation of pile installation, the models should be developed for the above factors and implemented in the software.

Finally, most of the existing numerical studies did not investigate the response for highly sensitive clays. As mentioned above, field tests show a very different response when a pile is installed in highly sensitive clay (e.g. pore pressure generation and soil disturbance) compared to non- to low-sensitive clays.

1.3 Objectives

The main purpose of the present study is to develop pile–soil interaction modeling techniques for large soil deformation scenarios. The large deformation finite element analyses are performed using a Coupled Eulerian-Lagrangian (CEL) approach. The simulations are performed for vertical pile installation in level ground and inclined pile installation in sloping grounds where the soil is highly sensitive. The piles are installed by jacking and impact driving. In addition, large deformation FE modeling is performed for piles in the sloping ground and the piles impacted by a sliding clay layer. The main objectives of this research include:

- Develop an Eulerian-based large deformation FE modeling technique to simulate pile installation in sensitive clay, calibrating against field test data. Also, examine the soil flow mechanisms, remoulding and resulting disturbance due to pile installation.

- Identify the key soil parameters that affect the response during installation by giving special attention to the effects of the amount and rate of softening with plastic shear strains.

- Implement appropriate soil models for strain-softening and strain-rate effects on undrained shear strength. Also, develop a mathematical framework to calculate the excess pore water pressure during pile installation.

- Conduct FE simulations of pile installation in sensitive clay by jacking and impact driving and identify the similarities and differences in the response for these two installation processes.

- Identify the potential reasons why pile installation near sloping ground caused some large landslides. Also, examine whether the failure triggered by pile installation is different from the landslide triggered by other factors (e.g., toe erosion) based on FE simulations and two landslide case studies.

- Conduct FE analysis to examine the performance of a row of piles used to stabilize the slope. Also, develop a method to calculate the lateral force on a pile when a sliding clay layer impacts a pile, and then develop a simplified procedure to analyze the structural response of the pile.

1.4 Outline of the thesis

This thesis is prepared in manuscript format. The outcome of the study is presented in seven chapters and two appendices.

Chapter 1 demonstrates the background, scope and objectives of the study.

Chapter 2 presents a general literature review. As this thesis is prepared in manuscript format, the problem-specific literature reviews are provided in Chapters 3–6 and Appendices I & II.

Chapter 3 presents a Large Deformation Finite Element (LDFE) modeling of pile jacking in sensitive clays. A soil model that considers strain-softening and strain rate effects on shear strength is implemented. The penetration resistance, strength degradations, changes in radial stress, and plastic shear strain development are presented. The performance of the developed numerical techniques is compared with the field test results in a highly sensitive clay in Québec, Canada. A part of this study has been published earlier as conference papers (Karmaker et al., 2019 in Appendix I, and Karmaker & Hawlader, 2022 in Appendix II).

Chapter 4 presents a comparative study of large deformation finite element modeling of impact pile driving and pile jacking. A mathematical framework is proposed to calculate the excess pore pressure during the installation of piles in sensitive clays.

Chapter 5 presents the potential reasons why pile installation in the sloping ground could cause a large landslide, as happened in some cases (e.g., Rigaud landslide in Québec). This chapter also shows the similarity between the Rigaud landslide and Daniel's Harbour landslide in Newfounfounland, which was triggered by other factors. The FE modeling of Daniel's Harbour landslide has been published in a conference paper (Karmaker et al., 2021).

Chapter 6 presents the LDFE modeling of the pile stabilized slope to investigate the increase in factor of safety of a slope by a row of piles. This chapter also presents the lateral force on a pile resulting from a downslope displacement of a clay layer. A part of this work has been published in two conference papers (Karmaker & Hawlader, 2018 & Karmaker et al., 2018).

Chapter 7 presents the conclusion of the studies and the recommendation for future works.

The references cited in Chapters 1 and 2 are listed in the "References" chapter at the end of the thesis.

Chapter 2

Literature Review

2.1 Introduction

The ground responses during pile installation can be investigated using analytical, experimental and numerical techniques. The method of installation of displacement piles could significantly affect the soil flow mechanisms and stress state in the surrounding soil. Pile installation in sensitive clays could disturb the surrounding soil and cause lateral movement of the soil, ground surface heave, and failure of a slope if the pile is installed near the sloping ground. The post-failure investigation of landslide events in sensitive clays shows that similar to other triggering factors (e.g., toe erosion or human activities) (Locat et al., 2011; Perret et al., 2013; Demers et al., 2014; Locat et al., 2017), pile driving could initiate a large-scale landslide (Carson, 1979a, b). In other words, once the failure is triggered, the resulting landslide pattern could be similar, independent of triggering mechanisms. Large soil deformation occurs during the installation of pile and landslide events. A large deformation also occurs when the failed soil interacts with the pile, such as slope stabilization using piles and sliding of a soil layer.

A brief review of the literature related to the areas mentioned above is presented in this chapter. As the thesis is prepared in a manuscript format, a detailed problem-specific literature review is also presented in the following chapters. This chapter is organized as follows. Section 2.2 introduces the unique behaviour of sensitive clays based on field and laboratory tests. Section 2.3 describes the available analytical, experimental and numerical studies on pile installation in clay. This section also describes the type of pile installation methods used in the fields. Section 2.4

describes previous studies on pile installation in sensitive clays. Section 2.5 describes the large-scale landslides and their failure mechanisms. Section 2.6 mainly discusses the available works on the pile–slope stabilization techniques. Finally, Section 2.7 describes the recent development of large deformation finite element (LDFE) modeling techniques.

2.2 Behaviour of sensitive clay under undrained conditions

Many studies have been dedicated to understanding the behaviour of sensitive clays for drained and undrained loading conditions. As the focus of the present study is to simulate pile–soil interaction for undrained conditions, the studies available in this area are discussed in the following sections.

2.2.1 Stress–strain behaviour and pore pressure in soft sensitive clays

Several researchers have carried out laboratory tests (e.g., triaxial, direct simple shear and ring shear tests) and field tests (e.g., CPTu and vane shear tests) on sensitive clays. Theoretically, the soil could be sensitive if the sensitivity (S_t), the ratio between the undisturbed and remoulded shear strength, is greater than one. However, for practical purposes, if the sensitivity is 2–4, 4–8, 8–16 and >16, the soil is considered as low sensitive, medium sensitive, highly sensitive and quick clay, respectively (CGS, 2013), although there are several different classifications available in the literature (Rosenquist, 1953; Karlsson & Hansbo, 1989; CGS, 2006; Thakur & Degago, 2012). One of the unique characteristics of the sensitive clay is that shearing could cause the breakdown of the clay structure resulting in a tendency of rapid volumetric compression. However, as the permeability is low, water cannot flow out easily, generating significant excess pore water pressure. The undrained shear strength could be very low at the remoulded state, even less than 1 kPa for highly sensitive clays.

During undrained loading, two stages of post-peak shear strength degradation were found (Thakur et al., 2014b). In the first stage, a fully softened post-peak state is attained, which generally occurs within a shear strain level of 10–20% (Lacasse et al., 1985; Burland et al., 1997; Lunne et al., 1999; Sandven et al., 2004), and can be examined by the conventional laboratory tests. The soil could be brought to the residual state in the second stage, which occurs at very large strains. Ring shear tests and reversal shear box tests are generally carried out to find the residual state of the undrained strength.

Bjerrum (1961) suggested that, during shearing, the increase in excess pore water pressure reduces the undrained strength of sensitive clays. Thakur et al. (2014b) observed that strain-softening of soft sensitive clays is not governed by cohesion and friction softening, as commonly used to explain the softening of overconsolidated clays. However, cohesion and friction softening might have some role at very large strains. Figure 2.1(a) shows the test results of some anisotropically consolidated triaxial compression tests on Rissa clay for various strain rates (0.1–4.5 %/h) (Thakur et al., 2014b). The stress path is initially almost vertical for this lightly overconsolidated clay (OCR ~ 2.25), and, after reaching the peak, the strength reduces, and the stress path follows a line having a cohesion intercept of 5.1–10 kPa and the angle of internal friction of 22°–27°. Another important observation is that the shear strength reduces almost to half of the initial value only in ~ 10% strain (Fig. 2.1(b)). The excess pore water pressure (u_e) increases rapidly at the initial stage, and then a gradual increase is continued (Fig. 2.1(c)). Several other studies also gave a similar conclusion: the post-peak strength reduction in soft sensitive clays is governed by the shear-induced pore pressure rather than reduction of the strength parameters (Bernander, 2000; Jostad et al., 2006; Thakur et al., 2005, 2007, 2011; Gylland et al., 2012).
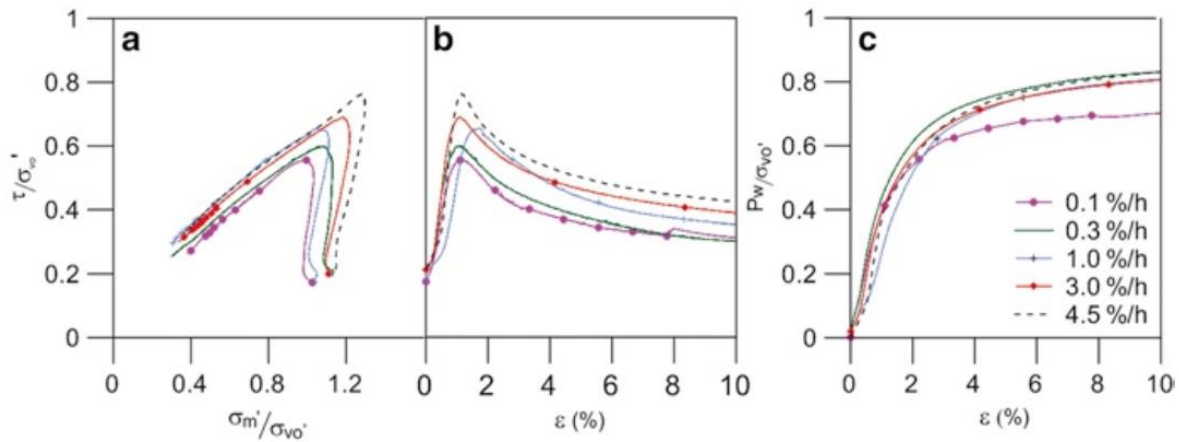
Fig. 2.1. Triaxial compression test results on block samples of Rissa clay (after Thakur et al., 2014b)

For a higher overconsolidation ratio, the stress path is somehow different. Laccasse et al. (1985) conducted anisotropically consolidated triaxial compression tests on overconsolidated Emmerstad clay ($OCR \sim 4.5$ and $S_t > 100$) and found that the stress path moves rightward, and some friction and cohesion softening occur even within the range of laboratory strains (Fig. 2.2).
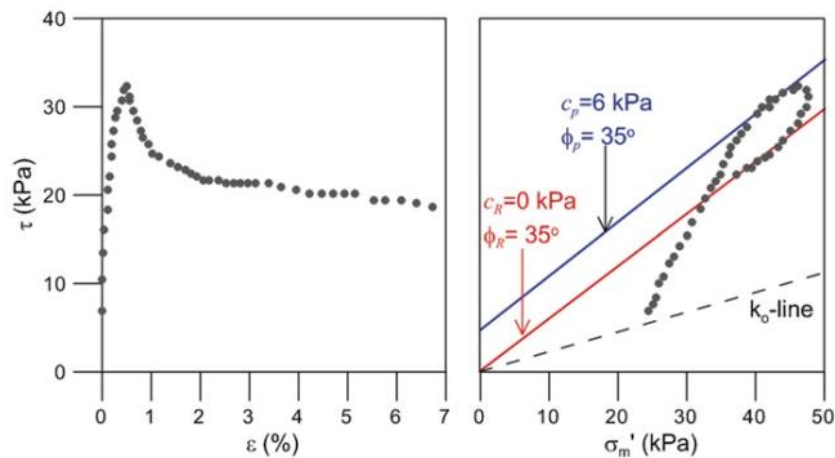
Fig. 2.2. Triaxial compression test results on Emmerstad clay (after Lacasse et al., 1985)

Figure 2.3 shows the idealized stress–strain behaviour and stress path for sensitive clays. The effective stress path (ESP) for undrained loading follows a unique failure line in the post-peak regions (Thakur et al., 2014b). The remoulded condition is attained at large strains by the development of significant excess pore water pressure.
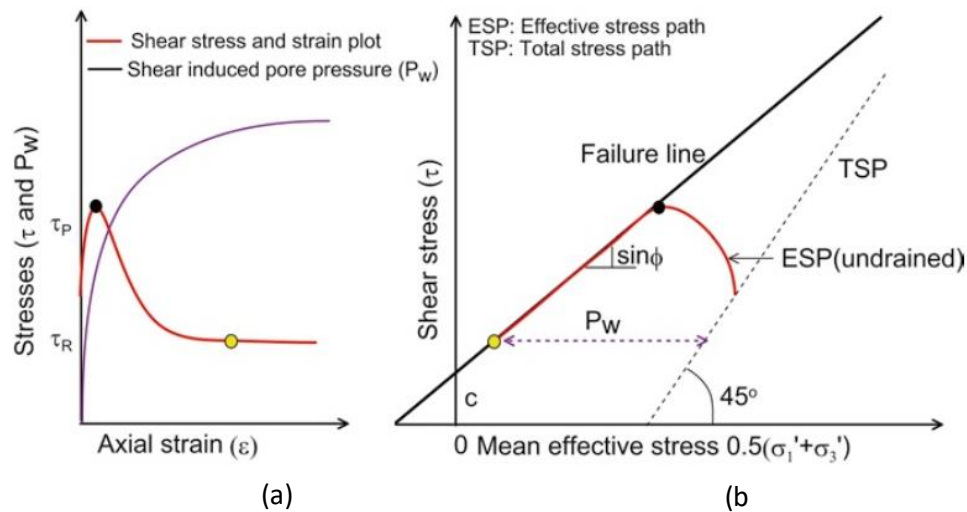
Fig. 2.3. Idealized sensitive clay behaviour: (a) stress–strain relation; and (b) stress path (after Thakur et al., 2014)

Field investigations show that sensitive clays at many sites (e.g., eastern Canadian clay, Finish clay) are lightly overconsolidated (e.g., Bjerrum & Landva, 1966; Länsivaara et al., 2014; Locat et al., 2015; Thakur et al., 2014a & 2014b; Lefebvre, 2017; Mayne et al., 2019).

2.2.2 Strain-softening of sensitive clays

The undrained shear strength of sensitive clay reduces from the peak to the remoulded value due to shearing. However, measuring the post-peak shear strength degradation for the full range of strains using typical laboratory and field test facilities is extremely challenging or may not be

possible. Stark and Contreras (1996) conducted ring shear tests to determine the undrained residual strength of cohesive soils. However, the tests were stopped at less than 60 mm displacement, which is relatively small compared to the actual shear displacement needed to attain the remoulded conditions. They suggested that a complete residual state may occur when the specimen is sheared to several hundred millimetres, corresponding to several hundred percent shear strain in the soil specimen.

Tavenas et al. (1983) conducted four different tests on sensitive Champlain clays collected from seven sites in Québec in eastern Canada, which had a sensitivity of 24 to > 600. They presented the post-peak shear strength degradation as a function of strain energy (Fig. 2.4(a)). Quinn (2009) showed that Tavenas et al.'s data could be used to develop post-peak stress–displacement curves (Fig. 2.4(b)). Einav and Randolph (2005) proposed an exponential relationship between the mobilized undrained shear strength and plastic shear strain. Recognizing the nonlinear degradation of strength in sensitive clays, Dey et al. (2015) used a similar exponential function for rapid degradation of strength after the peak followed by gradual strength reduction at large strains (Fig. 2.4(c); please see Dey et al. (2015) for further details, including symbols and equations).
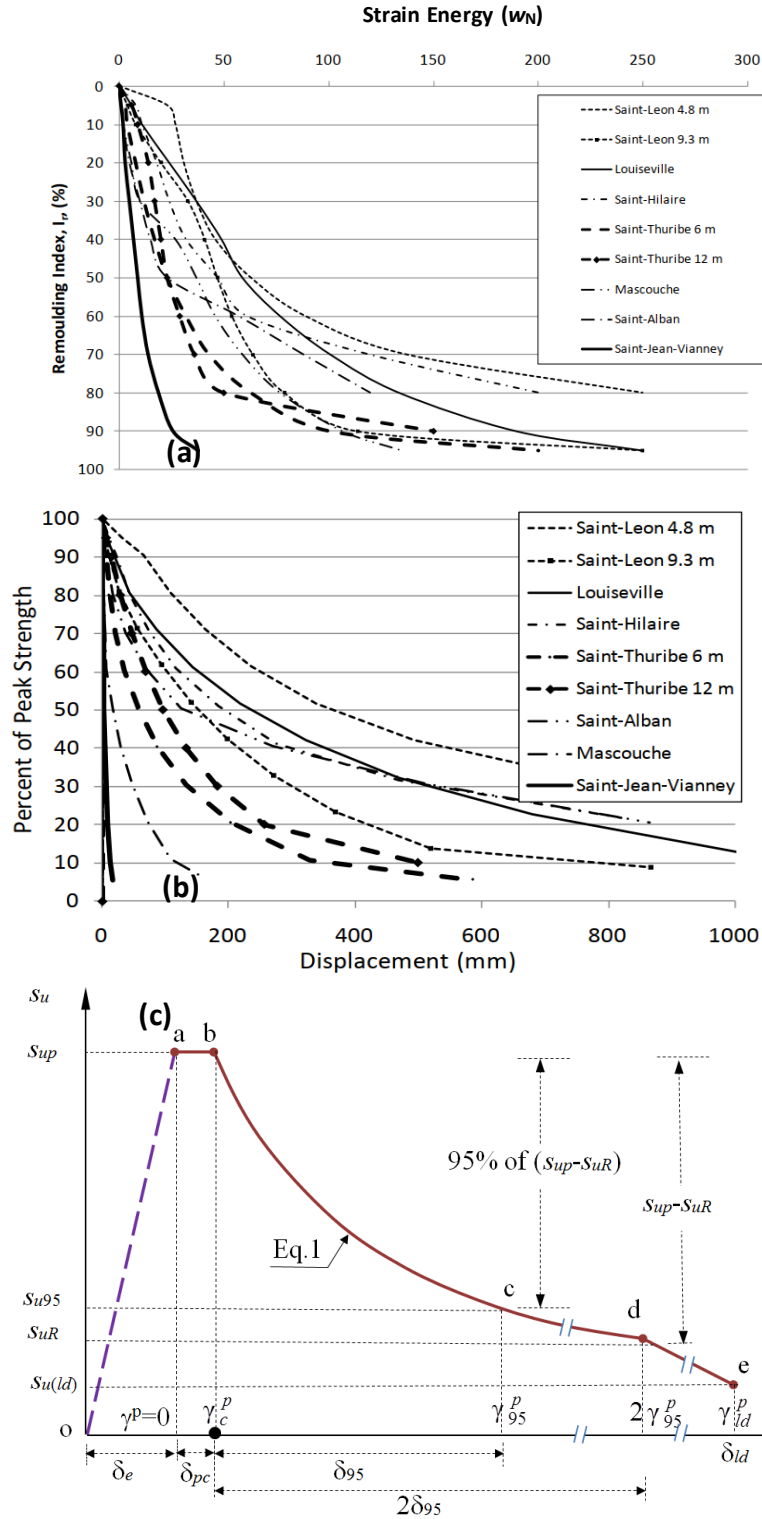
Fig. 2.4. Shear strength degradation: (a & b) test results on Champlain clay (Tavenas et al., 1983; Quinn, 2009); (c) stress–strain curve used for finite element analyses (Dey et al., 2015)

14

2.2.3 Strain-rate effects on undrained shear strength of sensitive clays

The undrained shear strength of clay typically increases by 5%–20% for each order of magnitude increase in shear strain rate (e.g., Crawford, 1963; Lo & Morin, 1972; Vaid et al., 1979). Graham et al. (1983) summarized the laboratory tests on a large number of eastern Canadian sensitive clays and found similar time-dependent behaviour of undrained shear strengths. They also suggested that similar strain-rate effects should also be applied to the in-situ vane shear tests. Lefebvre and LeBoeuf (1987) performed a series of triaxial tests on eastern Canadian sensitive clay and showed an increase in undrained shear strength with shear strain rate (Fig. 2.5). Lefebvre and Pfendler (1996) performed cyclic constant-volume direct simple shear tests on samples collected from the St. Alben site in Québec City, Canada and showed that, at an equivalent strain rate of 0.1 Hz cyclic loading, the mobilized undrained shear strength is 40% higher than that determined at a standard strain rate (2.1%/h).
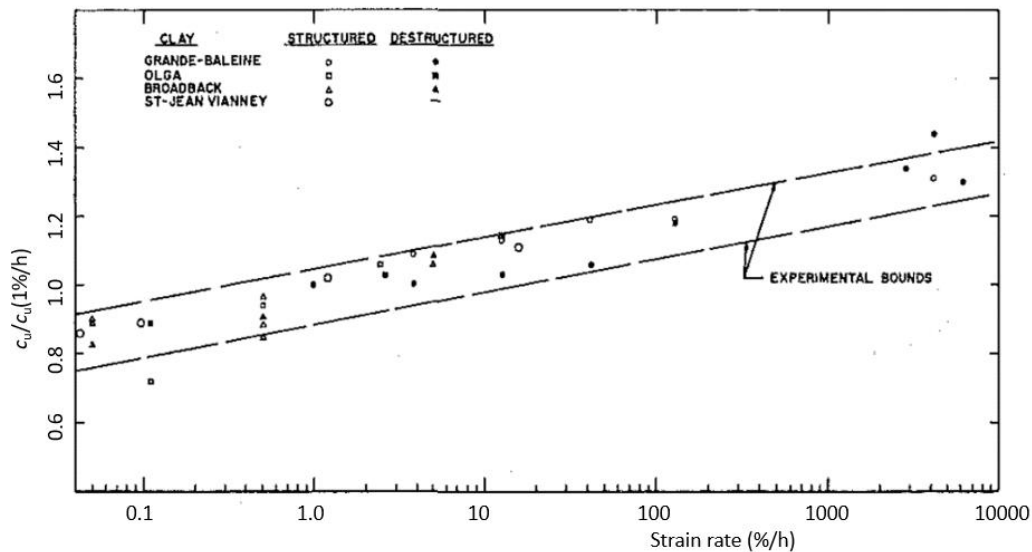
Fig. 2.5. Strain rate effects on undrained shear strength in triaxial tests (after Lefebvre & LeBoeuf, 1987)

Unlike non-sensitive to low sensitive clays, the shear strength of sensitive clay decreases significantly to a very small value at the remould state. The soil in the remoulded state behaves like a fluid. Two frameworks are commonly used to incorporate the strain rate effects: (a) geotechnical framework and (b) fluid dynamics framework. In the geotechnical framework, semi-logarithmic, hyperbolic sine, and power-law models are used. In the fluid mechanics framework, the strain rate effects are incorporated, assuming the material is a non-Newtonian fluid (e.g., Herschel–Bulkley model). Zhu and Randolph (2011) incorporated the Herschel-Bulkley and power-law model and proposed a combined model that can capture the behaviour of both soil and fluid-like materials, which is used in the present study.

The field vane shear test is commonly used for geotechnical characterization of soil. While undrained laboratory tests could be performed at sufficiently low strain rates (as the drainage valve is closed), drainage will occur in the field if the field vane shear test is conducted at a very low rotation rate, and the test will not give the undrained shear strength. Figure 2.6 shows the vane shear test results on two Canadian sensitive clays for varying rotation rates (Roy & Leblanc, 1988). For the rotation rates higher than the standard rate of 0.22°/s, the undrained shear strength of the Saint-Alben clay does not increase significantly; however, approximately 3% increase per log cycle is found for the Saint-Louis clay. Below 0.22°/s rotation rate, a significant increase in undrained shear strength occurs for both soils, indicating partial drainage at the slower rotation rate. During pile installation by impact driving or landslide, the soil might experience higher shear strain rates than the standard rate considered in the laboratory and field tests. Note also that remoulded soil could have a higher strain rate effect.
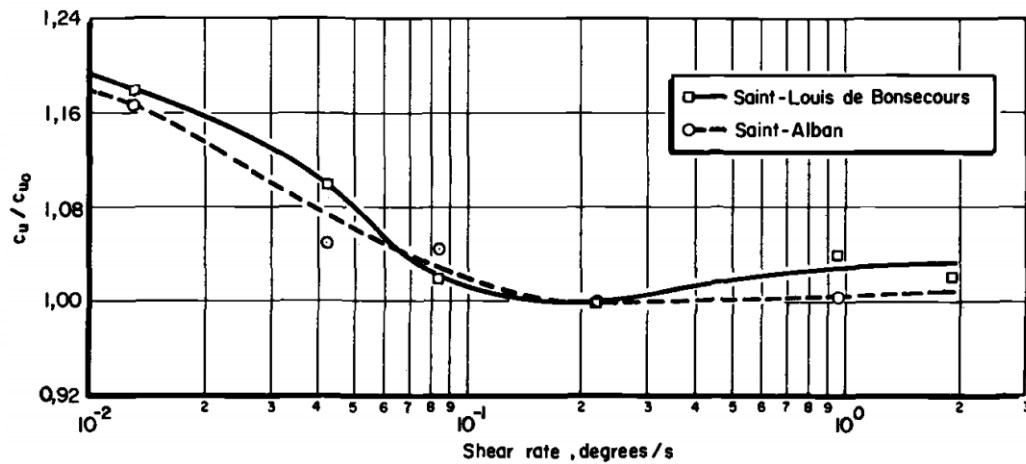
Fig. 2.6. Field vane shear tests on two Canadian clays (after Roy & Leblanc, 1988)

2.3 Ground response during pile installations

Numerous studies have been carried out to investigate the pile installation process and associated ground response, which includes analytical, small-scale and full-scale experiments and numerical analyses.

2.3.1 Analytical Methods

Wave equations

The effects of pile driving are similar to the longitudinal wave transmission. Smith (1960) gave a solution to the wave equations developed for idealized pile driving problems, which is widely used to assess pile drivability. The performance and limitations of this approach have been further evaluated by numerical analyses (Davis & Phelan, 1978; Smith & Chow, 1982) and incorporating improved soil models (e.g., spring and dashpot (Lee et al., 1988)).

Cavity expansion theories

The cavity expansion theories deal with the expansion of a cavity in the material of given properties to determine the stress and pore pressure changes (Bishop et al., 1945; Hill, 1950; Gibson & Anderson, 1961). Ladanyi (1963) extended this theory for undrained loading of an infinite medium of saturated clays, where the soils were modelled as the elastic-perfectly plastic and strain-hardening materials. Vesić (1972) presented an expansion of the spherical and cylindrical cavity in a soil defined by the Mohr-Coulomb failure criterion as well as by an average volumetric strain within the plastic region (Fig. 2.7). The volumetric strain can be determined from the known state of stress in the plastic zone and volume change versus stress relationships. The parameters that influence the cavity expansion results are the initial stress conditions, soil strength and volume change characteristics, and rigidity index. Vesić (1972) applied those solutions to determine the bearing capacity factors for a deep foundation. However, the above studies did not model the cavity expansion in sensitive clays where strain-softening occurs. Moreover, the cylindrical cavity expansion theory is applicable to soil elements away from the ground surface and the tip in case of a pile and away from the ends of the inflatable membrane in case of a pressuremeter.
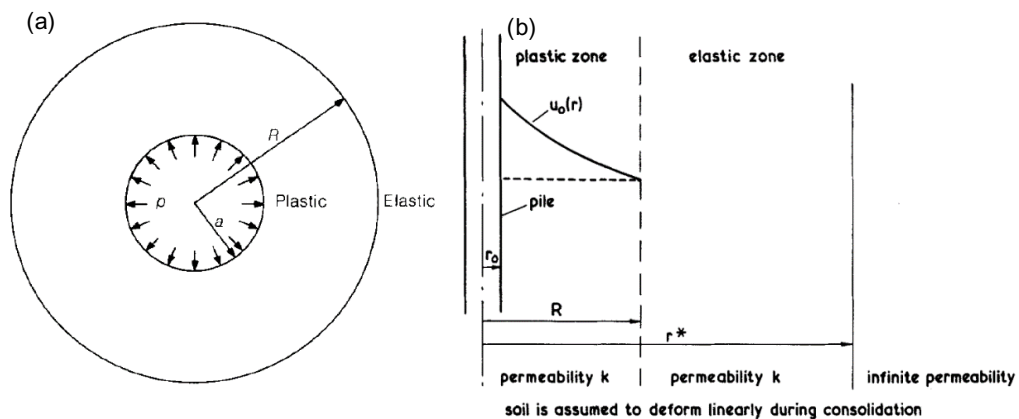
Fig. 2.7. Cavity expansion problems (after Vesić, 1972 and Carter et al., 1979)

18

Carter et al. (1979) modelled the cylindrical cavity expansion assuming plane strain conditions. The soil was considered as saturated two-phase clay materials and modelled as (a) elastic perfectly plastic based on Tresca criteria and (b) volumetric hardening elastoplastic material based on the critical state concepts (Schofield & Wroth, 1968). They found that the changes in stresses depend on the soil model. Randolph et al. (1979) investigated the effects of the stress history of the soil on the stress changes. Their model is capable of predicting the stress changes based on the basic soil parameters such as undrained shear strength and shear stiffness. Randolph et al. (1979) also incorporated the sensitivity of the soil based on the critical state soil mechanics approaches. Fig. 2.8(a) shows the conceptual effective stress path in q–p' space. During undrained shearing, the soil follows the effective stress path EF until it reaches the peak deviator stress, q_F. After that, the soil follows the effective stress path FG, as shearing is continued. However, the stress ratio q/p' remains constant, and the mean effective stress decreases until the stress path reaches point G (i.e., remoulded deviatoric stress q_G). As the effective stress drops from F to G, large pore pressure is generated. They assumed the radius of the post-peak zone and distributed the maximum shear stress linearly with the logarithm of radial distance.

Carter and Yeung (1985) presented numerical modeling of single-phase, strain-softening material to determine the stress changes around the driven piles. Carter et al. (1986) presented a closed-form solution of both cylindrical and spherical cavity expansion theory. They introduced a parameter k, which was used to differentiate the spherical and long cylindrical cavities. Strength parameters including cohesion were modified until a good fit between theoretical predictions and test results was obtained. Yu and Houlsby (1991) adopted a constitutive model the same as that used by Carter et al. (1986) but with logarithmic strain definition such that the large strain effects could be taken into account.
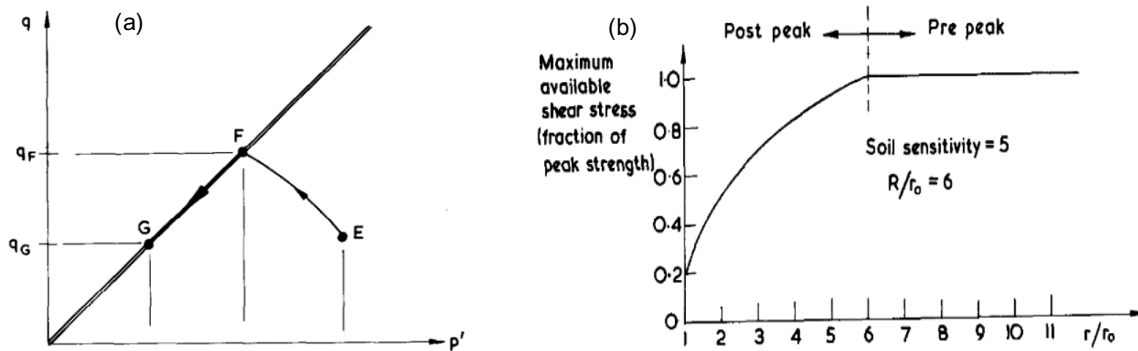
Fig. 2.8. Cavity expansion in sensitive clays: (a) conceptual undrained stress path; (b) assumed variation of soil strength (after Randolph et al., 1979)

Strain Path Method (SPM)

Baligh (1985) proposed an integrated and systematic analytical framework to predict soil disturbance caused by the deep penetration in saturated clays. The primary assumption of this concept is that the soil deformation and strain in deep penetrations are independent of the undrained shear strength of the soil. He proposed that the deformation and strain caused by the penetration are essentially strain-controlled and could provide minimal errors in the determination of approximate stresses and pore water pressures. He provided a closed-form-solutions using the velocity and strain rate components, which were used to solve the displacements and strains by numerical integration along the streamlines. The SPM is applicable to steady and deep penetration only. Gill and Lehane (2000) examined the effects of fluid viscosity and boundary conditions on SPM of analysis, while Baligh (1985) considered inviscid material in his formulation. Teh and Houlsby (1991) conducted numerical simulations of cone penetration using the strain path method and found that the cone factor N_{kt} is significantly influenced by the rigidity of the soil and in-situ stress conditions. They also found that the radial stress has more influence on N_{kt} than the vertical stress. Sagaseta (1987) proposed the "shallow strain path method" to incorporate the free-field

ground movements during pile penetration. This method has also been used to simulate soil flow during penetration of simple wall, pile and tube (Sagaseta et al. 1997; Sagaseta and Whittle 2001).

2.3.2 Pile installation methods

Impact pile driving

Pile driveability could be assessed using analytical methods or finite element modeling. Borja (1988) used an impulse function (force–time curve) for finite element analysis instead of giving hammer velocity, as used by Smith (1960). Goble and Rausche (1980) presented force versus time graphs for different hammers used for pile driving in the field. Mabsout and his co-workers conducted finite element simulations of pile driving for single and multiple hammers blows using one of the force–time curves presented by Goble and Rausche et al., called "forcing function," as shown in Fig. 2.9 (Mabsout & Tassoulas, 1994; Mabsout et al., 1995; Mabsout et al., 1999). Table 2.1 shows a brief summary of the studies on impact driving. Further details on impact driving in soft sensitive clays are provided in Chapter 4.
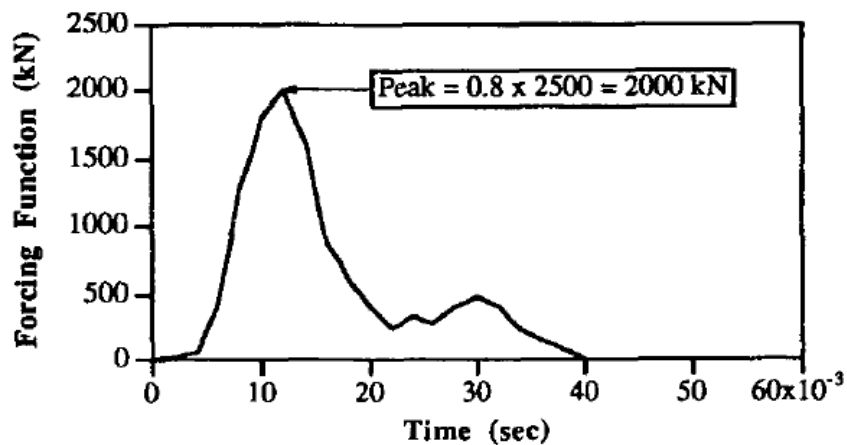
Fig. 2.9. Forcing function used in FE analysis by Mabsout et al. (1999)

Pile Jacking

Pile jacking is one of the popular pile installation methods, which causes less ground vibration and disturbances. White (2002) reported fewer ground vibrations in four pile-jacking sites than those created by conventional pile driving. Therefore, pile jacking is considered an effective technique to protect the adjacent structures, especially in urban areas. The pile can be inserted into the ground using displacement-controlled or velocity-controlled loading. Experimental and numerical studies were carried out on pile jacking to understand ground movement and its consequences. For example, Lehane and Gavin (2001) experimentally investigated the effects of in-situ stresses, diameter and wall thickness of the open-ended piles during jacking. The piles were installed using 40–80 mm jacking strokes. A detailed discussion on the effects of pile jacking in soft sensitive clays is presented in Chapter 3.

Table 2.1. Studies on pile installation and cone penetration

Authors	Type of studies	End condition of piles	Soil types	Installation process
Fellenius and Samson (1976)	Field test	Concrete pile	Soft sensitive clay	Drop hammer weight: 38 kN Dropping height: 0.3 m
Davis and Phelan (1978)	Numerical	Closed-ended	c-ϕ soil	Impact hammer blows
Cooke et al. (1979)	Experimental	Open-ended	clay	Displacement-controlled jacking
Roy et al. (1981)	Field Test	Open-ended	Soft Sensitive clay	Jacking velocity:1, 2, 7 cm/min
Baligh (1985)	Analytical and experimental	Open-ended and closed-ended	c-ϕ soil	Driven or jacked
Konrad and Roy (1987)	Field tests	Closed-ended	OC soft sensitive clay	Displacement-controlled jacking
Borja (1988)	Numerical	HP steel pile	Silty clay	Forcing function of rated energy 20.33 kN-m and falling height is 0.3 m
Lee et al. (1988)	Analytical	Open-ended and closed-ended	c-ϕ soil	Impact hammer blows
Smith and To (1988)	Numerical	Closed-ended	c-ϕ soil	Sinusoidal loading
Bond and Jardine (1991)	Field test	Closed-ended	OC clay	Displacement-controlled jacking (225 mm)
Randolph et al. (1991)	Analytical	Open-ended	c-ϕ soil	Driven pile
Mabsout et al. (1999)	Numerical	Closed-ended	clay	Impact hammer blows
Take et al. (1999)	Analytical	Open-ended and closed-ended	c-ϕ soil	Impact hammer blows
Hwang et al. (2001)	Field test	closed-ended	Both clay and sand	Impact hammer blows (DELMAG D100 diesel pile driver)
Sagaseta and Whittle (2001)	Analytical and experimental	Open-ended and closed-ended	clay	Driven or jacked
White (2002)	Field test	H-section piles	Sand	Pressed-in pile
Gavin and Lehane (2003)	Experimental	Open-ended and closed-ended	Sand	Displacement-controlled jacking (stroke length 0.25D to 1.3D)
Sheng et al. (2005)	Numerical	Closed-ended	clay	Displacement-controlled jacking
Yang et al. (2006)	Field tests	H-section piles	sand	Jacking rate 1.0–1.8 m/min
Alves et al. (2009)	Experimental	Closed-ended steel pile	Soft sensitive clay	A 0.65 kN hammer weight with 0.15, 0.3 & 0.45 m falling height
Doherty and Gavin (2011)	Experimental	Open-ended	clay	Displacement-controlled jacking (100 to 250 mm per stroke)
Konkol (2015)	Numerical	Close-ended	Sand	Velocity-controlled jacking (25 cm/s)
Kou et al. (2015)	Field test	Open-ended	clay	Jacking rate = 1.5 m/min. (penetration per stroke = 1.8 m)
Wang et al. (2015)	Numerical	Close-ended	clay	Jacking rate = 0.5 m/sec.
Afshin and Rayhani (2015)	Experimental	Open-ended and closed-ended	Soft sensitive clay (Leda clay)	Hydraulic jack in increment of 10 mm
Ko et al. (2016)	Numerical	Open-ended	Sand	Impact hammer blows
Davidson et al. (2019)	Field test	Open-ended	Sand	Impact hammer blows
Zhou et al. (2019)	Numerical	XCC pile	Clay	Jacking rate = 0.5 m/sec.

2.4 Pile installations in sensitive clays: Level and sloping grounds

Several studies have been carried out to understand penetration mechanisms, generation of excess pore water pressure and its dissipation, soil disturbance around the piles, and regain of strength with time. This section presents some of those studies, especially the generation of excess pore pressure, soil disturbances, and changes of stress during pile installation in sensitive clays. Note that the cone penetrometer can be considered as the small diameter piles and could have similar effects on the soil during penetration.

2.4.1 Generation of excess pore water pressure

Bjerrum et al. (1958) were the first to observe the driving-induced pore pressure in clay around piles. The excess pore pressure (u_e) due to undrained shearing of NC clays is a function of initial consolidation pressure prior to shearing (Lo, 1961; Bjerrum & Lo, 1963; Lo & Stermac, 1965). Lo and Stermac (1965) observed that the maximum excess pore pressure, u_{e_max} (~1.0–1.3 times of the initial effective overburden pressure), develops within a very limited zone around the pile, and u_e reduces rapidly with radial distance. Orrje and Broms (1967) investigated the effects of pile driving in soft sensitive clays and found u_{e_max} is greater than the total overburden pressure. Fellenius and Broms (1969) installed two 0.3-m diameter precast concrete piles in soft sensitive clay and found u_{e_max} exceeds locally 20% of the total overburden pressure (σ_{v0}).

Bozozuk et al. (1978) presented the results of 116 concrete piles driven into sensitive marine clays in eastern Canada. They found that u_e exceed by 35%–40% of the initial total overburden pressure. Blanchet et al. (1978) reported that the tapered piles generate higher u_e than that of straight-walled piles. Roy et al. (1981) carried out a field investigation by jacking 0.219-m diameter piles in highly sensitive clays at a site in Saint Alben, Québec. They observed the induced pore pressures of $1.6\sigma_{v0}$ and $0.8\sigma_{v0}$ at the pile tip and pile surface, respectively. The pore pressure

was also measured at a distance of 0.2 m from the pile wall at four different depths, as shown in Fig. 2.10. They found that the excess pore pressure reduces at the beginning of the installation (below hydrostatic), but it begins to increase rapidly as the pile tip moves towards the cell. The maximum excess pore water pressure is obtained when the pile tip reaches $0–0.2$ m above the cell. Once the pile tip passes the level of the piezometer, the excess pore pressure starts to reduce again and reaches the equilibrium condition. Roy et al. (1982) carried out cone penetration tests in highly sensitive clays for varying penetration rates (i.e., $3–240$ cm/min) and observed little influence on the induced excess pore pressure. Konrad and Roy (1987) reported the results of two instrumented piles installation at the St. Alben test site and found $u_e \approx 1.6\sigma_{v0}$ near the toe, which is 90% of the pore pressures reported by Roy et al. (1982) from CPTu.
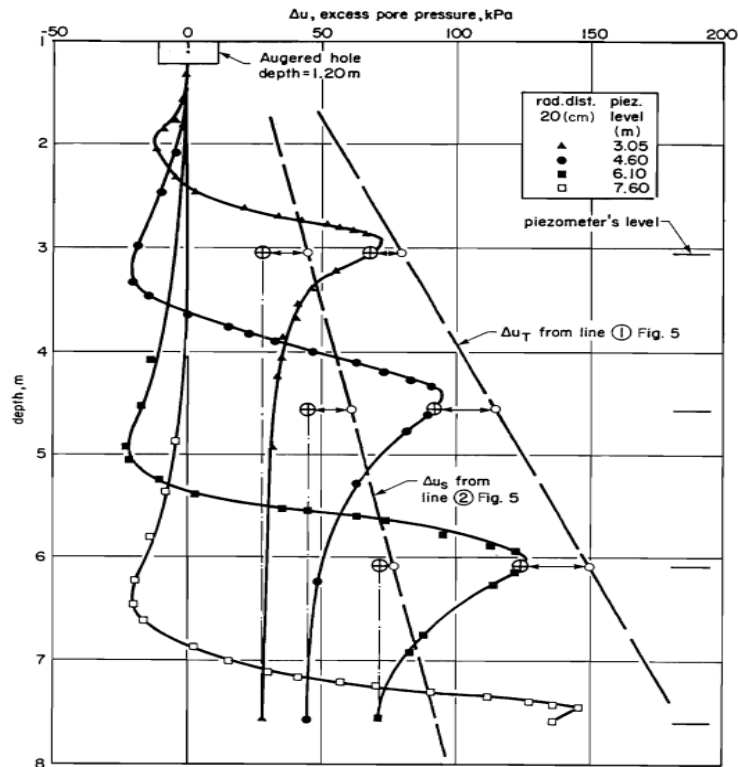
Fig. 2.10. Pore pressure generation during pile installation in sensitive clay (after Roy et al., 1981)

2.4.2 Soil disturbances due to pile driving

Casagrande (1932) observed that the clay becomes completely or largely remoulded within a 1.5D radial distance from the pile centre during pile installation. Cummings et al. (1950) reported the disturbances within 2D, while Orrje and Broms (1967) found some shear strength reduction within 1.5D from the pile surface. Flaate (1971) found 10–15 cm of the severely remoulded zone around the pile shaft due to the installation of piles in sensitive clay, and the disturbance depends on clay properties, driving method and size of the piles. Torstensson (1973) reported that the soil within 1.5D experienced approximately a 10% reduction of strength, and no time-dependent regain of strength occurred. Bozozuk et al. (1978) found a 15% reduction of initial undrained shear due to pile driving and concluded that a minimum of 5D spacing is required to avoid significant disturbance. Roy et al. (1981) found ~ 30% reduction of undrained shear strength near the pile surface, and the disturbance is negligible after three pile diameters.

Stress change during pile installation

Kallstenius (1967) studied the stresses around a cylindrical piston sampler inserted into clay and observed that the total radial stress is almost equal to the pore water pressure. Also, the total radial stress magnitude during insertion was 8 to 10 times the undrained shear strength. Koizumi and Ito (1967) reported that, immediately after pile driving, the total radial stress is three to four times the initial total overburden pressure and is almost equal to the pore water pressure, which indicates that the radial effective stress next to the pile surface vanishes during and immediately after pile installation (Fig. 2.11). Flaate (1971) also observed high total stress and pore pressure around the pile, which reconsolidates rapidly after installation.
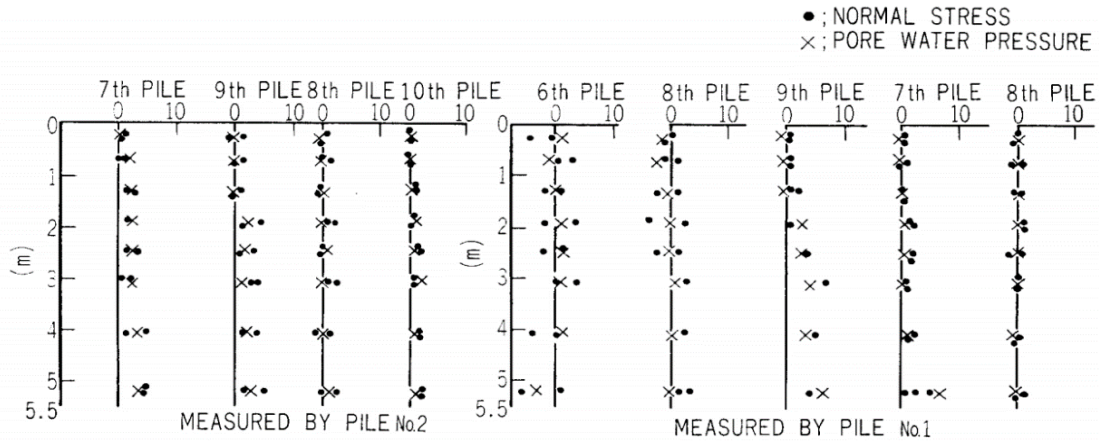
Fig. 2.11. Total radial stress and pore water pressure immediately after pile installation (after Koizumi & Ito, 1967)

Azzouz and Morrison (1988) compared the pore pressure generation due to pile installation and subsequent dissipation for two clays of varying sensitivities. For the high sensitive Lower Boston Blue clay ($S_t = 7 \pm 2$), the effective stress immediately after driving became close to zero (Fig. 2.12), while considerable effective stress remained in the case of non-sensitive Lower Empire Clay ($S_t = 2 \pm 1$) (compare effective horizontal stress ratio at a small-time in Fig. 2.12).
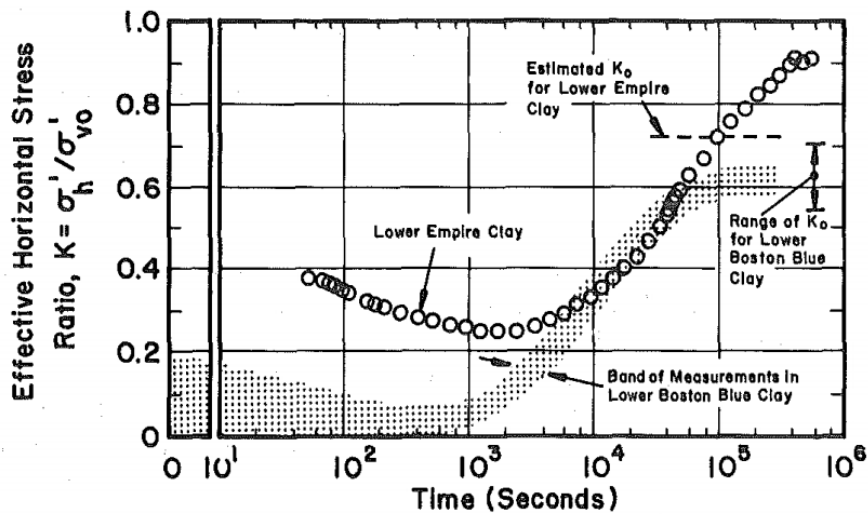
Fig. 2.12. Effects of sensitivity on effective stress and pore water pressure during installation of the pile and subsequent dissipation (after Azzouz & Morrison, 1988)

27

2.4.3 Landslide due to pile installation

Brand and Krasaesin (1970) documented the failure of a slope of a road embankment on soft Bangkok clay due to excess pore water pressure generation during the installation of concrete piles. The existing traffic loads might also contribute to the failure. The primary mode of failure was rotational slip originating on the roadside, and failure was completed at the bottom of the main canal.

Bernander (1978) reported several landslide events that occurred due to pile driving. In a minor piling project at Rävekärr 1971, a crack was formed during driving of the 5th pile. Finally, the crack of 0.2–0.3 m propagated swiftly 50 m in one direction and 500 m in the opposite direction. At Björlandavägen, a 0.1-m wide and 200-m long crack formed during piling operation in a mild slope (not more than 1:20). At Rollsbo, another landslide occurred during the sand drains installation, resulting in 20,000 m^2 of ground movements, although the factor of safety from the conventional stability analysis was 2.3.

Carson (1979a) discussed the May 1978 Rigaud Landslide in sensitive muddy sediments. The failure of the slope occurred during the pile driving. A detailed discussion on this landslide and numerical simulations are presented in Chapter 5 of the present study. LaGatta and Whiteside (1984) provided evidence of an underwater slope failure at Merrill Marine Terminal during pile driving and dredging at the same time in highly sensitive silty clay. Shen et al. (2005) presented the failure of a riverbank dike along the bank of Bailianjing River in Shanghai, P. R. China due to pile driving. Degradation of soil strength was identified as the main cause of the failure of the dike. Pile driving induced excess pore pressures and reduction of shear strength. The first slip surface was formed from the ground surface as a crack.

2.5 Large scale landslides in sensitive clays

In section 2.4, several landslide events during pile driving in soft-sensitive clay slopes have been discussed. Among them, the May 1978 Rigaud landslide is an example of large retrogressive landslides. A retrogressive landslide might also be triggered by other reasons. This section briefly describes the types of onshore sensitive clay landslides and potential retrogression processes.

Large-scale landslides in sensitive clays in Eastern Canada and Scandinavia are considered one of the major geohazards. According to Tavenas (1984) and Karlsrud et al. (1984), the most common types of slope failure includes single rotational slides, multiple retrogressive slides, translational progressive and spreads (according to the classification of Cruden & Vernes, 1996). Among them, the last three types of progressive failure in sensitive clays might initiate very quickly and affect a large area, sometimes more than 1 ha (Locat et al., 2011). These three types of slides are schematically shown in Fig. 2.13.

In a flowslide, successive failure of soil blocks occurs, as shown in Fig. 2.13(a). When the remoulded debris flows out of the crater, leaving an unstable scarp, the failure of another soil block occurs. This process is continued until a final stable back scarp is formed and the retrogression stops. This type of landslide occurs when the clays have a low remoulded shear strength, and the debris can flow out easily. Translational landslides result from the development of a shear surface parallel to the ground surface, above which the soil mass displaces downhill (Cruden & Vernes, 1996). Subsidence at the slope head and ground heave at the toe might be observed after the landslide (Fig. 2.13 (b). Spreads type of failure was first explained by Odenstad (1951) and further analyzed by several authors (e.g. Carson, 1977; Locat et al., 2011; Quinn et al., 2012; Dey et al., 2015). Spreads occur by the formation of horsts and grabens above a quasi-horizontal failure surface, as shown schematically in Fig. 2.13(c).
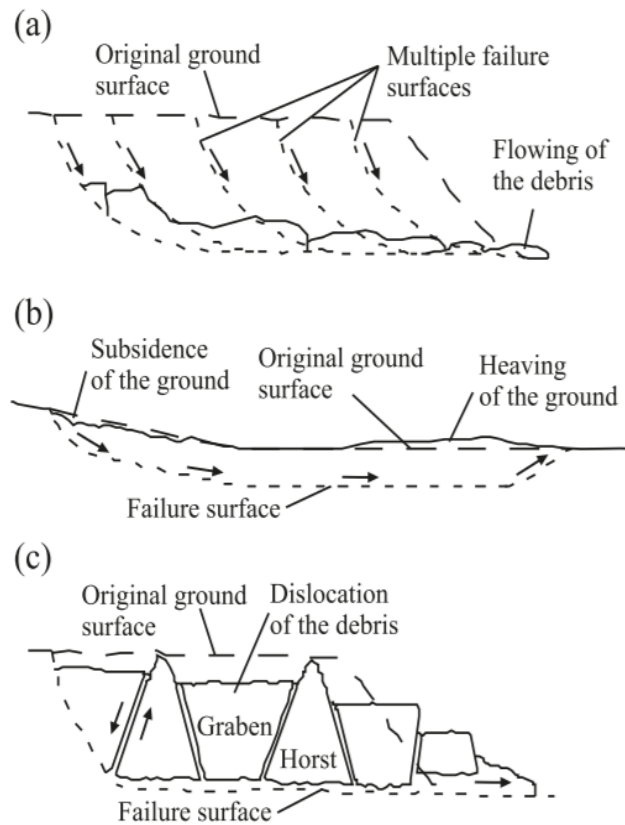
Fig. 2.13. Types of retrogressive landslides: (a) flow; (b) translational progressive landslide; and (c) spread.

A detailed discussion on the conditions required for retrogression and type of landslides is available in previous studies (Tavenas, 1984; Leroueil et al., 1996; Wang et al., 2020). However, the landside case studies considered in the present study are spread type, which was triggered by pile driving and other factors. Therefore, the failure mechanisms of spread are briefly described.

In a spread, a quasi-horizontal failure plane forms from the toe of the slope, and the soil mass above this failure plane fails successively in the form of horsts and grabens (Fig. 2.13(c)) (Odenstad, 1951; Carson, 1977, Cruden & Varnes, 1996; Locat et al., 2011). Locat et al. (2011) explained the quasi-horizontal failure plane formation in an infinite slope by applying a force

parallel to the ground surface. Their idealized model was verified later by conducting numerical simulations (Locat et al., 2013). Dey et al. (2015) used an Eulerian-based FE modeling approach and simulated the complete failure process in two-dimensional conditions, assuming that the failure was triggered by toe erosion (Fig. 2.14). As will be discussed in Chapter 5, spread type failure might also be triggered by other factors, such as pile driving, which will be investigated in the present study.
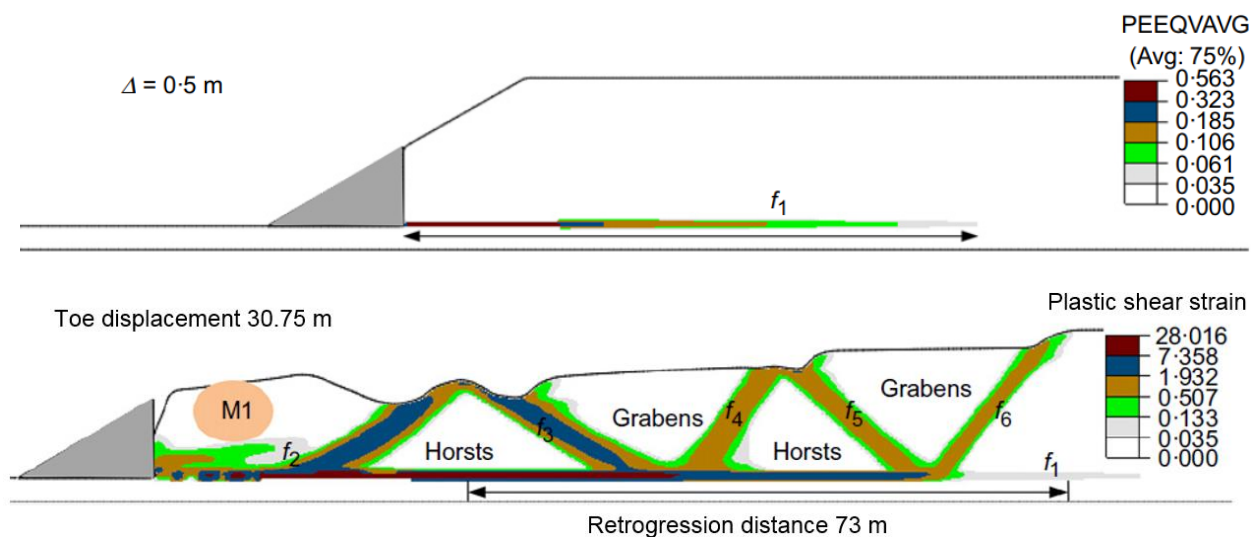
Fig. 2.14. Large deformation finite element simulation of spread (after Dey et al., 2015)

2.6 Slope stabilization using a piles

The use of piles to stabilize active landslides and slopes is one of the most innovative and effective slope reinforcement techniques. The analyses of the pile–slope stabilization can be classified into three main categories: (a) pressure-based method (Ito & Matsui, 1975; Viggiani, 1981), (b) displacement-based method (Poulos, 1995; Chow, 1996), and (c) continuum-based method (Cai & Ugai, 2000; Won et al., 2005).

The pressure-based method has been proposed by Ito and Matsui (1975) and Ito et al. (1981), which is based on the analysis of passive piles that are subjected to lateral soil pressure. They

considered the theory of plastic deformation as well as the plastic flow of the soil around the piles. The model was developed considering a rigid pile and only the soil near the piles is in plastic equilibrium. The main limitation of this method is that it only provides the ultimate pressure instead of the mobilized soil–pile pressure. In addition, the pile–soil interaction mechanisms are not considered. Viggiani (1981) proposed a dimensionless solution for the ultimate lateral resistance of a pile in a two-layer cohesive soil profile, where the ultimate soil–pile pressure (P_y) is calculated as $P_y = ks_uD$, where s_u is the undrained shear strength, D is the pile diameter, and k is the bearing capacity factor.

The displacement-based method calculates the lateral response of the pile due to the movement of soil above the failure surfaces. The lateral soil movements above the failure surface are used as an input to evaluate the associated lateral responses of the pile. This method involves an uncoupled analysis of pile–soil interaction, in which slope stability and pile response are considered separately. This method is better than the pressure-based methods because it can provide mobilized pile resistance with soil movement. Poulos (1995) and Lee et al. (1995) proposed an analysis method in which the pile is modelled as a simple elastic beam and the soil as an elastic continuum. Poulos (1995) proposed four different modes of failure depending on the embedment of the pile and the depth of failure surface: i) flow mode, ii) intermediate mode, iii) short pile mode, and iv) long pile mode. The main limitation of this method is that the slip surface location is predefined, which may not represent the actual failure phenomenon in a slope-pile system.

The continuum-based method can overcome the limitations of the other two methods. The slip surface location is not required to be considered in advance, as it develops progressively. The continuum-based finite element analysis can be performed in both two-dimensional (2-D) and three-dimensional (3-D) conditions. The slope-pile system can be represented more realistically in

a 3-D model. A number of previous studies used the 3-D finite element method (e.g. Cai & Ugai, 2000; Won et al., 2005) and showed that 3-D finite element modeling could be a better approach for slope stability analysis of a slope-pile system. For the pile stabilized slope, Cai and Ugai (2000) have considered the effect of piles on the stability of slope by a 3-D finite element analysis using the Strength Reduction Method (SRM). The SRM is the technique of artificial reduction of the shear strength of the soil to the point of failure. Some authors (e.g. Griffiths & Lane, 1999) have used this technique to find the maximum Strength Reduction Factor (*SRF*), leading to an unconverged computational solution due to an excessive mesh distortion in the failure plane.

Generally, the Lagrangian-based FE approach cannot handle large deformations. Moreover, the conventional limit equilibrium (LE) methods, which give only the location of the critical slip surface and factor of safety (FS) of the slope, cannot explain the mechanisms of those large-scale landslides. The recent development of Large Deformation Finite Element (LDFE) analysis can overcome those mesh convergence issues. A number of researchers successfully conducted large deformation finite element analyses for various geotechnical problems (Benson, 1992; Qiu et al., 2009, Dey et al., 2015; Karmaker et al., 2019; Wang et al., 2020). The following sections explain some important aspects of LDFE for soil–pile system analyses.

2.7 Large deformation finite element modeling

With the advancement of computational capabilities, different numerical techniques, such as finite element, finite difference, discrete element, and material point methods, have been used to model pile installation processes and subsequent impacts on various soils and slope stabilization using piles. This section briefly describes the main aspects of the large deformation finite element (LDFE) modeling technique.

Large deformation takes place when the initial and final geometry is completely different, as typical in failure analyses. Deformations can be expressed in terms of material kinematics. There are two types of material kinematics: i) Lagrangian formulation and ii) Eulerian formulation.

The movement of the continuum is specified as a function of the material coordinates and time in the Lagrangian formulation. The nodes of the Lagrangian mesh move together with materials. Therefore, the interface between two parts is precisely tracked and defined. In the large deformation simulations, large element distortion is expected.

On the other hand, the movement of the continuum is specified as a function of the spatial coordinate and time in the Eulerian formulation. In the Eulerian analysis, an Eulerian reference mesh that remains undistorted is needed to trace the motion of the material in the Eulerian domain. Material can move freely through an Eulerian mesh. No element distortion occurs during large deformation, which is the main advantage of using Eulerian formulation in FE modeling.

The coupling between Lagrangian and Eulerian formulation has started in the early 1960s in Los Alamos National Laboratory. The Arbitrary Lagrangian-Eulerian (ALE) and the Coupled Eulerian-Lagrangian (CEL) are two such methods, which have been proven as powerful and accurate alternatives of the analytical and experimental solutions.

Both ALE and CEL calculations are based on the operator-split scheme (Benson, 1992). In the first step, the Lagrangian simulation is performed, where the computational mesh deforms with soil particles. In the second step, a new mesh is generated which is called the rezoning step. The difference between CEL and ALE methods arises in this step, as shown in Fig. 2.15. In CEL, the rezoned mesh is simply the original mesh, while in ALE, a new distinct mesh is generated. Finally, the solution from the old mesh is transferred into the new mesh, which is called the remapping/advection step. This step is comparable to the solution in a classical Eulerian method.

For pile installation problems, many researchers have used large deformation numerical analyses, such as Remeshing and Interpolation Technique with Small Strain (RITSS) (Hu and Randolph, 1998; Wang et al., 2010, 2011), ALE (Wang and Gadala, 1997; Dong et al., 2018; Rooz et al., 2019) and CEL (Qiu et al., 2011; Ko et al., 2015; Konkol, 2015; Karmaker et al., 2019). However, pile installations in sensitive clays may exhibit some unique features, such as strain-softening and strain-rate effects, which is the main focus of the present study.
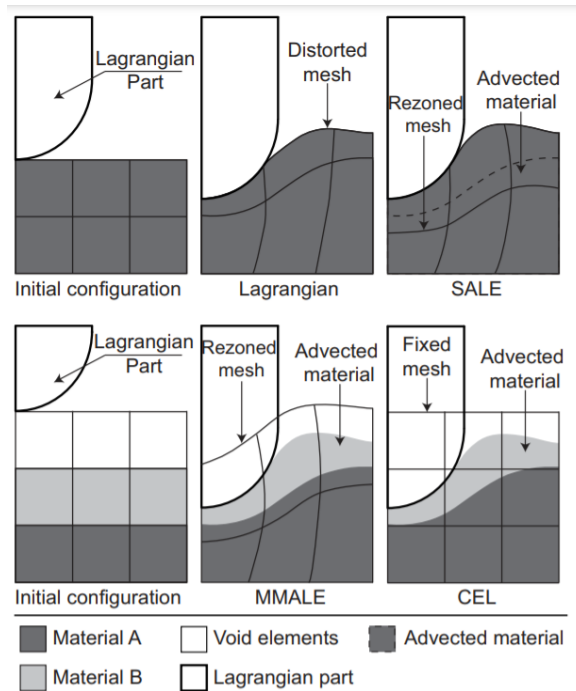
Fig. 2.15. Schematic diagram of single material ALE, CEL and Multi-material ALE approaches comparing the effects of mesh rezoning and advection steps of the solution (after Bakroon et al., 2017)

Because of the computational costs in 3-D analysis, 2-D FE techniques have been adopted to solve many geotechnical engineering problems. However, slope failures are actually 3-D in nature (Nian et al., 2012). Furthermore, according to previous studies, 2-D analysis results have been more conservative than 3-D analysis results (Chen and Chameau, 1985). Recent studies (Cai &

Ugai, 2000; Won et al., 2005; Wei & Cheng, 2009; Ho, 2015) reveal the advantages of using FE tools for stability analysis. Karmaker and Hawlader (2018) have successfully conducted slope stability analysis using the CEL method and showed its advantages over the LE method. The use of the CEL framework is useful for the determination of the factor of safety of the slope and can provide information on the formation and propagation of shear bands. The CEL approach is used in the present study, and further details are provided in Chapters 3–6.

2.8 Summary

Significant degradation of undrained strength of sensitive clay occurs when sheared. The formation of shear bands and excess pore water pressure generation due to the strain-softening behaviour of sensitive clays could play an important role in soil flow mechanisms during pile installation and possible slope failures. Although the consequences of these factors were observed in the field, they have not been properly investigated through numerical analysis. For example, during the installation of piles in sensitive clays, the effective horizontal stress near the pile surface was found to be almost zero in the field investigations, which implies no pile–soil interface resistance. Also, the sensitive clay around the pile surface could be severely remoulded during pile installation. Therefore, the displaced soil could flow through this remoulded zone. Also, calculating the excess pore water pressure during the penetration of a pile over a large distance needs to be studied. Moreover, if the pile is installed near a slope, the displaced soil will have a tendency to move towards the slope as it is in a less constrained condition. Such displacement could trigger the failure of sensitive clay slopes. Therefore, in the present study, the pile installation process, its impact on the sloping ground (e.g. slope failures) and lateral pile–soil interaction are analyzed using large deformation FE modeling techniques.

Chapter 3

Numerical modeling of pile jacking in sensitive clays

Co-Authorship: This chapter has been submitted as a technical paper for publication in a journal as: Karmaker, R., Hawlader, B., Perret, D. and Dey, R., 'Numerical modeling of pile jacking in sensitive clays.' Most of the research presented in this chapter has been conducted by the first author. He also prepared the draft manuscript. The other authors mainly supervised the research and reviewed the manuscript.

3.1 Abstract

Installation could heavily deform the soil around a displacement pile. The increase in stresses and strains together with resulting shear strength degradation and ground heave are concerns in the construction of piles and estimation of axial capacity. A numerical investigation of pile penetration in highly sensitive clays is presented in this study. Simulations are performed using a Coupled Eulerian-Lagrangian (CEL) finite-element (FE) modeling technique considering the effects of strain softening and strain rate on the undrained shear strength of sensitive clay. A significantly different soil deformation is obtained for sensitive clays because of its strain-softening behaviour compared to the responses for non- to low-sensitive clays. The radial stress due to pile installation decreases significantly with an increase in the rate of softening of sensitive clay and could be almost half of that for non-sensitive clays. The limitations of simplified approaches, such as cavity expansion and strain path methods, are highlighted to analyze pile installation effects in sensitive clays.

3.2 Introduction

The conventional pile installations, such as pile driving and vibro-driving, could cause unacceptable ground vibration and disturbance. Pile jacking is an alternative method to avoid such issues, where a pile is pushed into the soil at a constant velocity using a jacking machine up to the jack stroke length. White et al. (2002) reported two sites near an urban environment, where the use of press-in piling reduced the ground vibration 10–50 fold compared to diesel hammer or vibratory piling methods. However, the pile jacking process involves the displacement of a large volume of soil which might create several issues, especially in soft sensitive clay soils, such as the degradation of strength of the soil, reduction of axial load capacity, changes in radial stresses during pile jacking, disturbance in soil, large soil deformation and ground heave. The strain-softening and strain-rate effects on the shear strength of sensitive clay might cause complex ground responses during pile jacking.

Comprehensive reviews of field investigations of pile installation effects are available in previous studies (e.g., Flaate, 1972; Fellenius & Samson, 1976; Bozozuk et al., 1978; Blanchet et al., 1980; Roy et al., 1981; Bond & Jardine, 1991; Lehane & Jardine, 1994; Chow, 1997; Jardine et al., 1998; De Chaunac & Holeyman, 2018). Some of these limited field studies focused on the behaviour of piles in highly sensitive clays. An experimental study was carried out at the Saint-Alban site in Québec, Canada, where six instrumented piles of 219-mm outer diameter (D) were jacked into a highly sensitive clay layer ($S_t = 17$) below the crust (Roy et al., 1981; Roy & Lemieux, 1986). By measuring the end bearing (f_b) using a load cell, the contribution of skin friction (f_s) was identified. In addition, the change in undrained shear strength (s_u) and increase in pore water pressure (u_e) from the in situ hydrostatic pressure (u_0) were measured. During the penetration of a pile in sensitive clay without interruption, f_b increased with depth; however, the increase in f_s was

small. A significant decrease in s_u in the soil near the pile was observed, while s_u after $3D$ of radial distance was almost the same as the s_u of the intact clay. Azzouz and Morrison (1988) evaluated the shaft friction during installation by inserting a piezo-lateral stress cell where the pile was installed in a Boston Blue Clay layer ($S_t = 7 \pm 2$) from the bottom of a prebored hole. They also measured the total horizontal stress (σ_h) and pore water pressure (Azzouz & Morrison, 1988). During installation, σ_h is slightly larger than u, which implies that the effective horizontal stress $\sigma'_h (= \sigma_h - u)$ acting on the pile shaft during penetration is very small. The installation earth pressure coefficient K_i ($= \sigma'_h/\sigma'_{v0}$, where σ'_{v0} is the in situ effective vertical stress) is 0.05–0.2, which is significantly lower than the earth pressure coefficient at rest K_0 ($= \sigma'_{h0}/\sigma'_{v0}$, where σ'_{h0} is the in situ effective lateral stress) of 0.55–0.7. However, such a significant decrease in the lateral earth pressure coefficient was not found during the penetration of piles in low sensitive Lower Empire clay ($S_t = 2 \pm 1$), where K_i and K_0 were 0.38 and 0.72, respectively (Azzouz & Lutz, 1986; Azzouz & Morrison, 1988). This implies that the remoulding of sensitive clay significantly affects pile penetration. Karlsrud and Haugen (1985) investigated the penetration behaviour of a 5-m long 153-mm diameter instrumented pile in overconsolidated ($OCR = 5$) clay at the Haga test site outside Oslo, Norway. An approximately 15-mm thick soil layer near the pile surface was completely remoulded due to penetration; however, the penetration effects on s_u were negligible after about $1.0D$–$1.3D$ from the pile surface. Also, σ_h and u near the pile surface were almost the same during penetration (i.e. $\sigma'_h \sim 0$). Lehane and Jardin (1994) jacked 102-mm diameter instrumented piles in Bothkennar clay ($S_t \sim 5$, $OCR \sim 1.7$, $LL \sim 0.7$) and showed high pore pressure development during penetration. A clear trend of decreasing radial stress ratio (σ'_h/σ'_{h0}) with increasing sensitivity was found during installation and subsequent pore pressure equalization

(Lehane, 1992; Jardine et al., 1998). The shaft friction generally increases with depth for non-sensitive clays (Chow, 1997).

Undrained installation of the pile in clays has been modelled using mainly three approaches: (*a*) cavity expansion method (CEM), (*b*) strain path method (SPM), and (*c*) FE analysis. In CEM, a long cylindrical cavity is created by radial expansion from a zero initial radius, which is considered analogous to the soil deformation around the pile during installation at locations sufficiently far from the ground surface and pile tip (Butterfield & Banerjee, 1971; Vesić, 1972; Randolph & Wroth, 1979). The CEM is relatively simple; however, it does not model soil shearing along the pile shaft and soil flow around the pile tip, which could induce significant shear strength degradation of sensitive clays. The SPM assumes that the penetration behaviour can be reasonably modelled by kinematic consideration only, independent of soil resistance, because of severe kinematic constraint during deep penetration (Baligh, 1985). According to Baligh (1985), the process of penetration is reduced to a flow problem where the soil particles move along the streamlines around a fixed rigid body. Early analyses considered steady deep penetration of a pile in incompressible soil in an undrained condition based on total stress analysis (Baligh, 1985; Teh & Houlsby, 1991). Later improvement of SPM includes using an effective stress approach to calculate stresses and pore pressure (Whittle et al., 1993) and developing shallow SPM to simulate penetration from the stress-free ground surface (Sagaseta & Whittle, 2001). Many studies focused on the development of large deformation FE modeling techniques in the past several decades, which include the arbitrary Lagrangian-Eulerian (ALE) approach, remeshing and interpolation technique with small strain (RITSS), and Coupled Eulerian-Lagrangian (CEL) approach (Benson, 1989; Hu & Randolph, 1998; Walker & Yu, 2006; Qui et al., 2011; Tho et al., 2012; Wang et al., 2015; Ko et al., 2016; Zhou et al., 2019). These techniques have been used to simulate penetration

of offshore pipeline (Merifield et al., 2009; Chatterjee et al., 2012; Dutta et al., 2015), cone (Walker & Yu, 2006; Liyanapathirana, 2009), spudcan (Hossain & Randolph, 2009; Yi et al., 2012) and piles (Henke & Grabe, 2009; Ko et al., 2016). The penetration of piles has been simulated mainly for non-sensitive to low-sensitive clays and, in some studies, without considering the strain-rate effects on undrained shear strength (Karmaker et al., 2019; Zhou et al., 2019).

In summary, field investigations show a significantly different pile penetration response in moderate- to highly sensitive clays than that in non- to low-sensitive clays, which has been investigated in the present study by conducting large-deformation FE analysis. The paper has been organized as follows. The first part presents CEL modeling of pile penetration. The second part compares the FE simulations with the results of field tests in a highly sensitive clay in Québec, Canada. Finally, a detailed parametric study is presented, specifically the effects of post-peak shear strength degradation on penetration resistance and soil disturbance.

3.3 Methodology

Steady penetration of a solid cylindrical pile into soft sensitive clay under undrained conditions is simulated for two soil conditions:

a) Idealized soil profiles

In this case, the initial undrained shear strength (s_{u0}) of the sensitive clay layer (i.e., prior to softening and at the reference strain rate, as discussed later) increases linearly with depth as

$$s_{u0} = s_{ug} + kz \tag{3.1}$$

where s_{ug} is a constant (kPa); k is the strength gradient (kPa/m), and z is the depth of the soil element below the ground surface (m). The same soil profile is used in simulations without the strain rate and strain softening effect to compare the model performance with previous analytical and numerical studies. The groundwater table is considered at the ground surface, and the soil is

assumed to be fully saturated. A solid pile of 0.4-m diameter (D) is jacked under a constant velocity

(Fig. 3.1). The bottom of the pile is modelled as a half-sphere. The pile is penetrated to a maximum

depth of 10D because the rate of increase in normalized penetration resistance and soil flow

mechanisms below this depth is similar. At any instant, the depth of the pile tip (point T in the

inset of Fig. 3.1) from the ground surface is denoted as z_{tip}. At the start of the calculation, the pile

tip is placed slightly above the ground surface (0.01 mm) to avoid any pile–soil interaction during

the *in-situ* stress establishment step by gravity loading. The radial distance of a soil element from

the pile centerline and pile surface is denoted by w_i and w_s, respectively (Fig. 3.1(b)).
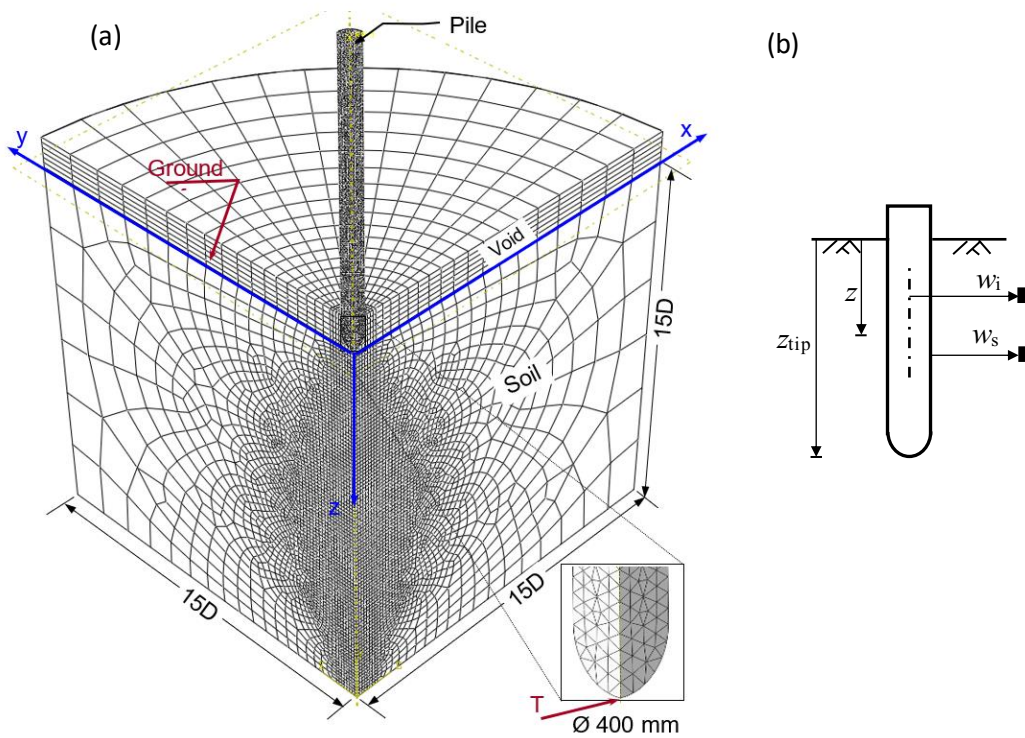
Fig. 3.1. Problem statement: (a) typical finite element mesh for parametric study with

idealized soil profile; (b) notations

b) Saint-Alban field test

In this field test, FE analysis is performed to simulate pile jacking in highly sensitive clay with a sensitivity of ~ 17 determined by the field vane test (Roy & Lemieux, 1986). The tests were conducted at a site in Saint-Alban in Québec, Canada. A detailed geotechnical investigation was carried out, which includes field vane (FV) shear, static cone penetrometer, pressuremeter, isotropically consolidated undrained and unconsolidated undrained triaxial compression tests (La Rochelle et al., 1974; Roy et al., 1974; Tavenas & Leroueil, 1977). As shown in Fig. 3.2, the soil profile consists of 0.4-m topsoil, 1.2-m weathered clay crust, 8.2-m soft silty clay of glaciomarine origin, 4.0-m very soft clayey silt, and a strong and dense sand layer below 13.4 m. Six instrumented steel piles of 219-mm outer diameter (D) and 7.5-m length were jacked statically and slowly from a pre-bored hole of 1.5 m depth in the crust. Among the six, the details of two tests (piles 2 and 5) have been presented in previous studies, which includes the response during and immediately after the installation and long-term behaviour after pore pressure dissipation (Roy et al., 1981; Roy & Lemieux, 1986; Konrad & Roy, 1987). In the present study, only the short-term behaviour during the installation of piles 2 and 5 is simulated. Note that the penetration rate of the piles was 1 cm/min and 7 cm/min, respectively, in the field study carried out by Roy et al. (1981).

Figure 3.2 shows that, although scattered, there is a clear trend of increasing undrained shear strength (s_{u0}) with depth below the crust. The upper bound values of s_{u0} from the FV tests reasonably match with the available triaxial test results. Note that s_{u0} in FV tests in sensitive clays might be higher or lower than that of triaxial tests, depending upon the disturbance due to insertion of vane, undisturbed sample collection for triaxial tests, mode of shearing, stress-strain behaviours, and rate of loading, including drainage (Lefebvre et al., 1988; Roy & Leblanc, 1988). In this study, FE analyses are performed with two initial shear strength profiles, where the s_{u0} profile-1

approximately represents the triaxial and upper bound FV s_{u0}, whereas the s_{u0} profile-2 represents

a case similar to the average value of FV tests. For both cases, s_{u0} in the crust is assumed to be

decreased from 45 kPa to 15 kPa at the bottom of the crust. Weathering and environmental effects

might significantly change the shear strength and drainage conditions of the crust. Also, whether

the crust should be modelled as an undrained or drained condition is still questionable (Perret et

al., 2019; Wang et al., 2020). In any case, the crust does not have a significant effect in these

simulations because the jacking started from a pre-drilled hole which is only 0.4 m above the

bottom of the crust.

3.4 Numerical modeling

The Coupled Eulerian-Lagrangian (CEL) approach available in Abaqus/Explicit FE software is

used in the present study. Unlike traditional Lagrangian-based FE methods, where the mesh

deforms with the displacement of the material, CEL allows the Eulerian materials (e.g., soil) to

flow through the fixed mesh. Therefore, numerical issues related to mesh distortion are not

encountered. The Eulerian material is defined and tracked by Eulerian Volume Fraction (EVF)

tools. EVF = 1 represents the element completely filled with Eulerian material, EVF = 0 represents

no materials in the element (i.e. void), and 0 < EVF < 1 represents the elements partially filled

with Eulerian materials.

In Abaqus/Explicit, the Eulerian approach has been implemented only for three-dimensional

elements. Only one-fourth of the total model is simulated by taking advantage of symmetrical

conditions. Figure 3.1(a) shows the FE mesh for a parametric study with the idealized soil profile.

Fine mesh is used where a considerable soil displacement occurs during installation. A similar FE

mesh is used for the Saint-Alban field test simulation, except for a larger depth of soil domain (15

m) and smaller pile diameter (219 mm). The Eulerian domain is discretized with 8-node linear brick elements. The pile is modelled as a rigid body.

A zero-velocity boundary condition is applied normal to all the vertical faces. At the bottom of the domain, zero-velocity boundary conditions are applied in all three directions (i.e., $v_x = v_y = v_z = 0$), meaning that the soil elements next to this boundary are restrained from any movement. No boundary condition is applied at the soil–void interface so that the soil can displace into the void during the penetration of the pile when needed (e.g., ground surface heaving near the pile).

Most of the simulations are performed with smooth pile–soil interface conditions; however, in some simulations, a maximum interface resistance (τ_{max}) of 6 kPa is given using the general contact algorithm.
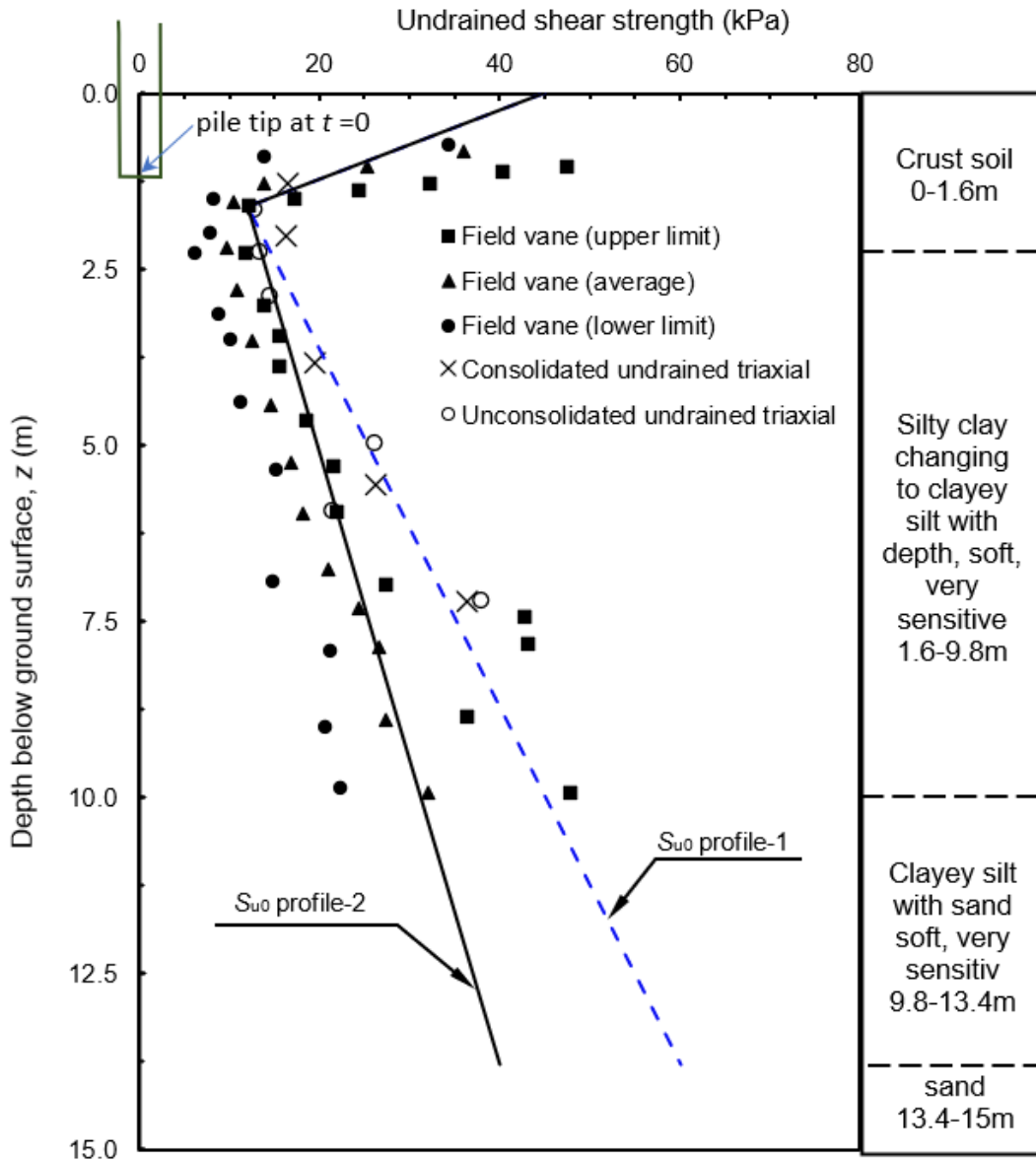
Fig. 3.2. Soil profiles used for Saint-Alban test simulation (data points are from Roy et al., 1981)

To establish the in-situ stress condition, initial stresses ($K\sigma_{v0}$, $K\sigma_{v0}$, σ_{v0}) are applied first to the soil elements (EVF $\neq$ 0), where σ_{v0} is the vertical total stress, and K is the ratio between horizontal and vertical total stresses. Then the gravitational load is applied to the soil elements and brings in an equilibrium condition. If the groundwater table is at the horizontal ground surface, K is related

46

to the effective earth pressure coefficient at rest (K_0) as $K = K_0 + (1 - K_0)\gamma_w/\gamma$. By defining the initial condition in this way, the simulation can be performed for $K_0 > 1$, as observed in some sensitive clays (e.g., in eastern Canada; Hamouche et al., 1995).

The pile is penetrated at a constant velocity of 0.1 m/s. Review of field investigations shows that jacking was carried out at $v = 0.01$–0.001 m/s (e.g., Roy et al., 1981; Yang et al., 2006; Kou et al., 2015), which are 10 to 100 times slower than the adopted velocity in the present numerical study. In numerical analysis, such a slow penetration rate is not required because it unnecessarily increases the computational time (Tho et al., 2012; Wang et al., 2015). However, it is important to establish a quasi-static loading condition for all analyses, which will be discussed later.

3.5 Modeling of sensitive clays

The undrained analysis is performed by adopting the von Mises yield criterion. The mobilized undrained shear strength (s_u) of sensitive clays is modelled using Eq. (3.2), incorporating a strain-softening factor, f_1 (≤ 1.0) and strain-rate factor, f_2 as

$$s_u = f_1 f_2 s_{uy} \tag{3.2}$$

where s_{uy} is the undrained shear strength at a very low strain rate. The sensitive clays show anisotropic undrained shear strength (e.g., Karlsrud & Hernandez-Martinez, 2013); however, this study has not considered it.

3.5.1 Strain softening behaviour of sensitive clay

Linear and exponential reduction factor f_1 as the function of accumulated plastic shear strain or plastic shear displacement (δ) has been used in previous studies (Locat et al., 2013; Dey et al., 2015, 2016). The following equations are used in the present study for modeling post-peak s_u degradation.

$$
f_1 = \begin{cases} \dfrac{s_{uR}}{s_{u0}} + \left(1 - \dfrac{s_{uR}}{s_{u0}}\right) e^{-3\delta/\delta_{95}} & \text{if } 0 \le \delta < 2\delta_{95} \\[3mm] \dfrac{s_{uR}}{s_{u0}} - \dfrac{s_{uR} - s_{uld}}{s_{u0}} \dfrac{\delta - 2\delta_{95}}{\delta_{ld} - 2\delta_{95}} + c & \text{if } 2\delta_{95} \le \delta < \delta_{ld} \\[3mm] \dfrac{s_{uld}}{s_{u0}} + c & \text{if } \delta \ge \delta_{ld} \end{cases}
\tag{3.3}
$$

Where s_{u0} is the peak undrained shear strength at the reference shear strain rate ($\dot{\gamma}_{ref}$) before softening; s_{uR} is the value of s_u at sufficiently large δ; δ_{95} is the value of δ at which 95% reduction of ($s_{u0} - s_{uR}$) occurs; $c = (1 - s_{uR}/s_{u0})e^{-6} \approx 0$; and δ_{ld} is a very large value of δ ($> \delta_{95}$) when the soil becomes completely remoulded to $s_u = s_{uld}$. Equation (3.3) represents a quick exponential degradation of s_u at $0 \le \delta < 2\delta_{95}$ followed by a linear degradation at $2\delta_{95} \le \delta < \delta_{ld}$ and then a constant s_u ($= s_{uld}$) at $\delta \ge \delta_{ld}$. Equation (3.3) for $0 \le \delta < 2\delta_{95}$ is similar to the s_u degradation equation proposed by Einav & Randolph (2005).

As will be shown later in this chapter, the plastic shear strain or shear displacement developed during the installation of a pile is not extremely large, as happened in some other large deformation problems (e.g. landslides). Therefore, the strain-softening is mainly governed by the exponential degradation (first part of Eq. (3.3)). In other words, the rate and magnitude of post-peak shear strength degradation primarily depend on s_{uR} and δ_{95}. Therefore, in the later sections, a detailed investigation of the effect of these two factors is performed.

Dey et al. (2016) showed a wide variation of s_{uR}, $\delta_{95,}$ and δ_{ld} when the model was compared with test results on sensitive clays from different sites conducted by Tavenas et al. (1983). Table 3.1 shows the model parameters used in FE modeling unless otherwise mentioned. The values of these parameters are obtained from a detailed review of previous studies (Tavenas et al. 1983; Quinn et al., 2011; Dey et al., 2016).

3.5.2 Strain-rate effects on undrained shear strength of sensitive clays

A detailed discussion on strain-rate effects on undrained shear strength is available in previous studies (e.g., Zhu & Randolph, 2011; Zakeri & Hawlader, 2013; Wang et al., 2021). In the present study, an "additive power-law model" proposed by Zhu & Randolph (2011), which combines the Herschel-Bulkley (fluid mechanics approach) and power-law model (geotechnical approach), is used:

$$f_2 = \left[1 + \eta \left(\dot{\gamma}/\dot{\gamma}_{ref} \right)^{\beta} \right] \tag{3.4}$$

where η and β are the soil parameters. The value of η depends on the reference shear strain rate. The typical range of β is 0.05–0.15, which increases with the plasticity index. Based on previous studies (Boukpeti et al., 2012; Randolph et al., 2012; Wang et al. 2020), $\eta = 0.5$ and $\beta = 0.1$ are used in the present study. Using $\dot{\gamma} = \dot{\gamma}_{ref}$ in Eq. (3.4) and then inserting f_2 in Eq. (3.2) with $f_1 = 1.0$ (no softening) and $s_u = s_{u0}$, the undrained shear strength at a very low strain rate can be calculated as $s_{uy} = s_{u0}/(1 + \eta)$. However, the process becomes partially drained or drained at a low shearing rate in the field. For example, vane shear tests in low plastic sensitive clays show that the shear strength does not decrease at a very slow rate of rotations; instead, it increases because of excess pore water pressure dissipation (Roy & Leblanc, 1988). Therefore, in the present study, $s_u = s_{u0}$ is used when $\dot{\gamma} \leq \dot{\gamma}_{ref}$ Also, as the numerical simulation is performed with a higher penetration rate than the typical field jacking rate (discussed above), a higher value of $\dot{\gamma}_{ref}$ is used to model comparable rate effects on s_u (Table 3.1).

The strain-softening and rate effects on undrained shear strength (Eqs. (3.2)–(3.4)) and the variation of s_{u0} with depth (Eq. (3.1) and Fig. 3.2) are implemented in the software using a user-defined subroutine. s_{u0} is called in the subroutine only for the first time and stored as a state

variable, which is used to calculate the mobilized s_u in the subsequent time increments to ensure the use of the initial s_{u0} of the soil element even though it might have displaced to a different location from the initial depth. The equivalent plastic shear strain ε_q^p (PEEQVAVG in the software) is called in the subroutine for each time increment and also stored as a state variable. Here, ε_q^p is a scalar quantity which is the integration of plastic deviatoric strain rate tensor $(\dot{\varepsilon}_{ij}^p)$ over the period of analysis (i.e., $\int_0^t \sqrt{2/3 \dot{\varepsilon}_{ij}^p \dot{\varepsilon}_{ij}^p} dt$). The "element size scaling rule" is used to reduce the mesh dependency of the solution. In the FE program, based on Eq. (3.3), the variation of s_u is given as a function of plastic shear strain by giving its value when 95% degradation of s_{u0}-s_{uR} occurs ($\varepsilon_{q\_95}^p$). Assuming simple shear condition, $\varepsilon_{q\_95}^p = \delta_{95}/\sqrt{3} t_{FE}$ can be obtained, where t_{FE} is the characteristic length of the finite element (cube root of the element volume). That means, the higher the element size, the smaller the $\varepsilon_{q\_95}^p$, indicating a steeper s_u–ε_q^p the curve for larger elements. In the subroutine, t_{FE} is calculated for each element, which is then used to calculate $\varepsilon_{q\_95}^p$ and then the strain-softening factor f_1.

Table 3.1. Soil parameters used in finite element modeling

Parameter	Sensitive Clay
Total unit weight, γ (kN/m^3)	17
Undrained Young's modulus, E_u (MPa)	10
Undrained Poisson's ratio, ν_u	0.49
Initial undrained shear strength of sensitive clay, s_{u0} (kPa)	$(s_{ug} + kz)^a$
Ratio between initial and remoulded undrained shear strength, s_{u0}/s_{uR}	5
Ratio between initial and large deformation undrained shear strength, s_{u0}/s_{uld}	50
Plastic shear displacement for 95% degradation of s_{u0}-s_{uR}, δ_{95} (m)	0.1
Plastic shear displacement to mobilize s_{uld}, δ_{ld} (m)	$20\delta_{95}$
Reference strain rate, $\dot{\gamma}_{ref}$ (s^{-1})	5.0
η	0.5
β	0.1

Note: $^a s_{u0}$ is constant for FE model verification; s_{u0} is shown in Fig. 3.2 for Saint-Alban test simulations; $s_{ug} = 20$ kPa and $k = 1.67$ kPa/m for idealized soil layer in the parametric study.

3.6 Results

In the following sections, the discussion is primarily focused on the force–displacement relation, development of plastic shear strain, shear strength degradation, changes in radial stress and soil failure mechanisms during penetration. The penetration resistance has two components: (a) the resistance from the shear strength of soil (F_s), and (b) self-weight, which is similar to buoyancy (F_b). A detailed discussion on interpreting the effects of buoyancy on undrained penetration of an object in soft clay is available in the work of Merifield et al. (2009).

In the present FE analysis, the total resistance (F) for a given pile tip depth (z_{tip}) is obtained from the reaction force at the reference point of the rigid pile. For clay, subtracting F_b from F, the soil resistance is obtained as $F_s = F - F_b$. The soil resistance is then presented as a normalized

penetration resistance (N) as $N = F_s/s_u A_p$, where A_p is the cross-sectional area of the pile. The F_b is calculated as $\gamma A_p z_{tip}$, where γ and $A_p z_{tip}$ are the total unit weight of soil and the volume of the displaced soil, respectively.

The result section is divided into three major subsections to describe the FE modeling of pile jacking in sensitive clay. First, a non-sensitive clay soil model is considered to check the FE model performance with various analytical and numerical solutions. Then, the chapter intends to validate the field investigation of Roy et al. (1981) using the Large Deformation Finite Element (LDFE) modeling technique. Finally, a detailed parametric study is carried out to find the effects of post-peak shear strength degradation during pile jacking.

3.6.1 Penetration resistance of non-sensitive clay soil

Firstly, FE model results are compared with different analytical and numerical approaches for uniform s_u with depth. Figure 3.3 shows the normalized penetration resistance versus pile tip depth for various analytical and numerical studies. Similar to some previous studies (Walker & Yu, 2006; Wang et al., 2015; Zhou et al.; 2019; Karmaker et al., 2019), a smooth soil–pile interface is considered in these simulations.

The present study provides a good agreement with CEL analyses presented by Wang et al. (2015); however, it gives a higher normalized resistance than obtained from RITSS. Note that, in RITSS, the soil-structure interface is considered fully bonded, whereas, in CEL, the separation is allowed between soil and structure. Meyerhof (1951) recommended an end bearing factor of 9.34 for perfectly smooth circular piles. Based on analytical solutions, Randolph and Houlsby (1984) recommended $N = 9.14$ and $N = 11.32$ for perfectly smooth and perfectly rough interface conditions. FE simulations of cone penetration show that the penetration resistance depends on the rigidity index of soil ($I_r = G/s_u$, where G is the shear modulus of the soil): N is 10–13 for the rigidity

index of 100–500 for the smooth interface condition (Teh & Houlsby, 1991; Walker & Yu, 2006).

The present study also shows an increase in N for higher values of I_r, at larger depths.
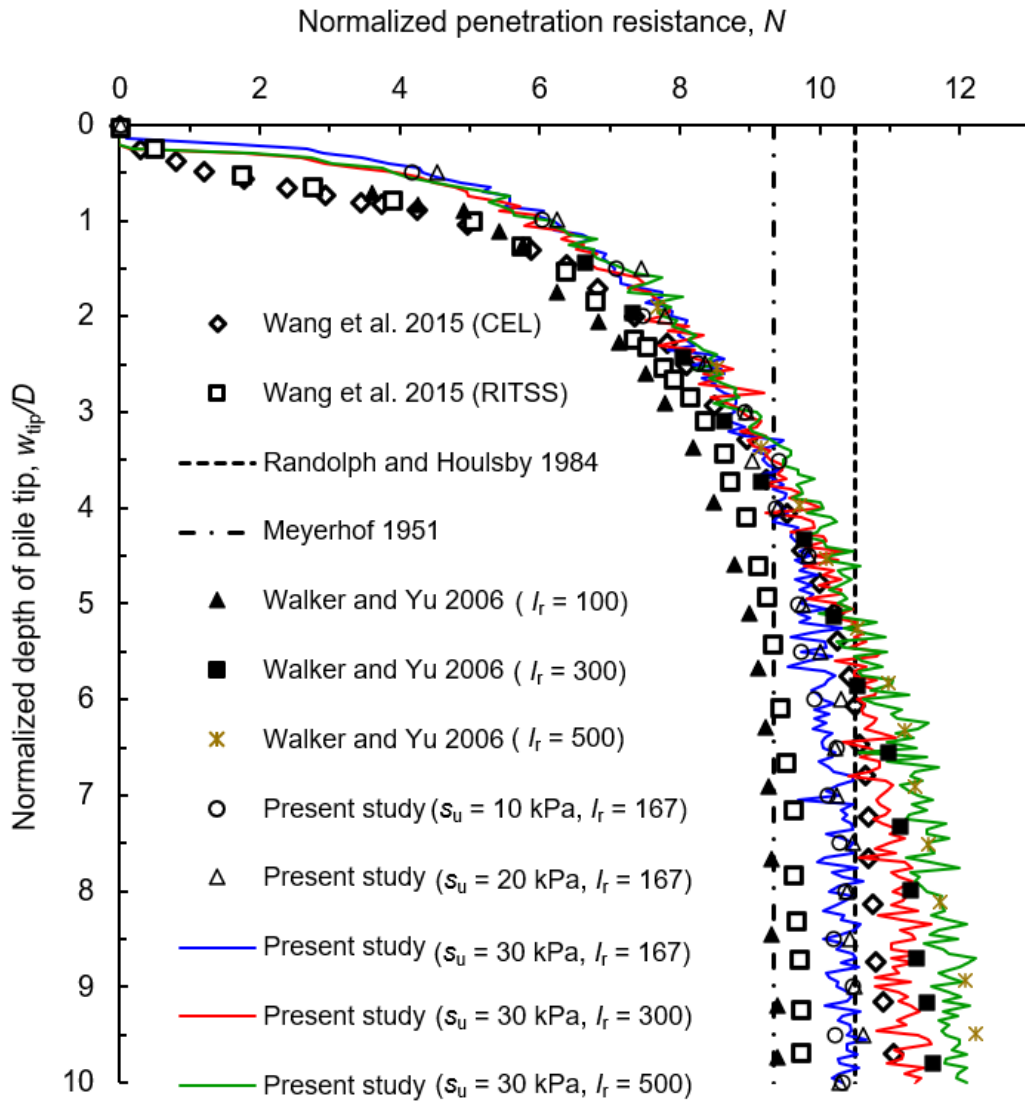
Fig. 3.3. Penetration resistance for uniform undrained shear strength

3.6.2 Saint-Alban test simulation results

Figure 3.4 shows the comparison between penetration resistance obtained from FE simulation and field test. The simulations are performed for two piles. In the field, pile-5 was jacked

continuously at a rate of 7 cm/min. However, pile-2 was jacked in two sequences—penetrated to 4.5 m depth at a rate of 1 cm/min and then after waiting ~ 16 hours, it was again penetrated at the same rate to the final depth.

For pile-5, the contribution of skin friction to the total penetration resistance did not increase significantly with depth (open triangle in Fig. 3.4(a)), which indicates relatively small skin friction from the sensitive clay layer. Therefore, the analysis was performed first with a smooth pile–soil interface condition, which would give only the tip resistance. Further discussion on skin friction is provided in the following section. Figure 3.4(a) shows that FE calculated tip resistance compares well with the measured values, where the s_{u0} profile-1 (Fig. 3.2) is slightly higher while the s_{u0} profile-2 gives slightly lower tip resistance than the field data. Note that the tip resistance was measured in the field using a total pressure cell located below the tip. Therefore, this value includes the buoyancy force (F_b), as discussed above. For example, at the maximum depth of penetration ($z = 8.2$ m), the total tip resistance is 15.7 kN for the s_{u0} profile-2, in which F_b is 5.25 kN (= volume of the penetrated segment × soil unit weight). Therefore, the soil resistance F_s is 10.45 kN, which gives $N = 10.0$. One analysis is performed for ideal soil (i.e., $f_1 = f_2 = 1.0$ in Eq. 3.2) to quantify the effects of strain rate and strain-softening. Figure 3.4(a) shows that this analysis can also reasonably calculate the tip resistance. However, it should be noted that strain-softening has a profound effect on soil remoulding and thereby the skin friction (assumed zero in this simulation) and subsequent consolidation process, as discussed in the following sections.

For pile-2, the penetration resistance due to skin friction did not increase significantly during penetration through sensitive clay (open triangle in Fig. 3.4(b)), which is similar to the observation for pile-5, as discussed above. However, there was a jump in penetration resistance of ~ 6 kN when the penetration was resumed after 16 hours, which was attributed to the dissipation of pore pressure

during this pause (Roy et al., 1981). In the second phase of penetration, more variation in the penetration resistance from the average value was observed, which might be due to the variation of soil properties of different layers (see Fig. 3.2). Based on the small change in the skin friction contribution during continuous penetration, a FE simulation is performed for pile-2 with a smooth pile–soil interface condition. Simulation is performed only for the second phase, starting from 4.5 m. Figure 3.4(b) shows that the tip resistance obtained from the FE simulation matches well with the measured values in the field. In summary, these simulations show that the tip resistance can be calculated using the present FE approach; however, the potential causes of low skin friction need to be examined further. The following were the key observations: (*a*) a small increase in F_s occurred with depth when the pile was penetrated continuously into the sensitive clay layer; (*b*) in a pile (#2 of their study), F_s increased significantly as the skin friction increased when jacking resumed after 16 hours; (*c*) excess pore water pressure dissipation occurred during the installation break, which may have increased the skin friction and F_s.

Disturbance of soil around the pile

Figure 3.5 shows the variation of mobilized s_u with radial distance from the outer surface of the pile when the tip of pile-5 is at 8.2 m depth. The variation is shown for four z values ($= 4, 8, 8.2$ & 10 m) of this tip position. No strength degradation occurs (i.e., $s_u/s_{u0} = 1$) in soil elements sufficiently below the pile tip (e. g., $z = 10$ m). s_u/s_{u0} decreases when the tip of the pile comes close to the soil element. However, once the tip moves sufficiently far from a level, further penetration does not cause an additional reduction of s_u/s_{u0}; therefore, s_u/s_{u0} for $z = 4$ and 8 meters are almost identical because there is no significant increase in plastic shear strain. s_u/s_{u0} increases with radial distance, and after $2.0D$–$2.5D$, strength degradation is negligible.
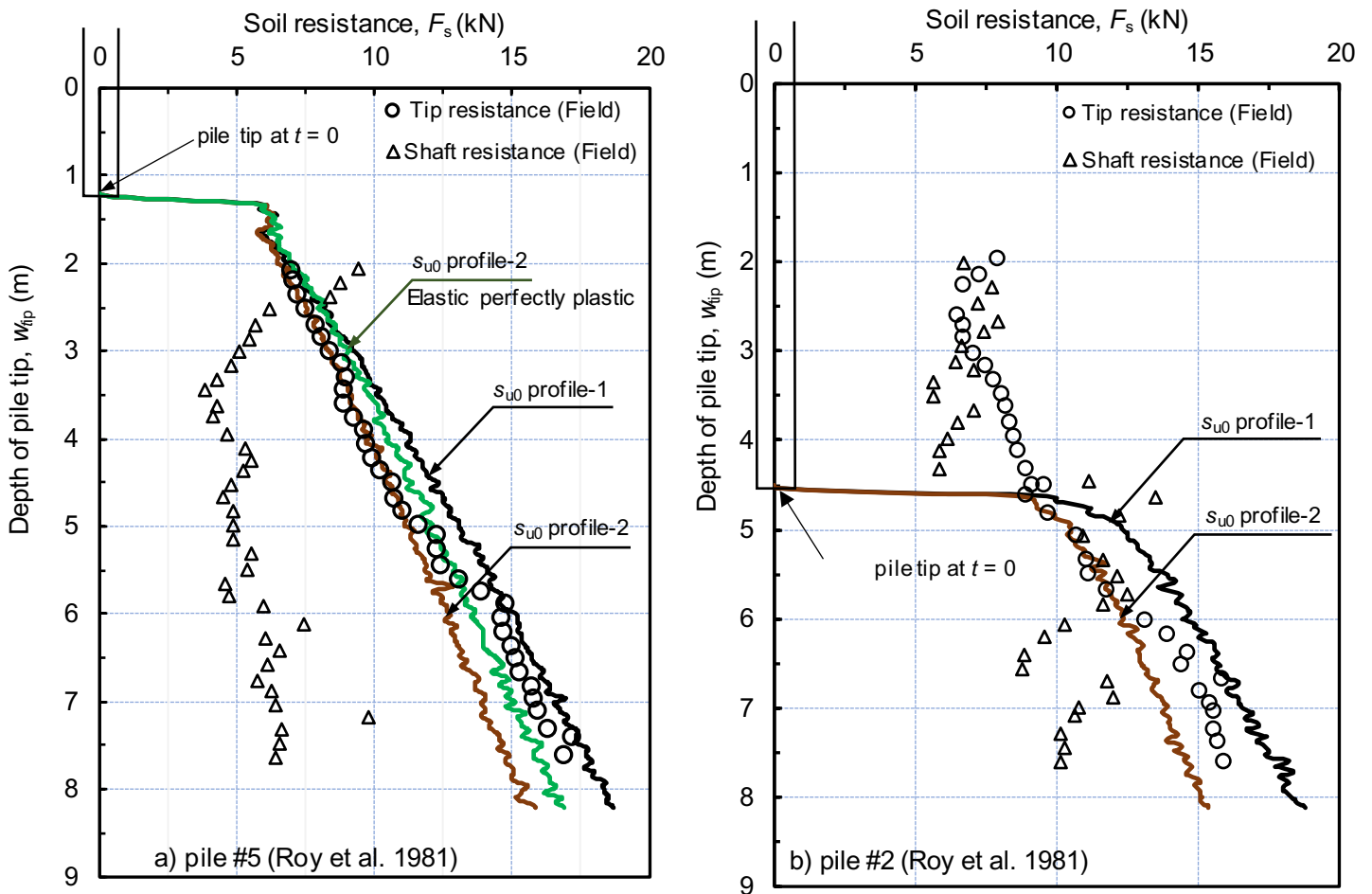
Fig. 3.4. Comparison of finite element calculated penetration resistance with field test results:

(a) for pile #5; (b) pile #2 (data points are from Roy et al., 1981)

Roy et al. (1981) also conducted in situ vane shear tests immediately after pile installation and

found a 25–40% reduction of shear strength in the soil elements within one diameter from the pile

wall, and the disturbance extended up to ~ 3.5D from the pile center (Fig. 3.5), which is somewhat

larger than some previous studies, where disturbance of 1.5D–2.0D was observed (Flaate, 1972;

Bozozuk et al., 1978). Figure 3.5 shows an average trend of larger reduction of s_u for $w_s = 1D$–$3D$

than the FE calculated values. The potential reasons for this difference include the strength degradation curve used in the present FE analysis and the variability of shear strength in the field (e.g., some elements far from the pile, even $w_s = 4.5D–6.5D$, show considerably low s_u/s_{u0}). The effects of the former are discussed later in the parametric study.
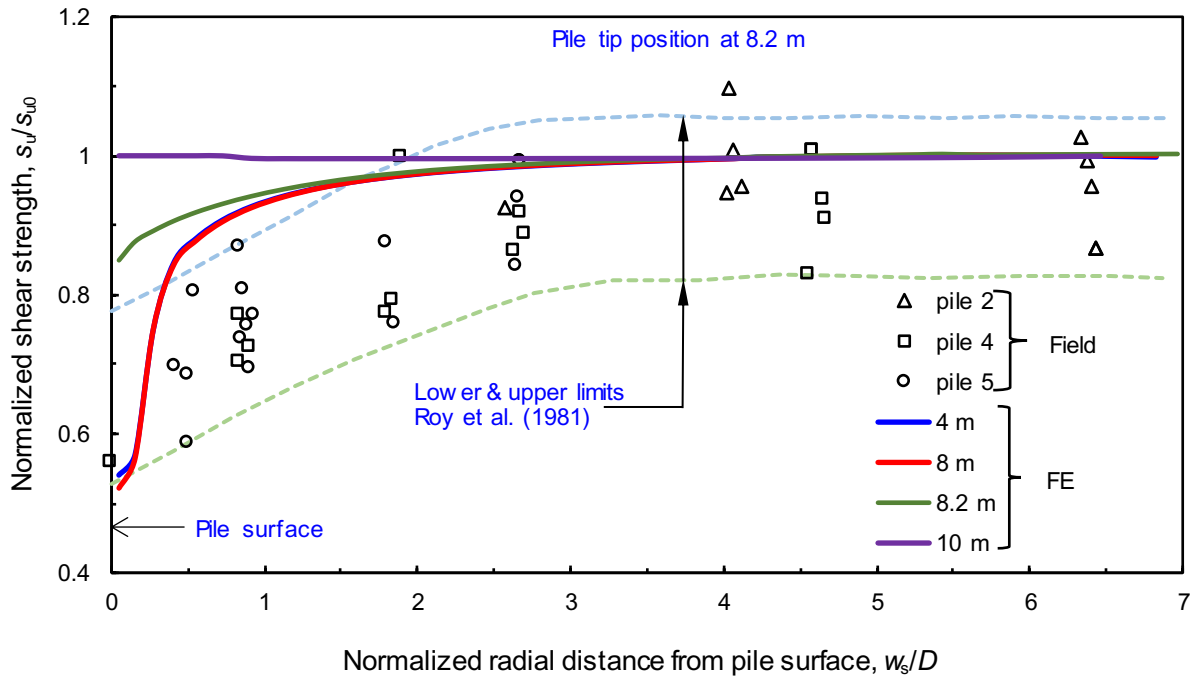
Fig. 3.5. Undrained shear strength of soil after installation of pile

Change in radial stress

The change in radial stress (σ_r) due to installation is one of the main concerns, as it affects the response of soil adjacent to the pile (Lo & Stermac, 1965; Randolph et al., 1979). Figure 3.6 shows the variation of radial stress (σ_r) at different depths for varying tip positions normalized by the initial vertical total stress, σ_{v0}. The penetration-induced radial stress reaches the maximum value when the pile tip passes that level; for example, when $z_{tip} = 2$ m, σ_r near the pile at $z = 2$ m is ~ $5\sigma_{v0}$ (Fig. 3.6(a)). The radial stress reduces with further penetration of the pile because of stress redistribution; therefore, σ_r at $z = 2$ m is ~ $2\sigma_{v0}$ when the pile tip reaches 4 m. The radial stress

near the tip increases with depth, and the normalized value (σ_r/σ_{v0}) is higher at a shallower depth (compare Figs. 3.6(a) and 3.6(c)), which also means σ_r is the major principal stress, as used in analytical solutions (e.g., cavity expansion). However, the analytical solutions do not consider the soil flow and change in stresses with pile penetration. When the pile is jacked into sensitive clay, the radial stress around the pile changes and a shear zone is formed around the pile (Kou et al., 2015; Randolph et al., 1979). The shear zone plays a major role in soil failure mechanisms, development of shear strain, and pile-soil interface resistance.
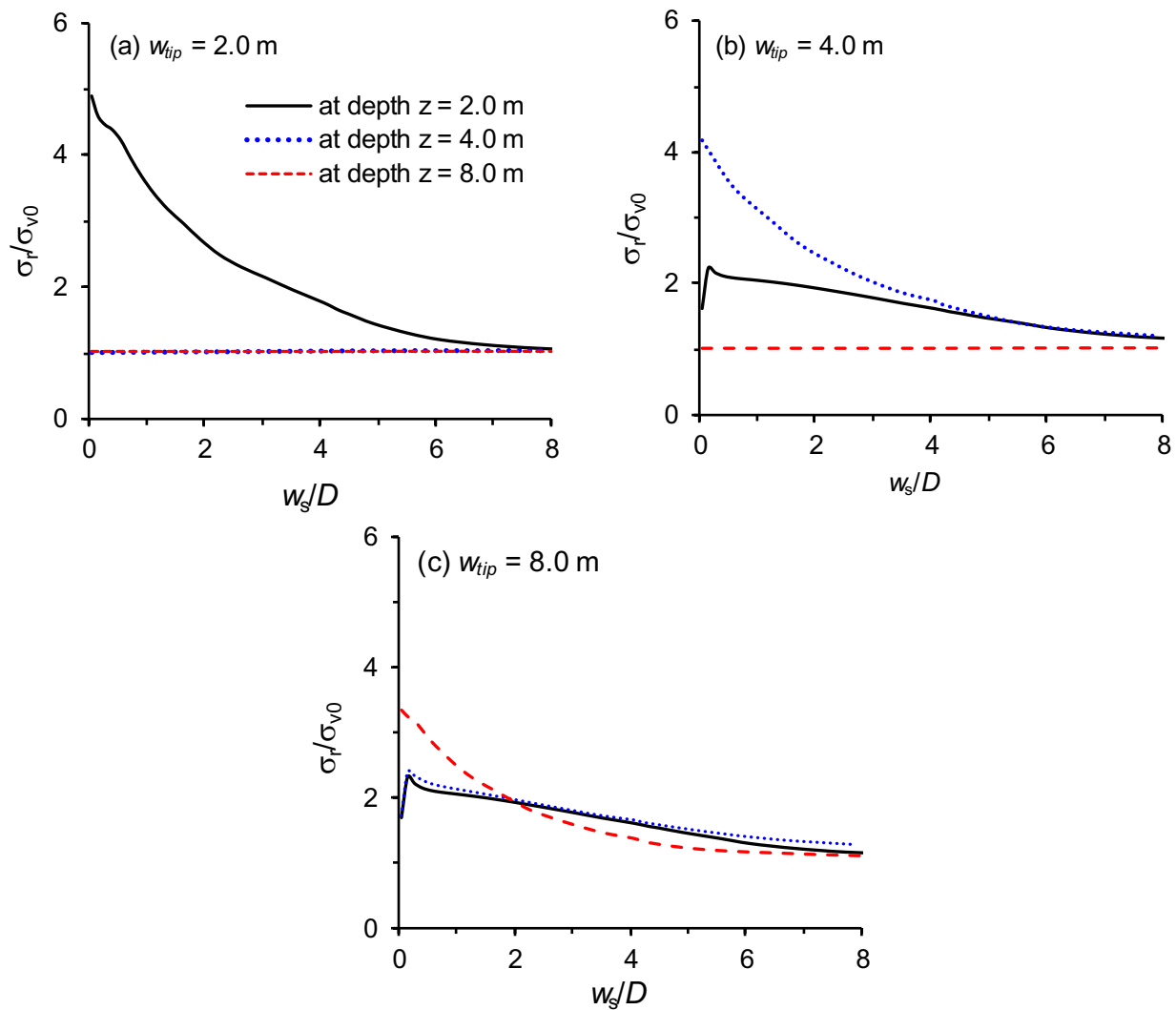
Fig. 3.6. Radial stress at different depths for three pile tip positions: (a) 2 m; (b) 4 m; (c) 8 m

Figure 3.7 shows the variation of normalized radial stress (σ_r/σ_{v0}) at two radial distances from the pile surface ($w_s = 0.55D$ & $3D$) for the two pile tip positions ($z_{tip} = 4$ m and 8 m). For $z_{tip} = 4$ m, the maximum σ_r/σ_{v0} at $w_s = 0.55D$ is 3.4. A considerable increase in σ_r also occurs even at $3D$ radial distance ($\sigma_r = 1.9\sigma_{v0}$). The stress at this level decreases with further penetration and then remains almost constant from ~ 1 m above the pile tip. The penetration-induced radial stress is negligible, ~ 0.9 m below the pile tip. Lower σ_r/σ_{v0} is found at a larger pile tip depth (e.g., $z_{tip} = 8$ m), although the radial stress distribution pattern is the same. Note that the constant σ_r/σ_{v0} from a meter above the pile tip means a linearly increasing σ_r after installation because σ_{v0} increases linearly with depth. Azzouz and Morison (1988) observed linearly increasing radial stress that was measured by piezo-lateral stress cells after penetration of piles in Boston Blue Clay. Maximum σ_r/σ_{v0} develops in a soil element near the pile shaft immediately below the tip, which is higher at shallower depths and decreases at greater depths (Fig. 3.7). $(\sigma_r/\sigma_{v0})_{max}$ has important practical implications and interpretations of field test results because the penetration-induced pore water pressure and mobilized shaft friction during installation are related to these parameters. For example, Blanchet et al. (1980) found a similar pore pressure distribution when cylindrical steel piles were installed in sensitive clay—the pore pressure reaches a maximum when the pile tip passes that level. However, note that $(\sigma_r/\sigma_{v0})_{max}$ depends on the rate of shear strength degradation, as discussed in the later sections.
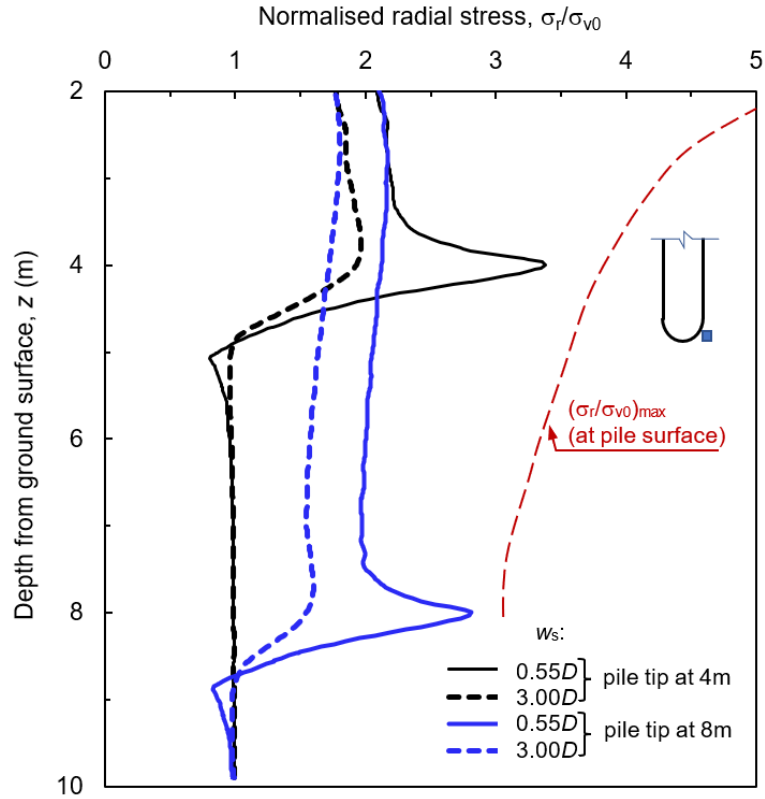
Fig. 3.7. Variation of radial stress with depth for two pile tip positions

Strain-softening effects

Figure 3.8(a) shows the contour of plastic shear strain ε_q^p around the pile for a penetration depth

of 8.0 m. The inset of this figure shows ε_q^p decreases rapidly with radial distance and is negligible

after $w_i/D \sim 2.5$ (i.e. < 3%). Close to the pile, a large plastic shear strain generates ($\varepsilon_q^p > 100\%$),

which means that typical Lagrangian-based FE cannot model such a large deformation. The strain

contours are almost vertical, approximately above one diameter (i.e. above 7.8 m) from the pile

tip, which implies that ε_q^p is primarily generated due to soil flow around the tip during penetration

at such deeper conditions. Note that the soil flow mechanisms and plastic shear strain generation

are different during penetration near the ground surface (inset Fig. 3.8(a)). The change in flow

patterns from shallow to deeper conditions is illustrated in video s1. The calculated strain pattern

is somewhat similar to that obtained from the shallow strain path method (Sagaseta et al., 1997) and deep penetration analysis of a cone using strain path and FE methods (Baligh, 1985; Teh & Houlsby, 1991; Yu et al., 2000; Yi et al., 2012); however, those studies were mainly limited to elastic perfectly plastic soil. The present study focuses on highly sensitive clays where the sensitivity has significant effects on soil flow, as discussed later.

Figure 3.8(b) shows the reduction of shear strength (f_1 in Eq. (3.3)) for the same pile tip position, as in Fig. 3.8(a). A significant strength reduction ($f_1 < 0.6$) occurs near the pile; however, the strength reduction is negligible after $w_i > 3D$, where only $< 2\%$ strength reduction occurs due to the development of plastic shear strain. The reduction of s_u depends on sensitivity and rate of strain-softening.
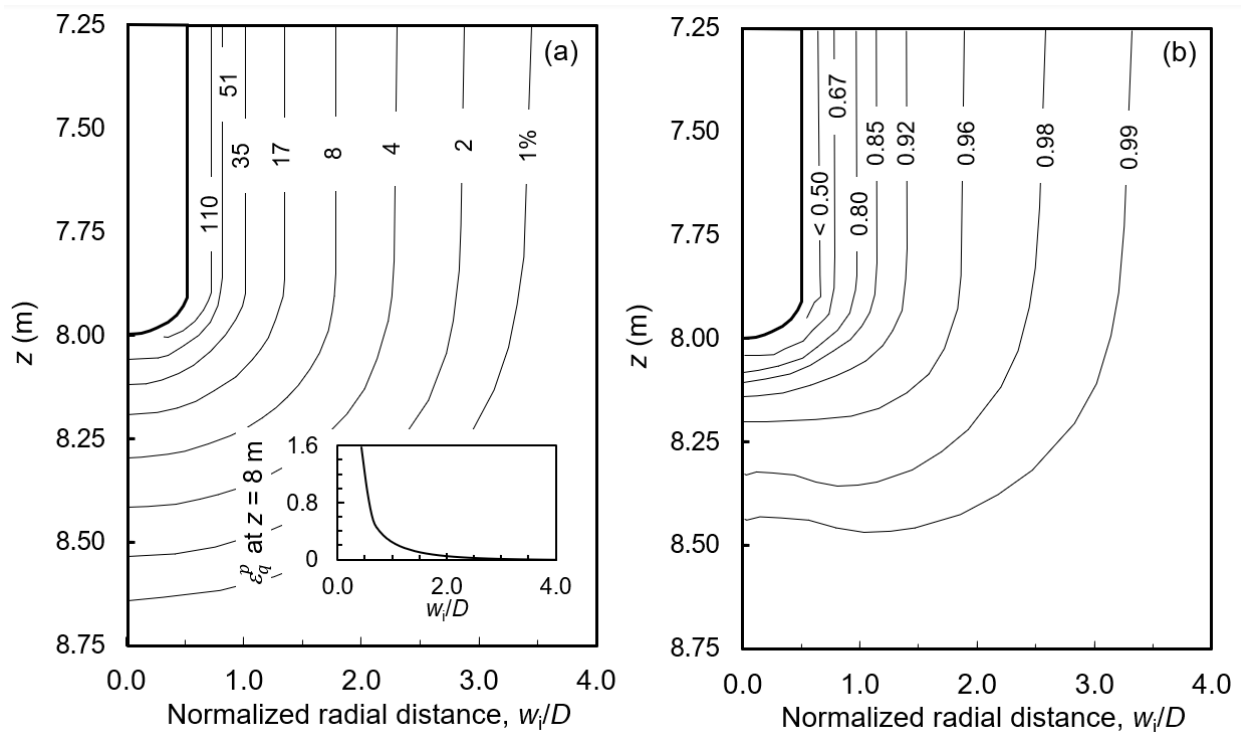
Fig. 3.8. Contours: (a) equivalent plastic shear strains in percent; (b) strain-softening effect

von-Mises stress

In some studies, because of computational costs and mesh distortion issues, the simulations have been done only for a small penetration distance, starting from a pre-bored condition, although the jacking in the field is generally done from the ground surface (White et al., 2002; Kou et al., 2015). Figure 3.9 shows the von-Mises stress (σ_e) around the pile when the pile tip is at 8 m. For penetration from a shallower depth (1.2 m), σ_e increases over a larger zone (Fig. 3.9(a)), while σ_e increase is limited to a smaller zone in the case of jacking from a deeper condition (4.5 m). While penetration resistance does not vary significantly for jacking from 1.2 m or 4.5 m (compare the resistance below 4.5 m in Figs. 3.4(a) and 3.4(b)), the disturbance of soil around the pile is very different (post-peak plastic zone; this refers to the left side of the dashed lines in Figs. 3.9(a) and 3.9(b)). As the strength degradation is high near the pile, σ_e contours curve downward near the pile in the post-peak plastic zone, which will not occur if the soil is not sensitive. As the linearly increasing undrained shear strength profile is used, a bulb-shaped von Mises stress distribution is found with maximum σ_e near the pile tip.

3.6.3 Parametric studies

A number of simulations are performed to investigate the effects of penetration rate, strain-softening and strain rate effects on s_u, rate of post-peak shear strength degradation (s_{u0}/s_{uR}, δ_{95}), and pile–soil interface conditions. All the simulations are performed for an idealized linearly increasing soil shear strength profile as in Eq. (3.1) with $s_{ug} = 20$ kPa and $k = 1.67$ kPa/m to clarify the effects of these parameters. The parameters used in these analyses are listed in Table 3.1, except for those which are varied. The FE analysis with varied mesh sizes is computationally less expensive. For example, the FE simulations take 8–12 hours, depending on the parameters used in the numerical modeling with a 3.41 GHz Intel Core i7 processor and 32 GB RAM.
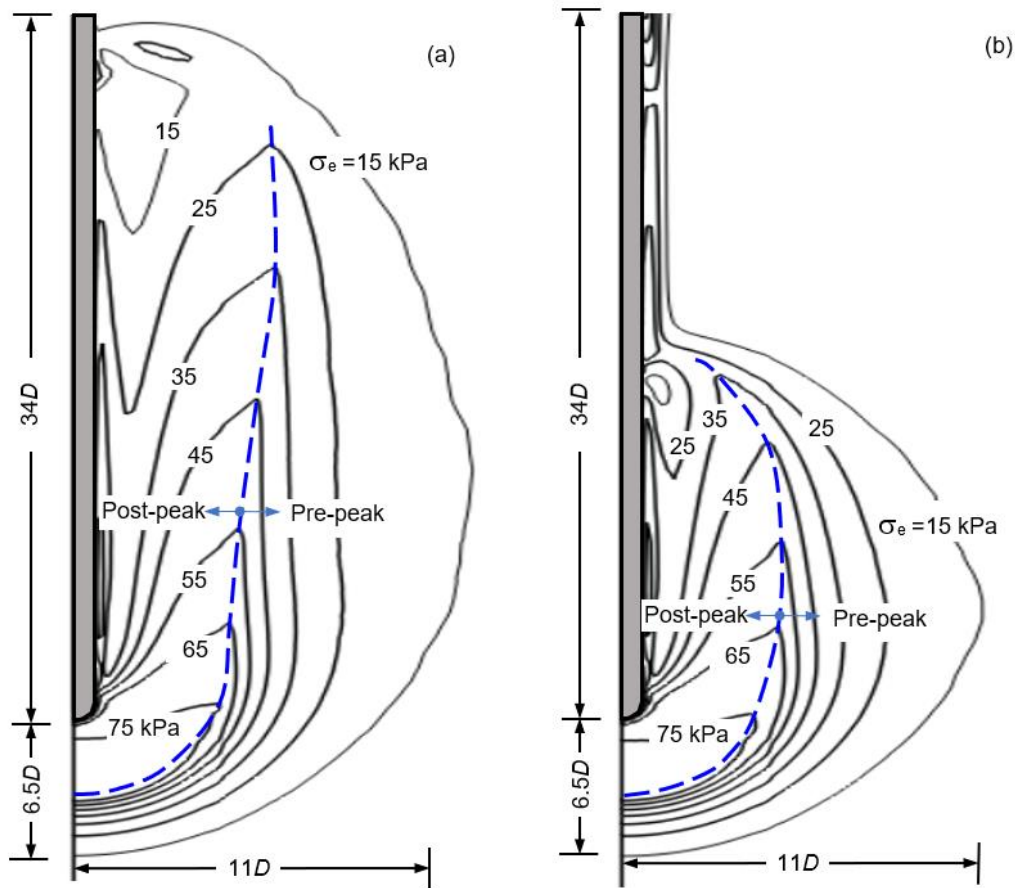
Fig. 3.9. Effects of pre-bored condition on pile jacking in soft sensitive clay

Penetration rate to maintain quasi-static conditions

Figure 3.10 shows the effects of penetration rate on normalized penetration resistance. No significant change in N is overserved for lower penetration rates (v = 0.05 to 0.5 m/s). Some oscillations in explicit FE results are common due to their algorithms, sampling rate, and parameters used in the analysis (Tian et al., 2011; Wang et al., 2015). Note again that a high jacking rate is not used in the field. However, in numerical simulations, a higher penetration rate than that of the field is used to save computational costs but maintain quasi-static conditions. As a general rule, the analysis is quasi-static if the kinetic energy does not exceed 5%–10% of the internal energy throughout the analysis (Wang et al., 2015; Robert et al., 2020), which is satisfied when v

= 0.05 to 0.5 m/s is used. Analyses are also performed with higher velocity but do not satisfy the quasi-static conditions. In the present study, $v = 0.1$ m/s is used in all other analyses.
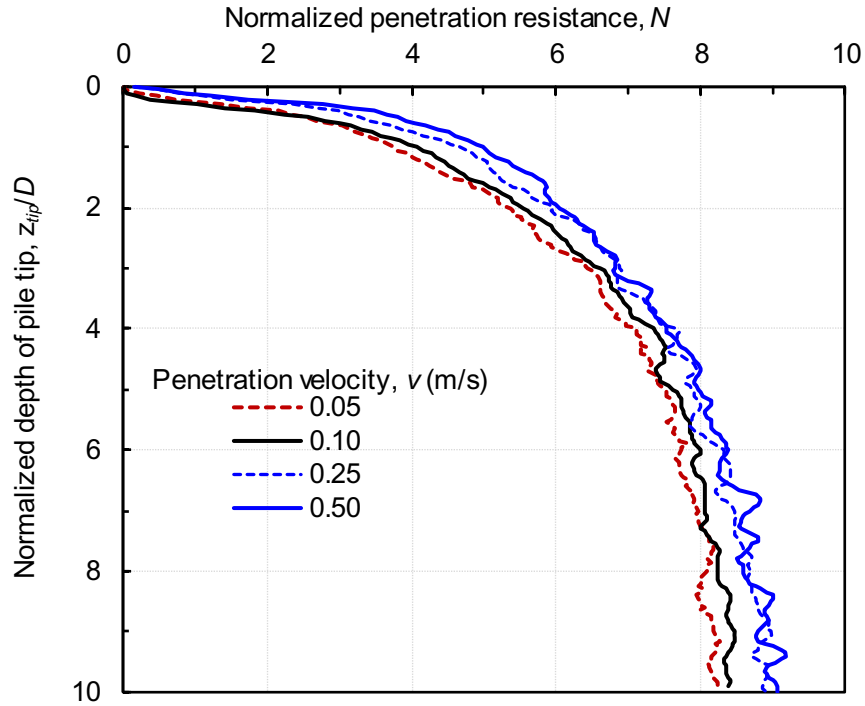
Fig. 3.10. Effects of penetration rate

Effects of strain softening and interface conditions

The penetration resistance depends on several factors, including strain-softening, which is primarily related to s_{u0}/s_{uR} and δ_{95} (Eq. 3.3), and pile–soil interface conditions (Fig. 3.11(a)). The first two simulations (a and b) are performed for a smooth condition, while the other four (c–f) are with 6 kPa maximum interface resistance ($\tau_{max} = 6$ kPa). For a given interface condition, smaller penetration resistance is found for higher softening rates (i.e. higher s_{u0}/s_{uR} and lower δ_{95}). For a higher rate of strain-softening (e.g. simulation f), the shear strength reduces significantly near the soil around the pile, and therefore the penetration resistance does not increase, although $\tau_{max} = 6$

kPa is used. This implies that shaft friction could be very small during the installation of a pile in highly sensitive clays, as observed in the field tests conducted by Roy et al. (1981).

Figure 3.11(b) shows that, for $\delta_{95} = 0.05$ m, N decreases significantly with an increase in s_{u0}/s_{uR}. However, for $\delta_{95} = 0.4$ m, s_{u0}/s_{uR} has less effect on N because the plastic shear strain developed around the pile is not sufficient for considerable degradation of s_u.
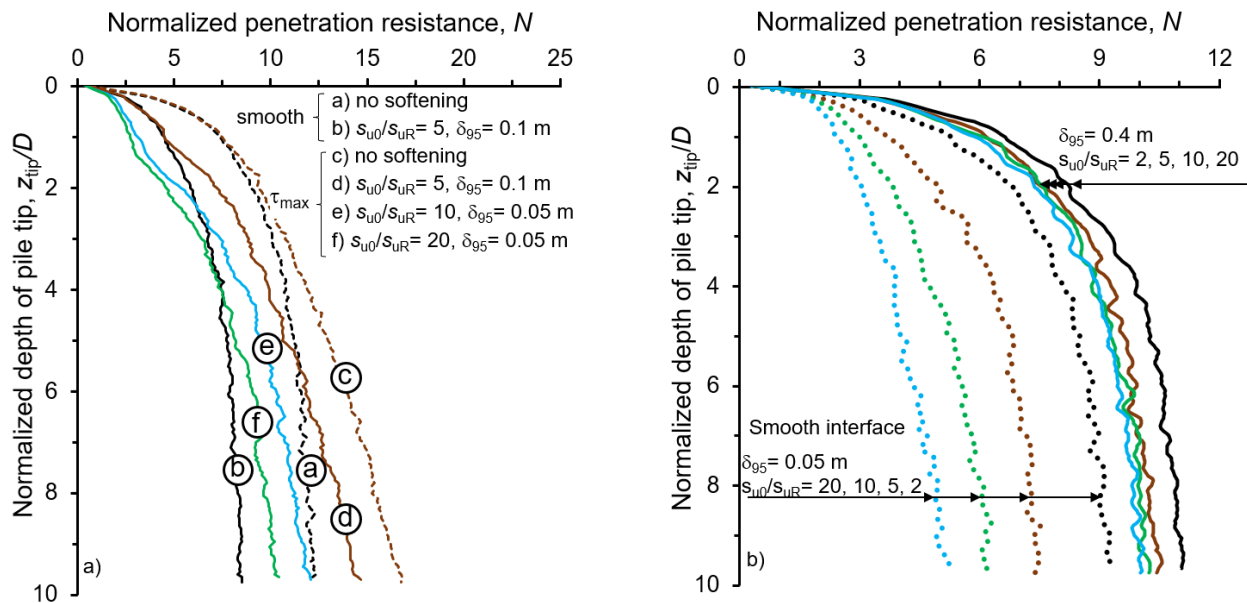
Fig. 3.11. Effects of strain-softening rate: (a) pile–soil interface conditions; (b) varying s_{u0}/s_{uR} and δ_{95}

Effects of in-situ stresses

Figure 3.12 shows no significant effects of the ratio between in situ horizontal and vertical total stresses at the shallower depth of penetration. However, at greater depths, a lower K value gives a lower penetration resistance. The earth pressure coefficient at rest (K_0) increases with OCR and is more than 1.0 for some Canadian sensitive clays, even for OCR = 2−6 (Lefebvre et al., 1991;

Hamouche et al., 1995). Therefore, the analyses are performed for a wide range of K. The relationship between K and K_0 has been discussed in the numerical modeling section.
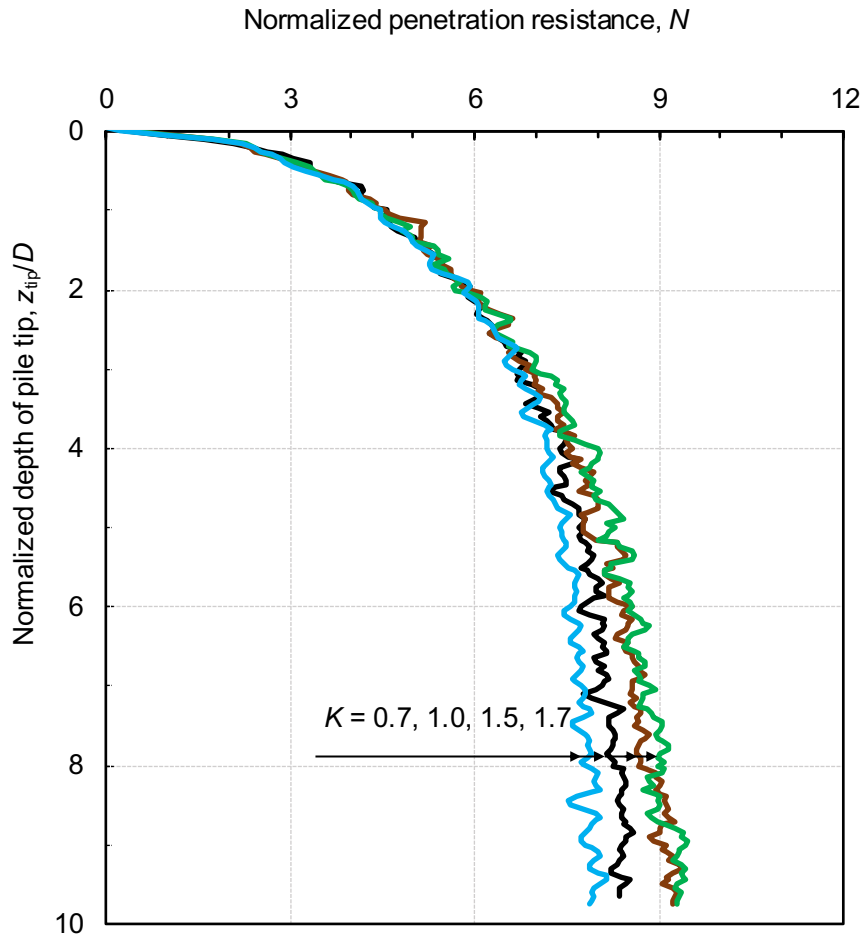
Fig. 3.12. Effects of in situ earth pressure ratio

Effects of soil parameters on radial stress

Figure 3.13(a) shows the variation of radial stress with radial distance from the pile shaft for three values of δ_{95} when the pile tip is at 2 m. Significant radial stress develops at the pile tip level (solid lines). Near the pile shaft, σ_r is $4.5\sigma_{v0}$–$5.6\sigma_{v0}$ and it gradually decreases to the in-situ condition ~ $5D$ from the pile shaft. The higher the value of δ_{95} (slower post-peak strength

reduction), the higher the radial stress. The change in radial stress 1 m below the pile tip ($z_{tip} = 3$ m) is negligible (Fig. 3.13(a)).

Figure 3.13(b) shows the variation of σ_r when the pile tip moves to 3 m. For this pile tip position, σ_r reduces at the level of $z = 2$ m because of further penetration (compare Figs. 3.13(a) and 3.13(b)) while it increases at $z = 3$ m (i.e. current location of the pile tip).

Figure 3.14(a) shows that an increase in s_{u0}/s_{uR} reduces the magnitude and extent of the radial stress increase zone. For example, σ_r near the pile shaft is $5.3\sigma_{v0}$ and $3\sigma_{v0}$ for s_{u0}/s_{uR} of 2 and 20, respectively. Also, the radial stress increase continues up to ~ $6D$ for $s_{u0}/s_{uR} = 2$, while it is limited within $2D$ for $s_{u0}/s_{uR} = 20$. Figure 3.14(b) shows the radial stress variation at the same depths ($z = 2$ m and 3 m) when the pile tip is at 3 m. In a given simulation, the maximum radial stress adjacent to the pile at the pile tip level decreases with the penetration depth.

Figure 3.15 shows a small variation in normalized radial stresses for two pile–soil interface conditions (smooth and $\tau_{max} = 6$ kPa). Moreover, the ratio between the in-situ horizontal and vertical stresses (K) does not affect the radial stresses significantly, at least within a $3D$ distance from the pile shaft (Fig. 3.16).

Figures 3.17(a, b) show the effects of softening on maximum normalized radial stress $(\sigma_r/\sigma_{v0})_{max}$ that develops in the soil element next to the pile surface and immediately below the tip. $(\sigma_r/\sigma_{v0})_{max}$ decreases with an increase in sensitivity; for example, when the pile tip is at ~ 3 m, $(\sigma_r/\sigma_{v0})_{max}$ for $s_{u0}/s_{uR} = 20$ is ~ 55% of that of non-sensitive clay (Fig. 3.17(a)). Figure 3.17(b) shows that a faster rate of softening (i.e., smaller δ_{95}) reduces $(\sigma_r/\sigma_{v0})_{max}$ significantly. However, in situ earth pressure ratio has negligible effects on $(\sigma_r/\sigma_{v0})_{max}$ (Fig. 3.17(c)).
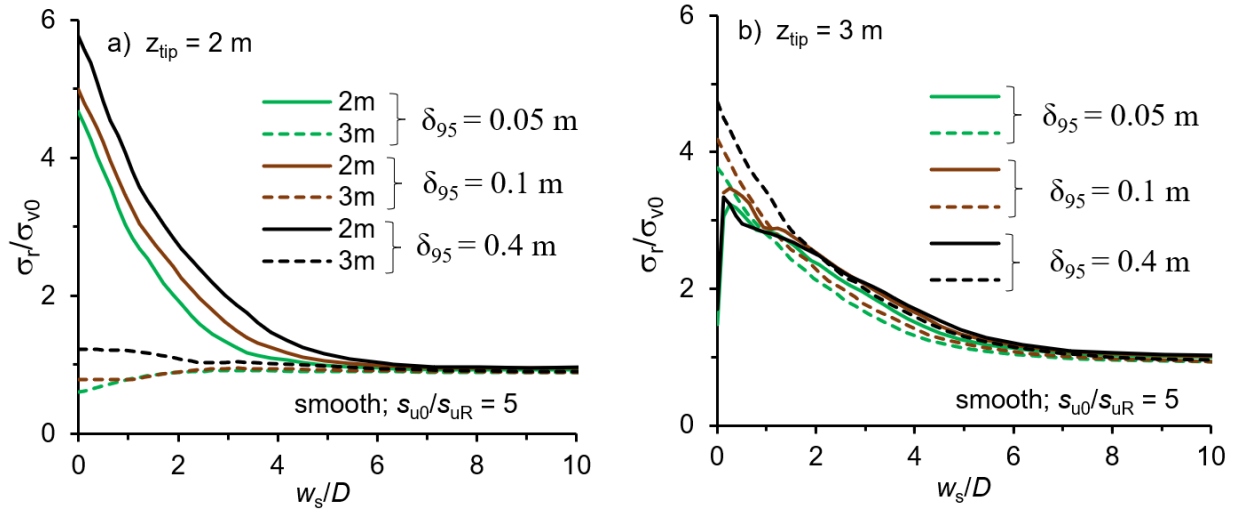
Fig. 3.13. Radial stress for varying δ_{95}: (a) pile tip at 2 m; (b) pile tip at 3 m
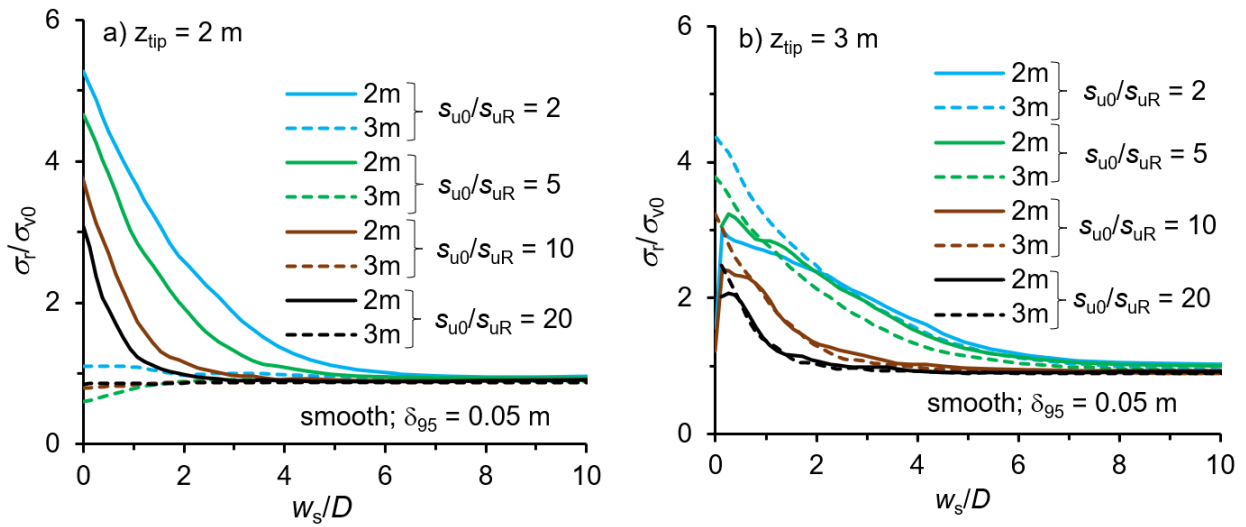
Fig. 3.14. Radial stress for varying s_{u0}/s_{uR}: (a) pile tip at 2 m; (b) pile tip at 3 m
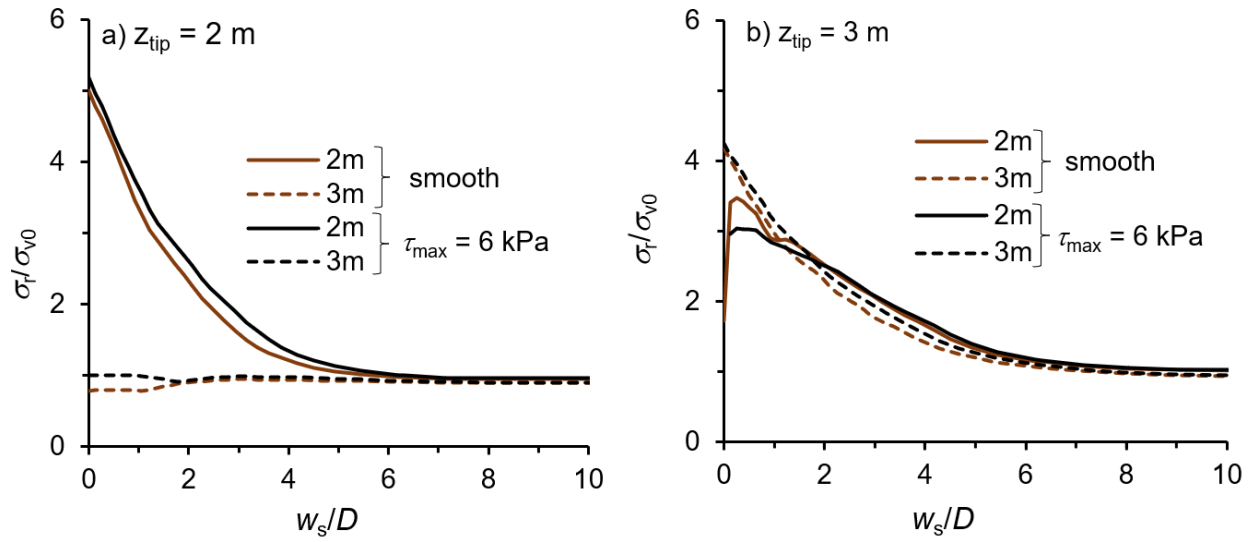
Fig. 3.15. Effects of pile–soil interface condition on radial stress: (a) pile tip at 2 m; (b) pile tip at 3 m
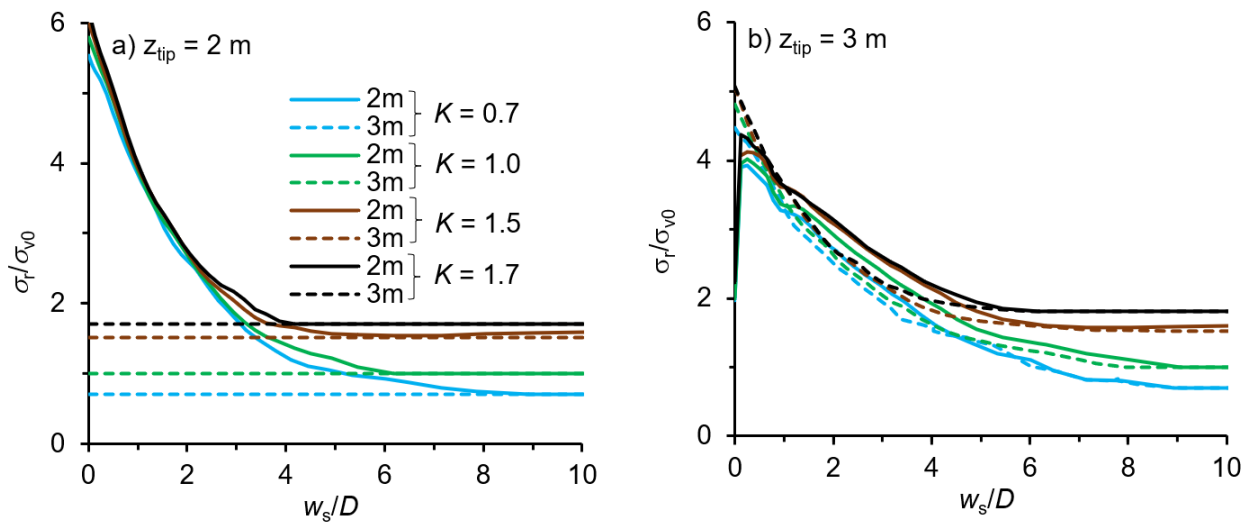
Fig. 3.16. Effects of in-situ earth pressure on radial stress: (a) pile tip at 2 m; (b) pile tip at 3 m
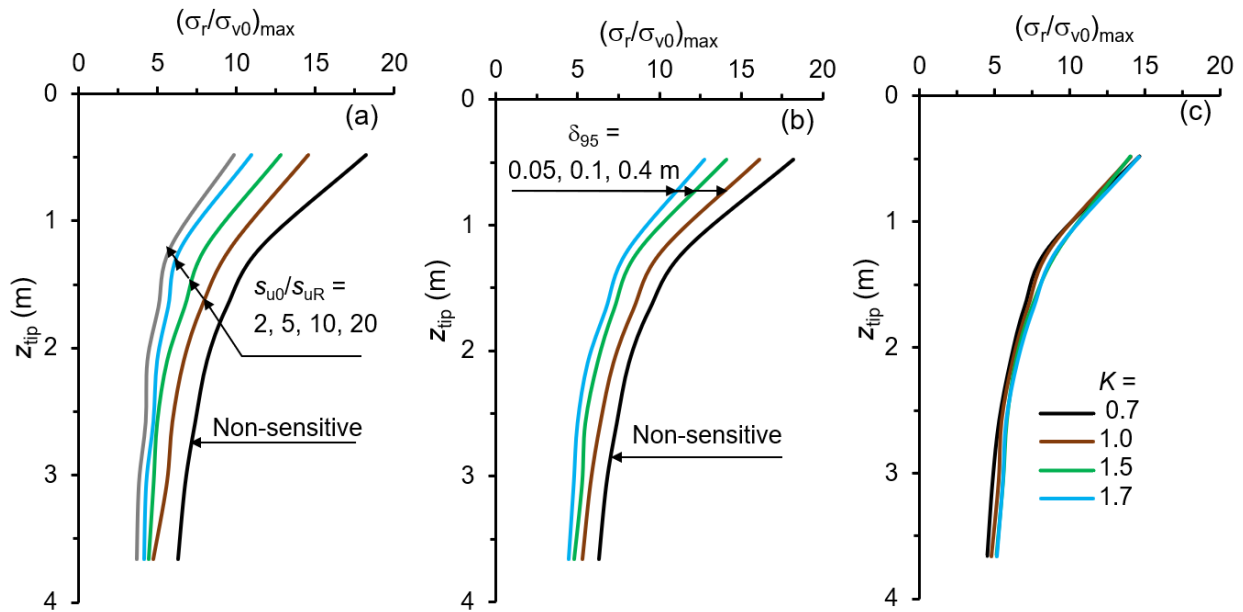
Fig. 3.17. Maximum normalized radial stress with depth of penetration: (a) effects of s_{u0}/s_{uR}; (b) effects of δ_{95}; (c) effects of in situ earth pressure ratio

Development of plastic shear strain

Figure 3.18 shows the development of plastic shear strain (ε_q^p) with penetration of the pile. When the pile starts to penetrate from the ground surface, a spherical-shaped plastic zone forms (Fig. 3.18 (a)). As the pile penetrates further, the shape of the plastic zone changes to a combination of spherical and cylindrical shapes (Figs. 3.18(b)–3.18(d)). However, the width of the plastic zone does not increase significantly after a certain depth of penetration. The simplified cylindrical cavity expansion theories for pile penetration cannot model the whole process properly, as they do not incorporate the effects of the presence of the ground surface and soil flow. The plastic shear strain in the soil elements around the pile is 100%–400%, which implies a significant remoulding of sensitive clay.

Figures 3.19–3.21 show the plastic shear strain for various $s_{u0/s_{uR}}$ and δ_{95}. The key observations from these parametric studies are:

a) Severe remoulding occurs in the soil near the pile, where more than 100% plastic shear strain develops.

b) A wider plastic zone forms for the slower rate of s_u degradation cases (i.e., low $s_{u0/s_{uR}}$ and high δ_{95}) (Figs. 3.19(a), 3.20(a) and 3.21(a–d). In these cases, the maximum ε_q^p is less than that of other cases.

c) A round bottom flask type plastic zone forms in the intermediate rate of s_u degradation cases (Figs. 3.19(b), 3.19(c), 3.20(b) and 3.20(c)). The plastic zone is narrow near the ground surface, through which highly remoulded soil flows above the ground surface. At larger depths (e.g., at the level of the pile tip), the plastic zone is wider, and the width of this zone reduces with an increase in s_u degradation rate (e.g., compare Figs. 3.19(b) and 3.19(c)).

d) For high s_u degradation rates, only a narrow plastic zone is formed where extremely large ε_q^p of ~ 100%–3,000% develops (Figs. 3.19(d) and 3.20(d)). Similar to pushing a needle into soup, such a condition was observed during pile installation in sensitive clays (personal communication with piling contractors).

Figures 3.22(a and b) show that, for non-sensitive clays, the interface friction resistance does not significantly affect the size and shape of the plastic zone and the magnitude of plastic shear strains. However, for sensitive clays, the plastic zone is slightly smaller for smooth interface conditions (Fig. 3.22(c)), especially near the ground surface, than that with $\tau_{max} = 6$ kPa (Fig. 3.22(d)). The smooth interface conditions allow the severely remoulded sensitive clays to flow up easily near the pile; therefore, a smaller plastic zone is formed. However, no strength reduction

occurs in the non-sensitive clays; therefore, an almost similar plastic zone is found for both interface conditions.

a) $z_{tip} = 1$ m   b) $z_{tip} = 2$ m   c) $z_{tip} = 3$ m   d) $z_{tip} = 4$ m
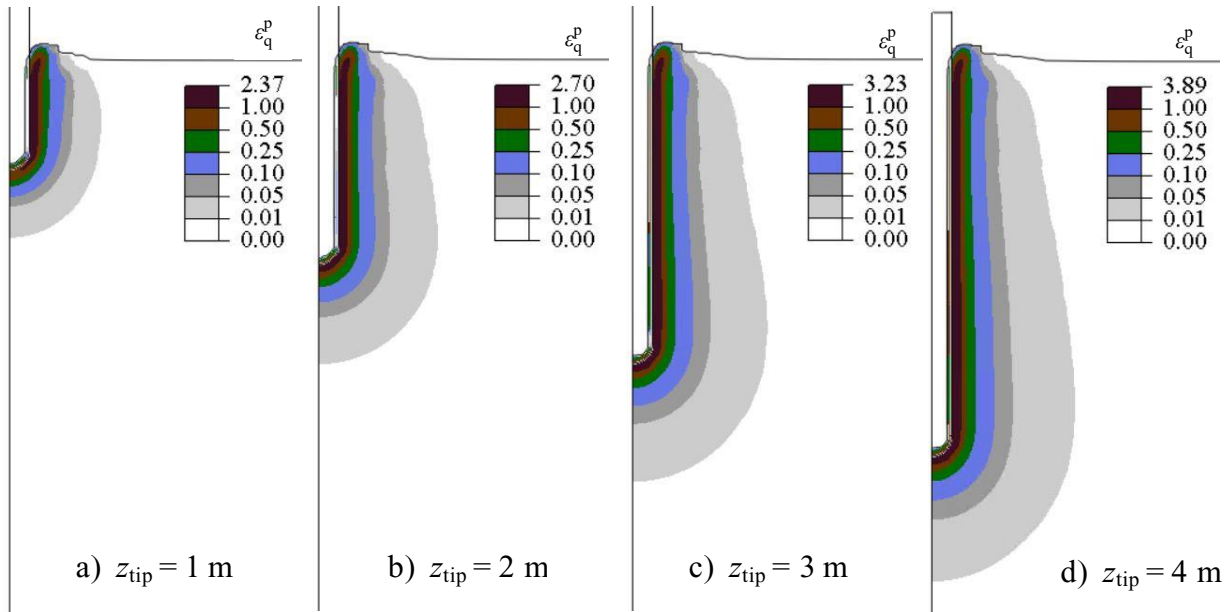
Fig. 3.18. Development of plastic shear strain with pile penetration ($\delta_{95} = 0.4$ m, $s_{u0}/s_{uR} = 2.0$)

a) $s_{u0}/s_{uR} = 2$ b) $s_{u0}/s_{uR} = 5$ c) $s_{u0}/s_{uR} = 10$ d) $s_{u0}/s_{uR} = 20$
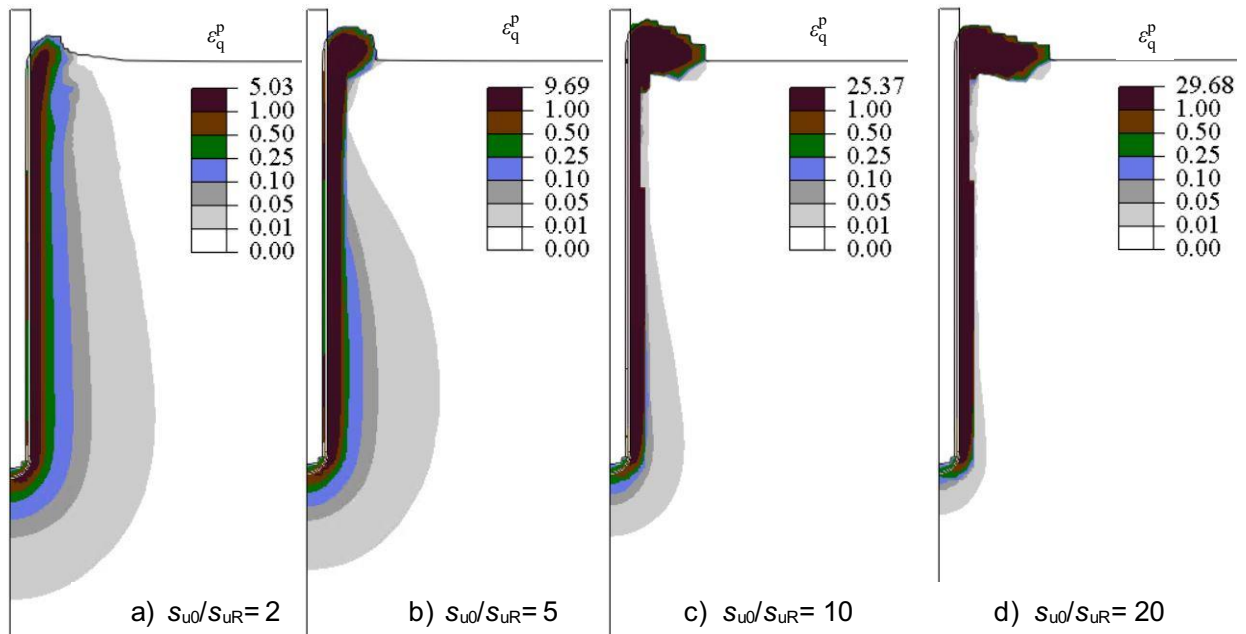
Fig. 3.19. Plastic shear strain distributions with $\delta_{95} = 0.05$ m
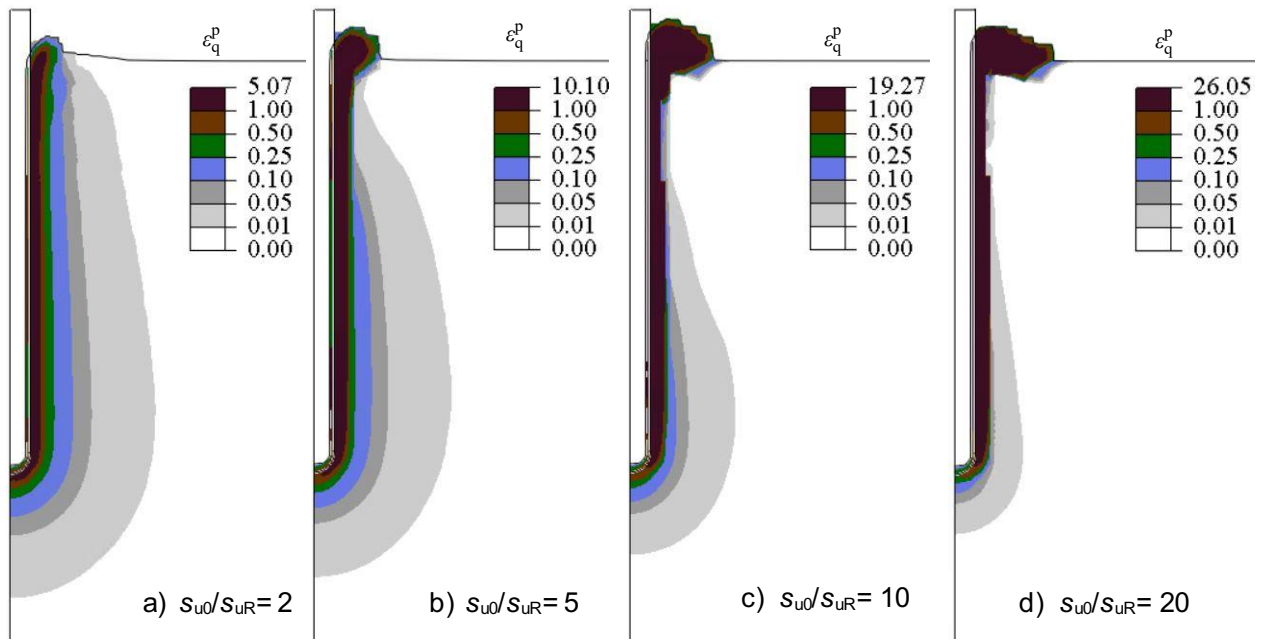
Fig. 3.20. Plastic shear strain distributions with $\delta_{95} = 0.1$ m
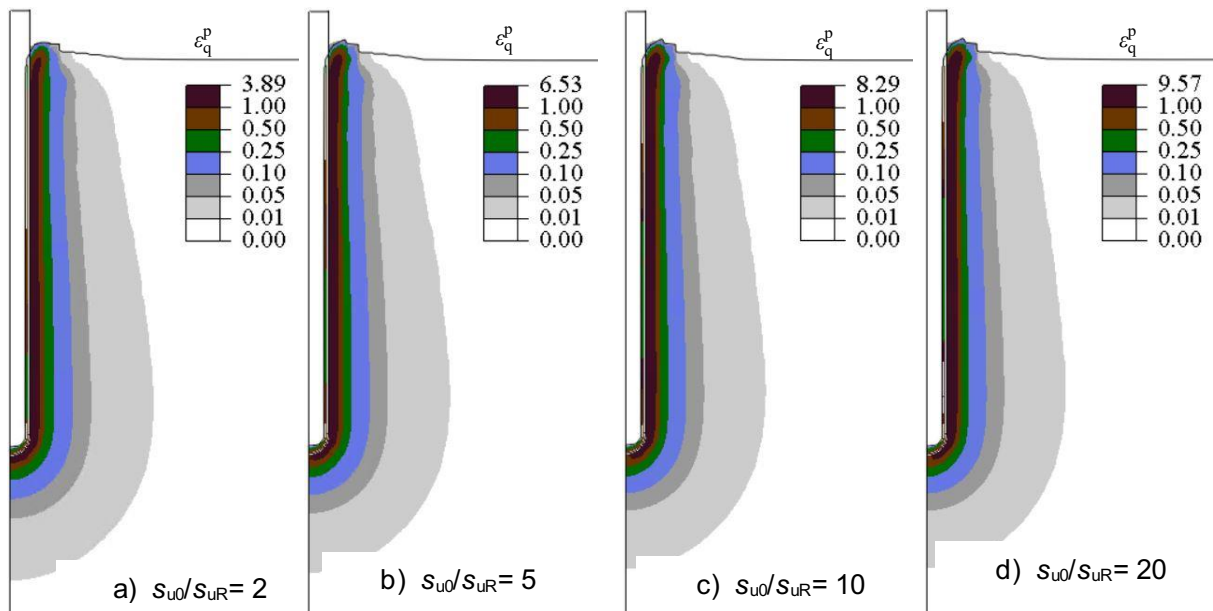
Fig. 3.21. Plastic shear strain distributions with $\delta_{95} = 0.4$ m
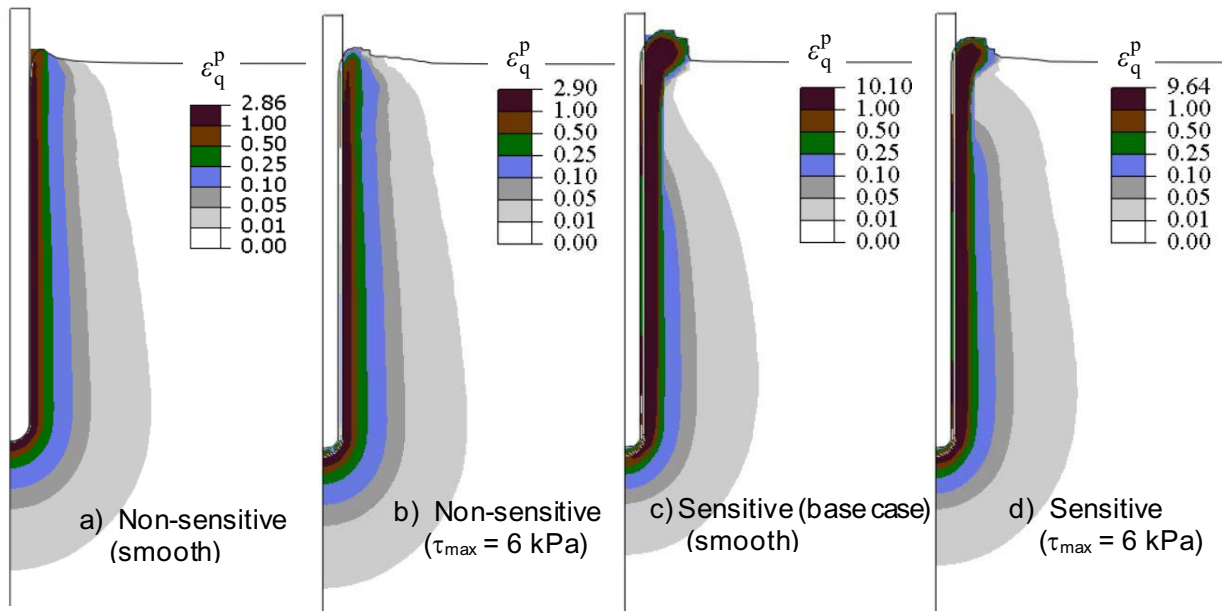
Fig. 3. 22. Plastic shear strain in non-sensitive and sensitive clays for two pile–soil interface conditions

3.6 Conclusions

Pile jacking in sensitive clay is simulated using an Eulerian-based finite element program. Soil flow mechanisms, changes in stresses, and development of plastic shear strains due to penetration of the pile over a large distance are successfully modelled. The FE simulated results compare well with the results of a field test program. A comprehensive parametric study identifies the key factors affecting pile installation into sensitive clays. The following conclusions can be drawn from this study:

(a) The penetration resistance calculated with the smooth pile–soil interface conditions compares well with the field test results, which implies substantial remoulding and pore pressure generation near the pile surface that could reduce the interface resistance.

(b) Significant shear strength degradation (50%–70%) occurs near the pile surface, which is comparable to the field measurements.

(c) Changes in stresses and strains for pre-bored conditions are limited to a smaller zone near the pile tip; however, a continuous plastic zone is formed if the pile is penetrated from the ground surface, resulting in different soil flow mechanisms.

(d) A large radial stress increase near the pile surface occurs when the pile tip is close to that level. With further penetration, the radial stress decreases considerably near the pile shaft and then remains almost constant. The higher the rate of post-peak shear strength degradation (i.e., higher s_{u0}/s_{uR} and lower δ_{95}), the lower the remaining radial stress.

(e) The plastic shear strains due to penetration of the pile develop in a wider area for non-sensitive to low-sensitive clays. However, for highly sensitive clays, a round bottom flask-shaped plastic shear strain zone is formed. Also, for highly sensitive clays and rapid shear strength degradation rates, the shear strain localizes only in a narrow zone.

Supplemental Data: The supplementary data of this chapter are available at:

https://drive.google.com/drive/folders/1BAkI4Z6BKgXHNKoeXNEvPfsCDKZYQ2Bq?usp=sharing

Notations

β	soil parameter for strain-rate relation
δ	accumulated plastic shear displacement
δ_{95}	δ at which s_u reduced by 95% of $(s_{u0}\text{-}s_{uR})$
δ_{ld}	δ at large shear displacement
ε_q^p	equivalent plastic shear strain
$\varepsilon_{q\_95}^p$	Equivalent plastic shear strain at which s_u reduced by 95% of $(s_{u0}\text{-}s_{uR})$
$\dot{\varepsilon}_{ij}^p$	plastic deviatoric strain rate tensor

γ	total unit weight of soil
γ_w	unit weight of water
$\dot{\gamma}$	strain rate
$\dot{\gamma}_{ref}$	reference strain rate
η	soil parameter for strain-rate relation
ν_u	undrained Poisson's ratio
σ_e	von Mises stress
σ_h	total horizontal stress
σ'_h	effective horizontal stress
σ'_{h0}	initial effective horizontal stress
σ_r	total radial stress
σ_{v0}	initial total vertical stress
σ'_{v0}	initial effective vertical stress
τ_{max}	interface shear stress limit
A_p	cross-sectional area of the pile
D	pile outer diameter
dt	derivative of time
E_u	undrained Young's modulus
F	total resistance
F_b	buoyancy force
F_s	resistance from the shear strength of soil
f_b	end bearing resistance force

f_s	skin friction resistance force
f_1	strain-softening factor
f_2	strain-rate factor
G	shear modulus of the soil
I_r	rigidity index
K	ratio between total horizontal to total vertical stress
K_0	effective earth pressure coefficient at-rest
K_i	installation earth pressure coefficient
k	shear strength gradient with depth
LL	liquid limit
N	normalized penetration resistance
OCR	overconsolidation ratio
S_t	sensitivity
s_u	mobilized undrained shear strength
s_{u0}	initial (peak) undrained shear strength
s_{ug}	undrained shear strength at ground surface
s_{uld}	undrained shear strength at large displacement
s_{uR}	remoulded s_u at large plastic shear displacement
s_{uy}	undrained shear strength at a very low strain rate
t_{FE}	thickness of the FE element
u	total pore water pressure
u_0	hydrostatic pore water pressure
u_e	excess pore water pressure

v	velocity
v_x	the component of velocity in x-direction
v_y	the component of velocity in y-direction
v_z	the component of velocity in z-direction
w_i	radial distance of soil element from the pile centre
w_s	radial distance of soil element from the pile outer surface
z	depth of the soil element below the ground surface
z_{tip}	depth of pile tip from the ground surface

References

Azzouz, A. S. & Lutz, D. G. (1986). Shaft behaviour of a model pile in plastic empire clays. *J. Geotech. Engng.* **112,** No. 4, 389–406.

Azzouz, A. S. & Morrison, M. J. (1988). Field measurements on model pile in two clay deposits. *J. Geotech. Engng.* **114,** No. 1, 104–121.

Baligh, M. M. (1985). Strain path method. *J. Geotech. Engng.* ASCE **111**, No. 9, 1108–1136.

Benson, D. J. (1989). An efficient, accurate, simple, ALE method for nonlinear finite element programs. *Comput. Methods in Appl. Mech. Eng.* **72**, No. 3, 305–350.

Blanchet, R., Tavenas, F. & Garneau, R. (1980). Behavior of Friction Piles in Soft Sensitive Clay. *Can. Geotech. J.* **17**, No. 2, 203–224.

Bond, A. J. & Jardine, R. J. (1991). Effects of installing displacement piles in a high OCR clay. *Géotechnique* **41,** No. 3, 341–363.

Boukpeti, N., White, D. J., Randolph, M. F. & Low, H. E. (2012). Strength of fine-grained soils at the solid–fluid transition. *Géotechnique* **62,** No. 3, 213–226.

Bozozuk, M., Fellenius, B. H. & Samson, L. (1978). Soil disturbance from pile driving in sensitive clay. *Can. Geotech. J.* **15,** 346–361.

Butterfield, R. & Banerjee, P. K. (1971). The elastic analysis of compressible piles and pile groups. *Géotechnique* **21,** No. 1, 43–60.

Chatterjee, S., Randolph, M. F. & White, D. J. (2012). The effects of penetration rate and strain-softening on the vertical penetration resistance of seabed pipelines. *Géotechnique* **62** No. 7, 573–582.

Chow, F. C. (1997). *Investigations into the behavior of displacement piles for offshore foundations*. Ph.D. thesis, University of London, Imperial College, London.

De Chaunac, H. & Holeyman, A. (2018). Numerical analysis of the set-up around the shaft of a closed-ended pile driven in clay. *Géotechnique* **68**, No. 4, 332–344.

Dey, R., Hawlader, B., Phillips, R. & Soga, K. (2015). Large deformation finite-element modeling of progressive failure leading to spread in sensitive clay slopes. *Géotechnique* **65**, No. 8, 657–668.

Dey, R., Hawlader, B., Phillips, R. & Soga, K. (2016). Modeling of large-deformation behaviour of marine sensitive clays and its application to submarine slope stability analysis. *Can. Geotech. J.* **53**, No. 7, 1138–1155.

Dutta, S., Hawlader, B. & Phillips, R. (2015). Finite element modeling of partially embedded pipelines in clay seabed using coupled Eulerian–Lagrangian method. *Can. Geotech. J.* **52**, No. 1, 58–72.

Einav, I. & Randolph, M. F. (2005). Combining upper bound and strain path methods for evaluating penetration resistance. *Int. J. Numer. Methods Engng.* **63**, No. 14, 1991–2016.

Fellenius, B. H. & Samson, L. (1976). Testing drivability of concrete piles and disturbance to sensitive clay. *Can. Geotech. J.* **13**, 139–160.

Flaate, K. (1972). Effects of pile driving in clays. *Can. Geotech. J.* **9**, 81–88.

Hamouche, K. K., Leroueil, S., Roy, M. & Lutenegger, A. J. (1995). In situ evaluation of K0 in eastern Canada clays. *Can. Geotech. J.* **32**, No. 4, 677–688.

Hawlader, B., Fouzder, A. & Dutta, S. (2016) Numerical modeling of suction and trench formation at the touchdown zone of steel catenary riser. *Int. J. Geomech.* **16**, No. 1, 04015033.

Henke, S. & Grabe, J. (2009). Numerical modeling of pile installation. In *Proceedings of the 17th International Conference on Soil Mechanics and Geotechnical Engineering*, Egypt, 1321–1324.

Hossain, M. S. & Randolph, M. F. (2009). Effect of strain rate and strain softening on the penetration resistance of spudcan foundations on clay. *Int. J. Geomech.* **9**, 122–132.

Hu, Y. & Randolph, M. F. (1998). A practical numerical approach for large deformation problems in soil. *Int. J. Numer. Anal. Methods Geomech.* **22**, No. 5, 327–350.

Jardine, R. J., Chow, F. C., Matsumoto, T. & Lehane, B. M. (1998). A new design procedure for driven piles and its application to two Japanese clays. *Soils Found.* **38**, No. 1, 207–219.

Karlsrud, K. & Haugen, T. (1985). Behaviour of piles in clay under cyclic axial loading– results of field model tests. In *Proceedings of the 4th International Conference on Behaviour of Offshore Structure*, Delft, Netherland, 589–601.

Karlsrud, K. & Hernandez-Martinez, F. G. (2013). Strength and deformation properties of Norwegian clays from laboratory tests on high-quality block samples. *Can. Geotech. J.* **50**, No. 12, 1273–1293.

Karmaker, R., Hawlader, B. & Chen, W. (2019). Finite element modeling of jacked piles in clay and loose sand. In *Proceedings of 72nd Canadian Geotechnical Conference, GeoSt.John's 2019*, St. John's, NL, Canada. Paper No-436.

Ko, J., Jeong, S. & Lee, J. K. (2016). Large deformation FE analysis of driven steel pipe piles with soil plugging. *Comput. Geotech.* **71**, 82–97.

Konrad, J. M. & Roy, M. (1987). Bearing capacity of friction piles in marine clay. *Géotechnique* **37**, No. 2, 163–175.

Kou, H., Zhang, M. & Yu, F. (2015). Shear zone around jacked piles in clay. *J. Perform. Constr. Facil.* **29**, No. 6, 04014169-6.

La Rochelle, P., Trak, B., Tavenas, F. & Roy, M. (1974). Failure of a test embankment on a sensitive Champlain clay deposit. *Can. Geotech. J.* **11**, No. 1, 142–164.

Lefebvre, G., Ladd, C. C. & Pare, J. J. (1988). Comparison of field vane and laboratory undrained shear strength in soft sensitive clays. *Vane shear Strength Testing in Soils: Field and Laboratory Studies*, ASTM STP 1014, A. F. Richards, Ed. ASTM, Philadelphia, 233–246.

Lefebvre, G., Bozozuk, M., Philibert, A. & Hornych, P. (1991). Evaluating K_0 in Champlain clays with hydraulic fracture tests. *Can. Geotech. J.* **28,** No. 3, 365–377.

Lehane, B. (1992). *Experimental investigations of pile behaviour using instrumented field piles*. Ph.D. thesis. University of London, Imperial College, London.

Lehane, B. M. & Jardine, R. J. (1994). Displacement-pile behavior in a soft marine clay. *Can. Geotech. J.* **31**, 181–191.

Liyanapathirana, D. S. (2009). Arbitrary Lagrangian-Eulerian based finite element analysis of cone penetration in soft clay. *Comput. Geotech.* **36**, 851–860.

Lo, K. Y. & Stermac, A. G. (1965). Induced pore pressures during pile driving operations. In *Proceedings of 6th International Conference on Soil Mechanics and Foundation Engineering*, Montréal **11**, 285–289.

Locat, A., Jostad, H. P. & Leroueil, S. (2013). Numerical modeling of progressive failure and its implications for spreads in sensitive clays. *Can. Geotech. J.* **50**, No. 9, 961–978.

Merifield, R. S., White, D. J. & Randolph, M. F. (2009). Effect of surface heave on response of partially embedded pipelines on clay. *J. Geotech. Geoenviron. Engng.* **135**, No. 6, 819–829.

Meyerhof, G. G. (1951). The ultimate bearing capacity of foundations. *Géotechnique* **2**, No. 4, 301–332.

Perret, D., Therrien, J., Locat, P. & Demers, D. (2019). Influence of surficial crusts on the development of spreads and flows in Eastern Canadian sensitive clays. In *Proceedings of the 72nd Canadian Geotechnical Conference*, St. John's.

Qiu, G., Henke, S. & Grabe, J. (2011). Application of a Coupled Eulerian–Lagrangian approach on geomechanical problems involving large deformations. *Comput. Geotech.* **38**, 30–39.

Quinn, P. E., Diederichs, M. S., Rowe, R. K. & Hutchinson, D. J. (2011). A new model for large landslides in sensitive clay using a fracture mechanics approach. *Can. Geotech. J.* **48**, No. 8, 1151–1162.

Randolph, M. F. & Wroth, C. P. (1979). An analysis of the vertical deformation of pile groups. *Géotechnique* **29**, No. 4, 423–439.

Randolph, M. F., Carter, J. P. & Wroth, C. P. (1979). Driven piles in clay-the effects of installation and subsequent consolidation. *Géotechnique* **29**, No. 4, 361–393.

Randolph, M. F. & Houlsby, G. T. (1984). The limiting pressure on a Circular pile loaded laterally in cohesive soil. *Géotechnique* **34**, No. 4, 613–623.

Randolph, M. F., White, D. J. & Yan, Y. (2012). Modeling the axial soil resistance on deep-water pipelines. *Géotechnique* **62**, No. 9, 837–846.

Robert, D. J., Britto, A. & Setunge, S. (2020). Efficient approach to simulate soil–pipeline interaction. *J. Pipeline Syst. Eng. Pract.* **11**, No. 1, 04019046.

Roy, M. & Leblanc, A. (1988). Factors Affecting the Measurements and Interpretation of the Vane Strength in Soft Sensitive Clays. in *Vane Shear Strength Testing in Soils: Field and Laboratory Studies*, ed. A. Richards (West Conshohocken, PA: ASTM International, 1988), 117–128.

Roy, M., Michaud, D., Tavenas, F., Leroueil, S. & La Rochelle, P. (1974). The interpretation of static cone penetration tests in sensitive clays. In *Proceedings of the European Symposium on Penetration Testing*, Stockholm **2**, 323–330.

Roy, M., Blanchet, R., Tavenas, F. & Rochelle, P. L. (1981). Behaviour of a sensitive clay during pile driving. *Can. Geotech. J.* **18**, No. 1, 67–85.

Roy, M. & Lemieux, M. (1986). Long-term behaviour of reconsolidated clay around a driven pile. *Can. Geotech. J.* **23**, No. 1, 23–29.

Sagaseta, C. & Whittle, J. (2001). Prediction of ground movements due to pile driving in clay. *J. Geotech. Geoenviron. Engng.* **127**, No. 1, 55–66.

Silvestri, V., Karam, G., Tonthat, A. & St-Amour, Y. (1989). Direct and simple shear testing of two Canadian sensitive clays. *Geotech. Testing J.* **12**, No. 1, 11–21.

Tavenas, F. & Leroueil, S. (1977). Effects of stresses and time on yielding of clays. *In Proceedings of 9th International Conference on Soil Mechanics and Foundation Engineering*, Tokyo, 1, 319-326.

Tavenas, F., Flon, P., Leroueil, S. & Lebuis, J. (1983). Remolding energy and risk of slide retrogression in sensitive clays. In *Proceedings of the Symposium on Slopes on Soft Clays,* SGI Report, Linköping, Sweden, **17**, 423–454.

Teh, C. I. & Houlsby, G. T. (1991). An Analytical Study of the Cone Penetration Test in Clay. *Géotechnique* **41**, No. 1, 17–34.

Tian, Y., Wang, D. & Cassidy, M. (2011). Large deformation finite element analysis of offshore geotechnical penetration tests. In *proceeding of the second International Symposium on Computational Geomechanics, USA* **1**, 925–933.

Tho, K. K., Leung, C. F., Chow, Y. K. & Swaddiwudhipong, S. (2012). Eulerian finite-element technique for analysis of jack up spudcan penetration. *Int. J. Geomech.* **12**, No. 1, 64–73.

Vesić, A. S. (1972). Expansion of cavities in infinite soil mass. *J. Soil mech. Found. Div.* **98**, No. 3, 265–290.

Walker, J. & Yu, H. S. (2006). Adaptive finite element analysis of cone penetration in clay. *Acta Geotech.* **1**, No. 1, 43–57.

Wang, C., Hawlader, B., Perret, D. & Soga, K. (2020). Effects of Geometry and Soil Properties on Type and Retrogression of Landslides in Sensitive Clays. *Géotechnique*, 1–15.

Wang, C., Hawlader, B., Perret, D., Soga, K. & Chen, J. (2021). Modeling of Initial Stresses and Seepage for Large Deformation Finite-Element Simulation of Sensitive Clay Landslides. *J. Geotech. Geoenviron. Engng.* **147**, No. 11, 04021111.

Wang, D., Bienen, B., Nazem, M., Tian, Y., Zheng, J., Pucker, T. & Randolph, M. F. (2015). Large deformation finite element analyses in geotechnical engineering. *Comput. Geotech.* **65**, 104–114.

White, D., Finlay, T., Bolton, M. & Bearss, G. (2002). Press-in piling: ground vibration and noise during pile installation. *Deep Foundations 2020*, 363–371.

Whittle, A. J., Hashash, Y. M. A. & Whitman, R. V. (1993). Analysis of deep excavation in Boston. *J. Geotech. Engng* **119**, No. 1, 69–90.

Yang, J., Tham, L. G., Pee, P. K. K., Chan, S. T. & Yu, F. (2006). Behaviour of jacked and driven pile in sandy soil. *Géotechnique* **56**, No. 4, 245–259.

Yi, J. T., Lee, F. H., Goh, S. H., Zhang, X. Y. & Wu, J. F. (2012). Eulerian finite element analysis of excess pore pressure generated by spudcan installation into soft clay. *Comput. Geotech.* **42**, 157–170.

Yu, H. S., Hermann, L. R. & Boulanger, R. W. (2000). Analysis of steady cone penetration in clay. *J. Geotech. Geoenviron. Engng.* **126**, No. 7, 594–605.

Zhu, H. & Randolph, M. F. (2011). Numerical analysis of a cylinder moving through rate-dependent undrained soil, *Ocean Eng.* **38**, No. 7, 943–953.

Zhou, H., Liu, H., Yuan, J. & Chu J. (2019). Numerical simulation of XCC pile penetration in undrained clay. *Comput. Geotech.* **106**, 18–41.

Chapter 4

Comparative numerical modeling of impact pile driving and pile jacking in sensitive clays

Co-Authorship: This chapter has been submitted as a technical paper for publication in a journal as: Karmaker, R., Hawlader, B., Perret, D. and Dey, R., 'Comparative numerical modeling of impact pile driving and pile jacking in sensitive clays.' Most of the research presented in this chapter has been conducted by the first author. He also prepared the draft manuscript. The other authors mainly supervised the research and reviewed the manuscript.

4.1 Abstract

This chapter represents a comparative numerical study of impact pile driving and pile jacking using a large deformation finite element modeling technique. A simple mathematical framework is proposed to calculate the excess pore pressure generation due to pile installation in sensitive clays. Numerical results show that the degree of undrained shear strength degradation remains the same for both cases, although the zone of soil degradation is slightly higher in impact pile driving. Unlike jacking, an impact driving changes the stress state during loading-unloading phases of a blow, which is not observed in pile jacking cases. Soil elements undergo a large deformation near the pile, depending upon the rate of strength reduction, which is higher in the case of pile jacking due to the continuous insertion of the pile. In impact pile driving, the strength reduction parameters also influence the depth of penetration and plastic shear strain in each blow. When the soil reaches the remoulded condition very quickly (i.e., small δ_{95}), a high rebound of pile top is obtained. For highly sensitive clay (i.e., large s_{u0}/s_{uR}), the smaller rebound is observed, although the depth of

penetration is high. The permanent set of pile heads decreases with the number of blows, which implies that the resistance to drive increases over depth.

4.2 Introduction

Installation of a displacement pile by jacking or impact driving changes the stress condition in the surrounding soil due to vertical and radial displacements of soil. The resulting strain could increase the pore water pressure and cause soil disturbance due to strain softening in sensitive clays. Both of these factors significantly affect the subsequent load-carrying capacity. The conventional pile installation process by impact driving also creates ground vibrations that might affect the surrounding infrastructures, such as permanent settlements, densifications, liquefactions and damages in some cases. White et al. (2002) found up to $10-50$ times larger ground vibrations for diesel hammer and vibratory piling than that of a press-in piling method (one type of pile jacking) in two urban field investigations sites. However, pile jacking also causes displacement of a large volume of soil where undrained shear strength degradation occurs. The displaced soils predominantly cause ground heave at shallow depths and local radial displacement for the higher penetration depth (Randolph et al., 1979). Comparison between two installation processes in terms of soil stress state changes, soil displacements, plastic deformations and generation of excess pore pressure could provide a better insight into the failure mechanisms and subsequent capacity on the pile capacities in sensitive clays.

A detailed description of numerical modeling on pile jacking has been presented in Chapter 3. Therefore, the literature review in this chapter primarily focuses on impact driving. Several analytical (Smith, 1960; Randolph & Simons, 1986; Lee et al., 1988; Deeks & Randolph, 1993; Liang & Husein, 1993), experimental (Cummings et al., 1950; Alves et al., 2009; Hosseini & Rayhani, 2017), and numerical (Davis & Phelan, 1978; Smith & Chow, 1982; Borja, 1988; Smith

& To, 1988; Mabsout & Tassoulas, 1994; Ekanayake et al., 2013; Heins & Grabe, 2017) studies have been carried out to acquire knowledge in pile driving and its effects on the surrounding soils. Three commonly used approaches for analyzing pile driveability are dynamic pile formulas, wave-equation, and the Pile-Driving Analyzer. Several hundred dynamic formulas are available in the impact pile driving, which is not always competent in all cases. As a pioneer to propose one pile-driving formula, Smith (1960) developed a mathematical model using one-dimensional dynamic analysis in which the pile is modelled as a series of lumped masses interconnected to idealized soil springs. Smith & Chow (1982) showed a significant difference in the response between three-dimensional (axisymmetric) finite element (FE) analyses and one-dimensional wave theorem. Randolph & Simons (1986) and Lee et al. (1988) proposed improved models to overcome some of the limitations of Smith's wave equation and to simulate the pile–soil dynamic interaction. Alves et al. (2009) carried out a small-scale pile driving experiment and found a good agreement between the measured and simulated signals of shaft resistance using the model proposed by Randolph & Simons (1986).

More sophisticated numerical analyses of impact pile driving could provide a better insight into the ground responses and realistic soil–pile interactions. In the last several decades, a large number of researches has been carried out to develop the numerical modeling techniques for impact pile driving (Borja, 1988; Mabsout & Tassoulas, 1994; Mabsout et al., 1995; Liyanapathirana et al., 2000; Henke & Grabe, 2006; Masoumi & Degrande, 2008; Masoumi et al., 2009; Ko et al., 2016; Rooz & Hamidi, 2017). In previous studies, some essential assumptions were made to simplify the numerical analyses; however, these simulations cannot identify the influences of some key factors. For example, the one-dimensional wave theory can not capture the actual three-dimensional ground responses and soil–pile interactions. Previous studies mostly considered pre-bored piles

before applying the impact load to reduce the computational costs and numerical issues due to large deformation, which means discontinuous pile driving was simulated. Mabsout et al. (1995) admitted that discontinuous modeling could not properly simulate the effects of the disturbance of the soil around the piles, as continuous pile driving causes a large remoulding of the adjacent soils. However, such assumptions sometimes might lead to unrealistic stress–strain behaviour due to pile driving (Baligh, 1985; Borja, 1988; Mabsout et al., 1995; Masoumi et al., 2009; Ko et al., 2015). Mabsout & Tassoulas (1994) simplified the problem by applying a uniform overburden pressure on top of the soil domain used for FE analysis to avoid calculation costs for the large pre-bored depth. Some recent studies considered the Arbitrary Lagrangian-Eulerian (ALE) modeling techniques (Sheng et al., 2005; Rooz & Hamidi, 2017; Rooz & Hamidi, 2019). Although ALE offers modeling of relatively large deformations, the built-in remapping algorithm can not solve the complex changes of the free surface, for example, the ground heaving due to pile installation (Konkol, 2015). Recently, the Coupled Eulerian-Lagrangian (CEL) Framework has been efficiently used to model complex soil–structure interactions during penetration such as as-laid offshore pipeline (Merifield et al., 2009; Chatterjee et al., 2012; Dutta et al., 2015), cone (Walker & Yu, 2006; Liyanapathirana, 2009), spudcan (Hossain & Randolph, 2009; Yi et al., 2012) and piles (Henke & Grabe, 2009; Konkol, 2015; Ko et al., 2016).

Pile installation in sensitive clays causes increased pore pressure around the pile, which reduces the effective stress of the surrounding soils. Bjerrun et al. (1958) measured driving-induced pore pressure in clays around a group of concrete piles. After that, several studies reported the driving-induced excess pore pressure in sensitive clays and effects of reconsolidation on the post-driving dissipation of the excess pore pressure (Orrje & Broms, 1967; Broms & Bennermark, 1967; Fellenius & Broms, 1969; Bozozuk et al., 1978; Blanchet et al., 1980; Roy et al., 1982). Vesić

(1972) proposed the equations for cylindrical and spherical expansions for deep penetration problems based on cavity expansion theory. Roy et al. (1981) measured the excess pore pressure (u_e) around the tip, pile shaft and in surrounding soil during the installation of the pile at the St-Alben test site. Modified spherical and cylindrical cavity expansion theories were used to estimate u_e in the plastic zone. Adjusting the model parameters empirically (intact/destructured), u_e near the pile surface was reasonably matched. However, considerable discrepancies were found for the soil elements far from the pile shaft, which they attributed to the result of strain-softening that was not explicitly modelled. Randolph et al. (1979) provided a simplified closed-form solution based on the cavity expansion theory using the basic soil properties to estimate the excess pore pressure during pile driving and subsequent dissipation due to consolidation after the driving. Baligh (1985) proposed a "strain path method (SPM)," which can also calculate the excess pore pressure based on an approximate analytical solution of soil disturbances due to the deep penetration of piles, cone penetrometers, in-situ testing tools, soil samplers, etc. The SPM method in its original form and modified version has been used later to compare field test results, including pile installations, tube samplers penetration and cone penetration tests (Baligh, 1986; Baligh & Levadoux, 1986; Huang, 1989; Teh & Houlsby, 1991; Gill & Lehane, 2000; White & Bolton, 2004). However, there are very limited studies in the incorporation of the effects of the strain-softening behaviour in estimating the excess pore pressure in the literature (Randolph et al., 1979; Carter & Yeung, 1985).

This chapter has been organized as follows. The first part presents a mathematical framework to calculate the driving-induced excess pore pressure during pile installation and the implementation of that framework in numerical modeling. The second part describes the large deformation finite element modeling of pile driving in sensitive clays. Finally, detailed comparative studies have been carried out for pile driving and pile jacking in sensitive clays.

4.3 Methodology

Installation of a solid cylindrical pile into soft sensitive clay under an undrained condition is simulated. Field investigations at many sites show that the undrained shear strength of sensitive clays increases with depth (Lefebvre, 1992; Locat et al., 2015). In the present study, the initial undrained shear strength (s_{u0}) of the sensitive clay layer (i.e., prior to softening and at the reference strain rate, as discussed later) increases linearly with depth as:

$$s_{u0} = s_{ug} + kz \tag{4.1}$$

where s_{ug} is a constant in kPa, k is the strength gradient in kPa/m, and z is the depth of the soil element below the ground surface in meter.

A similar soil profile is used in Chapter 3 for a parametric study to simulate pile jacking in sensitive clays. The present study compares the change of the stresses, plastic deformation, soil displacements and generation of excess pore pressure during impact pile driving and pile jacking. The groundwater table is considered at the ground surface, and soil is assumed to be fully saturated. A solid pile of 0.4-m diameter (D) is driven using 30 blows (Fig. 4.1(a)). At any instant, the depth of the pile tip (point T in the inset of Fig. 4.1(a)) from the ground surface is denoted as z_{tip}. At the beginning of the calculation, the pile tip is placed slightly above the ground surface (0.01 mm) to avoid any pile–soil interaction during the in-situ stress establishment step by gravity loading. The radial distance of a soil element from the pile centerline and pile surface is denoted by w_i and w_s, respectively (Fig. 4.1(b)).

4.3.1 Generation of excess pore pressure

As mentioned above, one of the main focuses of the present study is developing an approach for estimating pore water pressure (u_e) generation during installation. For non-sensitive clays,

several approaches (e.g., Cam-clay model) are available to calculate u_e during undrained loading. While it cannot be directly used, the critical state framework can be modified to calculate u_e for undrained loading in sensitive clays. In this section, the development of the model, its implementation in the software using user subroutines, and simulations of a single element undrained loading are presented to show the model performance. This model has been used to calculate pore pressure generation during pile installation, as discussed in the later sections.
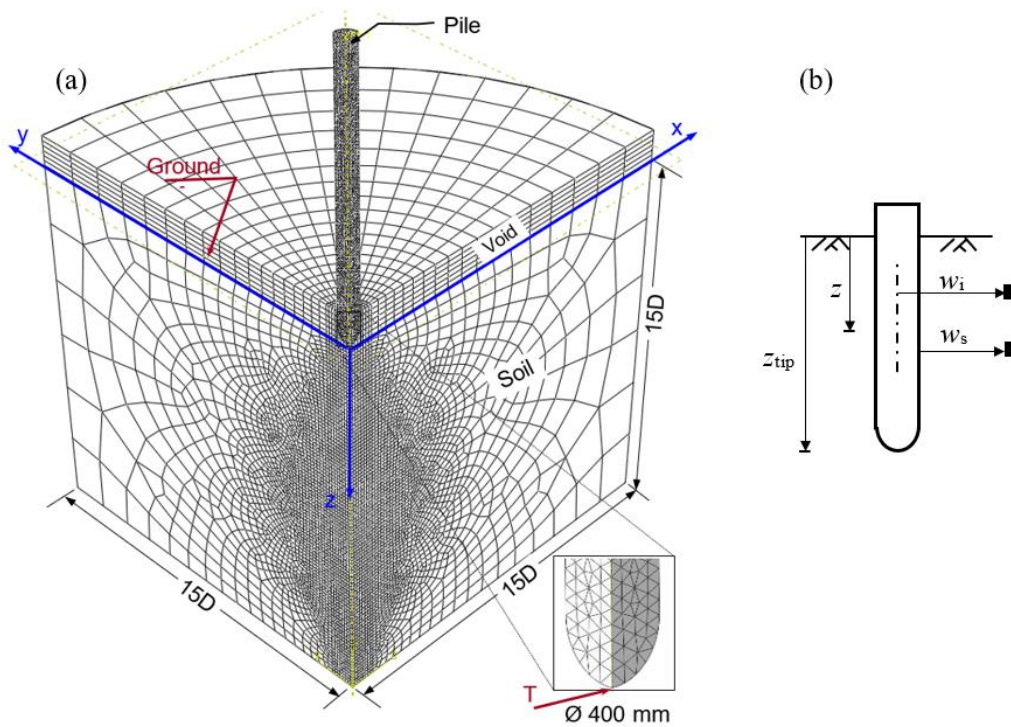
Fig. 4. 1. Problem statement: (a) Finite element mesh for parametric study with idealized soil profile; (b) notations

Field investigations show that sensitive clays at many sites (e.g., eastern Canadian clay, Finish clay) are lightly overconsolidated (Bjerrum & Landva, 1966; Flaate, 1971; Blanchet et al., 1980;

Azzouz & Lutz, 1986; Azzouz & Morrison, 1988; Länsivaara et al., 2014; Locat et al., 2014; Thakur et al., 2014a & 2014b; Lefebvre, 2017; Mayne et al., 2019). However, a higher overconsolidation ratio (OCR) is generally found in soil near the ground surface under the crust, and the soil might be normally consolidated at larger depths. Undrained triaxial tests show that the peak stress mobilized rapidly, typically within 1-2% axial strain (Thakur et al., 2014b; Lefebvre, 2017), and then strain-softening occurs primarily due to structural breakdown. In the present study, the pre-peak behaviour is assumed to be elastic (Fig. 4.2(a)). Pore pressure is generated both in pre-peak deformation and post-peak softening (Thakur et al., 2014b).

Figure 4.2(a) schematically shows the stress–strain curve used in the present study. The corresponding effective stress path is shown in Fig. 4.2(b). If the soil is normally consolidated, the mean effective stress (p') will reduce and follow a nonlinear effective stress path oa during pre-peak loading. However, if the soil is highly overconsolidated, p' will increase and follow the nonlinear path ob. As the Eulerian-based FE program allows the simulation only for single-phase material (no pore water flow), linear effective stress path (solid lines oa or ob in Fig. 4.2(b)) is used. Note that the actual (dashed lines) and assumed (solid lines) difference is higher for normally consolidated and highly overconsolidated clays. However, many sensitive clays at the in-situ state are lightly overconsolidated. The effective stress path follows approximately a linear line for this type of soil and moves almost vertically, as shown by Thakur et al. (2014b) for Rissa clay of OCR = 2.25. In other words, a linear pre-peak stress path assumption is reasonable.

Laboratory tests show that, except for highly overconsolidated clays, the undrained effective stress path of sensitive clays follows a Mohr-Coulomb failure line (Thakur et al., 2014b). Unlike cohesion and friction softening (i.e., reduction of these values with shear strains) in drained loading of overconsolidated clays, undrained softening of sensitive clays occurs rapidly due to shear-

induced structural breakdown and pore pressure build-up, at least up to laboratory test shear strain levels (<20%). Note that the cohesion and friction softening might be considered in highly overconsolidated sensitive clays (Lacasse et al. 1985), which is not the present study's focus as it is not very common. To capture the above observations in laboratory tests, it is assumed that the effective stress path after the peak will follow the line is drawn through the origin: a→g and b→h for normally and overconsolidated sensitive clays, respectively.
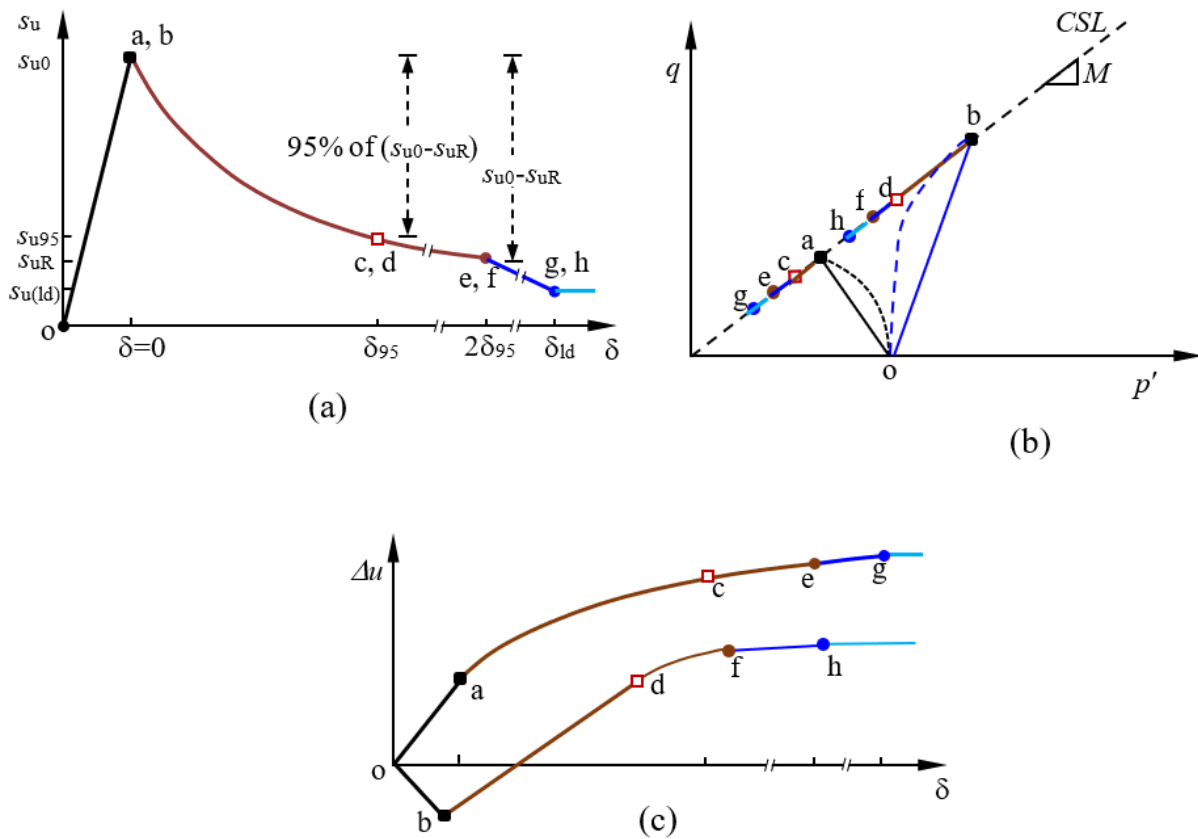
Fig. 4. 2. Modeling of soil: (a) stress-strain behaviour; (b) simplified stress path for pore pressure estimation; (c) pore pressure development

Now the bi-linear effective stress path shown in Fig. 4.2(b) (i.e., oag or obh) is used to estimate excess pore pressure (u_e) from total stress analysis. At the in-situ states, the mean total stress (p_0) and hydrostatic pore water pressure (u_0) can be calculated as:

$$p_0 = (1+2K)\sigma_{v0}/3 \qquad\qquad (4.2)$$

$$u_0 = \gamma_w z \qquad\qquad (4.3)$$

Where K is the ratio between total horizontal and vertical stresses; σ_{v0} is the vertical total stress; γ_w is the unit weight of water, and z is the depth from the ground surface. The mean effective stress (p') at the in-situ conditions (p_0') is $p_0 - u_0$.

The initial undrained shear strength of soil (s_{u0}) is given as an input parameter in the FE analysis. The slope of the failure line (M) in Fig. 4.2(b) can be obtained from the angle of internal friction using the critical state soil mechanics concept. It is understood that M depends on the mode of shearing (e.g., triaxial compression/extension); however, a constant value of M is used in this study. Now, from the geometric relationship shown in Fig. 4.2(b), the mean effective stress when the peak shear strength is mobilized (points a or b) (p_{cs}') is $2s_{u0}/M$. The geometric relationships in Fig. 4.2(b) are also used to calculate the change in mean effective stress ($p_0' - p'$), which represents the shear-induced excess pore pressure generation (u_s), using Eq. (4.4) and Eq. (4.5) for pre-peak and post-peak loading conditions, respectively.

$$u_s = \left(\frac{p_0'}{2s_{u0}} - \frac{1}{M} \right) \sigma_e \qquad\qquad (4.4)$$

$$u_s = p_0' - \frac{2s_u}{M} \qquad\qquad (4.5)$$

Where s_u is the mobilized undrained shear strength after the peak (Fig. 4.3(a)), which is obtained using a post-peak degradation relationship, as discussed in later sections. Now, adding u_s to the change in mean total stress change from the initial condition ($\Delta p = p - p_0$), the excess pore water pressure (u_e) during loading is calculated. In the FE analysis, the mean total stress (p) is obtained at each time increment, which is then used to calculate u_e as other parameters are known.

4.4 FE modeling of pile installation

The Coupled Eulerian-Lagrangian (CEL) method available in Abaqus/Explicit FE software is used in the present study. Unlike traditional Lagrangian-based FE methods, where the mesh deforms with the displacement of the material, CEL allows the Eulerian materials (e.g., soil) to flow through the fixed mesh. Therefore, numerical issues related to mesh distortion are not encountered. The Eulerian material is defined and tracked by the Eulerian Volume Fraction (EVF) tools. EVF = 1 represents the element completely filled with Eulerian material, EVF = 0 represents no materials in the element (i.e., void), and 0 < EVF < 1 represents the elements partially filled with Eulerian materials.

The CEL framework has been implemented only for three-dimensional FE modeling. A one-quarter of the domain is modelled by taking advantage of symmetrical conditions (Fig. 4.1(a)). The Eulerian domain is discretized with 8-node linear brick elements. The pile is modelled as a rigid body. Fine mesh is used where a considerable soil displacement occurs during installation. An advanced technique is used to implement the element size scaling, which eliminates the size dependency while calculating the shear strains in the elements. Further details of the FE modeling techniques have been discussed in Chapter 3.

A zero-velocity boundary condition is applied normal to all the vertical faces. At the bottom of the domain, zero-velocity boundary conditions are applied in all three directions (i.e. $v_x = v_y = v_z$

= 0), meaning that the soil elements next to this boundary are restrained from any movement. No boundary condition is applied at the soil–void interface so that the soil can displace into the void during the penetration of the pile when needed (e.g., ground surface heaving near the pile). Energy radiation and wave reflection from the boundary could play a significant role in dynamic FE analysis. Previous studies used boundary element formulations, infinite elements or artificial boundaries (Henke & Grabe, 2009; Masoumi et al., 2009; Khoubani & Ahmadi, 2014; Rezaei et al., 2016; Rooz & Hamidi, 2017). The present study applies an Eulerian outflow non-reflecting boundary condition at the curved outer boundary. Successful use of this boundary condition in the Eulerian FE modeling has been presented elsewhere (Wang et al., 2019; Islam et al., 2019). The present approach neglects the mass proportional damping. However, a stiffness proportional damping of 0.000375 is used. Further details on material damping are available in Wang et al. (2019).

For undrained loading, the pile–soil interface resistance (τ_{max}) depends on mobilized undrained shear strength as $\tau_{max} = \alpha s_u$, where $0 \leq \alpha \leq 1.0$. However, FE modeling of interface resistance as a function of mobilized s_u is challenging. Therefore, in previous studies, a constant value of τ_{max} has been used. For example, τ_{max} equal to the remoulded undrained shear strength was used for pile and pipeline penetrations in low to moderate sensitive clays (Einav & Randolph, 2005; Hossain & Randolph, 2009; Kim & Hossain, 2015; Liu et al., 2016). The present study performs analyses for smooth and $\tau_{max} = 6$ kPa.

To establish the in-situ stress condition, initial stresses ($K\sigma_{v0}$, $K\sigma_{v0}$, σ_{v0}) are given first to the soil elements (EVF $\neq$ 0), where σ_{v0} is the vertical total stress, and K is the ratio between horizontal to vertical total stresses. Then the gravitational load is applied to the soil elements and brings in an equilibrium condition. If the groundwater table is at the horizontal ground surface, K is related

to the effective earth pressure coefficient at rest (K_0) as $K = K_0 + (1-K_0)\gamma_w/\gamma$. By defining the initial condition in this way, the simulation can be performed for $K_0 > 1$, as observed in some sensitive clays (e.g., eastern Canada).

4.4.1 Forcing function for impact driving

FE modeling of impact driving requires a forcing function that provides a vertical stress wave on the pile head. Deeks & Randolph (1993) proposed an analytical method to develop the force–time curve based on three dimensionless parameters: cushion stiffness, anvil mass, and cushion damping. Previous studies used a widely varying maximum impact stress (0.5 MPa–24 MPa) depending upon soil conditions, hammer type, pre-bored conditions and method of analysis (Borja, 1988; Mabsout & Tassoulas, 1994; Liyanapathirana et al., 2000; Hussein et al., 2006; Alves et al., 2009; Khoubani & Ahmadi, 2009; Ko et al., 2015; Fan et al., 2021). For sensitive clays, the maximum impact stress is generally low. In addition, the time span of the impact load also plays an important role in drivability. A wide range of time spans has been used in previous studies; for example, 16 ms (Deeks & Randolph, 1993; Rooz & Hamidi, 2017; Fan et al., 2021), 40 ms (Gobble 1980; Mabsout & Tassoulas, 1994; Mabsout et al., 1995; Ko et al., 2015) and 80 ms (Jayawardana et al., 2018). In the present study, a forcing function shown in Fig. 4.3 is used. Similar forcing function have been used in previous studies (Deek & Randolph, 1993; Rooz & Hamidi, 2017). Note that while the impact force on the pile head ceases at 40 ms, the analysis is continued for 1 s for each blow.
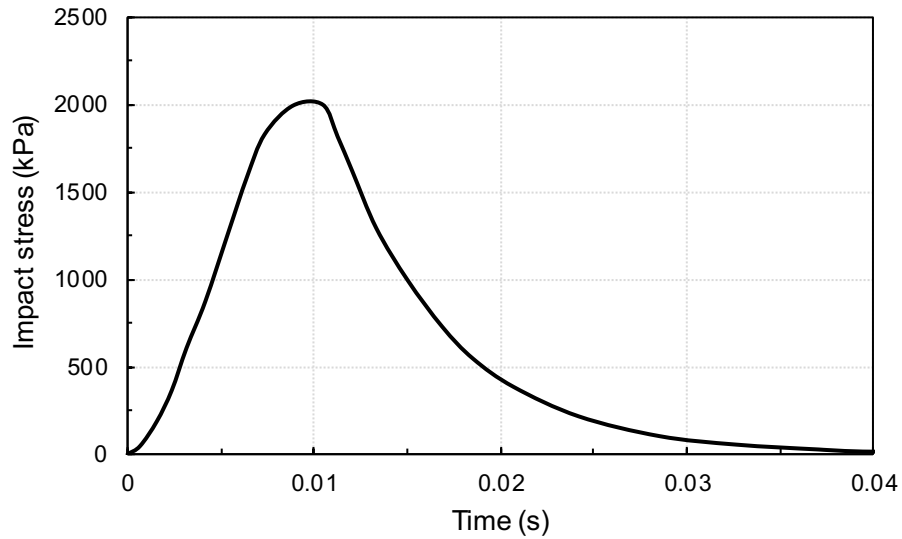
Fig. 4.3. Hammer impact loading on the pile head

4.4.2 Modeling of sensitive clays

The mobilized undrained shear strength (s_u) of sensitive clays is modelled using Eq. (4.6), incorporating a strain-softening factor, f_1 (≤ 1.0) and strain-rate factor, f_2 as:

$$s_u = f_1 f_2 s_{uy} \tag{4.6}$$

where s_{uy} is the undrained shear strength at a very low strain rate. Sensitive clays show anisotropic undrained shear strength (e.g. Karlsrud & Hernandez-Martinez, 2013); however, this study has not considered it.

Strain softening behaviour of sensitive clay

Linear and exponential reduction factor f_1 as the function of accumulated plastic shear strain or plastic shear displacement (δ), have been used in previous studies (Locat et al., 2013; Dey et al., 2015 & 2016). The following equations are used in the present study for modeling post-peak s_u degradation.

$$f_1 = \begin{cases} \dfrac{s_{uR}}{s_{u0}} + \left(1 - \dfrac{s_{uR}}{s_{u0}}\right)e^{-3\delta/\delta_{95}} & \text{if } 0 \leq \delta < 2\delta_{95} \\[3mm] \dfrac{s_{uR}}{s_{u0}} - \dfrac{s_{uR} - s_{uld}}{s_{u0}}\dfrac{\delta - 2\delta_{95}}{\delta_{ld} - 2\delta_{95}} + c & \text{if } 2\delta_{95} \leq \delta < \delta_{ld} \\[3mm] \dfrac{s_{uld}}{s_{u0}} + c & \text{if } \delta \geq \delta_{ld} \end{cases} \qquad (4.7)$$

Where s_{u0} is the peak undrained shear strength at the reference shear strain rate ($\dot{\gamma}_{ref}$) before softening; s_{uR} is the value of s_u at sufficiently large δ; δ_{95} is the value of δ at which 95% reduction of ($s_{u0} - s_{uR}$) occurs; $c = (1 - s_{uR}/s_{u0})e^{-6} \approx 0$; and δ_{ld} is a very large value of δ (> δ_{95}) when the soil becomes completely remoulded to $s_u = s_{uld}$. Equation (4.7) represents a quick exponential degradation of s_u at $0 \leq \delta < 2\delta_{95}$ followed by a linear degradation at $2\delta_{95} \leq \delta < \delta_{ld}$ and then a constant s_u (= s_{uld}) at $\delta \geq \delta_{ld}$. Equation (4.7) for $0 \leq \delta < 2\delta_{95}$ is similar to the s_u degradation equation proposed by Einav & Randolph (2005).

As will be shown later that the plastic shear strain or shear displacement developed during the installation of a pile is not extremely large, as happened in some other large deformation problems (e.g., landslides). Therefore, the strain-softening is mainly governed by the exponential degradation (first part of Eq. (4.7)). In other words, the rate and magnitude of post-peak shear strength degradation primarily depend on s_{uR} and δ_{95}. Therefore, in the later sections, a detailed investigation of the effect of these two factors is performed.

Dey et al. (2016) showed a wide variation of s_{uR}, $\delta_{95,}$ and δ_{ld} when the model was compared with test results on sensitive clays from different sites conducted by Tavenas et al. (1983). Table 4.1 shows the model parameters used in FE modeling unless otherwise mentioned. The values of these parameters are obtained from a detailed review of previous studies (Tavenas et al., 1983; Quinn et al., 2011; Dey et al., 2016).

Strain-rate effects on undrained shear strength of sensitive clays

A detailed discussion on strain-rate effects on undrained shear strength is available in previous studies (e.g. Zhu & Randolph, 2011; Zakeri & Hawlader, 2013; Wang et al., 2021). In the present study, an "additive power-law model" proposed by Zhu & Randolph (2011), which combines the Herschel-Bulkley (fluid mechanics approach) and power-law model (geotechnical approach), is used:

$$f_2 = \left[1 + \eta \left(\dot{\gamma}/\dot{\gamma}_{\mathrm{ref}} \right)^{\beta} \right] \tag{4.8}$$

where η and β are the soil parameters. The value of η depends on the reference shear strain rate. The typical range of β is 0.05–0.15, which increases with the plasticity index. Based on previous studies (Boukpeti et al., 2012; Randolph et al., 2012; Wang et al. 2020), $\eta = 0.5$ and $\beta = 0.1$ are used in the present study. Using $\dot{\gamma} = \dot{\gamma}_{\mathrm{ref}}$ in Eq. (4.8) and then inserting f_2 in Eq. (4.6) with $f_1 = 1.0$ (no softening) and $s_u = s_{u0}$, the undrained shear strength at a very low strain rate can be calculated as $s_{uy} = s_{u0}/(1 + \eta)$. However, the process becomes partially drained or drained at a low shearing rate in the field. For example, vane shear tests in low plastic sensitive clays show that the shear strength does not decrease at a very slow rate of rotations rather increases because of excess pore water pressure dissipation (Roy & Leblanc 1988). Therefore, in the present study, $s_u = s_{u0}$ is used when $\dot{\gamma} \leq \dot{\gamma}_{\mathrm{ref}}$.

The post-peak strength degradation is defined by s_{uR}, $\delta_{95,}$ and δ_{ld} (Eq. 4.7). Even though the sensitive clays can have a very low remoulded undrained shear strength, but they usually mobilize at very large shear strains. A wide variation of s_{uR}, $\delta_{95,}$ and δ_{ld} were found when the model was compared with test results on sensitive clays from different sites, conducted by Tavenas et al.

(1983). In the present study, analyses are performed for $s_{u0}/s_{uR} = 5, 10, 20$ & $\delta_{95} = 0.05$ m–0.4 m, and $\delta_{ld} = 1$ m, as shown in Table 4.1.

The strain-softening and rate effects on undrained shear strength (Eqs. (4.6)–(4.8)) and the variation of s_{u0} with depth (Eq. 4.1) are implemented in the software using a user-defined subroutine. s_{u0} is called in the subroutine only for the first time and stored as a state variable, which is used to calculate the mobilized s_u in the subsequent time increments to ensure the use of initial s_{u0} of the soil element even though it might have displaced to a different location from the initial depth. The equivalent plastic shear strain ε_q^p (PEEQVAVG in the software) is called in the subroutine for each time increment and stored as a state variable.

Table 4.1. Soil parameters used in finite element modeling

Parameter	Sensitive Clay
Total unit weight, γ (kN/m^3)	17
Undrained Young's modulus, E_u (MPa)	10
Undrained Poisson's ratio, ν_u	0.49
Initial undrained shear strength of sensitive clay, s_{u0} (kPa)	$s_{ug} + kz$
Ratio between initial and remoulded undrained shear strength, s_{u0}/s_{uR}	5 (2, 10, 20)
Ratio between initial and large deformation undrained shear strength, s_{u0}/s_{u_ld}	50
Plastic shear displacement for 95% degradation of s_{u0}-s_{uR}, δ_{95} (m)	0.05 (0.1, 0.4)
Plastic shear displacement to mobilize s_{uld}, δ_{ld} (m)	$20\delta_{95}$
Reference strain rate, $\dot{\gamma}_{ref}$ (s^{-1})	0.05[a], 5.0[b]
η	0.5
β	0.1
Stiffness damping coefficient	0.000375

Note: Values used for the parametric study are shown in parenthesis; [a]parameters for impact driving; [b]parameters for jacking.

4.5 Performance of pore water pressure model

The performance of the excess pore water pressure (u_e) generation model is shown first by simulating the response of single soil elements under undrained triaxial compression loading conditions. In many cases, field investigations show uniform peak undrained shear strength (s_{u0}) of sensitive clay layer (Lefebvre et al., 1992; Locat et al., 2015). In this set of simulations, three soil elements at a depth of 2 m, 5 m and 8 m are considered which has the same s_{u0} = 15 kPa. As these elements have different mean effective stress, the same s_{u0} means that the element at shallower depth has a higher overconsolidation ratio. In FE modeling, assuming K =1, an isotropic confining pressure of γz is applied on a 0.1 m cubical eight-node linear brick (C3D8R) element. The deviatoric stress is then applied by moving the top surface downward at a constant displacement rate of 0.0002 m/s for 50 sec. These simulations are performed for s_{u0}/s_{uR} = 5 and δ_{95} = 0.05 m, while the other parameters are the same as listed in Table. 4.1.

Fig. 4.4 shows the development of excess pore water pressure, which is obtained following the procedure described in Section 4.3.1. For the lightly overconsolidated clay elements at 5 m and 8 m depth, u_e increases rapidly during elastic loading prior to reaching σ_e = 2s_{u0}. Unlike non-sensitive clay modeling (e.g., using Cam-clay model), where σ_e remains constant after reaching the critical state, the increase of u_e continues due to post-peak softening of sensitive clay. The simulation results are similar to triaxial compression test results on Onsøy clay and Rissa clay (Lunne et al., 2008; Thakur et al., 2014). For the higher overconsolidated element at 2 m depth, u_e decreases first during pre-peak loading and then u_e increases with post-peak softening.

The total stress path (*TSP*) and estimated effective stress path (*ESP*) for these three elements are shown in Fig. 4.4(b). Starting from p', the *ESP* goes left or right depending upon *OCR* but meets at the same point, as a uniform s_{u0} is used, and then follows the failure plane towards the

origin. Similar stress paths have been reported from laboratory tests on different sensitive clays (Lacasse et al., 1985; Lunne et al., 2008; Thakur et al., 2014).

In summary, although the Eulerian-based FE approach in the software can model large deformation, it does not have any built-in method to calculate excess pore water pressure, which can be done using the proposed simplified approach. The following section calculates pore pressure generation during pile installation using this approach.
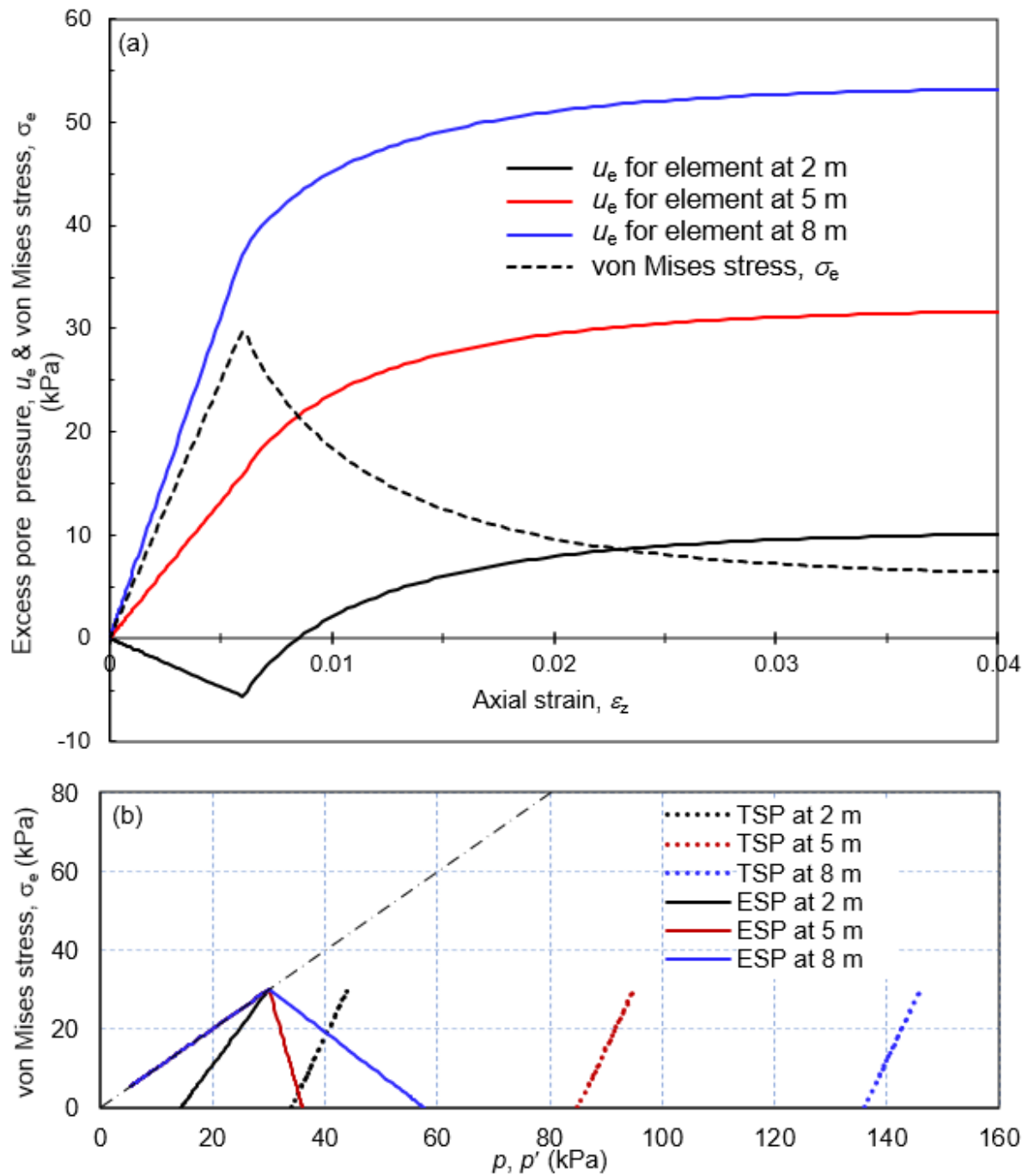
Fig. 4.4. Simulation of triaxial compression test: a) pore pressure and stress–strain behaviour;

b) stress paths

4.6 Simulation results of pile driving

Figure 4.5(a) shows the comparison of pile head penetration in 30 blows in non-sensitive and sensitive clays. A higher pile head penetration (d_p) occurs in sensitive clays, and consideration of 6 kPa interface resistance in case 3 gives slightly lower penetration than that of the smooth case. As the post-peak strength degradation occurs quickly in this case ($\delta_{95} = 0.05$ m), the mobilized s_u adjacent to the pile surface is less than τ_{max}; therefore, the failure occurs through those weak soil instead of the soil–pile interface. To verify, an analysis is also performed with $\tau_{max} = 15$ kPa and again, no significant difference in penetration has been observed. A similar response has been reported by Kim & Hossain (2015) for dynamically installed anchors penetration. Note, however, that if the strength degradation occurs slowly (i.e., large δ_{95}) or non-sensitive clays, τ_{max} considerably affects the penetration.

Figure 4.5(b) shows that the pile set (penetration per blow) decreases with an increase in penetration. Figure 4.5(c) shows the pile head displacement in 5th, 10th and 20th blows for the above four cases. In each blow, the pile penetrates quickly to the maximum distance at ~ 0.15 s and then rebounds up and remains almost at a constant penetration depth (pile set) during 0.45 s–1.0 s. No rebound occurs in the first five blows, and it is higher in the sensitive clays and at a larger depth of penetration depths. High rebounds adversely affect pile driveability. However, for higher interface conditions (i.e., $\tau_{max} = 15$ kPa), the pile penetrates to the maximum distance in a shorter time.
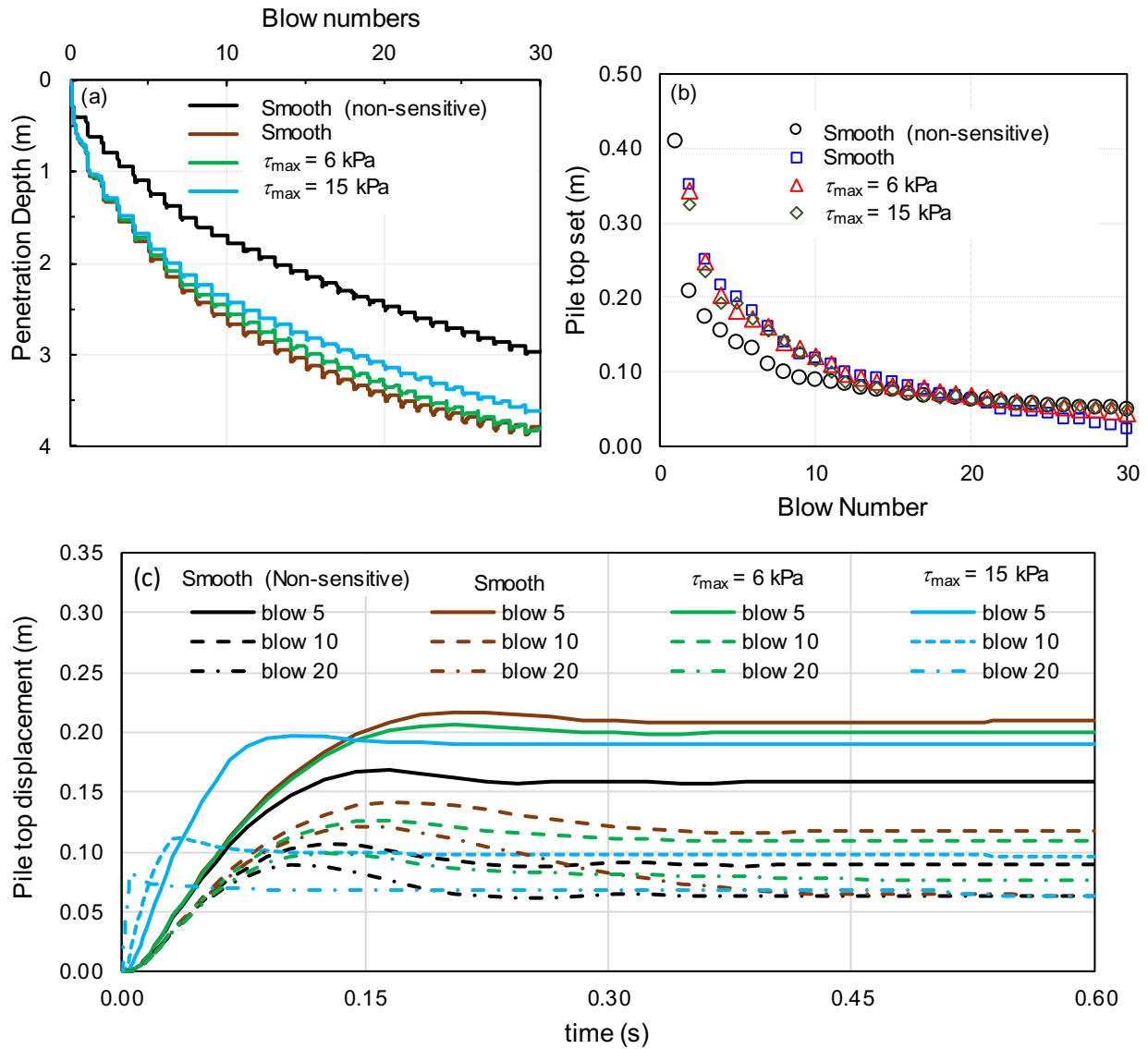
Fig. 4. 5. Pile head penetration due to impact driving

Figure 4.6 shows the pile head displacement for the varying rate of post-peak shear strength degradations (i.e., different s_{u0}/s_{uR} and δ_{95}). For a given s_{u0}/s_{uR} (= 5.0), pile head penetration increases with the decrease of δ_{95}. Also, for a given δ_{95} (= 0.05 m), the penetration increases with an increase in s_{u0}/s_{uR}. Note that an increase in s_{u0}/s_{uR} and decrease in δ_{95} increases the rate of post-peak shear strength degradation (Eq. (4.7)); therefore, the pile penetrates more through the weaker soil.

Figure 4.6(b) shows the effects of δ_{95} on penetration in a blow. For all the simulations, the maximum pile displacement is higher for a lower δ_{95} because of quicker soil strength reduction. The rebound increases with an increase in the number of blows. However, the pile set is highly dependent on δ_{95} at the early stage (e.g., 5th blow). Interestingly, the pile set at the 20th blow is almost independent of δ_{95} because, at such penetration depth, a major part of the soil around the pile reaches a similar level of soil strength due to the development of large plastic shear strain.

Figure 4.6(c) shows the effects of s_{u0}/s_{uR} on pile top displacement. The pile displacement is higher at the earlier stage (e.g., 5th blow). For a given blow, the maximum pile displacement is independent of s_{u0}/s_{uR}; however, the pile set increases with s_{u0}/s_{uR}. Note that, in the 5th blow, the permanent set is not achieved at $t = 0.6$ s (Fig. 4.6(c)).

The above simulations show that strength degradation significantly influences pile driving. Sensitivity parameters significantly influence the pile penetration due to impact pile driving. The main observations from the above analyses are that the highly remoulded clays show higher penetration due to impact loading. However, the soil resistance to the pile driving increases with the depth of soil, as the soil strength increases over the depth. The rebound of the pile top increases with the depth of penetration. Mabsout & Tassoulas (1994) considered an 18 m pre-bored pile before impact pile driving and simulated ten consecutive blows and found that a higher rebound occurs at blow#10 than that for blow#1.
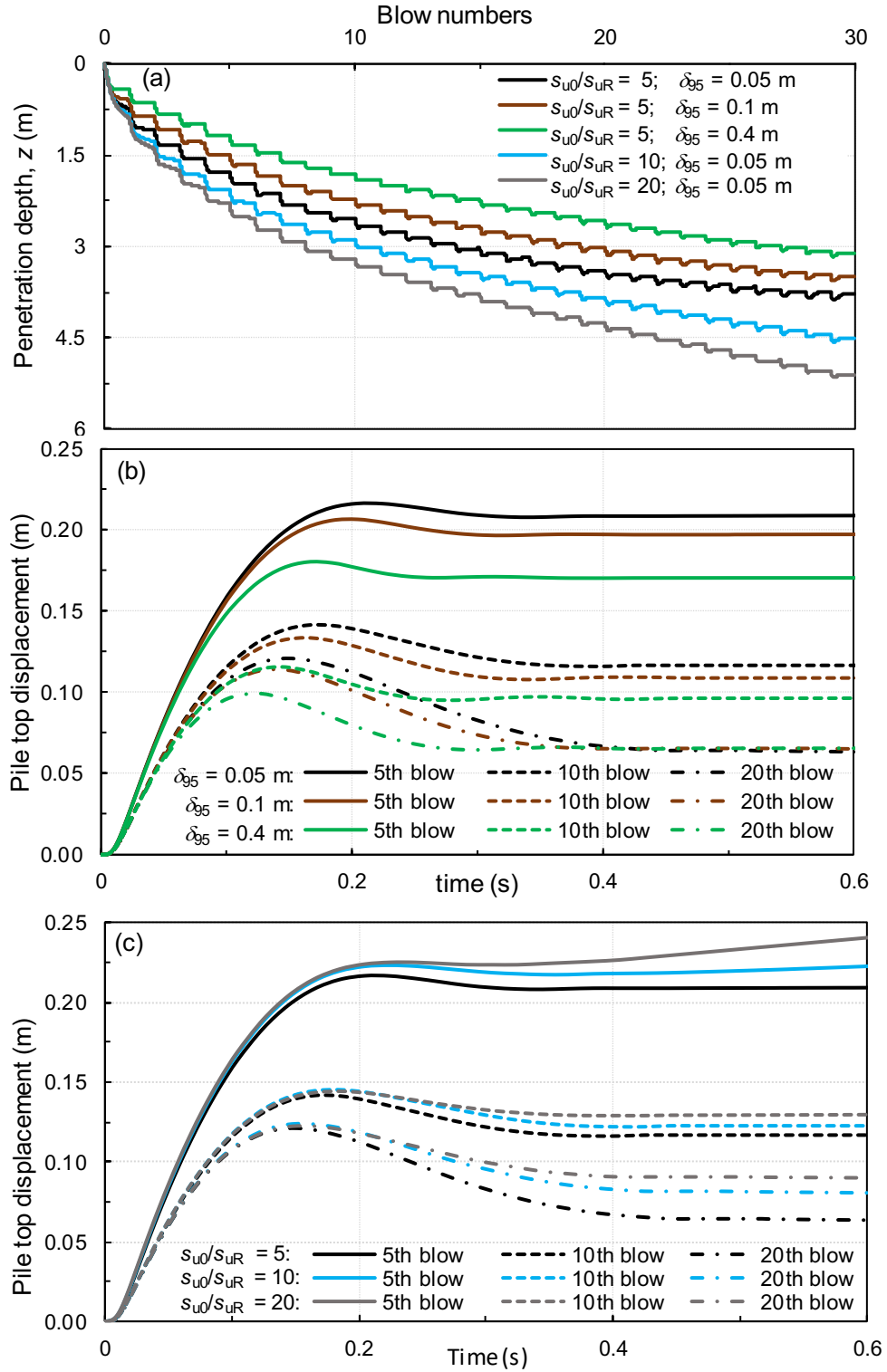
Fig. 4.6. Effects of post-peak shear strength degradation: (a) pile penetration in 30 blows; (b) effects of δ_{95}; (c) effects of s_{u0}/s_{uR}

Development of plastic shear strain

Figure 4.7 shows the development of plastic shear strain (ε_q^p) in impact driving when the pile tip is at 2.5 m depth. All the analyses are conducted with the same soil properties except for softening parameters (δ_{95} and s_{u0}/s_{uR}). The followings are the key observations:

- The number of blows required to penetrate the pile to this depth ($z_{tip} = 2.5$ m) is smaller for a faster rate of softening (i.e., lower δ_{95} and higher s_{u0}/s_{uR}). The maximum number of blows (= 22) is required for the non-sensitive clay (Fig. 4.7(f)) while only six blows are required or highly sensitive clay (Fig. 4.7(e)).

- The radial extent of the disturbed zone (i.e., ε_q^p development area) is larger for a non-sensitive and lower rate of softening cases (Figs. 4.7(c) and 4.7(f)). However, for the higher rate of softening cases, the ε_q^p develops in a smaller and rounded bottom flask-shaped area (Figs. 4.7(d) and 4.7(e)).

- For highly sensitive clays, large plastic shear strains develop in the soil elements close to the pile ($\varepsilon_q^p \sim 100\%–400\%$), which remould this soil severely, resulting in low shaft friction during installation.

Generation of excess pore water pressures

Figure 4.8 shows the generated excess pore pressure in the 5th and 20th blows. The corresponding penetrations for these two blows have been shown in Fig. 4.6(c) (i.e., $s_{u0}/s_{uR} = 5$ & $\delta_{95} = 0.05$ m). At the beginning of the 5th blow, the maximum $u_e \sim 100$ kPa that generates below the pile tip. After that, u_e increases when the pile displaces downward; for example, at $t = 4.05$, the maximum u_e is ~ 260 kPa. The pore pressure decreases in the soil elements near the pile in the later stage of the blow due to rebound, as discussed before. The shallow failure mechanisms

expand the plastic zone; therefore, the excess pore pressure development area is larger at the end of the blow than in the beginning, including in the radial direction at the level of the tip. A similar response is found for the 20th blow, although the zone of u_e is larger because of accumulated pore pressure generation during previous blows. However, no significant increase in pore pressure zone in the radial direction is found for this blow because the deep failure mechanisms govern the penetration at the stage. In other words, the radial extent of the pore pressure development zone will not change significantly after a certain depth of penetration.

Blanchet et al. (1980) observed a similar response during pile driving in soft sensitive clays. They hypothesized the generation of excess pore pressure as the result of strain development by cylindrical cavity expansion due to pile penetration in intact clays. When the pile moves further from that level, the pore pressure is reduced to stresses necessary to maintain the cavity in remoulded clays.

Figure 4.9 shows the excess pore water pressures due at the end of the 10th blow for varying post-peak strength degradation (s_{u0}/s_{uR} & δ_{95}). The pile penetrated to $z_{tip} = 1.8$ m–3.3 m depending upon s_{u0}/s_{uR} & δ_{95}. Again, the maximum u_e at the end of the blow is slightly far from the pile surface because of rebounding.
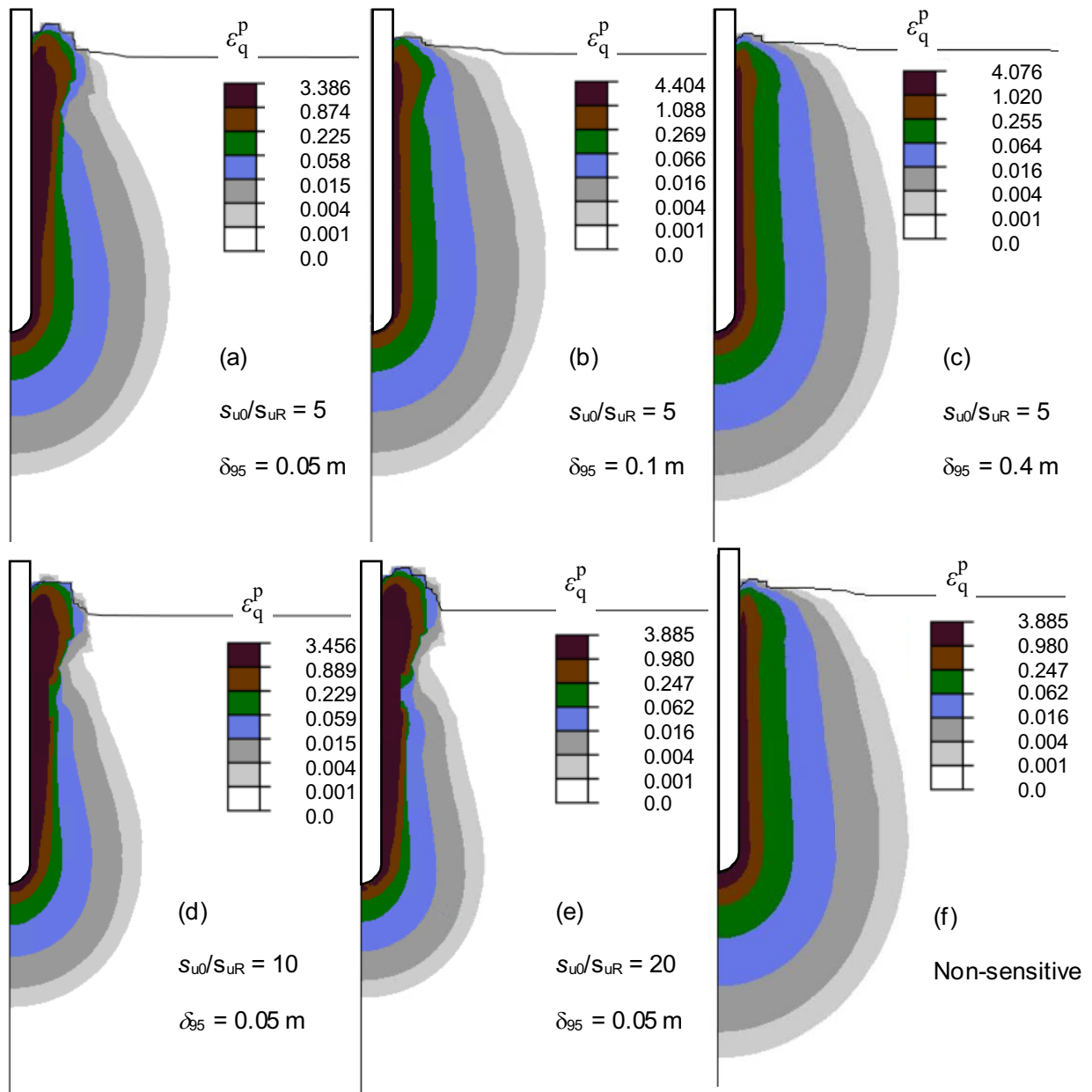
Fig. 4.7. Comparison of plastic shear strain for the various rates of softening
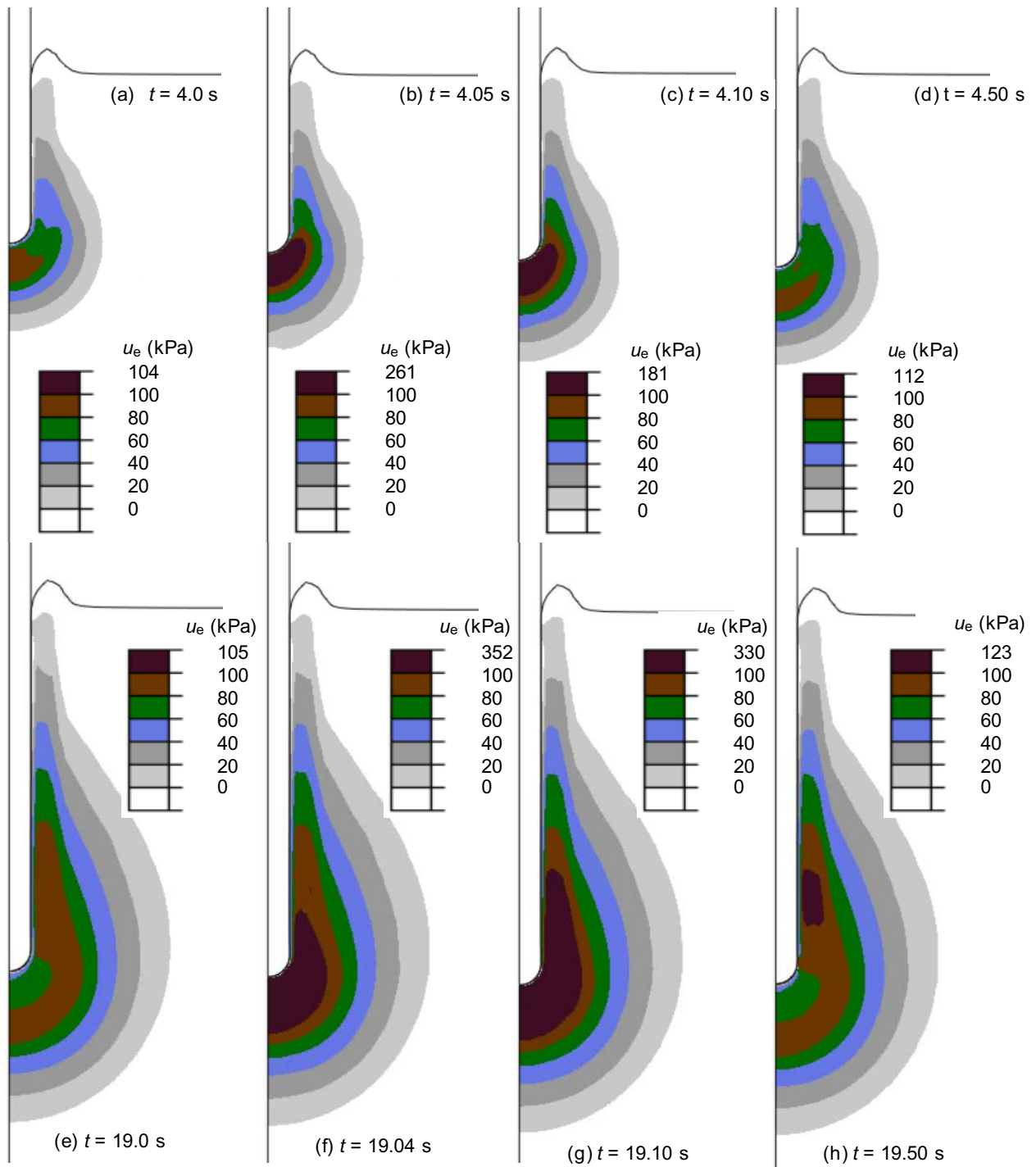
Fig. 4.8. Excess pore water pressure: (a–d) in 5th blow; (e–h) in 20th blow
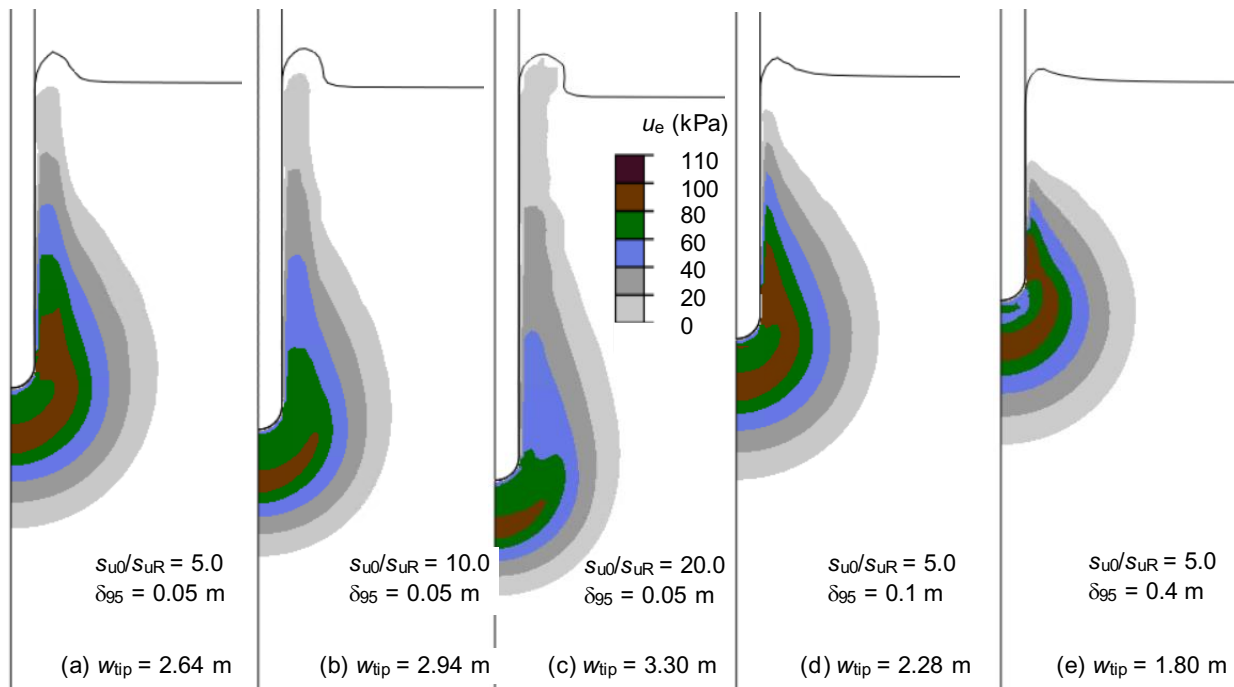
Fig. 4.9. Excess pore water pressure at the end of 10th blow for various s_{u0}/s_{uR} and δ_{95}

In the field tests, the excess pore pressure is measured at the surface of the pile (Azzouz & Lutz, 1986; Azzouz & Morrison, 1988) and also at the fixed location using a piezometer (Roy et al., 1981). Figures 4.10(a & b) show the variation of u_e in a soil element at $0.8D$ from the pile surface and 2 m depth. The oscillations in these curves are the results of dynamic impact loading. Figure 4.10(a) shows that a negative u_e starts to develop when the pile tip comes approximately 1.0–1.5 m above this point. Compared to the non-sensitive case, u_e in sensitive clays starts to increase when the pile tip is closer to this point because the plastic zone is smaller in sensitive clays. The maximum negative pore pressure is -30 kPa. As s_{u0} of this soil element represents an overconsolidated state, the proposed model calculates negative u_e during the elastic loading stage (Fig. 4.2(c)). With further penetration of the pile, u_e starts to increase, and the maximum positive pore pressure develops when the pile tip is at this depth ($z = z_{tip} = 2$ m). For sensitive clays, the shear strength of this soil element decreases due to plastic shear strain; therefore, the maximum u_e

is smaller for a larger s_{u0}/s_{uR}. With further penetration below 2 m, u_e decreases and becomes almost constant at one stage. The rate of u_e decrease is higher for non-sensitive clay.

Figure 4.10 (a) also shows that the shape of the u_e–z_{tip} curve for an element at $z = 3.0$ m and w_s = 0.8D is very similar to other curves. However, the maximum u_e and the depth of the tip when u_e is negative are larger, which is consistent with the field observation of Roy et al. (1981). Figure 4.10 (b) shows smaller effects of δ_{95} on the maximum negative and positive excess pore water pressure. However, the rate of decrease of u_e below 2 m is slower for smaller δ_{95}.

Roy et al. (1981) measured the generation of excess pore water pressure during the installation of piles in sensitive clay by installing a set of piezometers at various depths. They measured the maximum negative pore pressure of -10 kPa to -20 kPa and positive pore pressure of 70 kPa to 145 kPa during pile penetration in the piezometers located at 3.05 m to 7.6 m depths. The shape of their measured pore pressure development curves is also similar to that in Fig. 4.10.

4.7 Comparison between impact driving and jacking

The loading processes in impact driving and jacking are very different, although both methods aim to penetrate the pile to targeted depth. The following sections present an in-depth investigation of the mechanisms involved in pile driving and jacking. Further details on FE simulation of pile jacking are provided in Chapter 3.
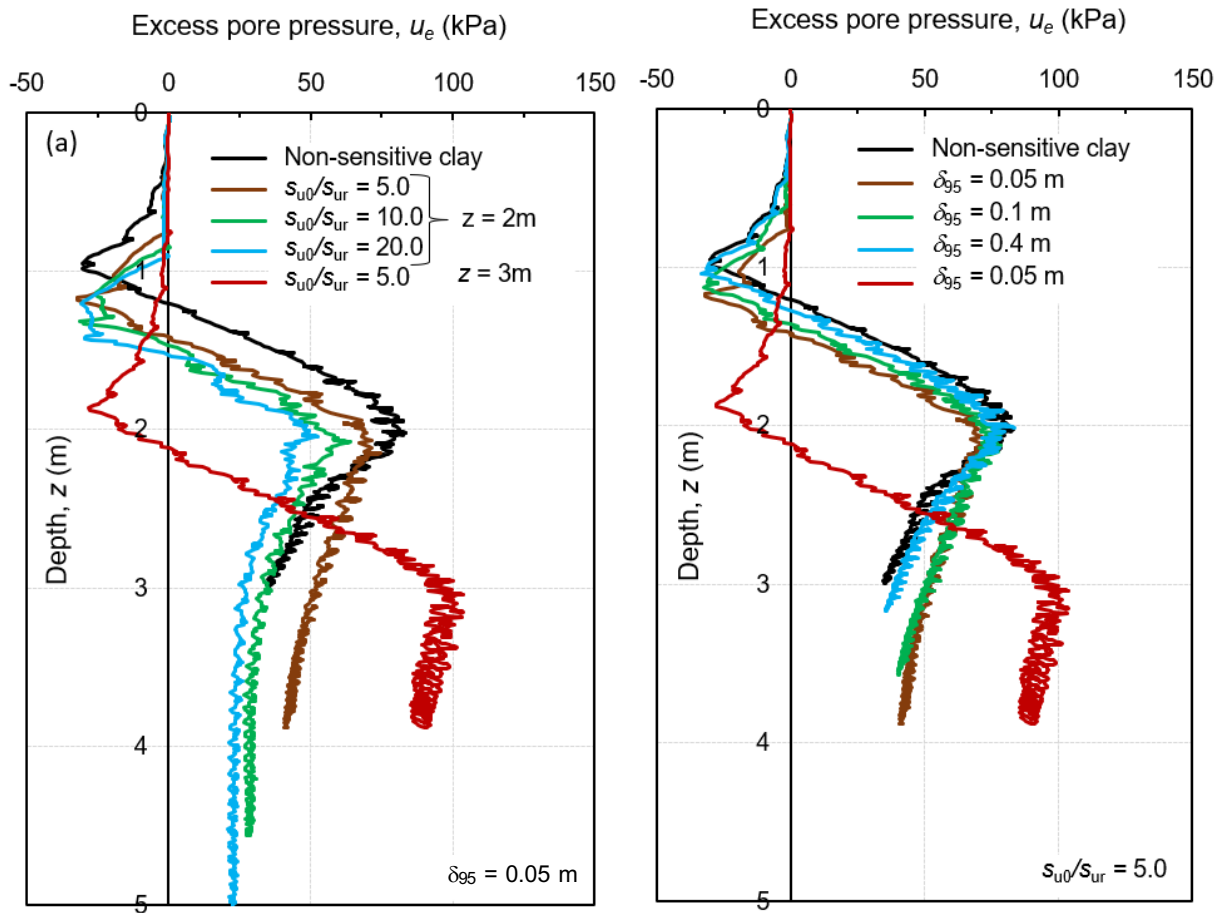
Fig. 4.10. Excess pore water pressure at $z = 2$ m & 3 m and $r = 0.8D$: (a) effects of s_{u0}/s_{uR}; (b) effects of δ_{95}

Mobilized shear strength

Pile installation response depends on mobilized shear strength, which is proportional to strain-softening and strain-rate factors (f_1 and f_2), as in Eq. (4.6). Therefore, f_1 represents the soil disturbance, and f_1f_2 represents the combined effects on mobilized shear strength. The variation of f_1f_2 is examined in this section. A similar pile tip depth is considered when comparing the response for driving and jacking. In the case of $s_{u0}/s_{uR} = 5$ & $\delta_{95} = 0.05$ m, the pile tip reaches $z_{tip} = 1.96$ m at the beginning of 7th blow. Figure 4.11 shows the variation of f_1f_2 with radial distance along a horizontal plane from the pile tip for the 7th blow. As the load on the pile top varies significantly

between two successive blows, five different times are considered from the forcing function (inset of Fig. 4.11). At the beginning of the 7th blow (i.e., $t = 6.00$ s), $f_1 f_2$ is 0.45. When the maximum stress is applied on the pile head (point B on the forcing function), a slight increase in $f_1 f_2$ occurs due high strain rate. After that, $f_1 f_2$ curves move downward with time, even after stopping the loading at $t = 6.1$ s because the pile continues to move downward, and soil is being remoulded around the pile. After $t = 6.5$ s, the strength degradation due to pile driving stops and $f_1 f_2$ remains constant until the beginning of the 8th blow. At this level of penetration, the strength degradation occurs within a $3.5D$ radial distance from the pile surface.

Several field tests investigated the disturbance of adjacent soil due to pile driving in soft sensitive clays (Casagrande, 1932; Cummings et al., 1950; Flaate, 1972; Bozozuk et al., 1978). Casagrande (1932) found that soil around the pile becomes highly or completely remoulded up to $1.5D$ due to pile driving. Bozozuk et al. (1978) showed high disturbance within $2D$ from the pile surface; however, a significant amount of strength regained occurred rapidly after the end of pile installation. Flaate (1972) observed a highly remoulded zone between $0.3D$ and $0.5D$ for the timber pile surface due to pile driving. The present numerical simulation results are in good agreement with these field investigations. However, the degree of remoulding in impact driving depends on several factors, as discussed above. Moreover, remoulding depends on the type of installation (jacking or driving), as discussed in the following sections. In the present study, the $f_1 f_2 \sim 0.3$ after the 7th blow reveals the highly remoulded soil around the pile. Conducting field vane shear and cone penetration tests, Bozozuk et al. (1978) reported an overall reduction in undrained shear strength of 15% and 30 % from its initial value immediately after pile driving in high sensitive clays.
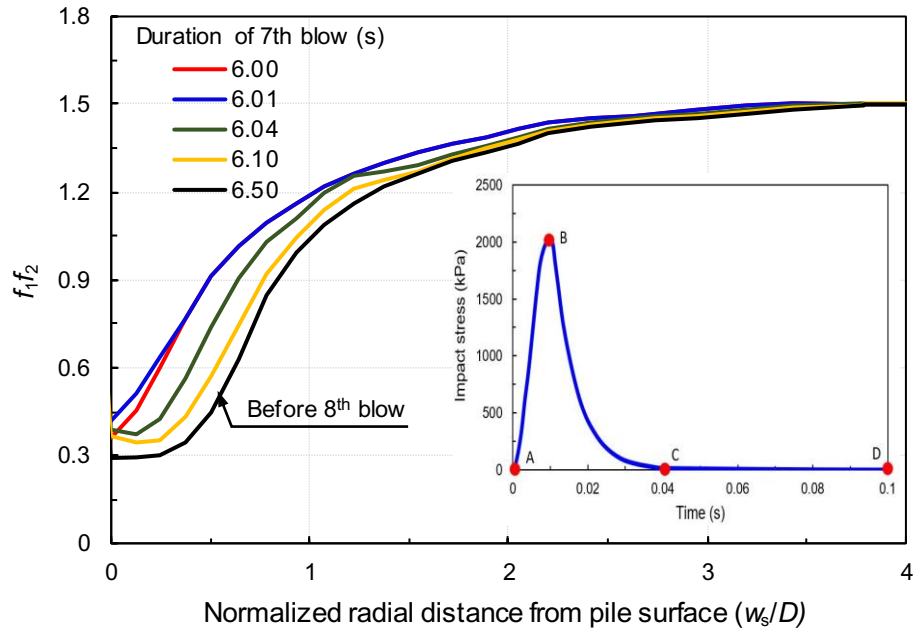
Fig. 4.11. Variation of mobilized shear strength factor in 7th blow

Similar geotechnical properties for the base case of impact driving are used in the pile jacking case. The soil disturbance (f_1) with radial distance at the level of the pile tip for these two cases is shown in Fig. 4.12. For the driving case, 5th blow is considered. For the jacking case, the variation of $f_1 f_2$ when the pile tip is at the depth same as that at the beginning and end of the 5th blow in the driving case (i.e., $z_{tip} = 1.34$ m and $z_{tip} = 1.55$ m) are shown. At the beginning of the 5th blow, $f_1 f_2$ near the pile is 0.4, which is considerably lower than that of the jacking case ($f_1 f_2 = 0.7$). However, at the end of the 5th blow, $f_1 f_2$ is almost the same for both cases when $z_{tip} = 1.55$ m. Another important observation is that, for jacking, soil disturbance primarily occurs within a narrow zone, and $f_1 f_2$ increases rapidly at ~ $0.5D$ from the pile surface. However, a disturbance occurs over a larger area and $f_1 f_2$ increases gradually over ~ $3D$ from the pile surface.

Soil disturbance and mobilization of s_u could be further investigated through a close examination of strain-rate effect (f_2). In driving, the impact load is applied rapidly (Fig. 4.3), which

causes high shear strain rate in the soil element near the pile. Figure 4.12(b) shows the variation of f_2 during the 5th blow at the level of the pile time. The strain rate effect f_2 is significantly high when the impact load is near the peak and then decreases. On the other hand, the jacking is performed under a constant velocity, which generated shear strain rate is less than the reference shear strain rate in this case. In other words, there is no strain rate effect on s_u for jacking; however, the higher strain rate increases mobilized s_u in driving. The higher s_u causes soil flow and disturbance over a larger area in the driving case. In conclusion, the installation method could have a significant practical implication because, in addition to soil disturbance, excess pore water pressure will generate over a larger area in case of driving and might take a longer time to dissipate that pore water pressure for strength regaining.

Changes of stresses due to pile installation

Figure 4.13(a) shows the development of the von Mises stress (σ_e) around the pile due to continuous pile penetration by jacking at a constant velocity. The soil near the tip flows upward and outward, while the soil around the pile far from the tip flows primarily upward. The von Mises stress is less than 12 kPa in a thin layer of soil near the pile surface, which represents a highly remoulded zone. Therefore, the interface resistance of 6 kPa does not significantly affect penetration, as discussed in Section 4.6. The von Mises stress distributions can be divided into pre-peak and post-peak zones. Low σ_e is found near the pile because the shear strength is low at high strains. Low σ_e is also calculated in the soil elements far from the pile because of negligible stress change.
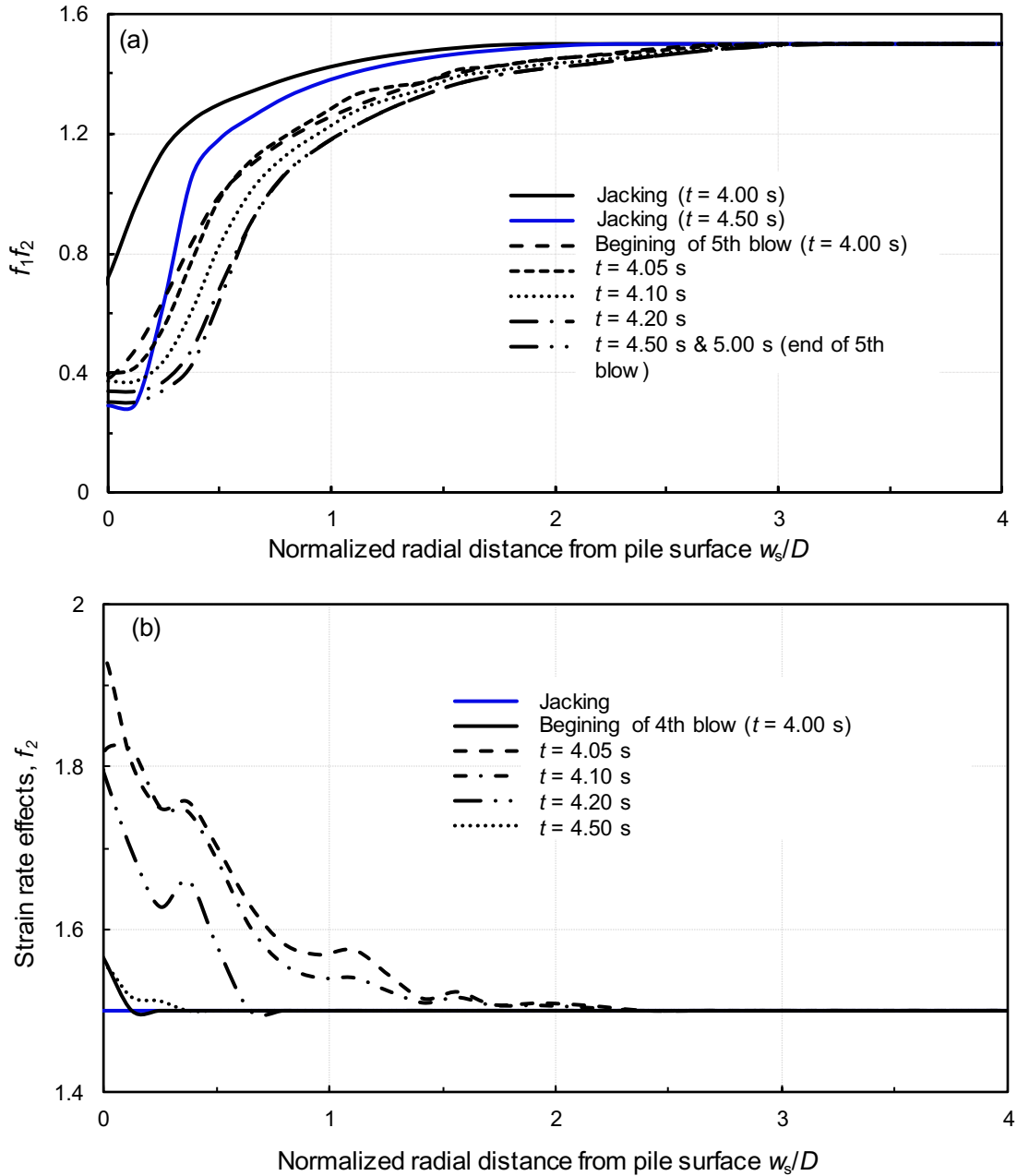
Fig. 4.12. Comparison of pile driving and pile jacking in terms of (a) f_1f_2; (b) the strain rate factor (f_2)

Figure 4.13(b) shows σ_e distribution in impact driving for the 6th blow when an impact force is ceased (0.04 sec, Fig. 4.3). At this stage, the pile moves downward. The von Mises stress change occurs in a wider zone in this case (Fig. 4.13(b)) than that of the jacking case (Fig. 4.13(a)). Figure

4.13(c) shows the σ_e distribution at the end of the 6th blow. Because of rebounding, as discussed in previous sections, stress redistribution occurs, especially near the pile tip; however, it does not alter the zone of the influence of pile installation.
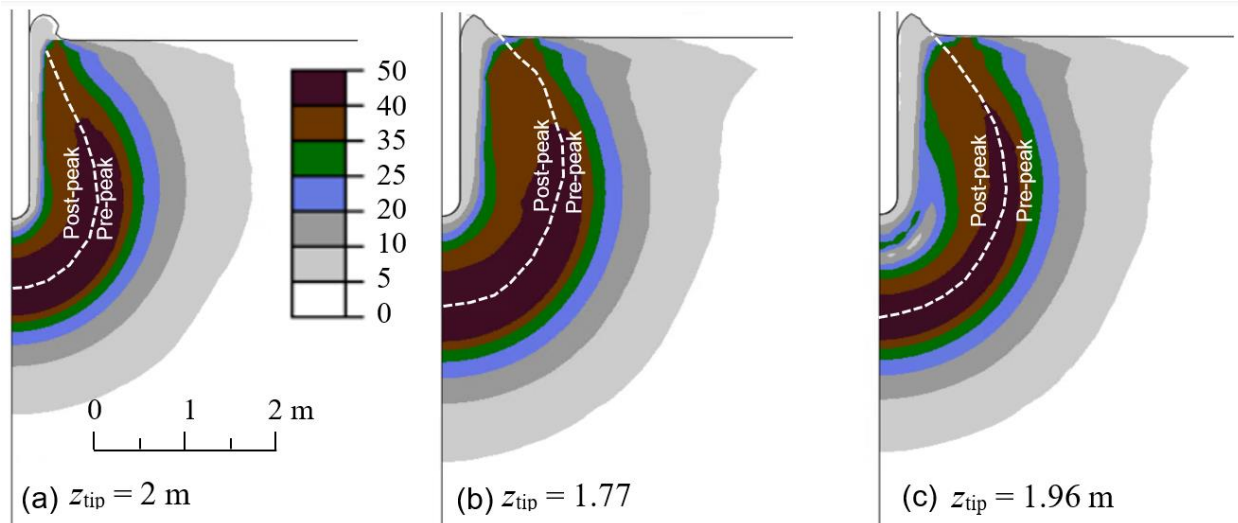
Fig. 4.13. von Mises stress: (a) jacking; (b) end of impact pulse in 6th blow; (c) end of 6th blow

Figure 4.14 shows the variation of von Mises, radial, and vertical stresses during the 7th blow at four times (A, B, C and D in the inset). Although the pile tip moves down during this blow, All the stresses are obtained at the level of the pile tip at the start of the blow. Figure 4.14(a) shows that when impact driving causes the penetration of the pile (e.g., pile tip is at point B), the maximum von Mises stress σ_{e_max} (= $2s_{u0}$) develops at ~ 3.5D from the pile surface. The lower value σ_e on the left side of σ_{e_max} is due to the post-peak reduction of undrained shear strength. The right side of σ_{e_max} represents the pre-peak region of the stress–strain curve. Unloading occurs during the latter part of the blow (i.e., the time at point C to 1 s) due to rebound and stress redistributions, which reduces σ_e, even $\sigma_{e\_max} < 2s_{u0}$, as shown for points A and D in Fig. 4.14(a).

To compare with jacking, the variation of σ_e at the same locations are shown in Fig. 4.14(a) when the jacked pile tip reaches the pile tip positions at the start and end of the 7th blow during impact driving (i.e. points A and D). In the case of jacking, σ_{e_max} develops at 2.4D–2.7D, which is considerably lower than that of impact driving case (3.2D–3.5D). This again implies a smaller plastic zone in jacking than in impact driving.

Another interesting observation is the shape of the curve for impact driving. At the end of each loading period (e.g., point D), when the impact load is ceased, the rebound of the pile results in upward displacement from the maximum penetration distance (Fig. 4.13), which causes upward movement of the soil elements near the pile surface. This stress reversal creates another peak at 0.5D–0.6D followed by a trough at ~ 0.9D (Fig. 4.14(a)). A similar pattern is obtained for point A because of the rebound in the previous (6th) blow. This trough disappears when the pile tip penetrates to points B and C because the pile again moves downward at these states. On the other hand, no such trough is found in σ_e distributions in jacking as the pile continuously moves downward.

For the locations described above to explain Fig. 4.14(a), the radial stresses (σ_r) are obtained. Figure 4.14(b) shows that σ_r gradually decreases with radial distance. In driving, σ_r near the pile depends on time (points A–D in the inset). However, for jacking, no significant difference in σ_r is found for this level of penetration. Only 1.96 m penetration occurs at this stage, so the ground surface affects the stress distribution. The radial stress is lower for jacking, which is potentially due to the higher flow of remoulded material near the pile and resulting in ground heave. At this stage, σ_r increases more than 8D, although the increase is not significant after ~ 5D from the pile surface. Figure 4.14(c) shows a significant increase in vertical stress near the pile tip within 2D–3D radial distance. Similar to σ_r, a lower vertical stress increase occurs in jacking.

Figures 4.15 (a–c) show σ_e, σ_r and σ_v distributions for 24th blow. At this stage, the pile penetrates to a large depth (3.5 m). Fig. 4.15 (a) shows σ_e redistributions similar to that described above for 7th blow. However, σ_{e_max} occurs at a larger radial distance (~ 4.5D) than that of the 7th blow (Fig. 4.14 (a)), which implies that a larger plastic zone forms at this stage. The developed trough due to rebounding is also large compared to that in Fig. 4.14 (a) for the 7th blow, which is due to stress redistribution at a higher stress level.

Figures 4.15(b) and 4.15(c) show that σ_r and σ_v increase to 3.5σ_{v0}–4.0σ_{v0} in the soil elements near the pile during the period when the impact force causes penetration. At this stage, σ_r and σ_v variations in jacking and impact driving are similar. However, the rebound and stress redistribution in impact driving reduce σ_r and σ_v considerably within 1D and 2D, respectively. A considerable radial stress increase occurs within 6D, while the vertical stress increase occurs within 4D from the pile surface.
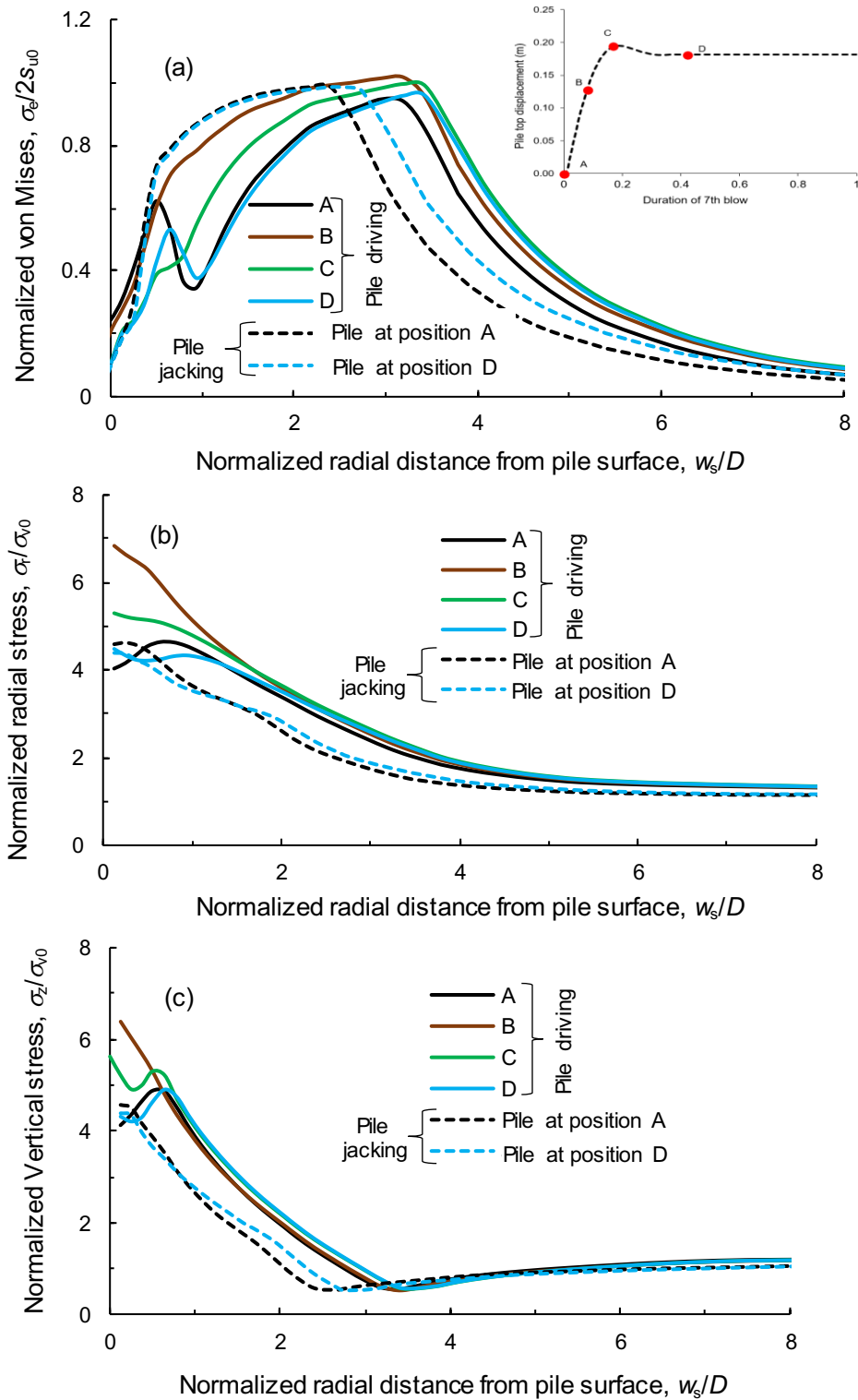
Fig. 4.14. Change in stresses in 7th blow for impact driving and jacking: (a) von Mises stress; (b) radial stress; and (c) vertical stress

124
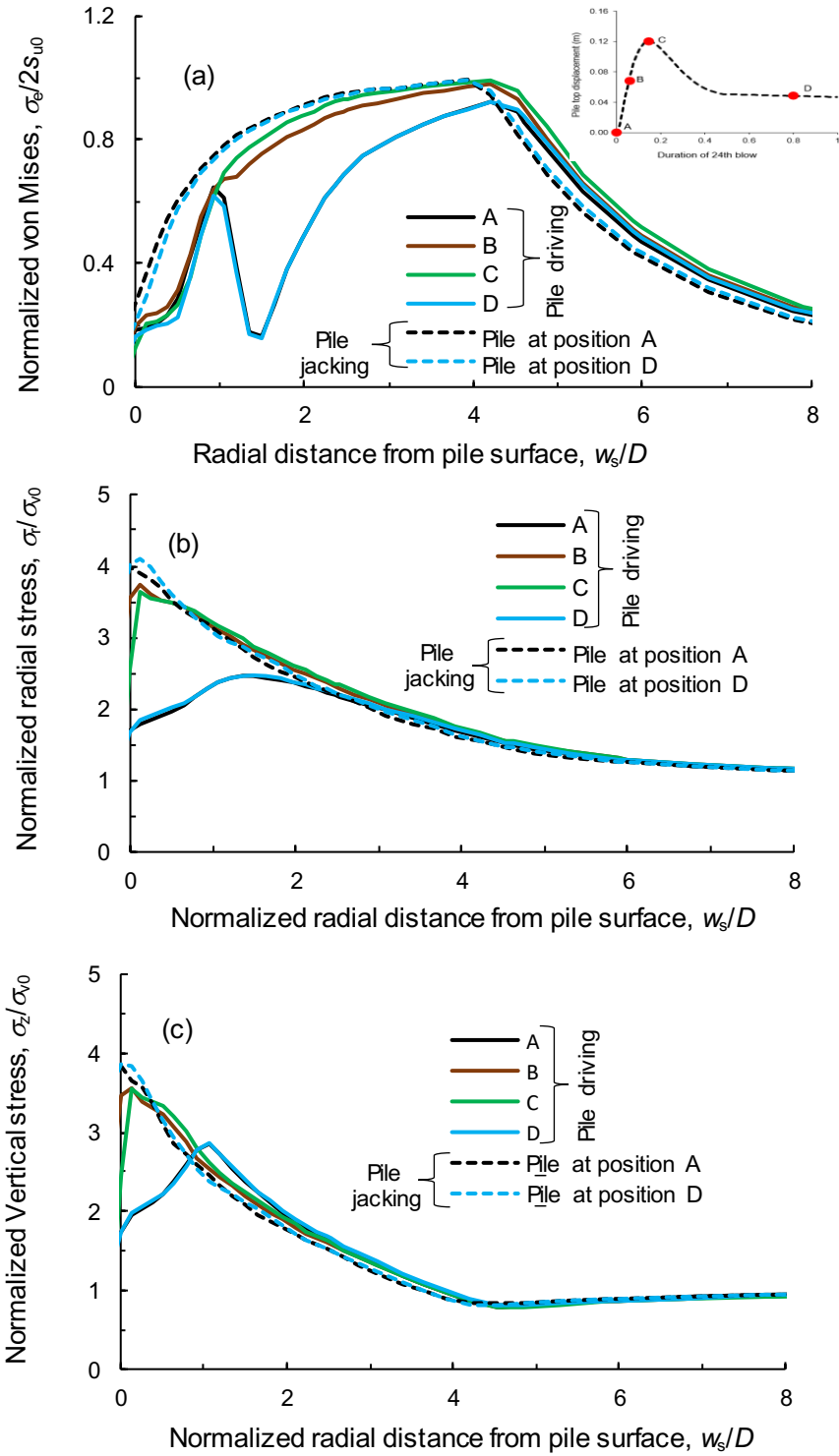
Fig. 4.15. Change in stresses in 24th blow for impact driving and jacking: (a) von Mises stress; (b) radial stress; and (c) vertical stress

Figure 4.16 shows the von Mises, radial and vertical stresses along a vertical plane at $0.25D$ radial distance from the pile surface for different pile tip positions. For a given pile tip depth (z_{tip}), the maximum σ_r and σ_v develop at $0.2D$–$0.4D$ below the tip, and these stresses are slightly higher in impact driving. On the other hand, the maximum σ_e develops at larger depths ($2D$–$5D$) below the pile, depending upon pile tip depth, installation method and radial distance from pile surface. Although the stress distribution pattern is the same in both impact driving and jacking, the maximum stresses (σ_e, σ_r and σ_v) develop at a larger depth in the case of driving than in jacking. The radial and vertical stresses decrease when the pile tip moves further and shows almost linear variation with depth, except for a zone near the tip. On the other hand, the von Mises stresses at a larger distance above the pile tip depend on the degree of remoulding, which is very small and almost constant near the pile (Fig. 4.16(a)).

Figure 4.17 shows the stresses measured at $0.5D$ radial distance from the pile surface, similar to those shown in Fig. 4.16. The radial and vertical stress distribution patterns in Figs. 4.16 and 4.17 are similar, although the magnitude is different. A significant difference is found in σ_e (compare Fig. 4.17(a) with Fig. 4.16(a)). In the case of pile jacking, a higher σ_e is observed near the ground surface at $0.5D$ distance, which is again due to less remoulding far from the pile.

Typical change in stresses in a single blow (blow #13) is shown in Fig. 4.18 for four time periods (A, B, C, D in the inset). When the pile moves downward due to driving (e.g., points B and C), σ_e, σ_r and σ_v increase near the pile tip. As discussed in the previous sections, stresses near the tip significantly reduce when the pile reaches point D due to rebounding and stress redistribution. The shape of the stress distribution curve for point D is similar to that at point A because similar rebounding occurred in the previous blow.
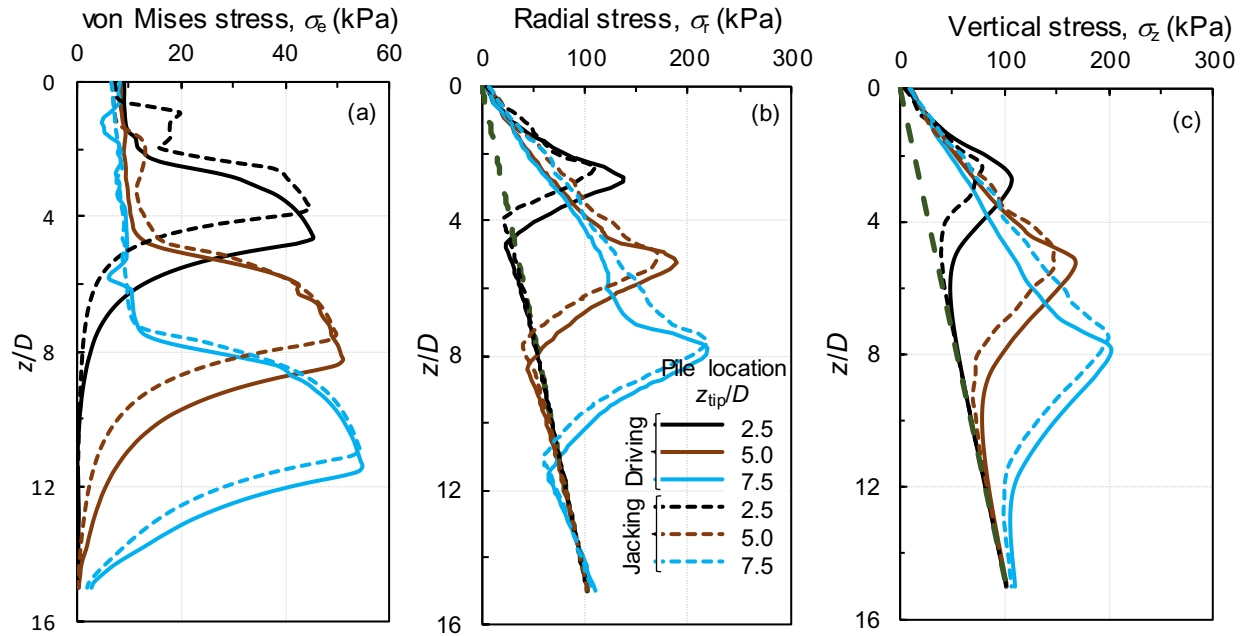
Fig. 4.16. Stress distribution in a vertical plane at 0.25 diameter radial distance from pile surface for different pile tip positions: (a) von Mises stress; (b) radial stress; and (c) vertical stress

Variation of stresses for jacking is also shown in Fig. 4.18 when the pile tip is at the locations of the start and end of the 13th blow in driving. No stress reduction due to rebounding is found as the pile continuously penetrates in jacking. The above simulations show that jacking and impact driving could create different stress conditions, especially near the pile tip. The rebound of the pile could cause stress redistribution and unload in each blow.

Development of plastic shear strain

Figure 4.19 shows the comparison of plastic shear strain in impact pile driving and pile jacking. Pile jacking creates a relatively smaller zone of disturbances around the pile. Figure 4.19 shows that for the pile tip position at 2 m, the maximum width of the disturbed zone is 2.6D and

3.3D for jacking and impact driving, respectively. However, the accumulated plastic shear strain ε_q^p is higher around the pile in the pile jacking case. Due to the continuous insertion of the pile by jacking, the adjacent soil undergoes a large deformation. In this case, deformed soil moves upward and radially, and the nearest soil experiences more deformation than in the case of impact pile driving.
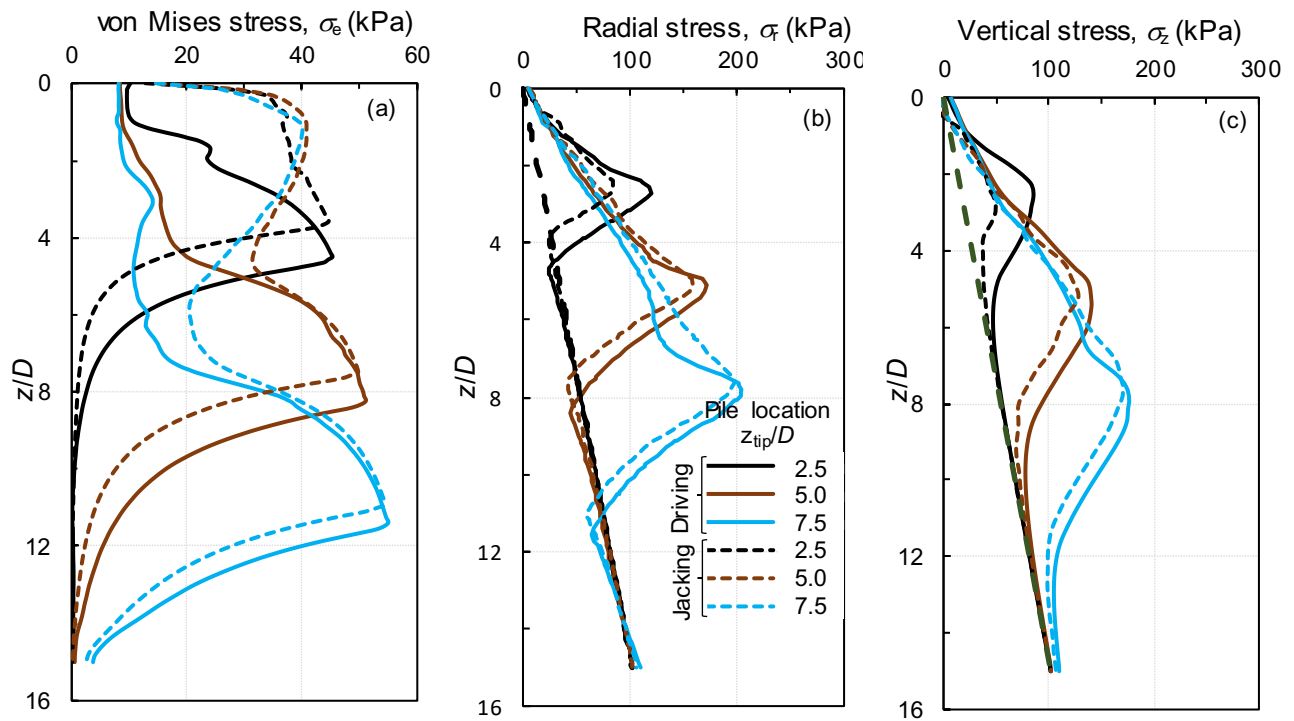
Fig. 4.17. Stress distribution in a vertical plane at 0.5 diameter radial distance from pile surface for different pile tip positions: (a) von Mises stress; (b) radial stress; and (c) vertical stress
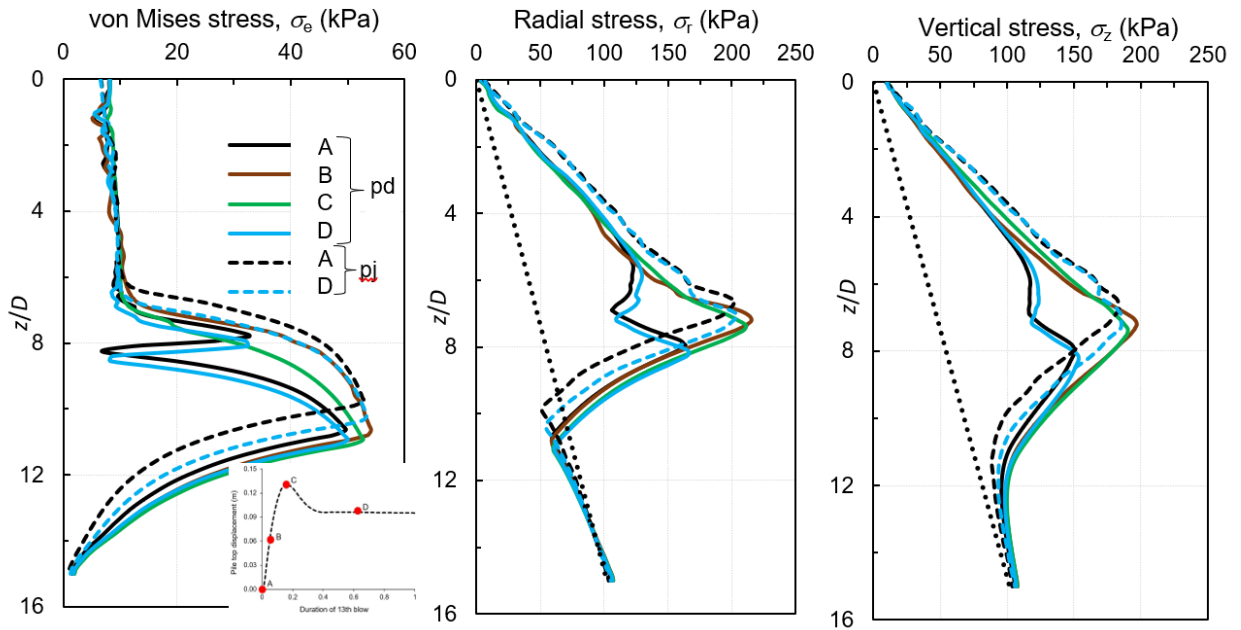
Fig. 4.18. Stress distribution in a vertical plane for 13th blow: (a) von Mises stress; (b) radial stress; and (c) vertical stress
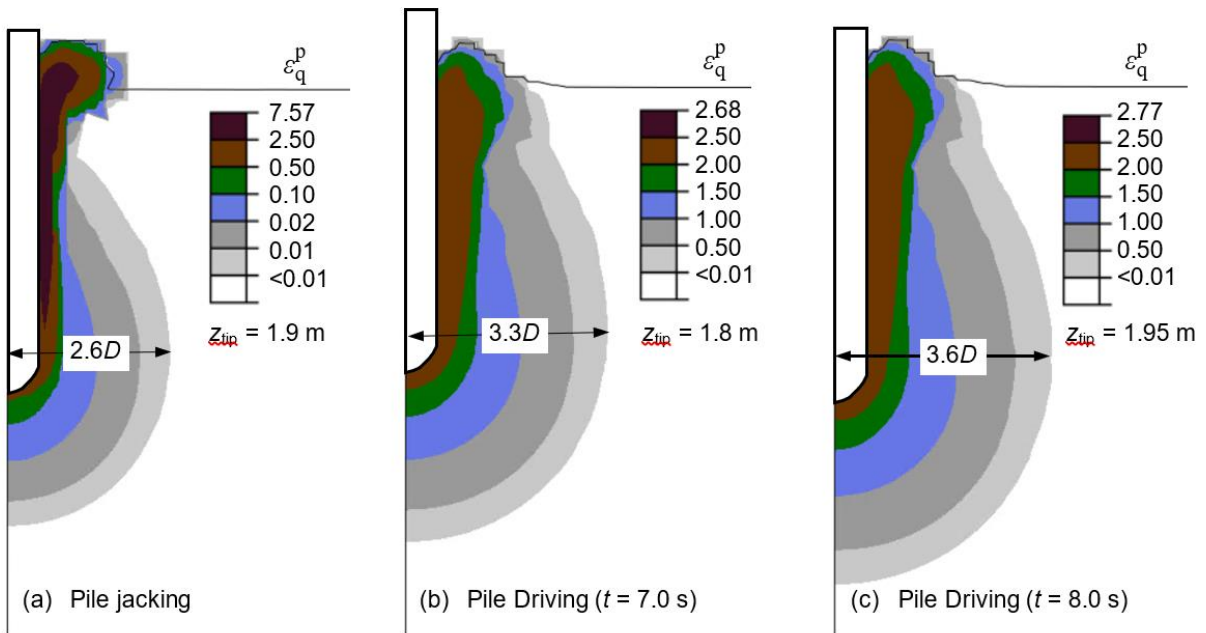
Fig. 4.19. Plastic shear strain in jacking and impact driving for 2 m depth pile tip depth

Excess pore pressures

Figure 4.20 shows the generated pore pressure for four soil elements at $0.57D$, $0.85D$, $1.14D$ and $1.82D$ from the pile surface at $5D$ depth during the penetration of the pile. Analyses are performed for both impact driving and jacking with the base case soil parameters (Table 4.1). Negative pore pressure generates before the pile tip approaches to level of the soil elements ($z = 5D$). The penetration distance when negative u_e exists (i.e. elastic loading, see Figs. 4.2 & 4.4) is larger for the soil element far for pile (i.e., $w_s = 1.82D$). For impact diving, the pore water pressure (u_{e_max}) in these soil elements develops when the pile tip is approximately at this level. However, for jacking, the u_{e_max} develops further below the pile tip because the continuous penetration in this case causes more soil remoulding near the pile tip than that of impact driving case where the high shear strain rate during impact driving increase the strength. Note that u_e is higher for higher undrained shear strength; for example, field investigation shows u_e near the pile is roughly 4–7 times of the undrained shear strength (Meyerhof, 1976; Blanchet et al., 1980; Roy et al., 1982). For the soil elements far from the pile ($w_s = 1.14D$ & $1.82D$), u_e is the same for jacking and driving when the pile tip moves ~$3D$ from the level where u_e was obtained. However, in the elements near the pile ($w_s = 0.57D$), the pore pressure is smaller in jacking because of higher remoulding. In summary, the present numerical simulations can explain u_e measured in the field, including its negative value, during pile installation (e.g. Blanchet et al., 1980; Roy et al., 1981).
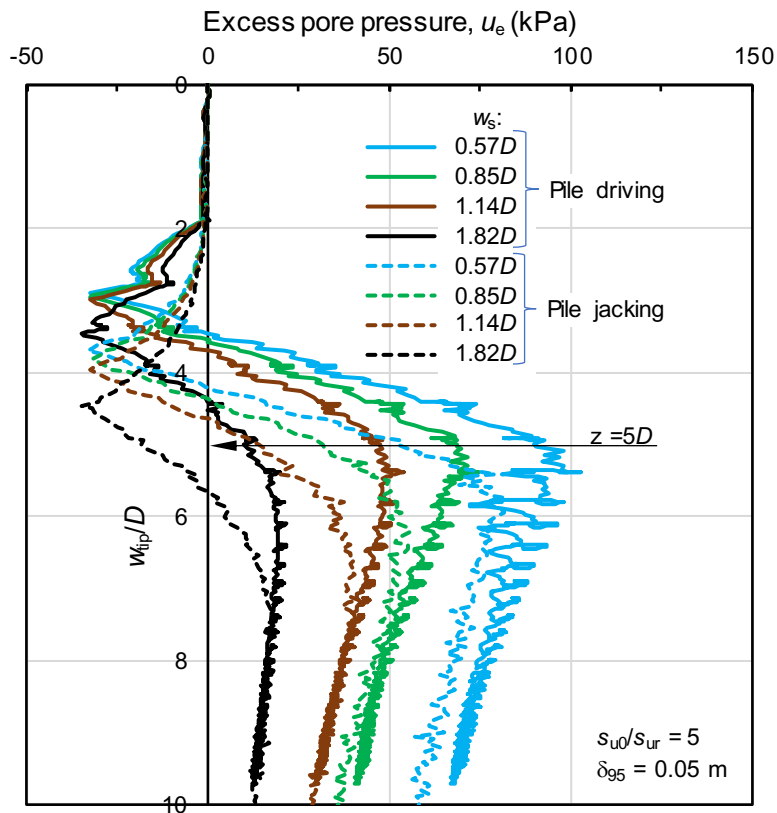
Fig. 4.20. Comparison of excess pore water pressure 5D depth for driving and jacking

4.8 Conclusions

Impact driving and jacking are the two commonly used pile installation methods. The driveability of an impact-driven pile is generally estimated using one-dimensional wave equations. Analytical approaches, such as cavity expansion and strain path methods, cannot properly model the soil flow mechanisms. Also, pile installation in sensitive clays needs special considerations, as the soils exhibit strain-softening behaviours. Several well-documented field tests are available for pile installation in sensitive clays; however, numerical studies on this problem are very limited. This study presents a detailed numerical investigation of pile installation in sensitive clays by impact driving and then compares installation by jacking. Large deformation finite element analyses are performed incorporating the effects of strain rate and strain softening on undrained

131

shear strength. A simplified model is proposed to calculate the excess pore water pressure (u_e) generation during installation based on the FE results of total stress analysis. A parametric study is performed to identify the effects of different parameters on pile installation.

In impact driving, the penetration per blow increases with the rate of post-peak strength degradation and decreases with depth. In each blow, the pile penetrates first during the impact and then rebounds a certain distance. The amount of rebound also depends on the rate of remoulding. The strain-rate effects on undrained shear strength play an important role in impact driving; however, it is negligible in jacking for the cases analyzed in this study

The proposed model calculates u_e similar to that observed in triaxial tests. During the penetration of the pile, the maximum u_e generates near the tip of the pile, which increases with the depth of penetration and is higher for non-sensitive clays. The pore pressure near the shaft at a given level decreases with penetration, and the rate of decrease of u_e with penetration is higher for non-sensitive clays. A negative pore pressure develops below the pile tip, which is similar to that measured in the field.

A higher plastic shear strain is developed in pile jacking; however, the plastic zone is larger in impact driving. Larger plastic shear strains are obtained in soil elements closer to the pile surface. A smaller plastic zone of higher remoulding forms in highly sensitive clay, and the displaced soil primarily flows through this remoulded zone. In summary, the response during pile installation in sensitive clay is very different from a non-sensitive clay, and the present study simulates the process properly for jacking and driving.

Notations

α	interface friction ratio
β	soil parameter for strain-rate relation
δ	accumulated plastic shear displacement
δ_{95}	δ at which s_u reduced by 95% of $(s_{u0}\text{-}s_{uR})$
δ_{ld}	δ at large shear displacement
ε_q^p	equivalent plastic shear strain
γ	total unit weight
γ_w	unit weight of water
$\dot{\gamma}$	strain rate
$\dot{\gamma}_{ref}$	reference strain rate
η	soil parameter for strain-rate relation
ν_u	undrained Poisson's ratio
σ_e	von Mises stress
σ_{e_max}	maximum von Mises stress
σ_r	total radial stress
σ_v	total vertical stress
σ_{v0}	initial vertical total stress
τ_{max}	equivalent interface shear stress limit
D	pile outer diameter
d_p	pile head penetration
E_u	undrained Young's modulus

f_1	strain-softening factor
f_2	strain-rate factor
K	ratio between horizontal to vertical total stress
K_0	effective earth pressure coefficient at-rest
k	shear strength gradient
M	slope of the failure plane
OCR	overconsolidation ratio
Δp	changes in mean total stress
p	Mean total stress
p_0	mean total stress
p'	mean effective stress
p_0'	mean effective stress at *in-situ* conditions
p_{cs}'	mean effective stress at s_{u0}
s_u	mobilized undrained shear strength
s_{u0}	initial (peak) undrained shear strength
s_{ug}	undrained shear strength at ground surface
s_{uld}	undrained shear strength at large displacment
s_{uR}	remoulded s_u at large plastic shear displacement
s_{uy}	undrained shear strength at a very low strain rate
t	time
u_0	hydrostatic pore water pressure
u_e	excess pore water pressure
u_s	shear-induced excess pore water pressure

v_x the component of velocity in x-direction

v_y the component of velocity in y-direction

v_z the component of velocity in z-direction

w_i radial distance of soil element from the pile centre

w_s radial distance of soil element from the pile outer surface

z depth of the soil element below the ground surface

z_{tip} depth of pile tip from the ground surface

References

Alves, A. M. L., Lopes, F. R., Randolph, M. F. & Danziger, B. R. (2009). Investigations on the dynamic behaviour of a small-diameter pile driven into soft clay. *Canadian Geotechnical Journal* **46**, 1418–1430.

Azzouz, A. S. & Lutz, D. G. (1986). Shaft behaviour of a model pile in plastic empire clays. *Journal of Geotechnical Engineering* **112**, No. 4, 389–406.

Azzouz, A. S. & Morrison, M. J. (1988). Field measurements on model pile in two clay deposits. *Journal of Geotechnical Engineering* **114**, No. 1, 104–121.

Baligh, M. M. (1985). Strain path method. *Journal of Geotechnical Engineering, ASCE* 111, No. **9**, 1108–1136.

Baligh, M. M. (1986). Undrained deep penetration, I: shear stresses. *Géotechnique* **36**, No. 4, 471–485.

Baligh, M. M. & Levadoux, J. (1986). Consolidation after undrained piezocone penetration. II: interpretation. *Journal of Geotechnical Engineering* **112**, No. 7, 727–745.

Bjerrum, L., Hansen, B. J. & Sevaldson, R. (1958). Geotechnical investigations for quay structure in Horten. *Norwegian Geotechnical Institute, Publ.* **28**, 1–18.

Bjerrum, L. & Landva, A. (1966). Direct simple-shear tests on a Norwegian quick clay. *Norwegian Geotechnical Institute*, Oslo, 1–22.

Blanchet, R., Tavenas, F. & Garneau, R. (1980). Behaviour of friction piles in soft sensitive clay. *Canadian Geotechnical Journal* **17**, 203–224.

Borja, R. I. (1988). Dynamic of pile driving by the finite element method. *Computer and Geotechnics* **5**, 39–49.

Boukpeti, N., White, D. J., Randolph, M. F. & Low, H. E. (2012). Strength of fine-grained soils at the solid–fluid transition. *Géotechnique* **62,** No. 3, 213–226.

Bozozuk, M., Fellenius, B. H. & Samson, L. (1978). Soil disturbance from pile driving in sensitive clay. *Canadian Geotechnical Journal* **15**, No. 3, 346–361.

Broms, B. B. & Bennermark, H. (1967). Stability of clay at vertical opening. *Journal of the Soil Mechanics and Foundations Division* **93**, No. 1, 71–94.

Carter, J. P. & Yeung, S. K. (1985). Analysis of cylindrical cavity expansion in a strain weakening material. *Computers and Geotechnics* **1**, No. 3, 161-180.

Casagrande, A. (1932). The structure of clay and its importance in foundation engineering. *Journal of the Boston Society of Civil Engineers* reprinted in contributions to Soil mechanics, 1925–1940, 72–113.

Chatterjee, S., Randolph, M. F. & White, D. J. (2012). The effects of penetration rate and strain-softening on the vertical penetration resistance of seabed pipelines. *Géotechnique* **62,** No. 7, 573–582.

Cummings, A. E., Kerkhopp, G. O. & Peck, R. B. (1950). Effect of driving piles into soft clay. *Transactions of the American Society of Civil Engineers* **115**, No. 1, 275–285.

Davis, R. O. & Phelan, P. J. (1978). Numerical approximation in pile-driving analysis. *International journal for numerical and analytical methods in geomechanics* **2**, 303–310.

Deeks, A. J. & Randolph, M. F. (1993). Analytical modeling of hammer impact for pile driving. *International Journal for Numerical and Analytical Methods in Geomechanics* **17**, No. 5, 279–302.

Dey, R., Hawlader, B., Phillips, R. & Soga, K. (2015). Large deformation finite-element modeling of progressive failure leading to spread in sensitive clay slopes. *Géotechnique* **65**, No. 8, 657–668.

Dey, R., Hawlader, B., Phillips, R. & Soga, K. (2016). Modeling of large-deformation behaviour of marine sensitive clays and its application to submarine slope stability analysis. *Canadian Geotechnical Journal* **53**, No. 7, 1138–1155.

Dutta, S., Hawlader, B. & Phillips, R. (2015). Finite element modeling of partially embedded pipelines in clay seabed using coupled Eulerian–Lagrangian method. *Canadian Geotechnical Journal* **52**, No. 1, 58–72.

Einav, I. & Randolph, M. F. (2005). Combining upper bound and strain path methods for evaluating penetration resistance. *International Journal for Numerical Methods in Engineering* **63**, No. 14, 1991–2016.

Ekanayake, S. D., Liyanapathirana, D. S. & Leo, C. J. (2013). Influence zone around a closed-ended pile during vibratory driving. *Soil Dynamics and Earthquake Engineering* **53**, 26–36.

Fan, S., Bienen, B. & Randolph, M. F. (2021). Effects of Monopile Installation on Subsequent Lateral Response in Sand. I: Pile Installation. *Journal of Geotechnical and Geoenvironmental Engineering* **147**, No. 5, 04021021.

Fellenius, B. H. & Broms, B. B. (1969). Negative skin friction for long piles driven in clay. In *Proc. 7th ICSMFE*, Mexico City **2**, 93–98.

Flaate, K. (1972). Effects of pile driving in clays. *Canadian Geotechnical Journal* **9**, 81–88.

Gill, D. R. & Lehane, B. M. (2000). Extending the strain path method analogy for modeling penetrometer installation. *International journal for numerical and analytical methods in geomechanics* **24**, No. 5, 477–489.

Goble, G. G., Rausche, F. & Likins, G. E. (1980). The analysis of pile driving – A state-of-the-art. *International Seminar on the Application of Stress-Wave Theory on Piles*, Stockholm, Sweden.

Heins, E. & Grabe, J. (2017). Class-A-prediction of lateral pile deformation with respect to vibratory and impact pile driving. *Computers and Geotechnics* **86**, 108–119.

Henke S. & Grabe, J. (2006). Simulation of pile driving by 3-dimensional finite element analysis. In *Proceedings of 17th European young geotechnical engineers' conference, Zagreb*, 215–233.

Henke, S. & Grabe, J. (2009). Numerical modeling of pile installation. In *Proc. of the 17th International Conference on Soil Mechanics and Geotechnical Engineering*, Egypt, 1321–1324.

Hossain, M. S. & Randolph, M. F. (2009) Effect of strain rate and strain softening on the penetration resistance of spudcan foundations on clay. *International Journal of Geomechanics* **9**, 122–132.

Hosseini, M. A. & Rayhani, M. (2017). Evolution of pile shaft capacity over time in marine soils. *International Journal of Geo-Engineering* **8**, No. 12, 1–15.

Huang, A. B. (1989). Strain-path analyses for arbitrary three-dimensional penetrometers. *International Journal for Numerical ana Analytical Methods in Geomechanics* **13**, No. 5, 551–564.

Hussein, M. H., Woerner, II, W. A., Sharp, M. & Hwang, C. (2006). Pile driveability and bearing capacity in high-rebound soils. In *GeoCongress 2006: Geotechnical Engineering in the Information Technology Age*, 1–4.

Islam, N., Hawlader, B., Wang, C. & Soga, K. (2019). Large-deformation finite-element modeling of earthquake-induced landslides considering strain-softening behaviour of sensitive clay. *Canadian Geotechnical Journal* **56**, No. 7, 1003–1018.

Jayawardana, P., Achuhan, R., De Silva, G. S. & Thambiratnam, D. P. (2018). Use of in-filled trenches to screen ground vibration due to impact pile driving: experimental and numerical study. *Heliyon* **4**, No. 8, e00726.

Karlsrud, K. & Hernandez-Martinez, F. G. (2013). Strength and deformation properties of Norwegian clays from laboratory tests on high-quality block samples. *Canadian Geotechnical Journal* **50**, No. 12, 1273-1293.

Khoubani, A. & Ahmadi, M. M. (2014). Numerical study of ground vibration due to impact pile driving. In *Proceedings of the Institution of Civil Engineers-Geotechnical Engineering* **167**, No. 1, 28–39.

Kim, Y. H. & Hossain, M. S. (2015). Dynamic installation of OMNI-Max anchors in clay: numerical analysis. *Géotechnique* **65**, No. 12, 1029–1037.

Ko, J., Jeong, S. & Lee, J. K. (2016). Large deformation FE analysis of driven steel pipe piles with soil plugging. *Computers & Geotechnics* **71**, 82–97.

Konkol, J. (2015). Numerical estimation of the pile toe and shaft unit resistances during the installation process in sands. *Studia Geotechnica et Mechanica* **37**, No. 1, 37–44.

Lacasse, S., Berre, T. & Lefebvre, G. (1985). Block sampling of sensitive clays. In *proceedings of the eleventh international conference on soil mechanics and foundation engineering*, San Fransisco, 12–16.

Länsivaara, T. & Poutanen, T. (2014). Safety concepts for slope stability. In *Landslides in Sensitive Clays*, Springer, Dordrecht, 395–407.

Lee, S. L., Chow, Y. K., Karunaratne, G. P. & Wong, K. Y. (1988). Rational wave equation model for pile-driving analysis. *Journal of geotechnical engineering* **114**, No. 3, 306–325.

Lefebvre, G., Leboeuf, D., Hornych, P. & Tanguay, L. (1992). Slope failures associated with the 1988 Saguenay earthquake, Quebec, Canada. *Canadian Geotechnical Journal* **29**, No. 1, 117–130.

Liu, H., Xu, K. & Zhao, Y. (2016). Numerical investigation on the penetration of gravity installed anchors by a coupled Eulerian-Lagrangian Approach. *Applied Ocean Research* **60**, 94–108.

Liyanapathirana, D. S., Deeks, A. J. & Randolph, M. F. (2000). Numerical modeling of large deformations associated with driving of open-ended piles. *International Journal of Numerical and Analytical Methods in Geomechanics* **25**, 1079–1101.

Liyanapathirana, D. S. (2009). Arbritrary Lagrangian Eulerian based finite element analysis of cone penetration in soft clay. *Computers and Geotechnics* **36**, 851–860.

Liang, R. Y. & Husein, A. I. (1993). Simplified dynamic method for pile-driving control. *Journal of Geotechnical Engineering* **119**, No. 4, 694–713.

Locat, A., Jostad, H. P. & Leroueil, S. (2013). Numerical modeling of progressive failure and its implications for spreads in sensitive clays. *Canadian Geotechnical Journal* **50**, No. 9, 961–978.

Locat, J. & St-Gelais, D. (2014). Nature of sensitive clays from Quebec. In *Landslides in Sensitive Clays* Springer, Dordrecht, 25–37.

Locat, A., Leroueil, S., Fortin, A., Demers, D. & Jostad, H. P. (2015). The 1994 landslide at Sainte-Monique, Quebec: geotechnical investigation and application of progressive failure analysis. *Canadian Geotechnical Journal* **52**, No. 4, 490–504.

Lunne, T., Berre, T., Andersen, K. H., Sjursen, M. & Mortensen, N. (2008). Effects of sample disturbance on consolidation behaviour of soft marine Norwegian clays. In *3rd International Conference on Site Characterization*, Taipei, Taiwan, 1471–1479.

Mabsout, E. M. & Tassoulas, J. L. (1994). A finite element model for the simulation of pile driving. *International journal for numerical methods in Engineering* **37**, 257–278.

Mabsout, E. M., Reese, L. C. & Tassoulas, J. L. (1995). Study of pile driving by finite-element method. *Journal of Geotechnical Engineering* **121**, No. 7, 535–543.

Masoumi, H. R. & Degrnade, G. (2008). Numerical modeling of free field vibrations due to pile driving using a dynamic soil-structure interaction formulation. *Journal of Computational and Applied Mathematics* **215**, 503–511.

Masoumi, H. R., Francois, S. & Degrande, G. (2009). A nonlinear coupled finite element-boundary element model for the prediction of vibrations due to vibratory and impact pile driving. *International Journal of Numerical and Analytical Methods in Geomechanics* **33**, 245–274.

Mayne, P. W., Cargill, E. & Miller, B. (2019). Geotechnical characteristics of sensitive Leda clay at Canada test site in Gloucester, Ontario. *AIMS Geosciences* **5**, 390–411.

Merifield, R. S., White, D. J. & Randolph, M. F. (2009). Effect of Surface Heave on Response of Partially Embedded Pipelines on Clay. *Journal of Geotechnical and Geoenvironmental Engineering* **135**, No. 6, 819–829.

Meyerhof, G. G. (1976). Bearing capacity and settlement of pile foundations. *Journal of the Geotechnical Engineering Division* **102**, No. 3, 197–228.

Orrje, O. and Broms, B. B. (1967). Effects of pile driving on soil properties. *Journal of the Soil Mechanics and Foundations Division, ASCE* **93**, 59–73.

Quinn, P. E., Diederichs, M. S., Rowe, R. K. & Hutchinson, D. J. (2011). A new model for large landslides in sensitive clay using a fracture mechanics approach. *Canadian Geotechnical Journal* **48**, No. 8, 1151-1162.

Randolph, M. F., Carter, J. P. & Wroth, C. P. (1979). Driven piles in clay-the effects of installation and subsequent consolidation. *Géotechnique* **29**, No. 4, 361–393.

Randolph, M. F. & Simons, H. A. (1986). An improved soil model for one-dimensional pile driving analysis. *In proceeding of the 3ʳᵈ International Conference on Numerical Methods in Offshore Piling, Nantes, France*, 1–17.

Rezaei, M., Hamidi, A. & Rooz, A. F. H. (2016). Investigation of peak particle velocity variations during impact pile driving process. *Civil Engineering Infrastructures Journal* **49**, No. 1, 59–69.

Roy, M., Blanchet, R., Tavenas, F. & La Rochelle, P. (1981). Behaviour of a sensitive clay during pile driving. *Canadian Geotechnical Journal* **18**, No. 1, 67–85.

Roy, M., Tremblay, M., Tavenas, F. & La Rochelle, P. (1982). Development of pore water pressures in quasi-static penetration tests in sensitive clay. *Canadian Geotechnical* Journal **19**, 124–138.

Roy, M. & Leblanc, A. (1988). Factors Affecting the Measurements and Interpretation of the Vane Strength in Soft Sensitive Clays. in *Vane Shear Strength Testing in Soils: Field and Laboratory Studies*, ed. A. Richards (West Conshohocken, PA: ASTM International, 1988), 117-128.

Rooz, A. F. H. & Hamidi, A. (2017). Numerical analysis of factors affecting ground vibrations due to continuous impact pile driving. *International Journal of Geomechanics* **17**, No. 12, 04017107.

Rooz, A. F. H. & Hamidi, A. (2019). A numerical model for continuous pile driving using ALE adaptive mesh method. *Soil Dynamics and Earthquake Engineering* **118**, 134–143.

Sheng, D., Eigenbrod, K. D. & Wriggers, P. (2005). Finite element analysis of pile installation using large-slip frictional contact. *Computers and Geotechnics* **32**, 17–26.

Smith, E. A. L. (1960). Pile driving analysis by the wave equation. *Journal of the Soil Mechanics and Foundations Division, ASCE* **86**, No. 4, 35–61.

Smith, I. M. & Chow, Y. K. (1982). Three-dimensional analysis of pile driveability. In *proc. of 2nd International conference of numerical methods on offshore piling, university of Texas, Austin*, **2**, 1–19.

Smith, I. M. & To, P. (1988). Numerical studies of vibratory pile driving. *International journal for numerical and analytical methods in geomechanics* **12**, 513–531.

Tavenas, F., Flon, P., Leroueil, S. & Lebuis, J. (1983). Remolding energy and risk of slide retrogression in sensitive clays. In *Proceedings of the Symposium on Slopes on Soft Clays,* SGI Report, No. 17, 423–454. Linköping, Sweden.

Thakur, V., Degago, S. A., Oset, F., Aabøe, R., Dolva, B. K., Aunaas, K., ... & L'Heureux, J. S. (2014a). Characterization of post-failure movements of landslides in soft sensitive clays. In *Landslides in sensitive clays* Springer, Dordrecht, 91–103.

Thakur, V., Jostad, H. P., Kornbrekke, H. A. & Degago, S. A. (2014b). How well do we understand the undrained strain softening response in soft sensitive clays?. In *Landslides in Sensitive Clays*, Springer, Dordrecht, 291–303.

Vesić, A. S. (1972). Expansion of cavities in infinite soil mass. *Journal of the Soil mechanics and Foundations Division* **98**, No. 3, 265–290

Walker, J. & Yu, H. S. (2006). Adaptive finite element analysis of cone penetration in clay. *Acta Geotech* **1**, No. 1, 43–57.

Wang, C., Hawlader, B., Islam, N. & Soga, K. (2019). Implementation of a large deformation finite element modeling technique for seismic slope stability analyses. *Soil Dynamics and Earthquake Engineering* **127**, 105824.

Wang, C., Hawlader, B., Perret, D. & Soga, K. 2020. Effects of Geometry and Soil Properties on Type and Retrogression of Landslides in Sensitive Clays. *Géotechnique*, 1–15.

Wang, C., Hawlader, B., Perret, D., Soga, K. & Chen, J. (2021). Modeling of Initial Stresses and Seepage for Large Deformation Finite-Element Simulation of Sensitive Clay Landslides. *Journal of Geotechnical and Geoenvironmental Engineering* **147**, No. 11, 04021111.

White, D., Finlay, T., Bolton, M. & Bearss, G. (2002). Press-in piling: ground vibration and noise during pile installation. *Deep Foundations 2020*, 363–371.

White, D. J. & Bolton, M. D. (2004). Displacement and strain paths during plane-strain model pile installation in sand. *Géotechnique* **54**, No. 6, 375–397.

Yi, J. T., Lee, F. H., Goh, S. H., Zhang, X. Y. & Wu, J. F. (2012). Eulerian finite element analysis of excess pore pressure generated by spudcan installation into soft clay. *Computers and Geotechnics* **42**, 157–170.

Zakeri, A. & Hawlader, B. (2013). Drag forces caused by submarine glide block or out-runner block impact on suspended (free-span) pipelines—numerical analysis. *Ocean Engineering* **67**, 89–99.

Zhu, H. & Randolph, M. F. (2011). Numerical analysis of a cylinder moving through rate dependent undrained soil. *Ocean Engineering* **38**, No. 7, 943–953.

Chapter 5

Two retrogressive landslide events case studies in eastern Canada–field observations and numerical analyses

Co-Authorship: This chapter has been submitted as a technical paper for publication in a journal as: Karmaker, R., Hawlader, B., Perret, D. and Dey, R., 'Two retrogressive landslide events case studies in eastern Canada–field observation and numerical analyses.' Most of the research presented in this chapter has been conducted by the first author. He also prepared the draft manuscript. The other authors mainly supervised the research and reviewed the manuscript.

5.1 Abstract

Two retrogressive landslide events that occurred in eastern Canada, namely the Rigaud landslide in Québec and the Daniel's Harbour landslide in Newfoundland, are discussed. The landslide incidents, post-slide investigations and potential failure mechanisms are discussed first. Large deformation finite element (FE) modeling is performed using an Eulerian-based FE approach to give insight into the failure mechanisms. In the Rigaud landslide, retrogressive failure occurred through sensitive clay during pile driving. FE modeling shows that pile installation could cause localized shear band formation and eventually a large landslide without additional external load. Soil stratification, sensitivity and rate of post-peak shear strength degradation play a major role in failure patterns. The Daniel's Harbour landslide might have occurred due to coastal retreats and soil weakening. While these time-dependent complex processes are difficult to model, FE modeling by triggering the landslide through the weakening of soil near the toe could simulate the failure similar to that observed in the field, including retrogression distance, failure pattern, and

downslope displacement of the failed soil block. Both landslides involved complex three-dimensional effects and triggering conditions; however, the present two-dimensional large-deformation FE simulations in-plane strain conditions provide insights into the progressive failure mechanisms, which cannot be obtained using the traditional limit equilibrium and FE analyses.

5.2 Introduction

Many landslides have occurred in Canadian sensitive clays that might have been triggered by toe erosion, seepage, generation of excess pore water pressure, strength degradation and human activities. Post-slide investigations could provide information about the triggering mechanisms and the key factors that influence the landslides. It provides insightful information for vulnerability analysis, risk assessment/management and land use around sloping areas. A complex failure mechanism might be involved in a landslide; however, a post-slide investigation always aims to develop a simplified explanation using all the available information and analysis techniques.

Although the Limit Equilibrium Method (LEM) is widely used to analyze the stability of the slope, it cannot explain the large-scale landslides. The failure surface develops progressively due to the strain-softening of sensitive clays, which cannot be captured using LEM. Therefore, advanced modeling techniques are required to explain the process. Several previous studies aimed to develop analytical and numerical methods, which can somehow explain the landslide events and identify the critical influencing factors (Odenstad, 1951; Carson, 1977; Quinn, 2009; Quinn et al., 2011; Locat et al., 2013; Dey et al., 2015; Locat et al., 2015; Dey et al., 2016a; Wang et al., 2020). The recent development of the large deformation finite element (FE) modeling technique can simulate the problems involving more complex slope geometries and soil profiles. However, the traditional Lagrangian-based FE still suffers from numerical issues due to excessive mesh distortions and a lack of convergences. In recent studies, the Eulerian-based FE method has been

used to simulate large-scale landslides in sensitive clays (Dey et al., 2015 & 2016a; Wang et al., 2020).

The objective of the present study is to investigate the mechanisms involved in the failure of a slope at the Rigaud landslide in Québec and Daniel's Harbour in western Newfoundland. The first part of this chapter describes the post-slide investigations and possible failure mechanisms inferred by the experts using available techniques, such as conceptual model and LEM. The second part presents two-dimensional large deformation FE simulations of the slides.

5.3 May 1978 Rigaud landslide

On the morning of May 3, 1978, a large landslide occurred at Ste Madeleine de Rigaud that caused the sliding of a 300-m valley slope. At the time of installation of displacement piles by impact driving was going on near the slope crest for a power transmission line when the landslide occurred (Chagnon et al. 1979). The crane operator used to drive the piles died in the event.

5.3.1 Geological settings at Rigaud site

Rigaud is a southwestern city of the province of Québec situated at the junction of the Ottawa river and Rigaud river, about 130 km east of Ottawa. The 1978 landslide involved typical glaciomarine clays deposited in the Champlain Sea between about 12,000 to 10,000 years ago (Corbeil 1984; Roy and Godbout 2014). The present clay plain, which corresponds to the old Champlain Sea bottom, is at an elevation of about 55 m. This plain is dissected by streams generally to the north that flows into the Rigaud River. The glaciomarine clay deposits, which can reach a thickness of more than 40 m in the landslide area, are underlain by sedimentary rocks of the Paleozoic age (Chagnon et al. 1979). Prefailure slope heights along the creek where the

landslide occurred range from 11 to 16 m. Interestingly, two other deadly retrogressive landslides occurred in 1829 and 1846 in the same area (Blais-Stevens et al. 2018).

5.3.2 Rigaud landslide event

The landslide area was located on the route of a power transmission line under construction connecting James Bay to Montréal. The landslide occurred when the pile driving was in operation (Chagnon et al. 1979). The rectangular-shaped pylon (hydro-electric tower) site is shown in Fig. 5.1. Fig. 5.1 is prepared by the Geological Survey of Canada (GSC)[1], which contains the locations of various field investigations carried out by various committees. Pylon #83 was supposed to be supported with four anchors, as shown in Fig. 5.1. Each anchor consisted of two HP14×73 piles of approximately 24.4 m in length. Using a conventional crane-equipped hammer, this pile was driven into the soil at a 34° angle to the vertical direction (toward the slope). A 2.8-ton hammer with a falling distance of ~ 1 m was used for pile driving. The pile had three sections of 12.2 m, 7.6 m and 7.6 m long, which were welded during the installation process.

Pile installation started at location A#4 in the morning (7h00 AM) of May 2, 1978 (Fig. 5.1). Two 24.4-m long piles were driven, and the installation was completed by 4h30 PM. Then the crane was moved to the location of A#1 (Fig. 5.1). The first section (12.2 m) of the third pile was driven up to 10.1 m depth at A#1, and the installation process was stopped at 6h00 PM.

Pile driving restarted at 7h00 AM on May 3, after welding the second section of 7.6 m with the previously installed sections. After insertion of the second section, the pile tip reached 16.4 m below the ground surface. The third section of 7.6-m long was immediately welded to the top of the second section, and the driving began. The landslide was triggered immediately after three

---

blows, and it took only a minute to slide 300-m of the valley slope. The previously installed piles at A#4 displaced over a horizontal distance of 15–18 m.

Point B in Fig. 5.2 indicates the point where the third pile was installed. Due to sliding, an elongated narrow strip of land (denoted as L in Fig. 5.2), located at the top of the slope, subsided vertically and created four ridges (denoted by 1, 2,3, & 4 in Fig. 5.2). Zones A, B and C represent the displaced west slope, zone D represents the frontal compression zone, zone E represents the upper part of the east slope, and zone F represents the back wall of the old slidescar.
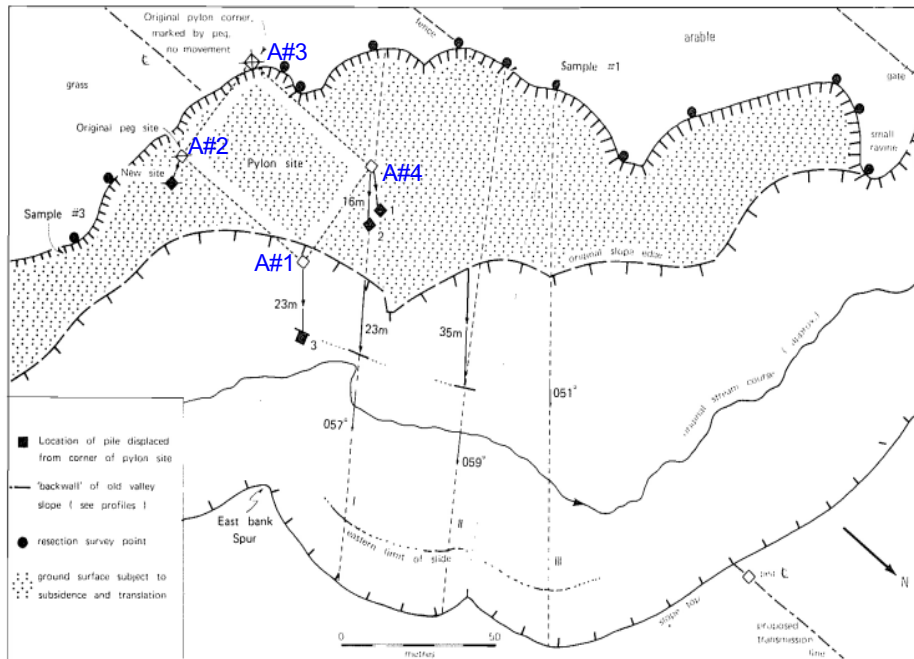
Fig. 5.1. Map of May 1978 Rigaud landslide bowl (after Carson, 1979a)
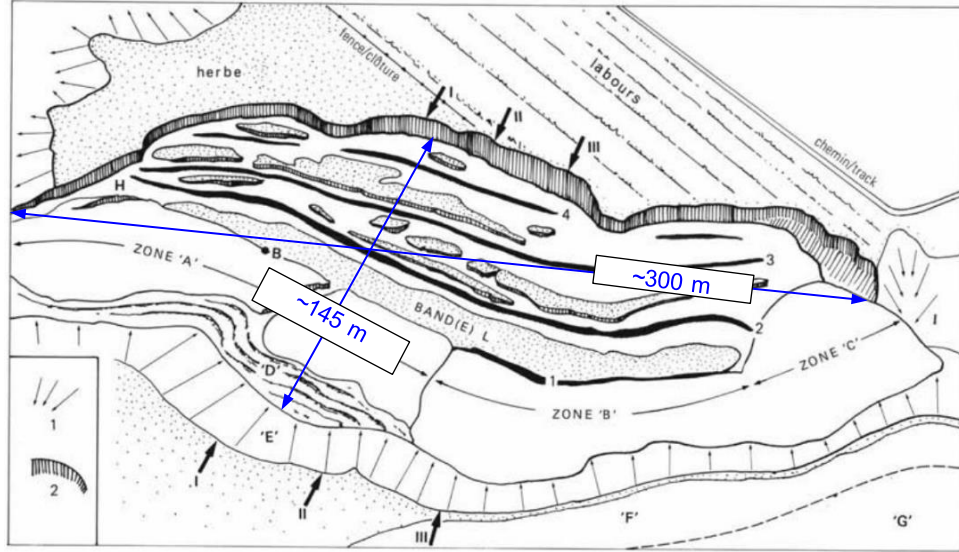
Fig. 5.2. Schematic representation of the morphology of the landslide bowl (after Carson, 1979b)

5.3.3 Post-slide investigations of Rigaud site

The landslide affected ~ 300 m of valley slope, and the horizontal distance from the landslide backscrap to the opposite side of the valley was about 145 m, as shown in Fig. 5.2. The maximum retrogression distance was measured as 45–75 m (Chagnon et al. 1979; Carson, 1979b; Locat et al., 2014) behind the crest of the initial slope. The landslide was a spread type of failure, and no rotational slip circle was found. The movement of soils created four ridges in the crater of the landslide, and horsts showed stratifications with almost horizontal surfaces. Carson (1979a & 1979b) indicates that there were no water ponds observed between the horsts, and no water seepage has occurred in the landslide backscrap. There were no traces of liquefied clay in the landslide zone. Carson (1979a) describes that the new backscrap was 7–8 m in height and the retrogression distance was only three to four times the initial slope height. Carson (1979a) noted that the Rigaud landslide is similar to the 1955 Hawkesbury slide that was triggered by blasting (Eden, 1956). Carson (1979a) also indicated the presence of a 15-cm thin, soft clay layer at this depth in the

extruded soil sample collected by the piston sampling from the landslide site, which was around 17.5 m below the original ground surface.

Several post-slide geotechnical investigations were conducted to identify the reasons behind this landslide, as shown in Fig. 5.1. Immediately after the landslide, an expert committee was formed in 1978/1979. In 2000–2002, Geological Survey Canada (GSC) carried out another geotechnical investigation and conducted slope stability analysis using limit equilibrium methods. Finally, in 2015, Ministre des Transports, Quebec has carried out a piezocone test on the opposite side of the creek.

Expert committee in 1979 (Chagnon et al. 1979)

This phase of geotechnical investigations includes eight borehole drilling outside the scar, thin-wall Shelby tube samples collection, laboratory testing, field vane shear testing at ten sites, laboratory testing, and installation of piezometers to locate the groundwater table and estimate the hydraulic gradient (Fig. 5.1). After examination of the geotechnical field and laboratory reports, the expert committee identified a sand layer of various thicknesses approximately at El. 36.0 m (~ 19.5 m depth from the ground surface) in a borehole outside the landslide scar. According to the expert committee report, this is the only elevation at which a sand layer has been observed in the clay deposit at the site, which is about 42.7 m thick. The presence of other small sand and silt pockets was also observed above El. 36.0 m, but no detailed information is given in the report.

The undrained shear strength profile obtained at the rear side of the pre-landslide slope crest indicated a deep failure surface at 19.8 m depth from the ground level and 3.7 m below the toe. The failure surface was deemed to be essentially horizontal and possibly controlled by the presence of a weaker layer. The clay sensitivity was significantly higher at this depth (10–80 with a Liquidity Index (*LI*) of 1.0–2.0).

The committee performed slope stability analyses using the drained soil parameters for a slope height of 14.4 m and a slope angle of 16.9°, corresponding to the pre-failure slope directly in front of the pile Anchor #1 (Fig. 5.1). The water table was considered at a depth of 2.5 m near the slope crest and at the ground surface near the toe. With drained geotechnical parameters of $c' = 6$ kPa and $\phi' = 29°$, the factor of safety (*FS*) of 1.70 was calculated. Considering the most critical pre-failure slope along the creek affected by the landslide (slope angle of 20.3°, 14.4 m high), an *FS* of 1.47 was obtained. It is important to note that the slope closest to pile Anchor #1 is not the most critical in terms of stability in drained conditions and that the reserve of stability is very high.

After examining different scenarios, the expert committee concluded that the presence of a thin sand or silt layer at the elevation of the horizontal failure plane played a vital role in the failure of this slope. They hypothesized that the liquefaction of this cohesionless layer might have triggered the failure following an increase in pore pressure induced by pile driving.

GSC in 2002 and Transports Québec in 2016

In 2002, the Geological Survey of Canada (GSC)[2] carried out a field investigation consisting of 11 piezocone tests (within and outside of the scar), one field vane test (outside the scar), two boreholes drilling (one within and one outside the scar) together with continuous Shelby tube sampling and a large diameter sampling with the Laval sampler close to the elevation of the failure surface.

The Shelby tube samples collected from boreholes just outside the scar were X-rayed with a medical CAT-Scan to identify any possible existence of the thin cohesionless soil layers. The CAT-Scan results showed no sand or silty layers throughout the soil profile. After the extraction

---

[2] Didier Perret, Geological Survey of Canada, personal communication and internal files sent to the Author.

of the samples from the Shelby tubes, direct visual observations also confirmed the absence of significant cohesionless soil layers. No cohesionless layers were detected from the piezocone test profiles which were obtained with a 5-mm vertical resolution. However, very thin horizontal silt parts or laminae were identified during sampling, although the thickness of those layers was not more than one millimetre. Based on their investigations, GSC concluded that no sand or silt layers of significant thickness were present at or near the location of the failure surface, which was, given uncertainties in elevations, horizontal. Instead, two different stratigraphic units were identified from the field investigations. It was observed that the failure surface passes at, or very near, near the interface between these two stratified units. Two seismic reflections and two electrical resistivity lines were also surveyed on the landslide site to detect any possible vertical or lateral heterogeneities in the deposit.

Transports Québec performed an additional geotechnical investigation outside the landslide scar in 2016, consisting of a piezocone test, a borehole with Shelby tube sampling, and field vane testing (Therrien 2020). They also did not find any cohesionless layers of any significant thickness.

Considerations before performing the numerical simulations

The above field investigations could not provide the exact cause(s) of the initiation of the failure; however, pile driving was considered the possible cause of the failure.

Using the similar soil parameters, limit equilibrium analysis is performed using SLOPE/W software, as shown in Fig. 5.3. Two important observations should be mentioned: (a) *FS* is considerably higher than 1.0, even for the critical slope angle, which implies no failure; and (b) failure plane is circular; however, the field investigations show the formation of a long horizontal failure plane prior to global failure. In other words, the limit equilibrium method cannot explain the failure of this slope.
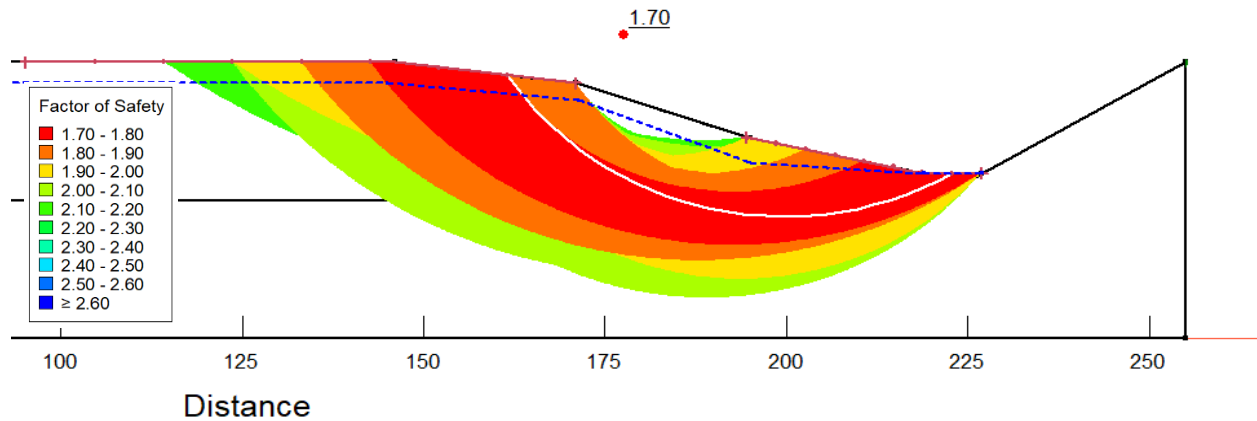
Fig. 5.3. Limit Equilibrium analysis using SLOPE/W using the drained parameters

Several field vane (FV) and piezocone tests were carried out from time to time in the Rigaud landslides zone to understand the failure mechanisms (Fig. 5.4). The undrained shear strength profile based on these tests clearly shows that, in addition to the crust of ~ 4 m, there are two main stratigraphic units in terms of the strength profiles. A relatively low undrained shear strength (~ 25kPa) is observed below the crust, and the strength increases with depth. At about 19–20 m depth, there is a sharp increase in undrained shear strength. Note that the failure occurred around this depth; therefore, the effects of this quick increase in strength are examined in this study.
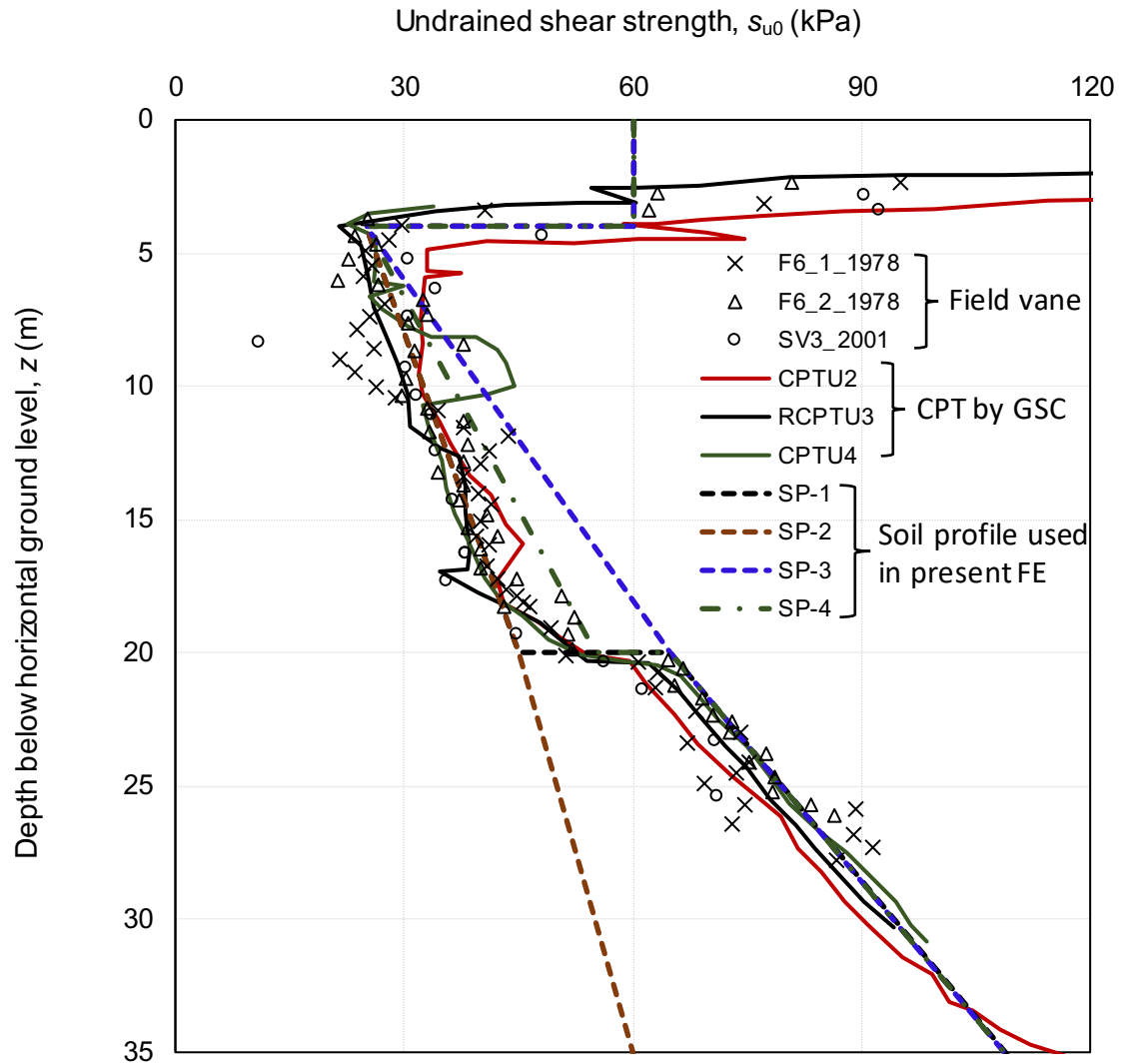
Fig. 5.4. Field test results for undrained shear strength

5.4 Daniel's Harbour landslide

In this section, the second landslide considered in this study is described. Daniel's Harbour is a small town containing steep coastal cliffs along the west coast of the Northern Peninsula, Newfoundland and Labrador. The community is located on a coastal platform that is approximately 25 m above sea level. The area has a history of landslides and ongoing coastal erosion that has led to the destruction and abandonment of homes and other nearby structures,

temporary and permanent re-routing of roads, and other inconveniences for the town's residents (Luther, 2013). Additional information related to these issues is available in previous studies (Whitford, 2006; Whitford, 2008; Batterson & Liverman, 2010; Luther, 2013; Spooner et al., 2013; Kilfoil et al., 2018).

5.4.1 Geological settings of Daniel's Harbour

Previous studies show the existence of glacial and post-glacial sediments in the area of the landslide at Daniel's Harbour (Proudfoot & St. Croix, 2001; Spooner et al., 2013). In general, the site has a thick layer of compact glaciomarine diamicton of silt-clay mixture with pebbles and some boulders up to a 50-cm diameter. At the toe level of the slope, a layer of silty clay was found. Proudfoot & St. Croix (2001) presented a landform classification map to denote the approximate percentage of landforms occurring within Daniel's Harbour location. The map indicates that 60–85 percent of the land is covered by Marine deposits consisting of clay, silt, gravel and diamicton and 15–40 percent of the land is covered by poorly drained accumulations of peat, peat moss and other organic matter. The marine deposits are underlain by either glacial till or bedrock. The glacial tills exist especially along the coastal belt, where the Crestline of the major moraine ridge is located. The compacted sediments are the result of the presence of a high proportion of the carbonate material that provides cemented behaviours to the fine-grained soils.

5.4.2 Landslide events in Daniel's Harbour

Geomorphological and air photograph interpretation indicates that landslides in Daniel's Harbour area have been ongoing for several decades. In Fig. 5.5(a), a 1988 aerial photograph shows the existence of several historical failure crests and scarp along the shoreline. While these features have been documented, until 2006, the stability and safety of the surrounding area were

not considered a major concern since no significant landslide events were recorded before that time.

During spring 2006, a small landslide was noticed and not documented as the landslide posed no danger to infrastructure. An estimated 5,000 m^3 of material was dislodged during this landslide. The first of the two significant landslide events occurred on October 20, 2006, which involved approximately 15,000 m^3 of materials. In Fig. 5.5(b), an aerial photograph shows the failed area. Considering the proximity of this slide to residential dwellings, concern regarding the overall stability and safety of the surrounding area was identified by town and provincial officials. Stantec (previously Jacques Whitford) was retained as a geotechnical consultant to investigate the cause of failure and provide recommendations regarding the stability of the remaining slope. Based on the recommendations provided by Stantec, an exclusion zone was established, and two residential dwellings, one convenience store and four detached sheds were evacuated within the zone.

On April 15, 2007, the October 2006 slide area became reactivated, and a significant landslide occurred between April 15 to 19, 2007. Approximately 110,000 m^3 of soil volume was displaced, producing a large debris fan that extended about 60 m in front of the slide area. The slide destroyed a residential dwelling and several detached buildings, and the government officials declared a state of emergency regarding the safety of the area. Several other homes were evacuated, and Highway 430 leading to the Northern Peninsula was closed. Figs. 5.5(c) & 5.5(d) show the photographs of the landslide and the damaged properties.
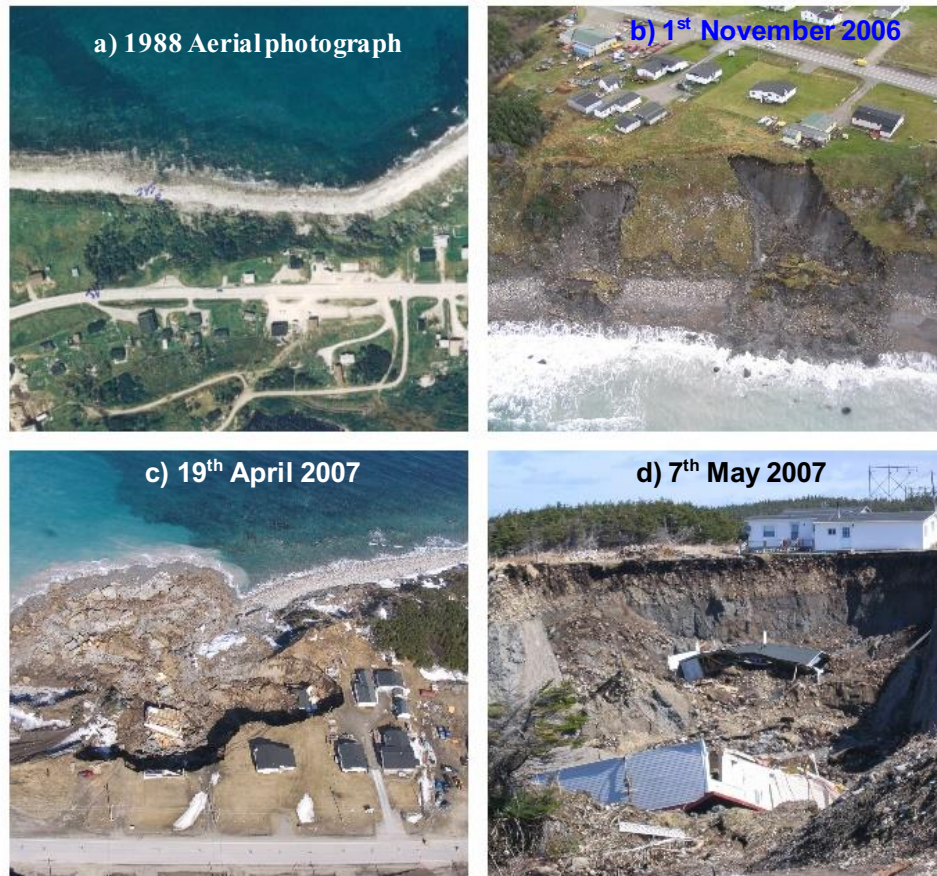
Fig. 5.5. Aerial photographs of Daniel's Harbour landslides events with dates of photographs taken

The 2006 exclusion zone was expanded, resulting in the permanent evacuation of several more residential dwellings and detached buildings. On June 18, 2007, a small landslide occurred approximately 230 m south of the 2007 slide area, and an estimated 1,500 m³ to 2,000 m³ of materials were dislodged during the slide. Stantec conducted a subsequent site investigation to review and document the occurrence of slope failure. Post slide investigation inferred that the 2007 slide was a combination of translational and rotational failures (Spooner et al., 2013).
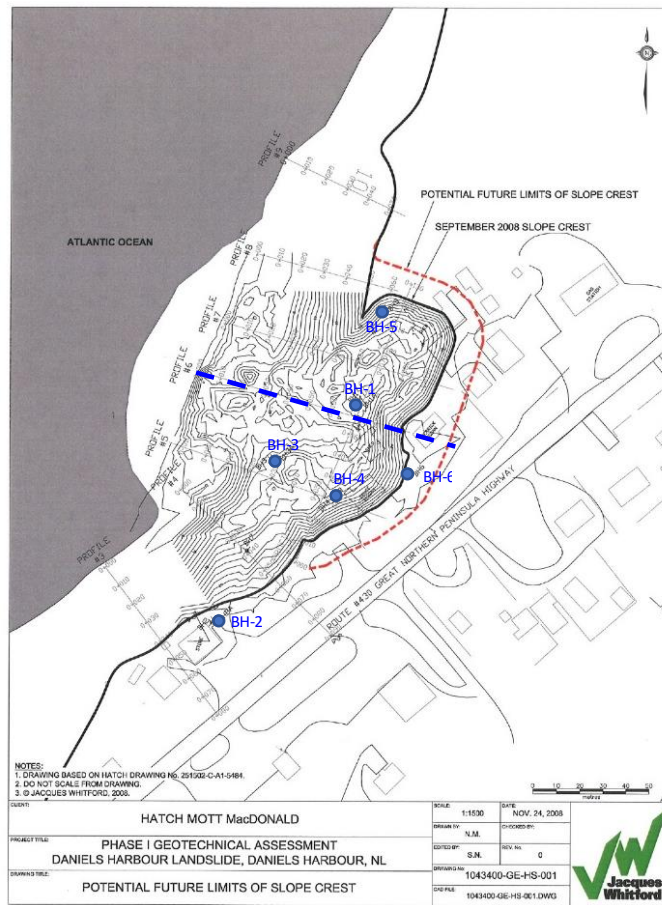
Fig. 5.6. A map provided by Stantec containing the topographic survey was updated in

September 2008

5.4.3 Geotechnical investigations of Daniel's Harbour landslide

Stantec carried out geotechnical site assessments for the Daniel's Harbour landslide, which included site visits from a landslide expert, reviewing the available information and site investigations. A subsurface geotechnical investigation was performed, consisting of drilling six geotechnical boreholes (BH), one dynamic cone penetration test (DCPT) and installing three slope inclinometers at the study area. The locations of the boreholes are shown in Fig. 5.6.
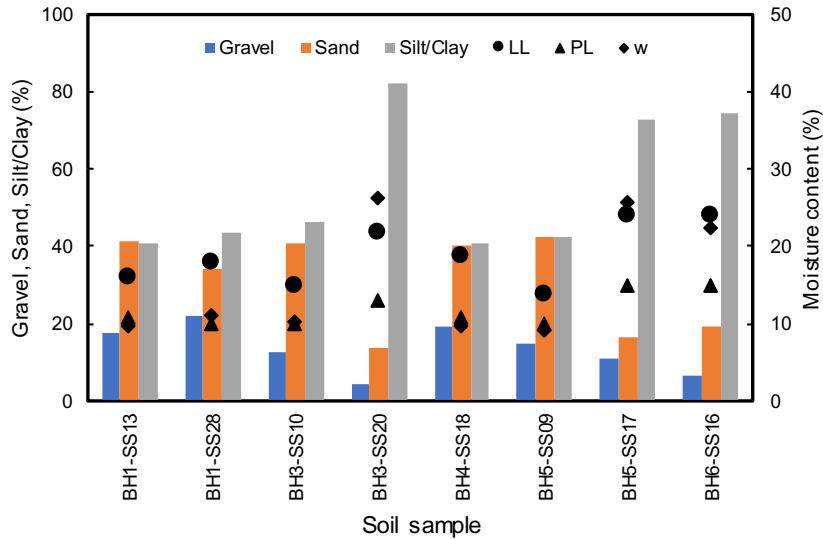
Fig. 5.7. Index test results

Disturbed soil samples (SS) were collected for laboratory tests. Particle size distribution, liquid

limit (*LL*) and plastic limit (*PL*) tests were conducted on selected soil samples. Fig. 5.7 shows the

percentage of gravel, sand and fines (silt & clay) in the soil samples obtained from different

boreholes. Three soil samples, BH3-SS20, BH5-SS17 and BH6-SS16, contain a high percentage

of silt/clay components, and they were at a depth of 26.4 m, 25 m and 22.5 m, respectively. Field

investigations show that the site has a thick (~20 m) layer of silty to clayey sand with gravel

(diamicton) overlain by a surficial sand and cobble mixture (Fig. 5.8). A lean clay layer of 3 to 4

m thick is underlain by the diamicton layer, which has fine (silt/clay) content of 73 to 82%.

The natural water content (*w*) of the soil above EL. 0 is 7 to 12%; however, *w* is as high as 26%

for soil at EL. between -5.0 to 0 (i.e., lean clay layer) (Fig. 5.9). In the lean clay layer, *w* is equal

to or greater than the *LL* (i.e., the Liquidity index (*LI*) is close to or greater than 1.0). That means

this soil layer is expected to have strain-softening behaviour and retrogressive undrained failure

potential. Fig. 5.9(b) shows that the SPT-*N* values above EL. 10 are considerably high; however,

it is less than 20 in the loose clayey sand and lean clay layers. The bedrock was not encountered within the borehole depths.
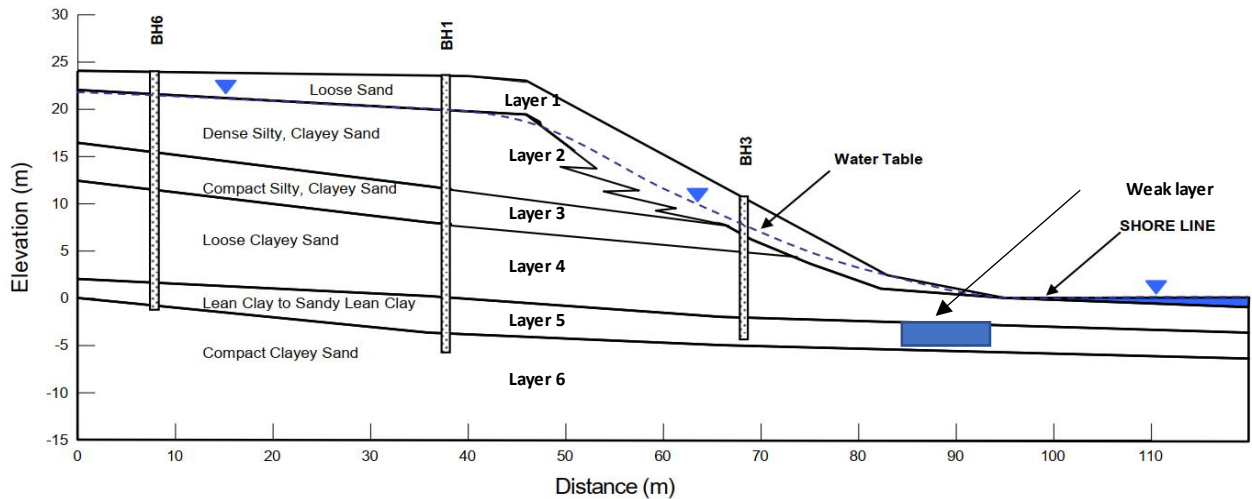
Fig. 5.8. An idealized soil profile prepared from field investigation results

Ten fall cone tests were conducted on this soil, and the remoulded undrained shear strength of 2–12 kPa was found, as shown in Fig. 5.10. The soil samples are taken from BH-1 and BH-3 at the locations where lean clay exists. From the Standard Penetration Test (SPT), the undrained shear strengths for that specific location at BH-1 and BH-3 are 50 kPa and 38 kPa, respectively. The reduction of undrained shear strength in remoulded conditions indicates the presence of medium to high sensitivity in those soil samples. Moreover, these geotechnical data provide an excellent agreement with the existence of retrogression potential at the lean clay soil layer.

During the 2008 site visit, seven water samples were collected from the seeps along the toe of the failure and from the water supply lagoon and pond on the east end of the slide area. The purpose of the water sampling was to determine if the water was capable of dissolving carbonates and if the downstream samples were enriched in carbonates. Samples collected at the toe of the slope are generally rich in the concentration of chloride, sulphate, sodium and potassium than the samples

from the sources (i.e., water supply lagoon and pond). The calcium and sulphate concentrations changes may indicate the gypsum dissolution along its flow path (Whitford, 2008).
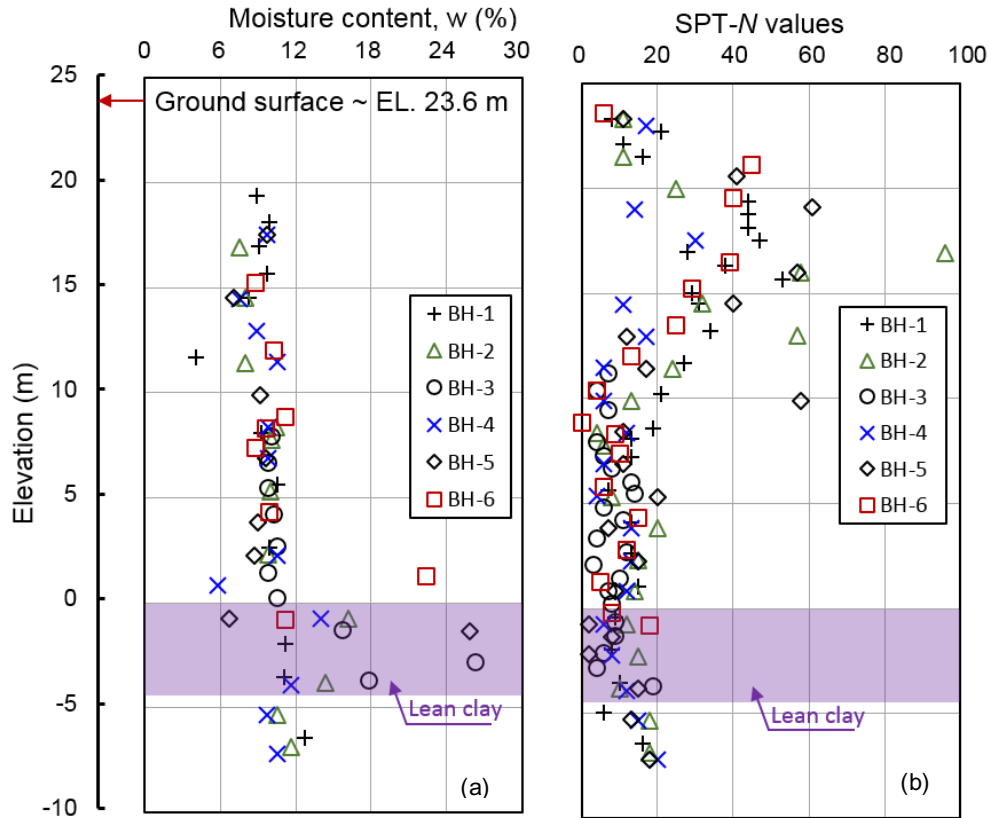
Fig. 5.9. Moisture content and SPT results

5.4.4 Possible failure mechanisms proposed by Stantec

Based on post-slide investigations, two hypotheses were proposed: (*a*) mudslide corrie and (*b*) presence of sensitive soils (Whitford, 2008).

Mudslide Corrie

According to this hypothesis, the landslide might have occurred due to the continued coastline retreating. The aerial photographs provide an indication of localized retrogression of the slope since 1947. In Fig. 5.5(a), the existence of such failure crests can be identified. Erosion could also

bring the frost susceptible soil near the toe closer to the exposed surface, which could accelerate ice melting and thaw weakening of this soil during the spring. This could also increase the excess pore water pressure within the lean clay layer. The climate data for 2007 show that the temperature in April remains above zero degrees, which might have initiated the spring thawing. The October 2006 investigation also shows that the soil along the cliff behaves as frost susceptible. In summary, the combined effect of toe erosion and thaw weakening might have triggered the failure from the toe (Whitford, 2008; Spooner et al., 2013).
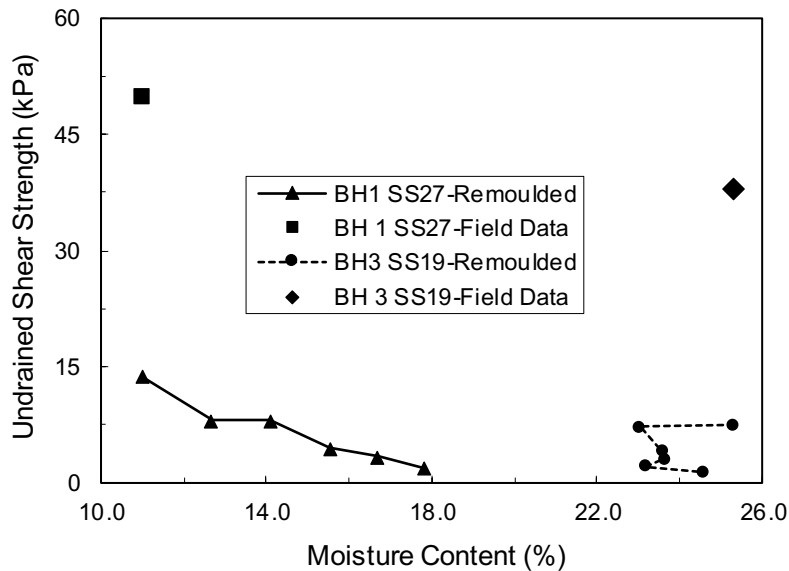
Fig. 5.10. Fall cone test and SPT results

Sensitive soils

The clay layer at the base of the slope might have become a sensitive cohesionless material due to the dissolution of calcite cement and initiated the retrogression (Froese & Cruden, 2001; Whitford, 2008). This hypothesis was given, assuming that the clay soils are bonded with calcium carbonate cement, which might become dissolved due to water flowing through it, resulting in a

brittle failure. Site investigation documented the presence of cemented soils that produced large intact blocks even after the landslides in April 2007. The materials in failed blocks were very hard and required several blows from a geology hammer to break them apart. Also, the residents observed vibrations/tremors during the landslide that might be caused by the gradual weakening of the underlying sensitive layer.

5.4.5 Limit equilibrium analyses and recommendations by Stantec

After the October 2006 slide, slope failure analyses were carried out considering rotational slip failure, in which the potential failure surface was assumed to be a circular arc or non-circular curve. Drained analyses were performed considering the soil parameters shown in Table 5.1.
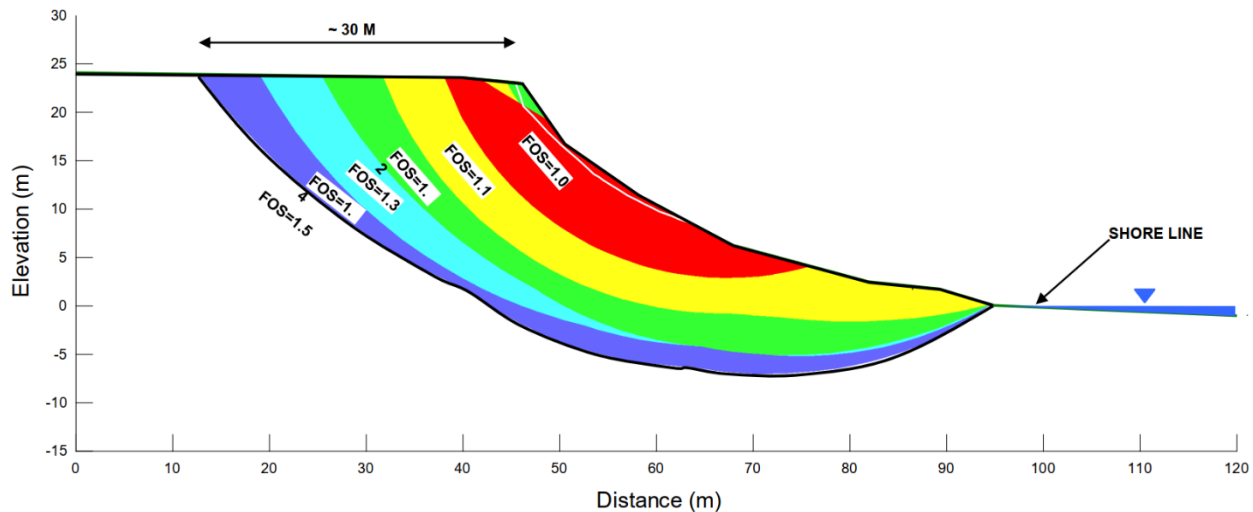
Fig. 5.11. LEM analyses considering drained parameters

Stantec also provided a slope stability safety map for an *FS* equal to 1.5 located 25 m far from the existing crest. Properties outside this boundary line (i.e., *FS* > 1) were considered safe (Fig. 5.11). An exclusion zone was identified based on the analyses, and evacuation within that zone was recommended. In addition, a conceptual plan was provided in which the area affected by the landslides can be stabilized through conventional earthwork. But in April 2007, a composite

rotational and translational failure occurred, which dislodged a huge amount of materials. The combined effects of these two landslide events extend the failure up to ~ 60 m from the crest, which is higher than the initial estimation of 25 m based on critical slip surface location in the limit equilibrium analyses. This implies that the limit equilibrium method cannot properly explain this failure, and progressive failure analysis is required.

Table 5.1. Parameters used in drained limit equilibrium analysis by Stantec

Strata	Unit weight γ (kN/m³)	Friction angle ϕ' (°)	Cohesion c' (kPa)
Loose sand	19	32	0
Dense silty clayey sand	21	36	15
Compact silty clayey sand	20	34	10
Loose clayey sand	19	32	5
Firm to stiff lean clay	20	30	10
Compact clayey sand	20	33	10

However, an improvised exclusion zone was recommended based on the field investigation after April 2007. Just after the April 2007 landslides, Stantec recommended that the restricted zone should be extended up to 30 m from the crest of the failure scrap, which is an additional zone to the zone already identified in the 2006 report. They also recommended carrying out phase 2 geotechnical investigations for an in-depth understating of the failure mechanisms.

5.5 Finite Element Modeling

For the Rigaud landslide, the field evidence shows that the failure of the slope was initiated when the pile driving was in operation. Pile driving could cause disturbance of adjacent soils,

which could increase the excess pore water pressure and reduce the shear strength due to accumulated plastic shear strain. Similarly, the stress state around the pile is highly altered near the toe, as discussed in Chapters 3 and 4, which might lead to the failure of the soil.

The post-slide investigations show that the retrogressive failure in the Rigaud landslide created horst and graben with a relatively small flow bowl. The clay deposits had a liquidity index of 1.0–2.0, which indicates the possibility of large retrogressive flow slides (Tavenas et al., 1983; L'Heureux, 2012; Thakur et al., 2014; Demers et al., 2014). Silvestri et al. (1989) conducted direct shear and simple shear tests on the samples collected from Rigaud along the Trans-Canada Highway, a few kilometres away from the Rigaud landslide site. The soil represents typical grey Champlain clays of eastern Canada, having a liquidity index of 1.40, plasticity index of 35, clay contents of 77% and silt content of 23%, sensitivity of 18 (using vane test). Also, the failure occurred within one minute, which justifies an undrained failure of the slope.

For the Daniel's Harbour landslide, the field evidence shows that the failure might have occurred by progressive formation of failure planes as the soil, primarily the lean clay and loose clayey sands, might have some strain-softening behaviour. Now the key question is whether the analyses should be performed for the drained or undrained conditions. As mentioned in sections 5.4.3 and 5.4.4, there might be strength weakening due to the reduction of bonds during water flow and spring thawing of soil near the toe. These complex processes are not be simulated in the present FE analysis. Therefore, the reduction of soil strength due to thawing and other activities near the toe is simply modelled using a Strength Reduction Method (SRM), which could trigger the landslides. Karmaker et al. (2018) successfully implemented SRM in a Coupled Eulerian-Lagrangian (CEL) framework to model pile stabilized clay slope.

Once triggered, the failure might have occurred very quickly. Also, most of the soil contained a significant percentage of fine materials that might hinder the flow of water. Note that the soil behaviour of this type of coarse and fine-grained mixture could be considered similar to the materials used for clay liner or earth core of a dam where the coarse contents govern the shear strength behaviour, and finer contents control the water flow. In summary, it is reasonable to model the rapid failure process as an undrained condition.

5.5.1 FE formulations

The Eulerian-based approach in Abaqus FE software is used in numerical analysis. The main advantage of this approach over the conventional Lagrangian-based FE is that it can handle large deformation problems without any numerical issues related to mesh distortion. Further details are available in previous studies and Chapters 3 and 4. The soil is modelled as an Eulerian material such that it can flow through the fixed mesh (Qui et al., 2011; Dey et al., 2015; Karmaker & Hawlader, 2018; Wang et al., 2020).
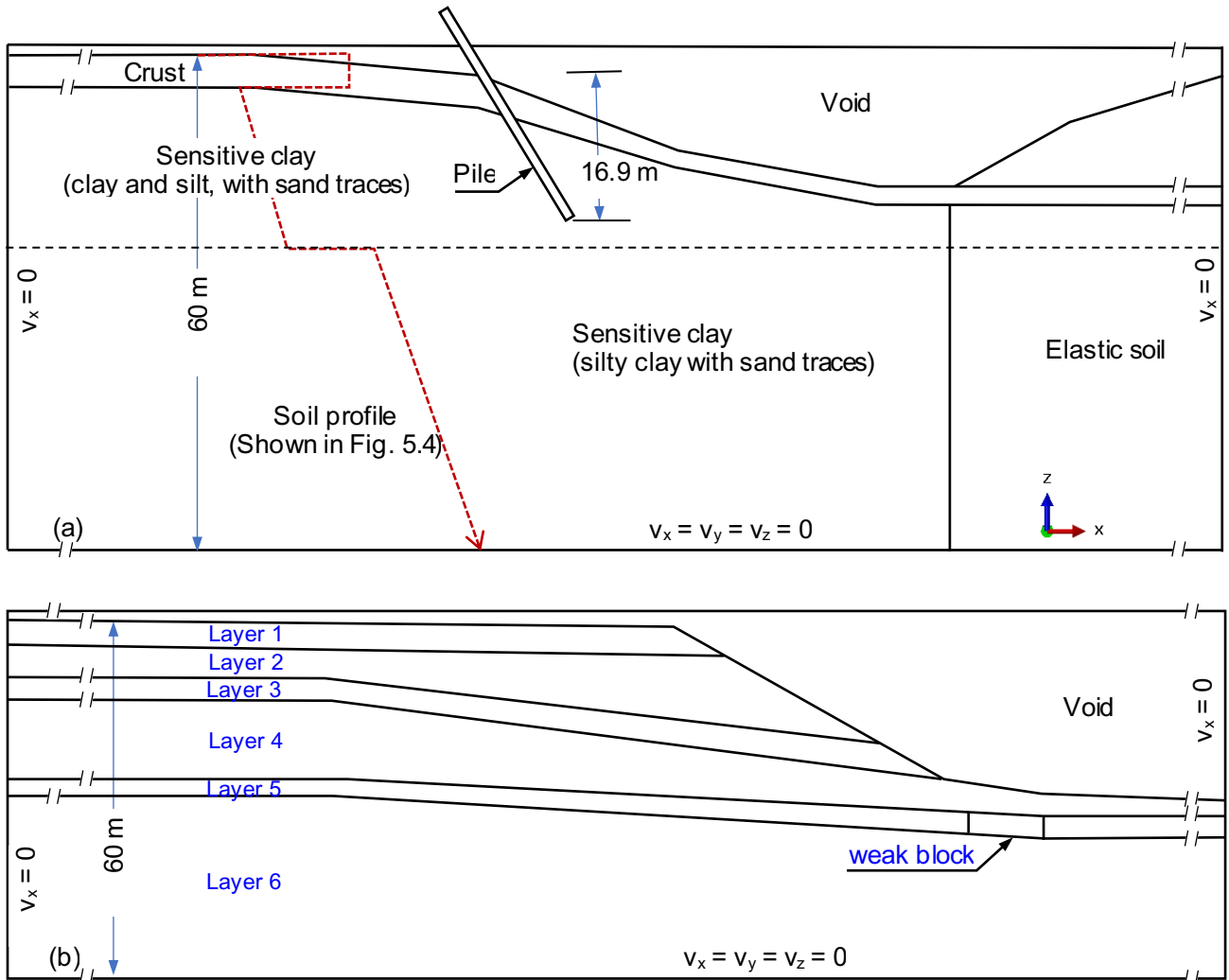
Fig. 5.12. FE models: (a) Rigaud landslide; (b) Daniel's Harbour landslide

A three-dimensional FE analysis is carried out by developing a soil domain shown in Fig. 5.12. The analyses are performed for one element thickness in the out-of-plane direction with 0.25 m cubical uniform mesh. The left and right boundaries are placed at 200 m and 100 m, respectively, from the toe of the slope to avoid boundary effects of the failure process. Zero velocity boundary conditions are applied to the bottom of the domain in all three directions (i.e., $v_x = v_y = v_z = 0$). Zero velocity boundary conditions are also applied normal to all the vertical faces of the domain. In the present FE analyses, the Eulerian material (soil) can be filled in the void of FE domain using the

Eulerian Volume Fraction (EVF) tool, in which $1 > EVF > 0$, $EVF = 1$, and $EVF = 0$ represent the elements of partially, fully and not filled with soil, respectively. No boundary conditions are applied at the interface between soil and void so that the soil can move to the void when it deforms.

The present study establishes the initial stress condition by considering the soil removal technique developed by Wang et al. (2020). In FE modeling, the initial total stresses are applied to the horizontal ground surface. The gravitational load is applied to the soil elements ($EVF \neq 0$), and the stresses are distributed to the sloping ground accordingly. The technique is similar to the 'mesh removal' technique used in typical Lagrangian-based FE modeling of excavation (Potts et al., 1997; Locat et al., 2013).

In the Rigaud landslide modeling, the upper crust has uniform undrained shear strength; however, the shear strength of sensitive clay increases linearly with depth Fig. 5.12(a). The soil below the toe of the opposite river bank is simply considered elastic, as no failure in this side occurred. A rigid part is placed at the right side as an opposite slope to reduce computational cost. Wang et al. (2020) emphasize that such opposite riverbanks might significantly control the retrogression and runout distances, especially in the case of spread type failure. Field observations found the presence of horst and graben in the Rigaud landslide site; therefore, such considerations might affect the mode of failure in the numerical analyses.

The present FE model has three steps: i) first, the gravity loading is applied to bring the soil in the in-situ state, ii) second, the pile is penetrated at a constant velocity up to 0.5 m of depth, and iii) third, no external load is applied for another 50 seconds. In the third step, the translation and rotation of the pile head are allowed in the x and z directions. The reference point of controlling the translation and rotation is placed very far from the pile head to ensure a large radius of rotation during the pile displacement. When a landslide is triggered, the pile can move without providing

any resistance to the failed soil mass. This technique is taken into account to simulate a realistic scenario during numerical modeling because the pile is translated with the failed soil mass during the landslide. Before applying gravity, the pile tip is placed at 16.9 m below the ground level at an inclination of 34° to the vertical. As the structural deformation is not considered in the present study, the pile is considered as a rigid body. The pile–soil interface is considered as a rough condition with maximum allowable shear stress $\tau_{max} = 5$ kPa.

In Daniel's Harbour landslide FE modeling, six soil layers are considered, as shown in Fig. 5.12(b). Soil is modelled using the EC3D8R elements, which are 8-node linear multi-material Eulerian brick elements. The failure is triggered by a gradual reduction of strength using the strength reduction method.

FE simulations of this landslide also consist of three steps. First, the gravity loading is applied to the soil gradually to bring it to the in-situ state. In the second step, by using SRM, the undrained shear strength of the small weak soil block near the toe (Fig. 5.12(b)) is reduced from its initial value (~75 kPa) to 1 kPa. In the third step, the analysis was continued without applying an external load or reducing strength by the user.

Soil parameters selection

Rigaud landslide

As mentioned above, the simulation of this landslide involves three zones: (i) crust, (ii) sensitive clays, and (iii) elastic soil. The undrained shear strength of the crust is considered as 60 kPa without softening. The effects of strain-softening of the soil in the crust are also investigated.

A user subroutine is developed to incorporate the strain-softening and strain-rate effects on undrained shear strength. A detailed discussion on modeling of sensitive clay and its

implementation in FE software has been presented in Chapter 3. Other important soil parameters considered in the soil model are represented in Table 5.2. The base model is compared with the Rigaud landslide, which contains the parameters: $s_{u0}/s_{uR} = 5$, $\delta_{95} = 0.1$ m, $\delta_{ld} = 20\delta_{95}$ & $s_{u0}/s_{uld} = 100$. Other values of the parameters are used in the parametric study.

Table 5.2. Soil parameters used in the sensitive clays for the FE modeling of Rigaud landslide

Parameter	Sensitive Clay
Total unit weight, γ (kN/m³)	17
Undrained Young's modulus, E_u (MPa)	10
Undrained Poisson's ratio, ν_u	0.49
Initial undrained shear strength of sensitive clay, s_{u0} (kPa)	$s_{ug} + kz$
Ratio between initial and remoulded undrained shear strength, s_{u0}/s_{uR}	5 (2, 10, 20)
Ratio between initial and large deformation undrained shear strength, s_{u0}/s_{u_ld}	50
Plastic shear displacement for 95% degradation of s_{u0}-s_{uR}, δ_{95} (m)	0.05 (0.1, 0.4)
Plastic shear displacement to mobilize s_{uld}, δ_{ld} (m)	$20\delta_{95}$
Reference strain rate, $\dot{\gamma}_{ref}$ (s⁻¹)	5.0
η	0.5
β	0.1

Note: Values used for the parametric study are shown in parenthesis

Daniel's Harbour landslide

As mentioned above, six soil layers, as reported from field investigations, are used in FE simulations. The topsoil layer (Layer 1) is above the groundwater level and might have experienced the seasonal freeze-thaw, which could increase the permeability. This soil layer is modelled using the Mohr-Coulomb failure criterion. Layers 2 and 3 consist of compacted and dense silty clayey sands. Field investigations show that these soils are bonded with calcium carbonate cement. When such bonded/structured soils are subjected to undrained loading, the

stress path is almost vertical initially until it goes closer to the failure conditions (Lade, 1978; Leroueil & Hight, 2003). This implies that the maximum undrained shear strength of these types of materials could be related as $s_{u0}/\sigma'_v = \tan \phi_y$, where $\tan \phi_y \leq \tan\phi'$. It is to be noted that such a concept was used to analyze the undrained failure of through sandy material in some dams, for example, the Lower San Fernando Dam (Gu & Morgenstern, 1993; Olson, 2001). However, for simplification of the numerical modeling, σ'_v is considered as an average value calculated at the middle of each soil layer. As the soil is bonded, a small level of softening is given to reduce the strength simply with strain, although the authors understand that the process of strength weakening might be more complex. However, a sensitivity (s_{u0}/s_{uR}) 2.0 is considered at the absolute plastic shear strain, ε_q^p of 0.2. For the loose clayey sand layer (Layer 4), a similar approach is used to find the peak undrained shear strength; however, a slightly higher value of sensitivity (~ 3.0) is used because the loose sand typically shows significant strain softening during undrained loading (Olson, 2001).

The lean clay (Layer 5) typically shows higher strength weakening. In fact, the fall cone tests on the remoulded lean clay show undrained shear strength ranging from 2.0 kPa to 10.0 kPa. Therefore, the strain-softening behaviour is modelled using a nonlinear curve similar to previous works (Dey et al., 2015; Wang et al., 2020). In the present study, the shear strength degradation curve is defined by an exponential function followed by a linear degradation up to the remoulded state of the lean clay. The detailed modeling technique is discussed elsewhere (Dey et al., 2015; Dey et al., 2016b; Wang et al., 2020). In FE analysis, the variation of the yield strength ($= 2s_u$) is defined as a function of plastic shear strain, which is calculated assuming $t = t_{FE}$, where t_{FE} is the thickness of the mesh.

Table 5.3. Summarization of soil parameters used in FE analysis

Layers	ϕ' (°)	ϕ_y (°)	s_{u0}/σ_v'	s_{u0}/s_{uR}	ε_q^p at s_{uR}	E_u (MPa)
Layer 1	32	25	0.46	-	-	10
Layer 2	36	30	0.58	2	0.2	50
Layer 3	34	30	0.58	2	0.2	30
Layer 4	32	25	0.46	3	0.2	20
Layer 5	30	25	0.46	5	-	15
Layer 6	33	-	-	-	-	15

The soil layer below the lean clay is compact clayey sand with higher strength parameters. Field investigations show that the failure has been initiated and propagated through the lean clay soil layer or the bottom part of the loose sand layer. For the modeling purpose, no post-peak softening is considered for the bottom layer. The soil parameters used in the FE analyses are summarized in Table 5.3. The analysis is carried out for undrained loading conditions. The undrained Young's Modulus (E_u) and undrained Poisson's ratio ($\nu_u = 0.495$) are used in the model.

5.6 Finite Element Results

The equivalent plastic shear strain (ε_q^p, which is PEEQVAVG in the software) is used to represent the strain localization and formation of shear bands. ε_q^p is a scalar quantity which is the integration of plastic deviatoric strain rate tensor ($\dot{\varepsilon}_{ij}^p$) over the period of analysis (i.e.,

$\int_0^t \sqrt{2/3\dot{\varepsilon}_{ij}^p \dot{\varepsilon}_{ij}^p} dt$). Note that ε_q^p is also related to the plastic shear strain in simple shear condition

(γ^p) as $\varepsilon_q^p = \gamma^p/\sqrt{3}$. Also, the simple shear strain is also related to plastic shear displacement (δ) as $\delta = \gamma^p/t_{FE}$, where t_{FE} is the thickness of the cubical element of the soil.

5.6.1 FE simulation results for the Rigaud Landslide

Initiation of failure and propagation of planes

Figures 5.13(a–g) show the development of plastic shear strain (ε_q^p) due to the pile jacking near the slope. Instead of simulating the whole driving process, the initial position of the pile (tip) is considered at 16.9 m depth with an inclination of 34° from the vertical. Figure 5.13(a) shows no plastic shear strain after the gravitational step, which implies that the slope is stable at this stage, in conformity with the high factor of safety (1.70) obviously obtained from a LE analysis. In the second step of loading, the pile is penetrated at a constant velocity ($v = 0.1$ m/s) to an inclined depth of 0.5 m. Figure 5.13(b) shows that the penetration causes the development of plastic shear strain, which propagates to the slope side and reaches the toe of the slope. The pile pushes the adjacent soil in the direction of the toe, causing the formation of a shear band. The failure is triggered when the slip circle reaches the toe. It should be noted that the slip surface passes through the interface between the two stratigraphic units identified from the pieozocone and field vane tests before reaching the toe.

In the next step, the rotation and translation of the pile head are allowed in the x and z directions so that the pile does not restrict the soil movement in this two-dimensional analysis. As the landslide has already been triggered, more plastic strains are accumulated at the toe, as shown in Fig. 5.13(c).
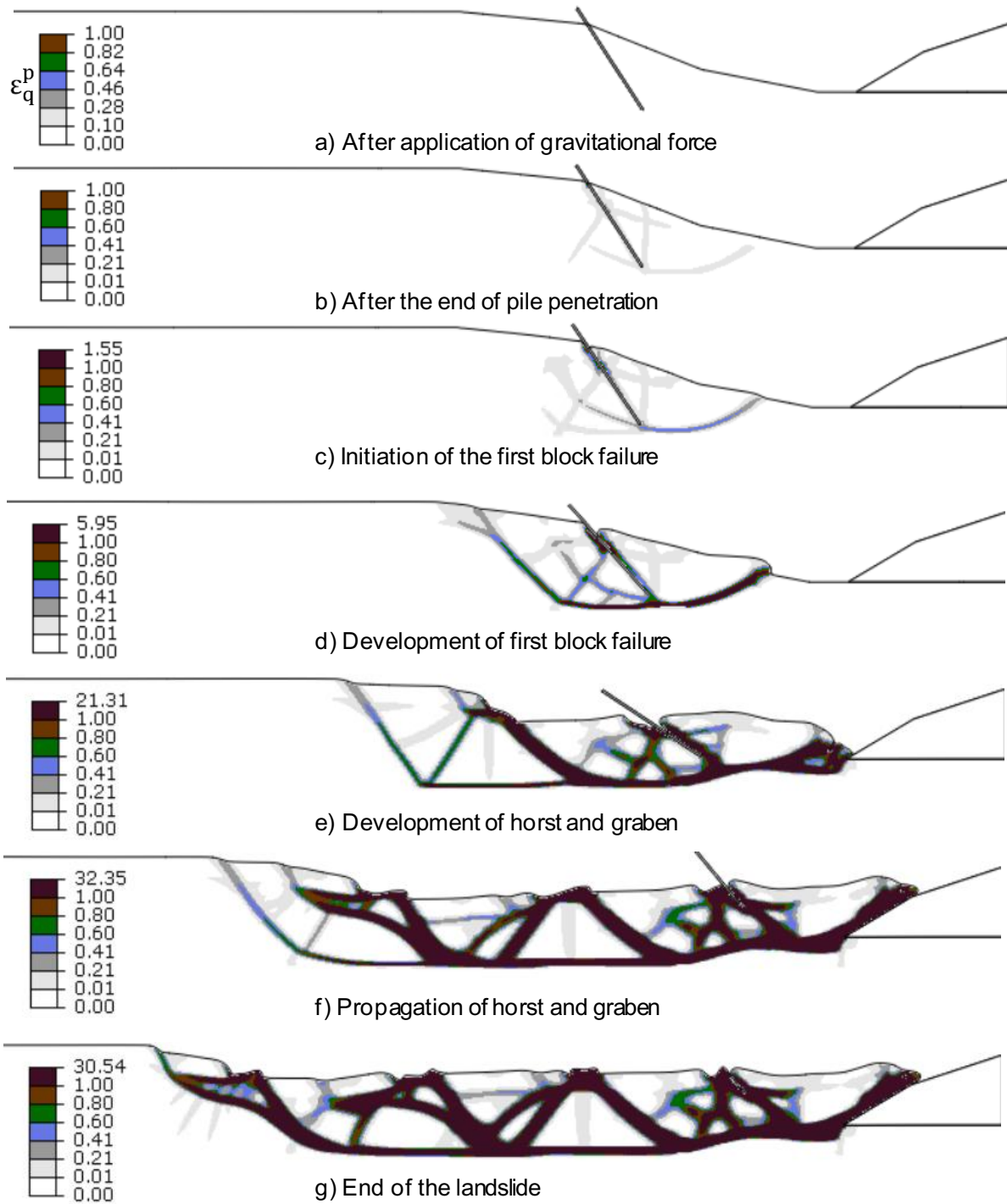
Fig. 5.13. Initiation and propagation of shear bands during pile installation and landslide

a) After application of gravitational force

b) After the end of pile penetration

c) Initiation of the first block failure

d) Development of first block failure

e) Development of horst and graben

f) Propagation of horst and graben

g) End of the landslide

ε_q^p

The failure of the first block during pile installation occurs by the combination of a curved shear band near the toe, a horizontal shear band ~ 20 m depth and an inclined shear band in the upslope area (Fig.5.13(d)). As the soil moves in the downslope direction (with the pile that does not provide any resistance), a number of shear bands form, creating horst and graben, as shown in Fig. 5.13(e). One important observation is that the failure block is at the location where the step increase in shear strength was found from field investigation (at $z = 20$ m in Fig. 5.4). Figure 5.13(f) shows the continuation of the propagation of the plastic shear strain. The propagation of the retrogression continues until it reaches a stable backscrap, as shown in Fig. 5.13(g).

Comparison with field observations

Carson & Lajoie (1979b) explained the Rigaud landslide as an earthflow, which is a result of retrogressive subsidence of wedges and translation of the residual prisms along a horizontal sliding surface. Carson (1979) used a schematic shown in Fig. 5.14(a) to explain the development and propagation of such horsts and grabens in a retrogressive landslide. The force exerted by the subsidence of the wedge is higher than the force on the face of the prism, which may lead to a subsequent sagging of the wedge and displacement of the prism. As the process continues, horsts and grabens form with a horizontal sliding surface. The extent of this subsidence becomes suddenly or gradually less than the threshold value to maintain the retrogression. The evolution of the retrogression stops at that point, as shown in Fig. 5.14(a). In the case of Rigaud landslides, the stabilization of the retrogression occurred quickly.

Figure 5.14(b) shows the formation of horsts and grabens due to the retrogressive failure in Rigaud landslides. The bottom sliding surface is found to be almost horizontal, which passes through the boundary of the stratified layer.
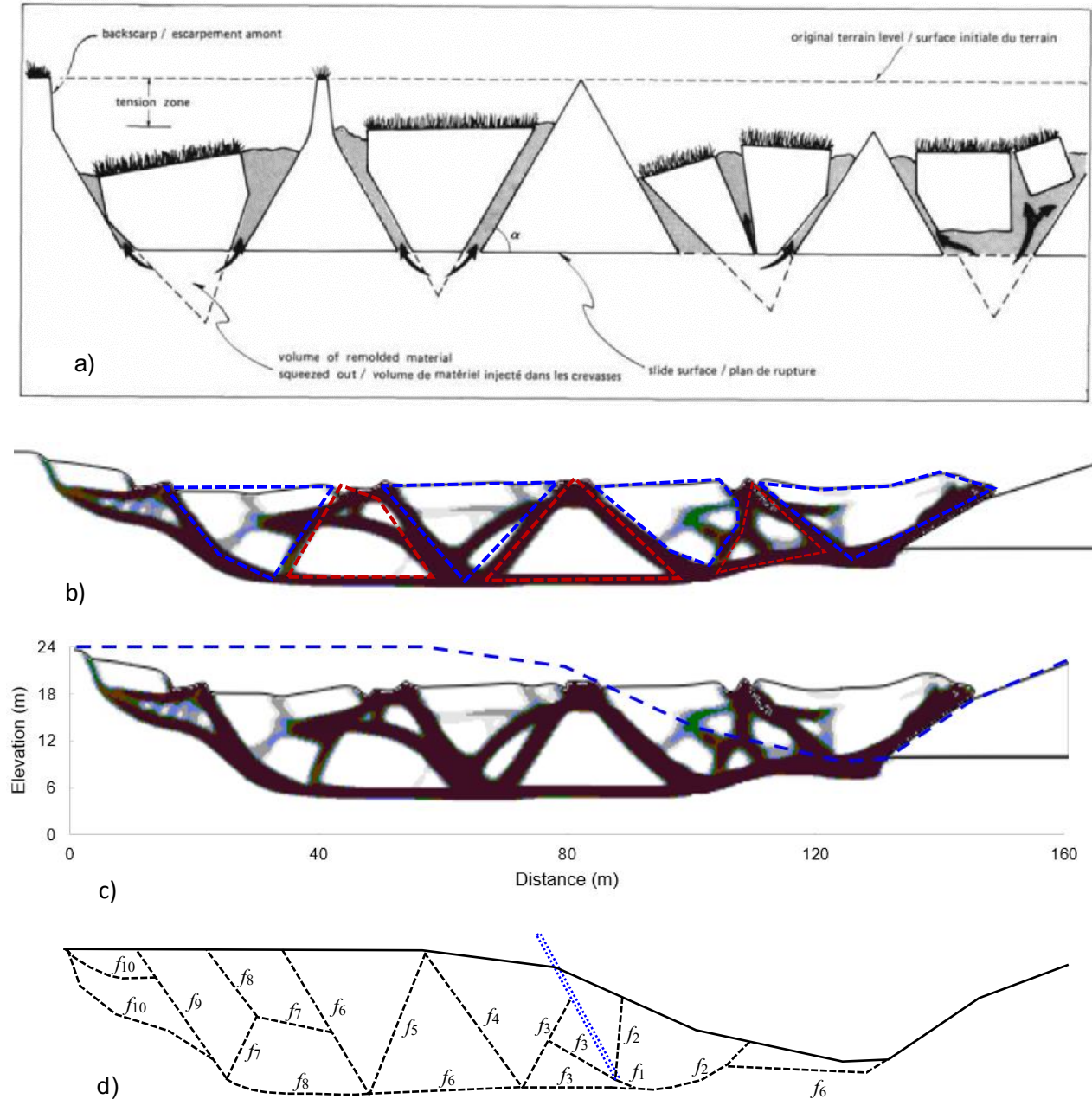
Fig. 5.14. Comparison with the field investigation: (a) schematic of earthflow (Carson, 1979b); (b–c) failure of soil blocks and translation; (d) sequence of shear band formation

From post-slide investigation, Carson (1979b) reported similar numbers of prism along the longitudinal section simulated in this study. Figure 5.2 shows the exposed parts of prisms, labelled

as 1 to 4, which also agrees well with the present FE model. Figure 5.14(c) shows the retrogression distance and the subsidence from the original ground surface. The FE calculated retrogression distance is 75-78 m, which is in good agreement with the field observation. Carson (1979a) also reported a 7–8 m high exposed backscrap and approximately at 45-75 m retrogression distance from the original slope edge.

Figure 5.14(d) shows the development of the failure plane after the pile is penetrated down to the specified depth. The first failure plane f_1 starts from the bottom of the pile and reaches the boundary of the stratified layer. It continues to propagate as f_2 and intersects the toe region, which is similar to a slip circle. A horizontal failure plane f_3 is developed simultaneously, and the first entire block failure is obtained. With a rightward movement of the first block, a horst is formed by developing the failure planes f_5 and f_6. The failure planes f_7, f_8 and f_9 are developed due to a combination of translational and rotational failures. Finally, the failure plane f_{10} is developed at a higher elevation, and the retrogression is stopped. At the end of the landslide, the debris climbs up approximately 10–12 m above the toe of the opposite bank. The global failure surface remains horizontal with the development of horsts and grabens. However, the depth of the final backscrap is 7-8 m, as reported by Carson (1979b). In summary, the present study could simulate the failure pattern, retrogression distance, and backscrap height similar to field observation.

Effects of sensitivity on the failure mechanisms

To show the effects of strain-softening, an analysis is performed with the same shear strength profile as before (i.e., SP-1 in Fig. 5.4); however, no post-peak shear strength degradation is given (i.e. non-sensitive). Figure 5.15(a) shows that very small plastic shear strains develop due to penetration of the pile, as compared to that calculated for sensitive clay (Fig. 5.13(b)). When the pile penetration is stopped and the constraints are released for free movement of the pile, as

discussed above, a small plastic shear strain generates only around the pile surface due to redistribution of stresses. Unlike the analysis with strain-softening, the plastic strain does not propagate further to initiate the failure of the slope. Therefore, it can be concluded that the presence of sensitivity played a vital role in the Rigaud landslide.

a) At the immediate end of pile penetration

b) After sometimes of the end of penetration
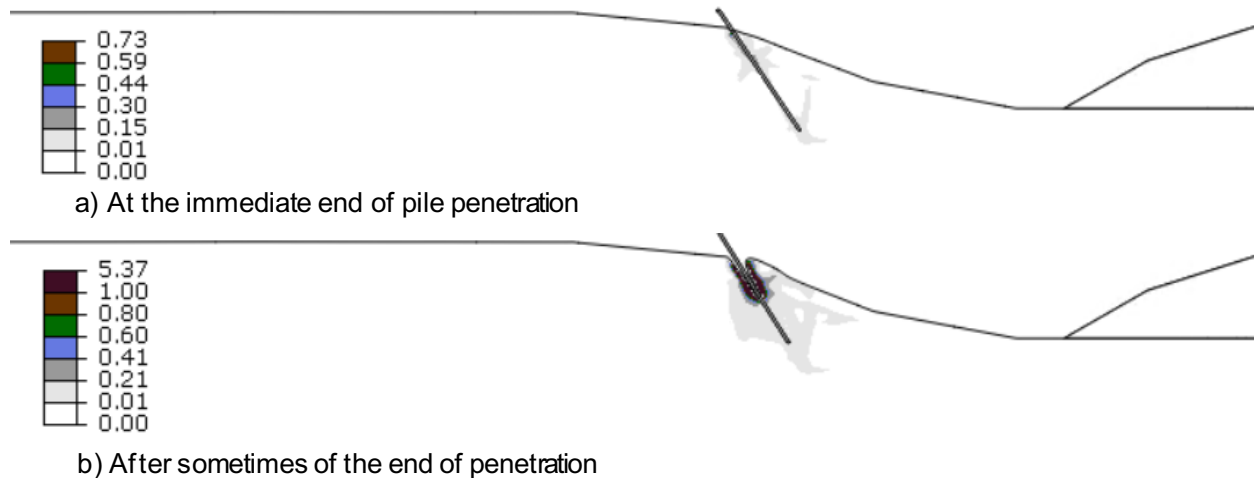
Fig. 5.15. FE modeling of the slope in Rigaud landslide with non-sensitive soil model

Effects of shear strength profiles

Figures 5.16(a–d) show the effects of peak undrained shear strength profile (SP-1, SP-2, SP-3 and SP-4 in Fig. 5.4) on the Rigaud landslide incident. Figure 5.16(a) shows the base case simulation results when s_{u0} increases from 45 kPa to 65 kPa at $z = 20$ m (Fig. 5.4). In the SP-2 profile, no step increase of s_{u0} is considered; instead, s_{u0} increases linearly at the same rate as the upper sensitive clay layer (i.e., the bottom layer is weaker than the previous case). The slope is still stable after the gravity step. However, due to the penetration of the pile, two deep-seated failure planes form (Figure 5.16(b)), which is entirely different from the failure pattern reported from the post-slide investigations. In other words, the shear strength profile, more specifically the

180

step-change in s_{u0} ~ 20 m depth, could be one of the main reasons for horizontal shear band propagation and the resulting failure pattern.
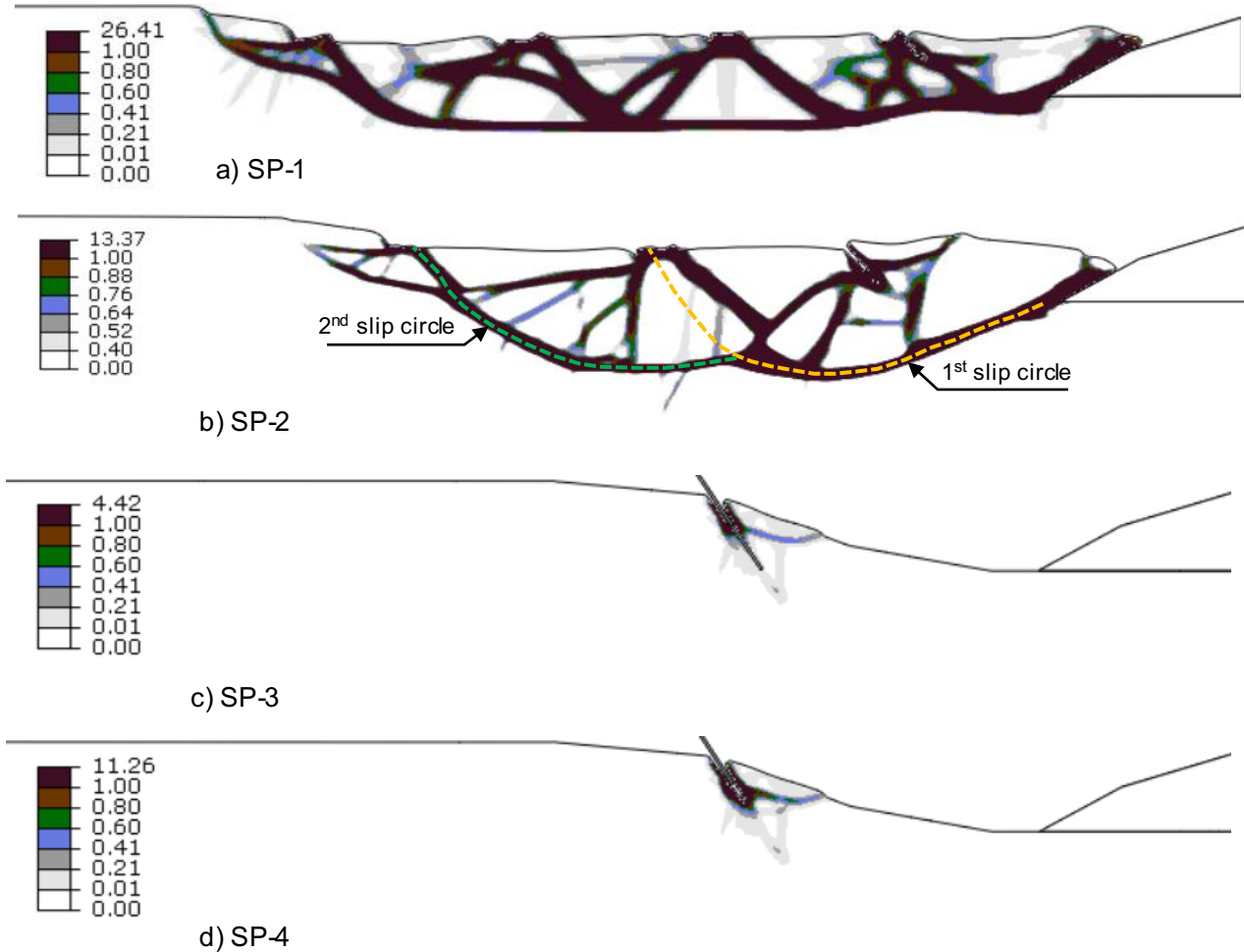
Fig. 5.16. Effects of shear profile on Rigaud landslide

No landslide is triggered due to the pile penetration for a higher strength profile (SP-3 in Fig. 5.4), as shown in Fig. 5.16(c). Also, when a slightly higher s_{u0} is used in the upper part of the sensitive clay layer (SP-4 in Fig. 5.4), a large retrogressive landslide does not occur, although a small local failure near the crest is observed. The slope remains stable due to the high strength

gradient is used in the present model. The analyses show the stratified layer presented in undrained strength gradient triggers the landslide in the Rigaud site. However, it is still difficult to consider the strength gradient as the only triggering mechanism for this landslide incident.

Effects of crust

Due to the long-term weathering process, the crust generally has a higher undrained shear strength profile (e.g., Perret et al., 2019). In general, modeling the crust is difficult because of the complex nature of the soil and drainage conditions under loading. The present study considers the undrained conditions for the crust. Peret et al. (2019) investigated the case of 37 large retrogressive landslides and found that the presence of crust does not control the occurrence of spreads and flows. However, the present study intends to find whether crust behaviour has any influence on the retrogressive distance and failure pattern. All the analyses are performed with the SP-1 s_{u0} profile (Fig. 5.4) and the soil parameters for the base case (Table 5.2) except for the parameters mentioned below. It should be emphasized that the experimental evidence does not indicate that a clay crust could exhibit strain-softening behaviour (e.g., Lefebvre et al. 1987). These parametric analyzes are only carried out to highlight the fact that the mechanical properties of the clay crust do have an impact on the regression process.

Figure 5.17(a) shows the end of retrogression for the surficial crust having a sensitivity, s_{u0}/s_{uR} = 1.50 and Figure 5.17(b) shows the landslide for the crust having no softening. Both figures show a similar pattern of failure at the beginning of the landslide. Due to the presence of non-sensitive behaviour of crust in the second case (Fig. 5.17(b)), the depth of failure reduces relatively at a smaller retrogression distance, as shown in Fig. 5.17(b), although the extent of the landslide is almost the same in both cases. Hence, the presence of strain-softening in the surficial crust might control the depth of failure when a large retrogression has already occurred in the landslide zone.

In Fig 5.17(c), no surficial crust is considered, and a higher retrogression distance is found. The surficial crust may provide higher resistance to the propagation of the failure and might change the failure mechanisms during the retrogression.
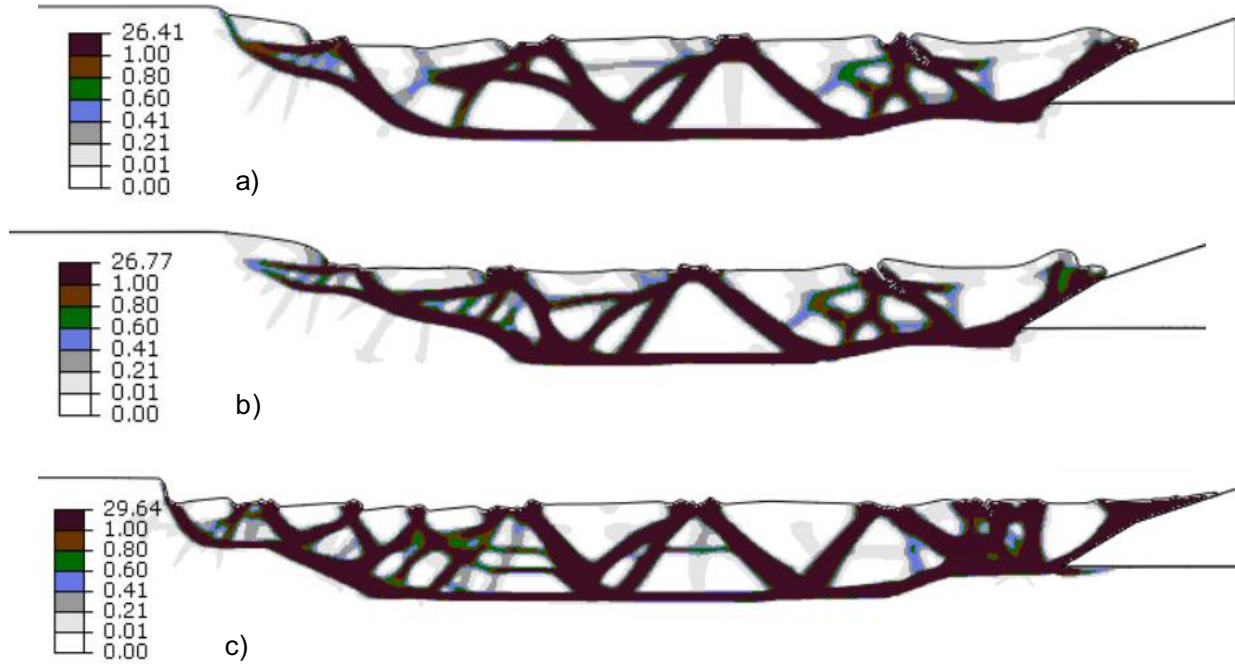
Fig. 5.17. Effects of the behaviour of the surficial crust

Effects of post-peak strength degradation rate (δ_{95} and s_{u0}/s_{uR})

The rate of post-peak strength degradation depends on s_{u0}/s_{uR}, δ_{95} and δ_{ld} (Eq. (3.2) in Chapter 3). Figure 5.18(a) shows that a faster rate of post-peak shear strength degradation with $\delta_{95} = 0.05$ m causes a spread failure with a retrogression distance of 120 m from the crest of the slope; however, the retrogression distance is only 80 m for a slower rate of shear strength degradation with $\delta_{95} = 0.1$ m (Fig. 5.18(b)). No failure is triggered for a high value of δ_{95} (= 0.4 m) (Fig. 5.18(c)).

Again, no landslide is triggered for a low sensitive clay (Fig. 5.18(d)). However, a large landslide occurs for $s_{u0}/s_{uR} = 5$, as shown in Fig. 5.18(b). For high sensitivity, the shear strength degrades rapidly, resulting in larger landslides, as shown in Figs. 5.18(e−f). In summary, the rate of shear strength degradation plays a major role in landslides in sensitive clays.
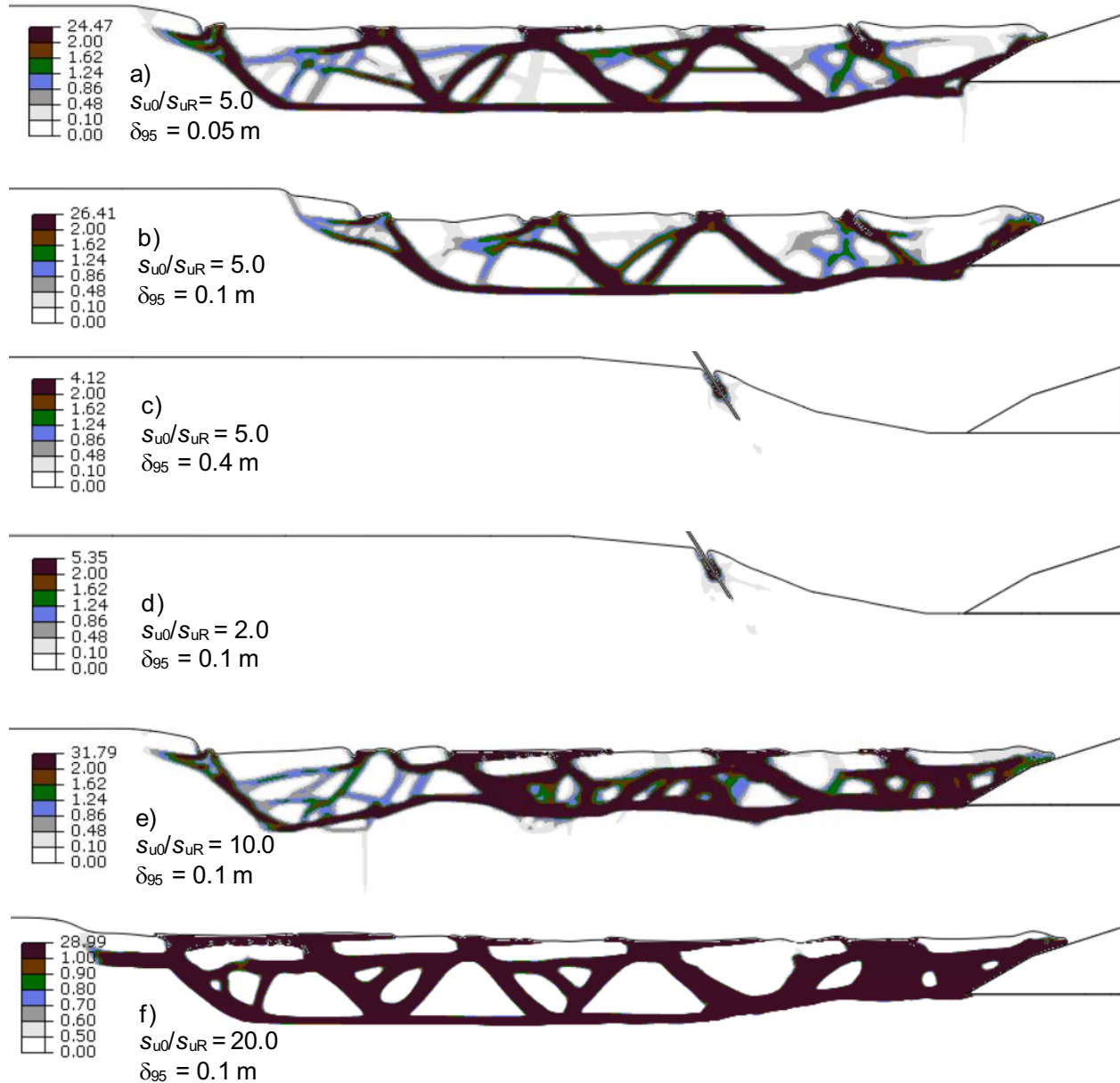
Fig. 5.18. Progressive failure for various post-peak strength degradation parameters (s_{u0}/s_{uR} & δ_{95})

5.6.2 FE results for the Daniel's Harbour landslide

Plastic shear strain initiation and propagation

Figures 5.19(a–h) show the initiation of the failure and subsequent propagation of failure planes. The slope is stable at the end of the gravity load (Fig. 5.19(a)). Plastic shear strains develop in the soil from the weak zone when the strength in this zone is reduced, which triggers the landslide (Fig. 5.19(b)). Once the landslide is triggered, the undrained shear strength of lean clay in layer 5 starts to reduce due to strain softening, and a horizontal shear band forms (Fig. 5.19(c)).

With the downslope movement of the soil, the shear band propagates further and, at one stage, a curved shear band forms that reach the ground surface, which results in failure of a large soil block (Fig. 5.19(d)). With further movement, the failed soil block breaks into small pieces by the formation of additional failure planes (Figs. 5.19(d)–(f)). Large plastic shear strain generates in the shear band through the lean clay that brings the soil to the remoulded shear strength. Therefore, the failed soil block might move at high speed. With the further displacement of the debris, the height of the back scarp increases (Fig. 5.19(f)), and, at one stage, the second block of soil fails (Fig. 5.19(g)). Finally, the movement of the debris is stopped after a large displacement of the debris.

The field observation confirms the failure of two large soil blocks. The reports also mention that the failure was a combination of translational slip failure and rotational slip failure. Although the report indicated that reducing the cohesion in the lean clay layer might create a fracture along with the vertical faces, resulting in collapse blocks, it is difficult to model that phenomenon in CEL. Still, the present model can provide a good representation of the Daniel's Harbour landslide. Also, there was a time lag between the failure of the first and second block; however, that process is not simulated in this study.
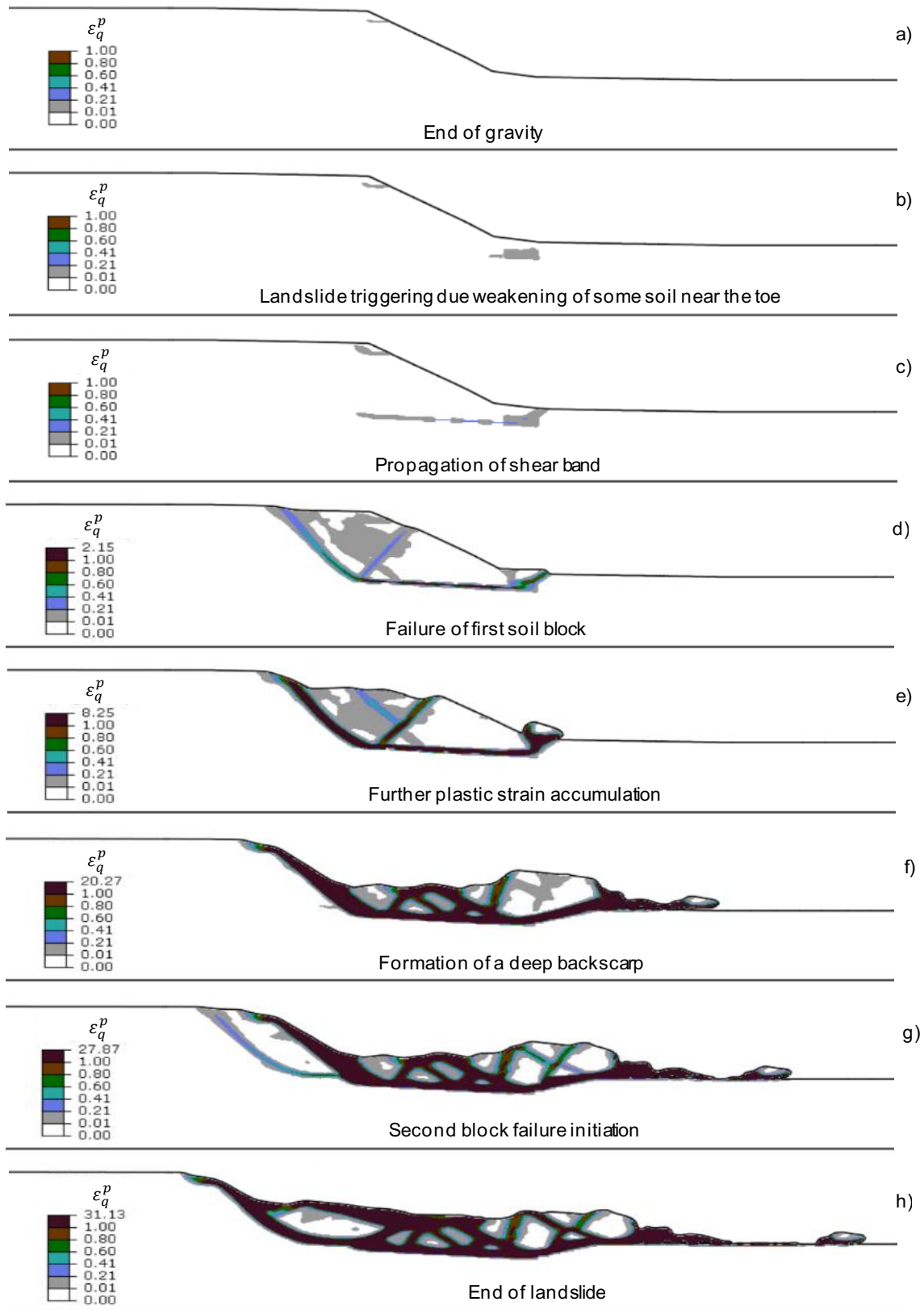
Fig. 5.19. Initiation and propagation of failures

Velocity vectors of the failed soil mass

Figures 5.20(a)–(c) show the velocity vectors of the soil elements during the landslide. In Fig. 5.20(a), the soil starts to move from the toe as the triggering condition is applied through a weak zone near the toe. As soon as the global failure occurs, the failed soil block starts to move in the downslope direction as a rotational slide (Fig. 5.20(b)). As the failed soil block moves further downslope, it translates almost horizontally. The rotational failure of the second soil block occurs when the debris of the first block becomes partially or fully remoulded, which flows almost horizontally (Fig. 5.20(c)). The mild slope on the right side of the toe also facilitated the movement of the debris. In summary, Figs. 5.19 and 5.20 show that the failure involved both rotational and translational failures, similar to the pattern reported from field investigations.

Comparison with field investigations

Field investigations were carried out after the landslide events in April 2007. Fig. 5.6 shows the affected area due to the April 2007 landslide, which has been developed based on the field investigation carried out in 2008. The present study simulated the landslide considering the cross-section of profile #6 in Fig. 5.6 (blue dashed line). The deformed shape ground observed in the 2008 field investigation is shown in Fig. 5.21 (red dashed line). The retrogression distance, measured from the crest of the slope, is 55 m in the FE analysis. The field investigations found the distance is about 60 m inland from the crest after the two landslide events in October 2006 and April 2007. Approximately 15 to 20 m almost vertical faces were found immediately after April 2007 landslide, and the debris was a combination of remoulded soils with several intact soil blocks and the remnants of buildings. FE simulation also shows some intact soil blocks which were generated by the formation of shear bands during movement; however, the present FE analysis cannot simulate such a steep backscarp.
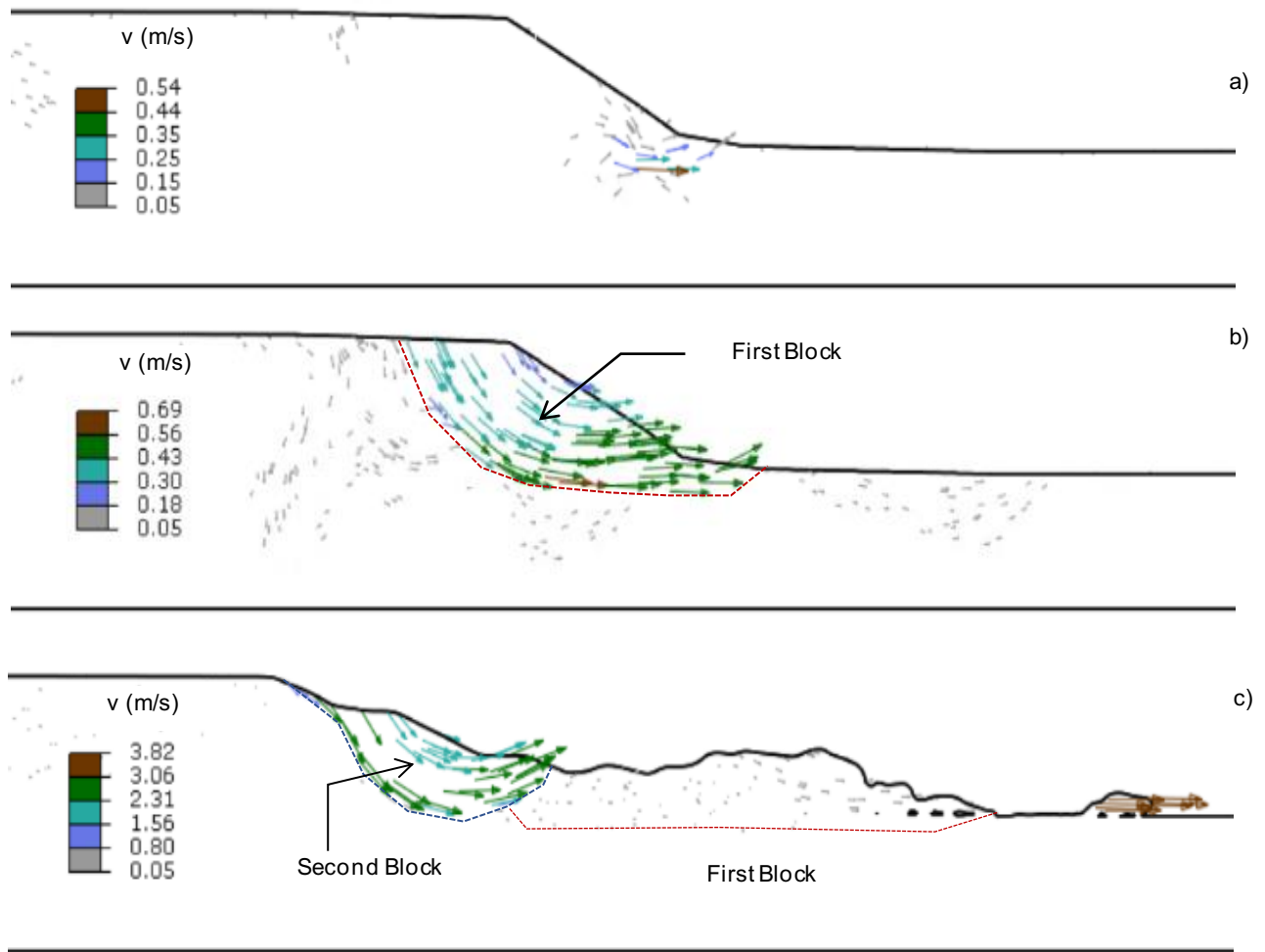
Fig. 5.20. Representation of velocity vectors (m/s) during soil movements

During the field investigation in 2008, the profile of the existing ground surface shows that coastal erosion might remove the failed soil from the downstream. Kilfoil et al. (2018) indicate that the coastal erosion of the unconsolidated sediments along the west of the Great Northern Peninsula has been ongoing for decades. However, in both field observations and numerical analyses, the slopes retrogress to a stable slope with grades on the order of 2.5H:1V to 3.0H:1V
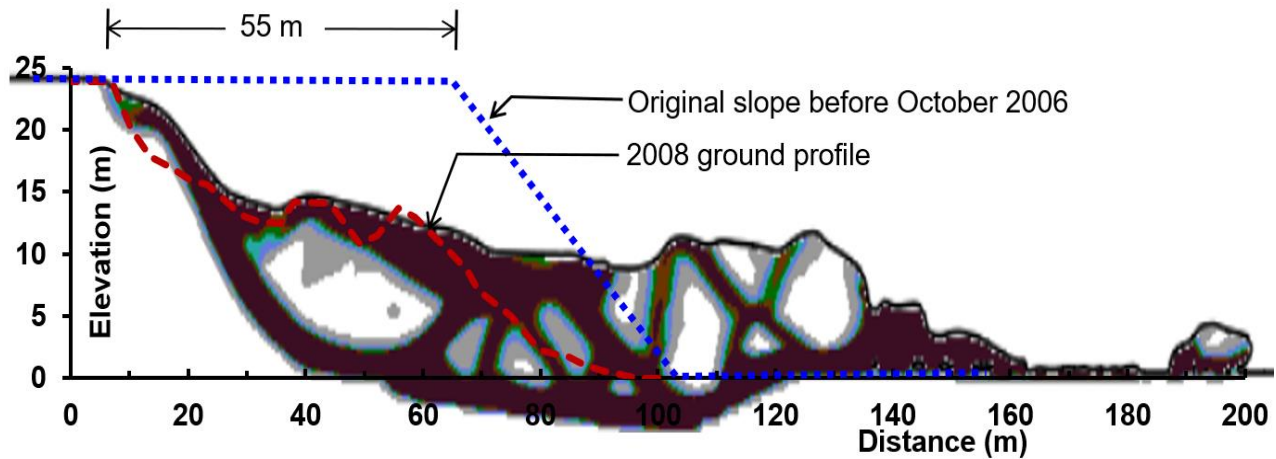
Fig. 5.21. Comparison of FE modeling with field investigation taken in 2008

5.7 Conclusions

Several case studies show slope failure due to pile driving, and, in some cases, large landslides occurred, especially in sensitive clays. Retrogressive landslides in strain-softening materials are triggered not only by pile driving but also by several other factors, such as toe erosion. The present study explains the 1978 Rigaud landslide in sensitive clays, which was triggered by pile driving, though updated field investigation results and large deformation finite element simulations. A comparison of failure patterns of Rigaud landslide with Daniel's Harbour landslide shows that, although different strain-softening materials were involved and the landslide triggering mechanisms were different, the undrained retrogressive failures could be explained by similar modeling techniques.

Since the occurrence of the Rigaud landslide, three expert groups conducted field investigations and numerical analyses to understand the potential causes and failure mechanisms. All of them identified a long horizontal failure plane approximately 5 m below the toe, and the formation of horsts and grabens, as commonly observed in a spread. The 1979 expert committee indicated the

presence of thin sand or silt layers at this depth and hypothesized that the dynamically induced liquefaction of this soil caused the horizontal failure. On the contrary, GSC in 2002 and MTQ in 2015 could not find such sand or silty layers even after taking an X-ray using CAT-Scan of the Shelby samples. Instead, they found that the horizontal failure plane passes through two different stratigraphic units. Consequently, the explanation of the failure by the liquefaction of a cohesionless layer can be questioned. However, it might be possible that a spatially discontinuous cohesionless layer or pockets of cohesionless soils, which were not found in the 2002 and 2016 site investigations, liquefied, resulting in the initiation of the retrogression process. The Eulerian-based finite element simulations performed in this study have shown that another mechanism can be invoked. The shear strains generated by pile driving (or simply by pushing a pile) and the resulting increase in pore pressure may have been the true cause of the failure initiation. The subsequent development of horsts and grabens can be easily explained by the typical strain-softening behaviour of the sensitive clays mobilized by the landslide.

The present study develops an Eulerian-based finite element modeling technique to investigate the potential mechanisms involved in the Rigaud landslide. Simulating the penetration of a pile, it is shown that the boundary between two stratigraphic units in the soil profile controlled the location of the failure surface. When the pile reaches close to the boundary between two soil layers, a horizontal shear band forms at the boundary and triggers the failure. As the strain-softening behaviour of soil is incorporated, the shear band propagates progressively, which cannot be modelled using the limit equilibrium methods, as used previously (e.g. the 1979 Expert Committee). Once the failure is triggered, horst and graben form in numerical simulations, which is similar to that observed in the field.

The Daniel's Harbour landslide involves a thinner, highly strain-softening material approximately at the toe level, and the failure occurred due to toe erosion and weakening of some soil near the toe. Considering the strain-softening behaviour of soil in the present FE models, the failure pattern observed in the field could be reasonably modelled, which could not be found from limit equilibrium analyses.

Finally, it is to be noted that the initiation of failure might be more complex than the idealized conditions considered in this study. The authors understand the pile driving process in the Rigaud site might be three-dimensional in nature, which is not simulated in the present study because of the huge computational costs. Also, the pile is considered at a particular depth as a wished-in-place condition to minimize the computational costs. The Daniel's Harbour landslide occurred in two different phases; that means the failure was very likely a time-dependent process, which is not simulated. This study primarily focused on rapid failure after triggering. Also, the soil parameters, especially the parameters required for strain-softening, were estimated based on some typical values. Further studies are required to address these issues.

Acknowledgement

Notations

β	soil parameter for strain-rate relation
δ	accumulated plastic shear displacement
δ_{95}	δ at which s_u reduced by 95% of $(s_{u0} - s_{uR})$
δ_{ld}	δ at large shear displacement
ε_q^p	equivalent plastic shear strain
$\dot{\varepsilon}_{ij}^p$	plastic deviatoric strain rate tensor
γ	total unit weight
$\dot{\gamma}_{ref}$	reference strain rate
γ^p	accumulated plastic shear strain
η	soil parameter for strain-rate relation
ν_u	undrained Poisson's ratio
σ_v'	vertical effective stress
τ_{max}	equivalent interface shear stress limit
ϕ_y	angle of failure plane
ϕ'	drained angle of friction
c'	drained cohesion
D	pile outer diameter
dt	Time increment
E_u	undrained Young's modulus
FS	factor of safety
LI	liquidity index

LL	liquid limit
PL	plastic limit
s_u	mobilized undrained shear strength
s_{u0}	initial (peak) undrained shear strength
s_{uld}	undrained shear strength at large displacment
s_{uR}	remoulded s_u at large plastic shear displacement
t_{FE}	thickness of the FE element
v_x	the component of velocity in x-direction
v_y	the component of velocity in y-direction
v_z	the component of velocity in z-direction
w	natural water content

References

Batterson, M. & Liverman, D. (2010). Past and Future Sea-Level Change in Newfoundland and Labrador: Guidelines for Policy and Planning. *Current research (2010) Newfoundland and Labrador Department of Natural Resources, Geological Survey* **10**, No. 1, 129–141.

Blais-Stevens, A., Behnia, P., and Castagner, A. (2018). Historical landslides that have resulted in fatalities in Canada (1771–2018). Geological Survey of Canada, Open File Report 8392, map poster.

Carson, M. A. (1977). On the Retrogression of Landslides in Sensitive Muddy Sediments. *Canadian Geotechnical Journal* **14**, No. 4, 582–602.

Carson, M. A. (1979a). On the retrogression of landslides in sensitive muddy sediments: Reply. *Canadian Geotechnical Journal* **16**, 431–444.

Carson, M. A. (1979b). Le glissement de Rigaud (Québec) du 3 mai 1978: une interprétation du mode de rupture d'après la morphologie de la cicatrice. Géographie physique et Quaternaire **33**, No. 1, 63–92.

Carson, M. A. & Lajoie, G. (1981). Some constraints on the severity of landslide penetration in sensitive deposits. *Géographie physique et Quaternaire* **35**, No. 3, 301–316.

Chagnon, J.-Y., Dascal, O., La Rochelle, P., and Lefebvre, G. (1979). Ligne Chateaugay-Chenier, glissement de terrain au site du pylône 83. Rapport du comité d'experts, Hydro-Québec, Direction Projets de lignes de transports, Direction construction de lignes. 64 p. + maps.

Demers, D., Robitaille, D., Locat, P. & Potvin., J. (2014). Inventory of large landslides in sensitive clays in the province of Quebec, Canada: preliminary analysis. *Natural hazards book: advances in natural and technological hazards research*, ISSN, 1878–9897.

Dey, R., Hawlader, B., Phillips, R. & Soga, K. 2015. Large Deformation Finite-Element Modeling of Progressive Failure Leading to Spread in Sensitive Clay Slopes. *Géotechnique* **65**, No. 8, 657–668.

Dey, R., Hawlader, B., Phillips, R. & Soga, K. (2016a). Numerical Modeling of Combined Effects of Upward and Downward Propagation of Shear Bands on Stability of Slopes with Sensitive Clay. *International Journal for Numerical and Analytical Methods in Geomechanics* **40**, No. 15, 2076–2099.

Dey, R., Hawlader, B., Phillips, R. & Soga, K. (2016b). Modeling of Large-Deformation Behaviour of Marine Sensitive Clays and its Application to Submarine Slope Stability Analysis. *Canadian Geotechnical Journal* **53**, No. 7, 1138–1155.

Eden, W.J. (1956). The Hawkesbury landslide. National Research Council of Canada, Division of Building Research, Ottawa, Canada, 14 p.

Froese, C. R. & Cruden, D. M. (2001). Landslide in weakly cemented glaciolacustrine sediments, Morkill River valley, British Columbia. *Can. Geotech. J.* **38**, 889–900.

Gu, W. H., Morgenstern, N. R. & Robertson, P. K. (1993). Progressive Failure of Lower San Fernando Dam. *Journal of Geotechnical Engineering* **119**, No. 2, 333–349.

Karmaker, R. & Hawlader, B. (2018). Modeling of Pile Stabilized Clay Slopes Using a Large Deformation Finite-Element Method. *7th Canadian Geohazards Conference,* paper no-155.

Kilfoil, G., Blagdon, A., Leitch, A., Campbell, H., Irvine, M., Batterson, M., Roberts, G. & Baker, B. (2018). The Application and Testing of Two Geophysical Methods (Direct-Current Resistivity and Ground Penetrating Radar) as Part of the Coastal Monitoring Program to Assess Terrain Stability. *Current research (2018) Newfoundland and Labrador Department of Natural Resources, Geological Survey* **18**, No. 1, 31–57.

L'Heureux, J. S., Locat, A., Leroueil, S., Demers, D. & Locat, J. (2014). Landslides in sensitive clays: from geosciences to risk management. *Advances in natural and technological hazards research 36. Springer*, Dordrecht.

Lade, P. V. (1978). Prediction of Undrained Behaviour of Sand. *Journal of the Geotechnical Engineering Division* **104**, No. 6, 721–735.

Lefebvre, G., Paré, J.J., and Dascal, O. 1987. Undrained shear strength in the surficial weathered crust. *Canadian Geotechnical Journal* **24**, 23–34.

Leroueil, S. and Hight, D. W. (2003). Behaviour and Properties of Natural Soils and Soft Rocks, *Characterization and Engineering properties of natural soils – Tan et al. (eds.)*, Swets & Zeitlinger, Lisse.

Locat, A., Jostad, H. P. & Leroueil, S. (2013). Numerical modeling of progressive failure and its implications for spreads in sensitive clays. *Canadian Geotechnical Journal* **50**, No. 9, 961–978.

Locat A., Leroueil S. & Jostad H. P. (2014). Failure Mechanism of Spreads in Sensitive Clays. In: L'Heureux JS., Locat A., Leroueil S., Demers D., Locat J. (eds) *Landslides in Sensitive Clays. Advances in Natural and Technological Hazards Research* **36**, 279–290.

Locat, A., Leroueil, S., Fortin, A., Demers, D. & Jostad, H.P. (2015). The 1994 landslide at Sainte-Monique, Quebec: geotechnical investigation and application of progressive failure analysis. *Canadian Geotechnical Journal* **52**, No. 4, 490–504.

Luther, M. (2013). Coastal Erosion in Daniel's Harbour, *Journal of Undergraduate Engineering Research and Scholarship*, Faculty of Engineering and Applied Science, Memorial University of Newfoundland, Paper Code- PT-13-Luther.

Odenstad, S. (1951). The landslide at Sköttorp on the Lidan River, February 2, 1946. *Royal Swedish Institute Proceedings* **4**, 1–38.

Olson, S. M. (2001). Liquefaction Analysis of Level and Sloping Ground Using Field Case Histories and Penetration Resistance, *Ph.D. Thesis*, University of Illinois, Urbana-Champaign, USA.

Perret, D., Therrien, J., LOcat, P. & Demers, D. (2019). Influence of surficial crusts on the development of spreads and flows in Eastern Canadian sensitive clays. *72nd Canadian Geotechnical Conference*, St. John's, NL

Potts, D., Kovacevic, N. & Vaughan, P. (1997). Delayed collapse of cut slopes in stiff clay. *Géotechnique* **47**, No. 5, 953–982.

Proudfoot, D. N. & St. Croix, L. (2001). Landforms and Surficial Geology of the Portland Creek Map Sheet (NTS 12I/04), *Newfoundland Department of Mines and Energy, Geological Survey*, Map 2001-33, Open File 012I/04/255.

Qui, G., Henke, S. & Grabe, J. (2011). Application of a Coupled Eulerian-Lagrangian Approach on Geomechanical Problems Involving Large Deformations. *Computers and Geotechnics* **38**, 30–39.

Quinn, P. (2009). Large Landslides in Sensitive Clay in Eastern Canada and the Associated Hazard and Risk to Linear Infrastructure. *Ph.D. thesis*, Queen's University, Kingston, Ontario, Canada.

Quinn, P. E., Diederichs, M. S., Rowe, R. K. & Hutchinson, D. J. (2011). A new model for large landslides in sensitive clay using a fracture mechanics approach. *Canadian Geotechnical Journal* **48**, No. 8, 1151–1162.

Shen, S. L., Han, J., Zhu, H. H. & Hong, Z. S. (2005). Evaluation of a Dike Damaged by Pile Driving in Soft Clay. *Journal of Performance of Constructed Facilities* **19**, No. 4, 300–307.

Silvestri, V., Karam, G., Tonthat, A. & St-Amour, Y. (1989). Direct and simple shear testing of two Canadian sensitive clays. *Geotechnical Testing Journal* **12**, No. 1, 11–21.

Spooner, I., Batterson, M., Catto, N., Liverman, D., Broster, B.E., Isenor, F. & McAskill, G.W. (2013). Slope Failure Hazard in Canada's Atlantic Provinces: a Review. *Atlantic Geology* **49**, 1–14.

Tavenas, F., Flon, P. & Lerouil, S. (1983). Remolding energy and risk of slide retrogression in sensitive clays. *In proceedings of the symposium slopes on soft clays*, Linköping, Sweden, 423–454.

Thakur, V., Degago, S.A., Oset, F., Dolva, B.K., Aabøe, R., Aunaas, K., Nyheim, T., Lyche, E., Jensen, O.A., Viklund, M., Sæter, M.B., Robsrud, A., Nigguise, D. & L'Heureux, J.S. (2014). Characterization of post-failure movements of landslides in soft sensitive clays. *Natural hazards book: advances in natural and technological hazards research*, ISSN: 1878–9897.

Wang, C., Hawlader, B., Perret, D. & Soga, K. (2020). Effects of Geometry and Soil Properties on Type and Retrogression of Landslides in Sensitive Clays. *Géotechnique*, 1–15.

Whitford, J. (2006). Geotechnical Consultation: Daniel's Harbour Landslide Assessment. *Report 1018871*.

Whitford, J. (2008). Phase I Geotechnical Assessment Daniel's Harbour Landslide. *Report 1043400*.

Chapter 6

Large deformation finite element modeling of slope stabilization and soil–pile interaction due to movement of a sliding block

Co-Authorship: This chapter has been submitted as a technical paper for publication in a journal as: Karmaker, R., Hawlader, B., Perret, D. and Dey, R., 'Large deformation finite element modeling of slope stabilization and soil–pile interaction due to movement of a sliding block.' Most of the research presented in this chapter has been conducted by the first author. He also prepared the draft manuscript. The other authors mainly supervised the research and reviewed the manuscript.

6.1 Abstract

Slope stabilization using passive piles is an effective and popular solution for both onshore and nearshore environments. The limit equilibrium (LE) method is commonly used for the stability analysis of slopes. However, this method of analysis cannot calculate the stress and deformation of a pile–soil system properly. The finite-element (FE) method could be used to overcome some of these limitations. The present study uses a Coupled Eulerian-Lagrangian approach to model pile stabilized clay slopes for undrained loading conditions. The strength reduction method is used to trigger the failure of the slope. The progressive formation of failure planes, large deformation of the failed soil mass, and soil flow between the piles are examined. The increase in factor of safety by a row of piles at the middle of the slope is presented. Piles might be subjected to passive loading from permanent ground deformations. The present study also investigates the lateral force on a pile resulting from a downslope displacement of a sliding clay layer. Finite-element (FE) analyses

are performed to calculate the total force on the pile due to the movements of a sliding clay layer. Analyses are performed for a single row of piles with varying centre-to-centre spacing and undrained shear strength of clay. The FE results show that the pile behaves as a single pile when the spacing is greater than five times its diameter. The arching effects in relation to pile spacing are discussed. The lateral force per pile decreases with a decrease in pile spacing. Using the calculated maximum lateral force, a separate analysis is performed to examine the structural response of a long pile installed through the liquefied layer on a stable soil layer.

6.2 Introduction

Piles are used to stabilize marginally stable slopes in onshore and nearshore environments. Unlike typical laterally loaded pile foundations, where the lateral load comes to the pile head and then transfers to the soil (active piles), the piles used for slope stabilization are considered passive piles because the lateral load comes from soil displacements. In the design of piles for slope stabilization, two key questions are:

(i)   For a given configuration (pile spacing, size and location), how much will the factor of safety (*FS*) be increased by the piles; and

(ii)   How much soil load will come to the piles, which is required to calculate the length and diameter and selection of pile type.

Piles can be subjected to two different types of lateral loads. In the active pile loadings, the lateral forces, which might come from superstructures, create a load on the pile and then transfer this load to the surrounding soil through pile–soil interaction. In this case, the soil surrounding the pile provides resistance to the movement of the pile. In passive piles, the displacement of a layer/block of soil near the ground surface creates a load on the pile, which is then transferred to the deeper soil layers through pile–soil interaction (Fig. 6.1). The failed mass could create a huge

load on the installed single pile or the pile groups that might cause structural damages to the piles. On the other hand, the ground deformation could be caused by slope failure, lateral spreading due to the formation of a weak failure plane or liquefaction of loose sand layer(s) due to an earthquake. In many cases, a non-liquefied soil layer above the liquefied sand layer/weak zone displaces a significantly large distance (Fig. 6.1(b)), especially in a slopping ground condition, even for a mild slope. For example, Cubrinovski et al. (2009) reported permanent lateral ground displacements of up to 4 m in some mild-sloped areas after the 1995 Kobe earthquake. The displacement of soil caused significant damage to piles in those areas. The upper sliding layer could be cohesionless, cohesive, or c-ϕ soil.
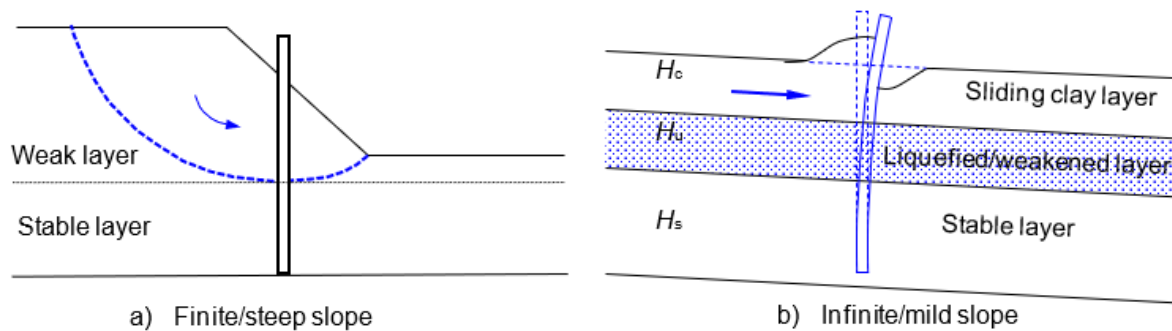
Fig. 6.1. Downslope soil movement effects on the pile in finite and infinite slopes

In the current design practice, the following three steps are followed: (i) calculate the additional resistive force required to achieve the desired factor of safety (*FS*), (ii) estimate the resisting force a pile can provide to resist the movement of the soil mass above the potential failure plane, and (iii) select appropriate type and size of the pile and also the location along the slope.

Proper estimation of force on the pile is difficult because it results from a complex process of soil displacement and even squeezing through the space between the piles. Empirical, analytical and numerical techniques have been used to estimate the lateral force on a pile. Among them, the

modulus of subgrade reaction method (e.g., Chow, 1996; Ashour et al., 1998; Kourloulis et al., 2012) is a very simple one for industry practice. However, appropriate judgement is required to estimate this parameter. For clays, the ultimate resistance per metre length of a single lateral loaded pile (p_u) can be related to the undrained shear strength of clay ($s_{u(in)}$) as $p_u = N_p s_{u(in)} D$, where D is the diameter of the pile and N_p is constant, which could vary between 9 and 12 (Matlock, 1970) and also could vary with depth (Poulos, 1995). Randolph & Houlsby (1984) developed a closed-form solution for a single pile where the clay was modelled as an isotropic rigid-plastic Tresca material. It has been shown that $N_p = 9.14$ and $N_p = 11.94$ for the fully smooth and perfectly rough pile–soil interface condition, respectively. Ito & Matsui (1975) proposed a theoretical solution to calculate the lateral force acting on rigid slope stabilizing piles that could squeeze the soil between the piles.

Physical and numerical modeling has been performed in the past to understand the response of piles in clay under active lateral loadings. For example, Welch & Reese (1972) and Matlock (1970) presented the response of instrumented piles under lateral loadings. Based on field test results, lateral load per unit length (p) versus displacement (y) curves have been developed to calculate the structural response of the pile. Centrifuge tests were also conducted to model the lateral pile–soil interaction (e.g., McVay et al., 1998; Taghavi et al., 2016). Conducting small-scale physical model tests, Bauer et al. (2014) showed a wide variation in the lateral force when a kaolin clay block interacts with a single pile or rows of piles. A summary of available model tests and various recommendations for the estimation of the normalized lateral force is available in Bauer et al. (2014).

Numerical techniques, such as finite element and finite difference, have also been used for improved pile–soil interaction modeling. Rowe & Poulos (1979) conducted a finite-element

analysis to investigate undrained pile–soil interaction with an idealized plane strain conditions of the three-dimensional problem. Oakland & Chameau (1986) conducted elastic finite-element analysis for pile stabilized surcharged slopes. Kourkoulis et al. (2012) proposed a hybrid method for analyzing and designing slope stabilizing piles. They decoupled the problem and calculated the lateral force on the pile by conducting a finite-element simulation where an upper soil block slides along a predefined horizontal slip surface over a stable soil block. Three-dimensional FE analyses have also been performed to calculate the load on the pile on the sloping ground (Cai & Ugai, 2000; Won et al., 2005; Ho, 2015). In these analyses, the "strength reduction" method is used to trigger the failure of the slope. In addition, a boundary-element method has been used to calculate the increase in *FS* and to develop simplified methods for the analysis and design of pile stabilized slopes.

The above FE modeling has been conducted using Lagrangian-based finite-element methods. It has also been recognized that when soil strength is low and/or pile spacing is large, the soil might squeeze or flow through the space between the piles. In such cases, large deformation of soil occurs. The objective of the present study is to simulate pile–soil interaction using a Coupled Eulerian-Lagrangian (CEL) approach that allows simulation of large deformation. In the first part of this chapter, pile stabilized slopes with two clay layers of varying geotechnical properties are investigated. After the slope failure, the soil moves downward between the pile spaces and squeezes in between. The downslope displacement of the sliding layer in lateral spreading is expected to cause a large lateral force on the pile. In the second part, finite element simulation is performed first to calculate the lateral force exerted on the pile by a horizontally moving clay layer for a varying pile spacing and undrained shear strength of clay. The calculated force is then used

for structural modeling of the pile. The LPILE software is used to calculate the bending moment, shear force and deflection of the pile.

6.3 Problem Statement

In the first part of this chapter, a 10-m high slope (2H: 1V) of two clay layers is analyzed in this study (Fig. 6.2(a)). The analysis is performed for undrained loading conditions. The slope is marginally stable, and a row of vertical piles ($D = 0.8$ m) is installed at the middle of the slope to increase the factor of safety. The pile is installed to a sufficiently large depth below the clay layer. However, the simulation is performed only for the clay domain, assuming the pile as a rigid body. The authors understand that the flexibility of the pile influences the factor of safety (FS), which is one of the limitations of this study. The present study assumes that the pile installation did not cause slope failure; the piles are considered "wished-in-place" conditions. The author understands that the pile installation process might generate plastic shear strain, altering the stress state around the pile, as discussed in previous chapters.
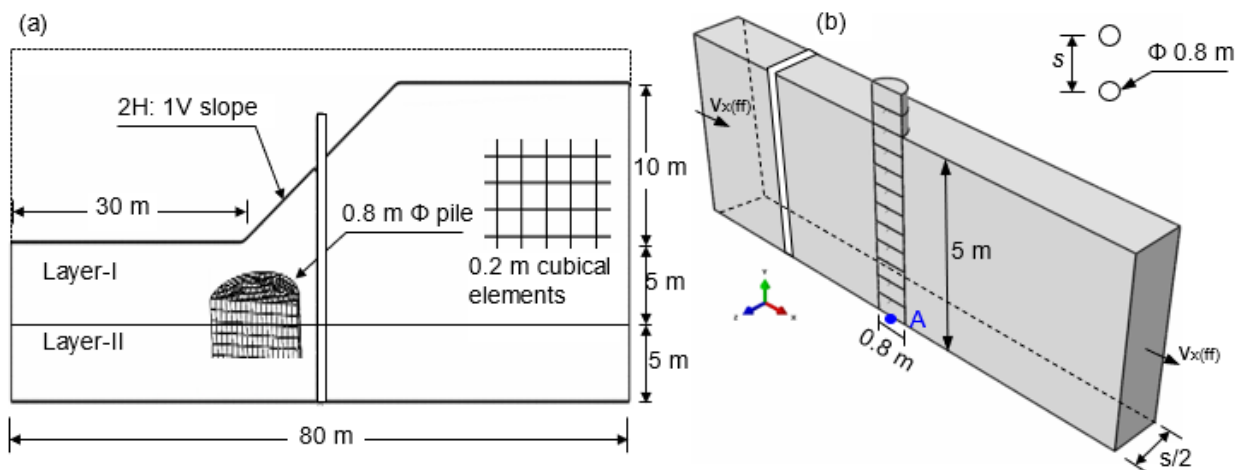
Fig. 6.2. Problem definition (a) pile stabilized clay slope; (b) pile in a sliding clay layer

In the second part of this chapter, a three-dimensional FE model is used to represent the problem shown schematically in Fig. 6.1(b). A row of long piles has been installed through varying soil compositions to the stable layer. The ground surface has a mild slope. For simplicity, all the layers are assumed to be parallel to the ground surface. The unstable soil layer can lose its strength by the effects of natural factors (e.g., an earthquake) or by human activities (e.g., pile driving). This could cause a significant downslope movement of the upper soil layer (Cubrinovski et al., 2009).

For an earthquake, the ground movement does not necessarily occur only by the inertia force during the earthquake but under the gravitational load after the end of shaking. Kokusho (1999) showed that if a loose sand layer is liquefied during an earthquake, the excess pore water pressure difference causes water flow towards the ground surface and might accumulate as a water film under the less permeable materials. Therefore, a water film might form below the clay layer, which could cause the sliding of the upper layer. Note that free-field downslope displacements might also occur in the liquefied layer. However, these are not considered in this study. In other words, the downslope movement of only the upper clay layer is considered.

Based on field investigation after the 1995 Kobe earthquake, Cubrinovski et al. (2009) showed that the permanent lateral ground deformation caused the largest damage of the pile at two locations: the pile head and below the interface between the liquefied and stable soil layers. The force resulting from the movement of the upper clay layer was one of the main causes of this damage.

6.4 Finite element modeling

The Coupled Eulerian-Lagrangian (CEL) approach in Abaqus 6.14-5 FE software is used for numerical analysis. The soil is modelled as an Eulerian material such that it can displace large

distances without causing any numerical issues related to mesh distortion. The pile is modelled as a rigid Lagrangian body and extended up to the bottom of the domain.

Three-dimensional finite-element analysis is performed with the thickness of the domain in the out-of-plane direction in Fig. 6.2 of $s/2$, where s is the centre-to-centre spacing between the piles. The model consists of three parts: soil, pile and a void space above the soil to accommodate displaced soil. An Eulerian domain is first created to develop the model, which is then filled with soil using the Eulerian Volume Fraction (EVF) tool in Abaqus. For an element, EVF = 1 means that the element is filled with soil and EVF = 0 represents the void elements.

Soil is modelled using the EC3D8R elements in Abaqus, which are 8-node linear multi-material Eulerian brick elements. The pile is discretized first using C3D8R elements, which are 8-node linear brick elements, and then defined as a rigid body.

The left and right boundaries are placed sufficiently far from the slope and pile in order to avoid boundary effects. Zero velocity boundary conditions are applied normal to all the vertical faces of the domain shown in Fig. 6.2. Zero velocity boundary conditions are applied at the bottom of the domain in all three directions (i.e., $v_x = v_y = v_z = 0$). No boundary condition is applied along with the soil–void interface. An unbonded rough pile–soil interface condition, which is based on a general contact algorithm, is used.

6.4.1 Pile stabilized clay slope

Mesh sensitivity analysis is carried out, and an optimum mesh size of $0.2 \text{ m} \times 0.2 \text{ m} \times 0.2 \text{ m}$ is obtained. The soil is modelled as an elastic–perfectly plastic material using the undrained shear strength ($s_{u(in)}$). The yield strength, which is an input parameter in Abaqus, is calculated as $\sqrt{3}s_{u(in)}$. The finite-element modeling consists of two loading steps. Firstly, the gravitational loading is

206

applied by increasing the gravitational acceleration to bring the soil to in-situ stress condition by maintaining the ratio between horizontal and vertical total stress equal to 1.0. It is understood that the earth pressure at rest could have a significant effect on slope failure. However, in this study, the effect of the at-rest earth pressure coefficient is not investigated. In the second step, s_u is slowly reduced with time to maintain quasi-static condition. During the reduction of s_u, the ratio between initial shear strength ($s_{u(in)}$) and reduced shear strength (s_u) at a time step is maintained the same for both clay layers (Layer-I & -II, Fig. 6.2(a)), and this ratio is called the "strength reduction factor, *SRF*." The *SRF* is equivalent to *FS* in typical slope stability analysis using limit equilibrium methods.

The geotechnical properties used in FE analysis are shown in Table 6.1. Analyses are performed for pile spacing $s = 2.0–5.0$.

Table 6.1. Geotechnical properties used in FE analysis

Soil properties	Case-A		Case-B	
	Layer I	Layer II	Layer I	Layer II
Unit weight, γ (kN/m³)	17	19	19	17
Undrained shear strength, $s_{u(in)}$ (kPa)	30	60	60	30
Undrained Young's modulus E_u (kPa)	10,000	10,000	10,000	10,000
Undrained Poisson's ratio, ν_u	0.495	0.495	0.495	0.495

6.4.2 Sliding clay layer movements around a pile

The force generated by soil movements on the section of the pile in the clay layer is modelled using a 3-D FE modeling approach. A single row of circular piles of diameter (*D*) installed at a

centre-to-centre spacing of s is modelled. Only the pile–soil interaction in the sliding clay layer is modelled. As the slope is mild, the movement of the soil block is assumed to be horizontal over the interface between the clay layer and liquefied soil layer.

Again a wished-in-place pile section (neglecting installation effects) in a 5.0 m thick clay layer of clay layer is modelled. The pile is 1.0 m above the initial ground surface, which is considered to model the accumulated soil behind the pile due to ground movement. The pile–soil interface behaviour is modelled as a fully bonded condition. The sliding could occur very quickly, so the soil is modelled with undrained behaviour.

No soil movement perpendicular to the faces of the domain is allowed, except for the left and right faces where a free-field displacement—a lateral free-field velocity ($v_{x(ff)}$) of 0.01 m/s, is applied. As will be discussed in the later sections, the instantaneous lateral velocity of the soil elements (v_h) near the pile will be different from $v_{x(ff)}$.

The FE modeling consists of two loading steps. First, the gravity loading is applied gradually in 20 s. After that, the lateral displacement with $v_{x(ff)} = 0.01$ m/s is applied over a period of 50 s. The automatic time increment, factored by 0.1, is used to avoid any numerical issues in the explicit analysis.

The numerical simulations are performed for $D = 0.8$ m and varying spacing of $s = 2$–8. For the first set of analyses, $s_{u(in)} = 40$ kPa is used. The undrained Young's modulus (E_u) of $250 s_{u(in)}$ and undrained Poisson's ratio of 0.495 are used. A parametric study for varying $s_{u(in)}$ is also performed. The von Mises yield criterion is adopted.

6.5 Results

6.5.1 Results of pile stabilized clay slope

The formation of failure planes with and without piles, the deformation of soil including the arching and squeezing between two piles, and the variation of load on the pile with the displacement of the failed soil block are the key factors in the design of slope stabilizing pile. In the present study, the former two are investigated.

Comparison of FE and limit equilibrium analyses

Figure 6.3 shows the development of plastic shear strain for Case-A soil parameters without piles. At SRF = 1.18, a large curved plastic shear zone develops, causing downslope movement of the soil above this, as observed from instantaneous velocity vectors. The same slope is analyzed using the SLOPE/W software that has been developed based on limit equilibrium (LE) methods, and FS_s = 1.18 are calculated. The dashed line shows the location of the critical slip circle obtained from SLOPE/W analysis in Fig. 6.3(a). This indicates the success of CEL for slope stability analysis.

SLOPE/W analysis does not provide any information about the deformation of the failed soil mass, which can be obtained from FE analysis. As shown in Fig. 6.3(b), large plastic shear strains generate in a narrow zone at SRF = 1.63, together with a considerable movement of the failed soil, from where the location of the failure plane in FE analysis could be better identified.
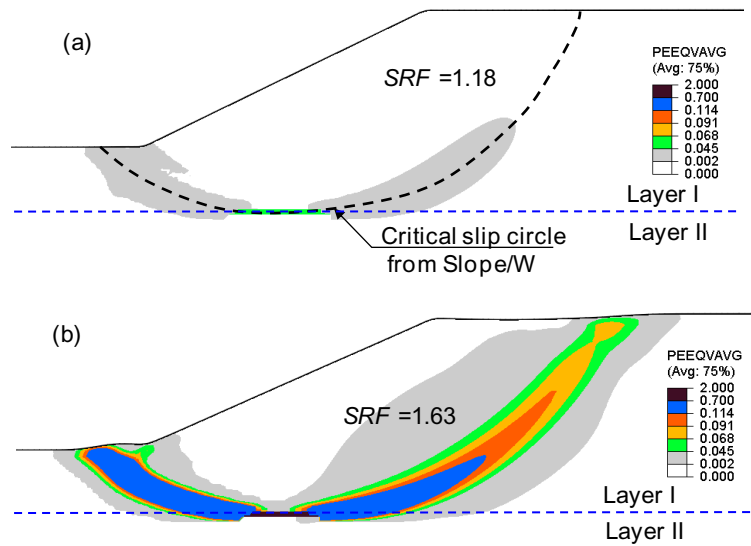
Fig. 6.3. Comparison between FE simulation and limit equilibrium results without piles

Simulation results for Case-A with pile spacing 3D

Figures 6.4(a–d) show the formation of shear bands with an increase in *SRF*. At the end of the geostatic step with initial $s_{u(in)}$ (i.e., *SRF* = 1.0), the plastic shear strain does not generate in the soil. For *SRF* = 1.74, two shear bands form, one from the toe of the slope and the other one from the pile at the interface between the two clay layers (point A) (Fig. 6.4(a)). Both of them propagate towards the upslope areas. With further increase in *SRF*, two shear bands, originated from the interface between two soil layers, propagate in the upslope and downslope directions (Fig. 6.4(b) & 6.4(c)). The propagation of these shear bands continues with an increase in *SRF*, and the shear bands reach the ground surface, generating large plastic shear strains in these bands (Fig. 6.4(c)). The shear strain accumulation continues along with the previously developed shear band even at large *SRF* (e.g., *SRF* = 2.45 in Fig. 6.4(e)). The failed soil mass displaces significantly, and a gap between the pile and displaced soil is formed behind the pile (on the left side) (Fig. 6.4(e)). Note that the pile–soil interface is modelled as an unbonded (no-tension) condition. Moreover, the

location of the global failure plane does not change, although a number of shear bands form locally in the failed soil mass, especially on the left side of the pile (Fig. 6.4(e)).

The location of the global failure plane is important in the design of pile stabilized slopes. In the current design practice, the increase in factor of safety is obtained from the additional resistance offered by the pile on the soil above the global failure plane (e.g. see Kourkoulis et al., 2012 for further discussion). The previous finite-element analysis considered the location of the maximum shear force in a flexible pile as the point where the critical slip plane intersects the pile. However, Wei & Cheng (2009) found that the location of the maximum shear force in a pile does not always represent the location of the critical slip circle. They also suggested that the critical slip surface should be identified from accumulated plastic shear strain.

In finite-element slope stability analysis, different approaches have been used to identify failure initiation (i.e., the value of SRF that could be considered FS in limit equilibrium analysis). Among them, the following three criteria are commonly used: (i) formation of a band of plastic shear strain that could be considered as a global failure plane (e.g., Matsui & San, 1992), (ii) sudden nodal displacement in the mesh (e.g., Zienkiewicz et al., 1975; Griffiths & Lane, 1999; Tan & Sarma, 2008), and (iii) non-convergence of the solution (Zienkiewicz et al., 1975; Tan & Sarma, 2008). As shown in Fig. 6.4, the failure initiates locally and then propagates gradually to form a global failure plane. Therefore, the displacement of the point that can be considered to define the failure should be carefully selected, depending upon the problem. The last criterion (non-convergence) might simply be a numerical issue, especially at large displacements in typical Lagrangian-based finite-element analysis. The numerical issues could be significant when piles are used to stabilize the soil because of the ill-conditioning of stiffness matrix and high-stress gradient in typical

Lagrangian FE models (Cai & Ugai, 2000). Day & Potts (1994) suggested using small elements near the interface between soil and structure to reduce this type of numerical issue.

The present CEL analysis does not have any numerical issue related to mesh distortion. Therefore, the solution does not stop after the partial formation of the failure plane due to significant mesh distortion. The mesh remains fixed, and the Eulerian material (soil) flows through the mesh. In the present study, the first criteria (i.e., formation of the shear band) is used to define the failure. The location of the failure plane could be better identified from the clear shear band of high plastic shear strain, as shown in Fig. 6.4(e). Note that such a large deformation generally cannot be simulated using typical Lagrangian FE programs.

For comparison, the location of the critical circle obtained from SLOPE/W without pile is shown by a dashed line in Figs. 6.4(c) and 6.4(e). For this case, the global failure plane obtained from FE analysis with pile is slightly outside the critical slip circle obtained from SLOPE/W analysis without pile. However, the global failure plane intersects the pile at the same depth—the interface between two clay layers—in both analyses (i.e., FE and LE). It is to be noted here that, for a $c-\phi$ soil, Wei & Cheng (2009) showed shallower failure planes in a pile stabilized slope than in the same slope without pile.
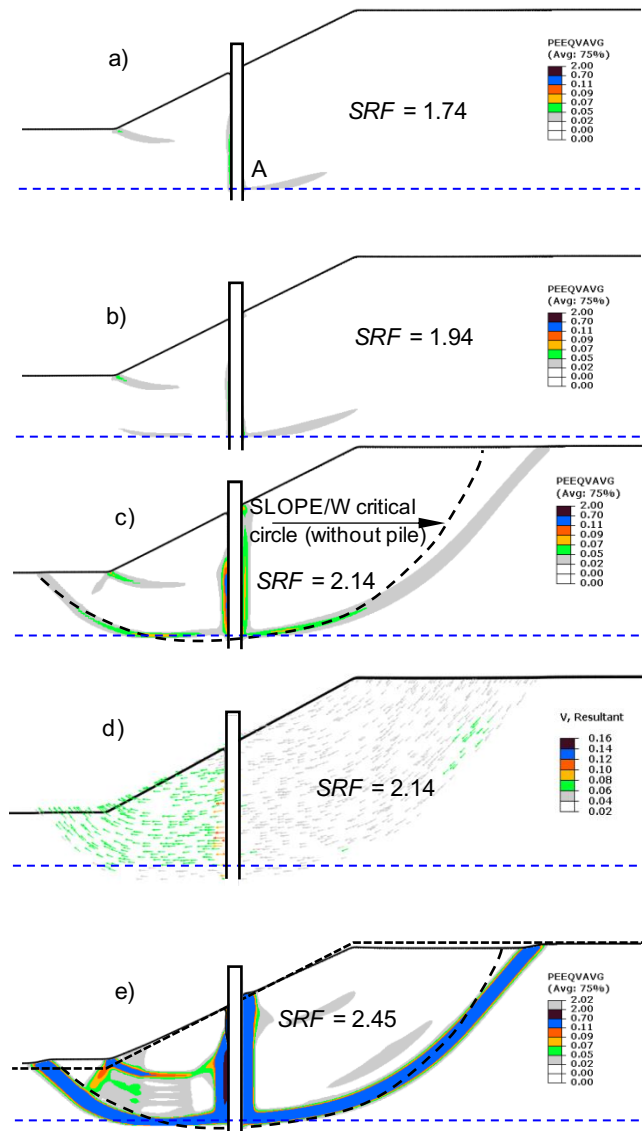
Fig. 6.4. Formation and propagation of failure planes for 3D pile spacing with Case-A soil parameters

Effects of pile spacing

Figures 6.5(a–d) show the plastic shear strains in the soil in four vertical planes starting from the centre of the pile ($z = 0$) to the halfway between two adjacent piles ($z = s/2$) for *SRF* = 1.67.

Here, z represents the coordinate in the out-of-plane direction, measured from the centre of the pile.

Figure 6.5(a) shows that plastic shear strains generate not only in the global failure plane but also in both sides of the pile. During the downslope movement of the failed soil block, soil elements move around the pile, as shown in the inset of Fig. 6.5(a), which generates plastic shear strain around the pile. The magnitude of plastic shear strain decreases with z and is highest on the plane that passes through the centre of the pile (i.e., $z = 0$, Fig. 6.5(a)) and the lowest at $z = s/2$ (Fig. 6.5(d)).

Simulation results for Case-B with pile spacing 3D

Figures 6.6(a–c) show the formation of failure planes with an increase in *SRF* for the Case-B soil parameters. As the weaker clay layer is below, the stronger clay, a deep-seated global failure plane originating from the base of the weak layer, is obtained. A complete global failure plane generates at a large *SRF* in this case as compared to Case-A (compare Figs. 6.4(c) and 6.6(c)). Moreover, the formation of local shear bands in the failed soil mass, in this case, is also different from Case-A, as shown in Fig. 6.4. Figure 6.6(d) shows the instantaneous velocity vectors for *SRF* = 2.41. The *FS* of this slope without pile is ~ 1.36, as obtained from SLOPE/W and FE analyses.
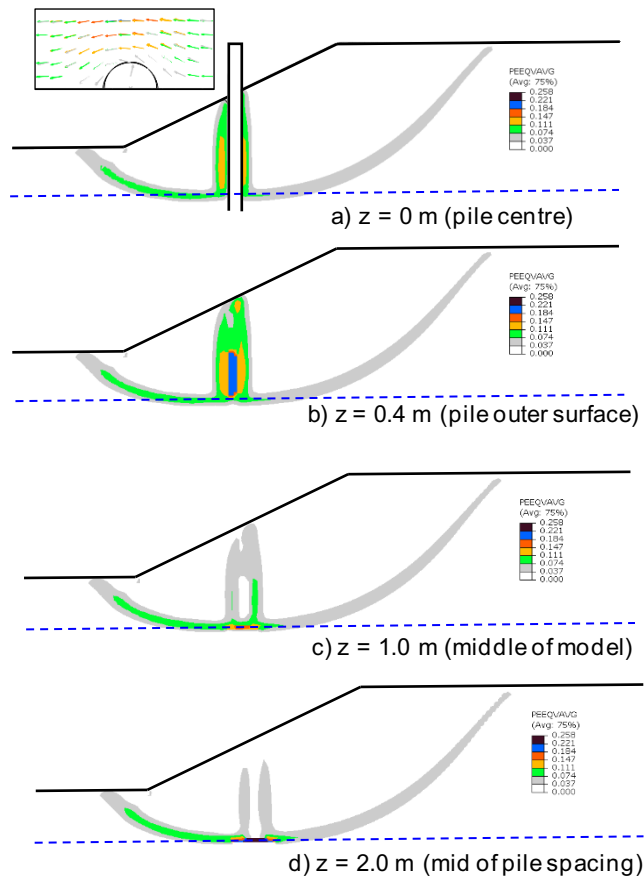
Fig. 6.5. Effect of the pile on strain development in soil (Case-A)

Effects on stability for the spacing of piles

Figures 6.7(a)–(g) represent the fully formed shear band due to the application of *SRF* to pile stabilized slope for case-A. As the pile spacing decreases, the soil becomes more rigid to flow between the piles. For example, at *s* = 2*D* in Fig. 6.7(a), the highest *SRF* = 3.33 is observed for Case-A. As *SRF* increases, the soil becomes weaker and local failure planes are formed instead of a well-formed slip circle. For spacing 2*D* and 2.5*D*, well-formed slip circles are observed. As the spacing increases, soil can easily pass between the piles, and the value of *SRF* decreases to form a global failure slip circle.
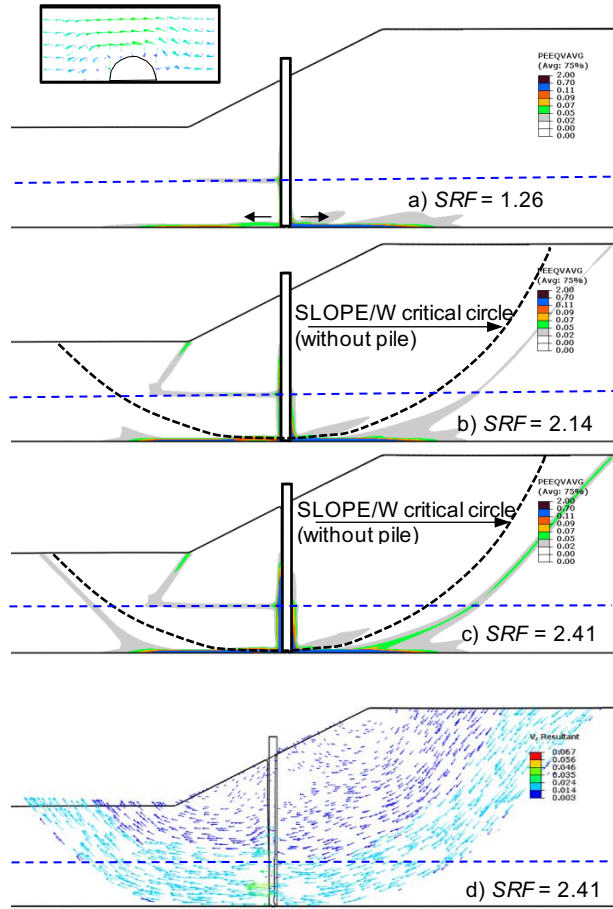
Fig. 6.6. Formation and propagation of failure planes for 3D pile spacing with Case-B soil parameters

Figures 6.7(h–n) represent the fully formed shear band for Case-B soil parameters. As the slope is more stable in Case-B, higher *SRF* is required to develop the fully formed shear band. However, as the failure plane passes through the interface between the weak and the strong layer, a deep-seated failure plane is expected for Case-B soil parameters. For *s* = 5*D*, high *SRF* = 2.86 is observed in Case-B, indicating a stability increase due to piles. However, in all cases of spacing, similar slip circles are found.
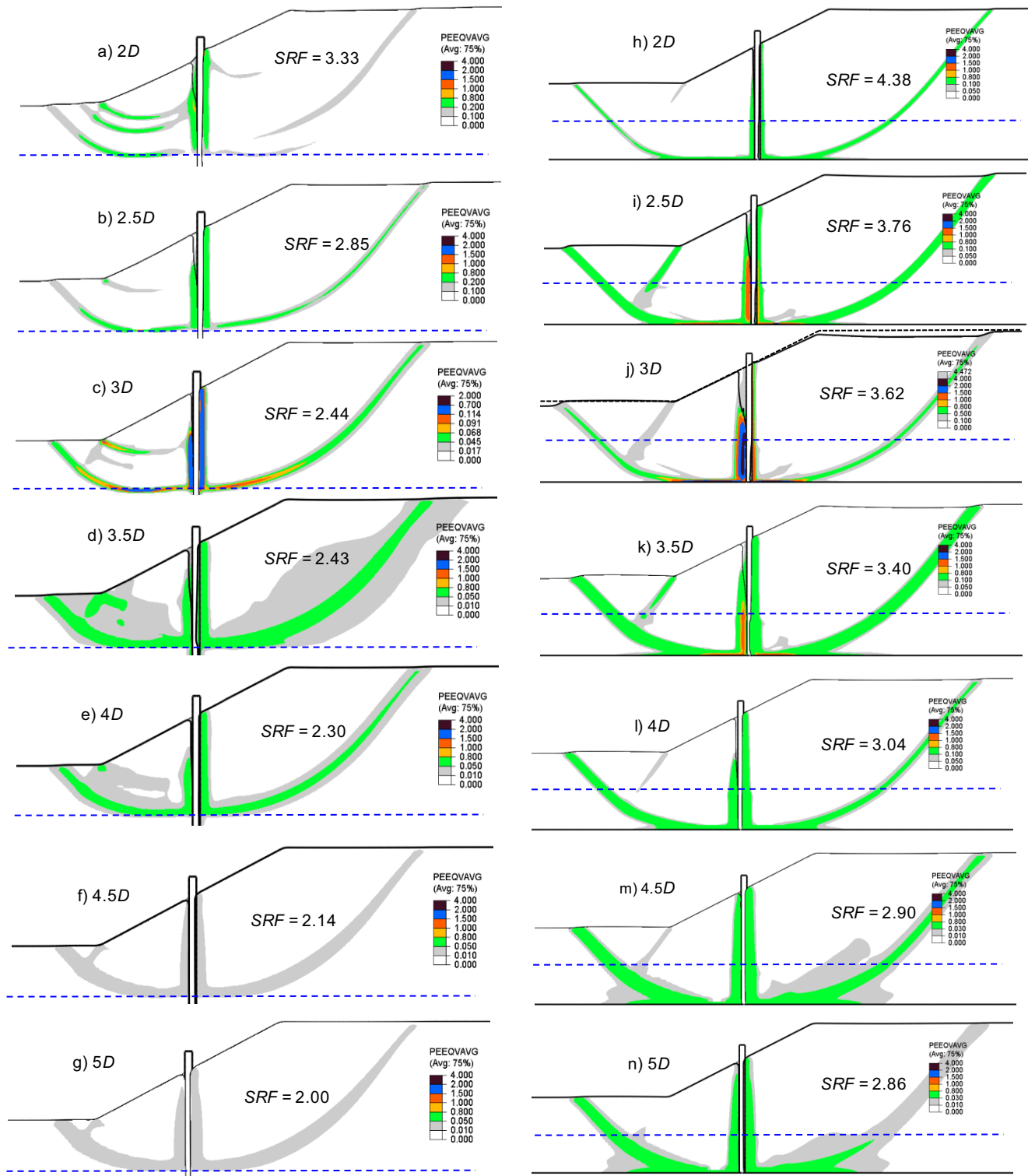
Fig. 6.7. Formation of slip circle for different pile spacings: (a–g) Case-A; & (h–n) Case-B

Effects on stability for the location of pile installation

For the parametric study of the location of the pile, $3D$ centre to centre spacing is considered. Piles are placed at the toe and crest of the slope, and the response is compared with the above base case analysis where the pile was at the middle of the slope. Comparison with pile at the middle of the slope, both cases provide smaller *SRF* or Factor of Safety (*FS*) for the slope. Figures 6.8(a–d) represent the formation and propagation of plastic shear strain of soil for Case-A and Figs. 6.8(e–f) represent Case-B. Figure 6.8(a) shows the formation of the shear band at *SRF*=1.71. It can be observed from Fig. 6.7(c), the pile at the middle of the slope has the larger factor of safety (*SRF*=2.44). At *SRF*=2.44, a large deformation occurs (Fig. 6.8(b) as compared to that shown in Fig. 6.7(c), where the pile was at the middle of the slope. It is clear from the comparison that the pile at the middle of the slope could provide better support to the upslope soil than the pile at the toe; hence the *FS* increases.

When the piles are installed at the crest, a relatively higher *FS* is found than that of the pile at the toe case. A clear shear band forms when *SRF* = 1.90 (Fig. 6.8(c)). At *SRF* = 2.44, the soil at the toe fully collapses and flows downstream, although the pile retains topsoil to flow at a $3D$ pile spacing model. It is evident that the position of the pile influences the factor of safety of the pile-slope system. It is best to place the pile in the middle of the slope to obtain the most stable slope. Figures 6.8(e–f) show the formation of failure surface for pile at toe and top for case-B. When the pile is placed at the toe of the slope, a deep slip circle is generated on the up-slope of the pile, as shown in Fig. 6.8(e). The entire soil block collapses very quickly with a small increase of *SRF*. When the pile is placed on the top of the slope, it protects the upside soil. Down-slope soil collapses with a big slip circle due to the position of weak soil in the deep region. It is evident that the placement of the pile at the top of the slope ensures a large *FS* to the up-side soil.
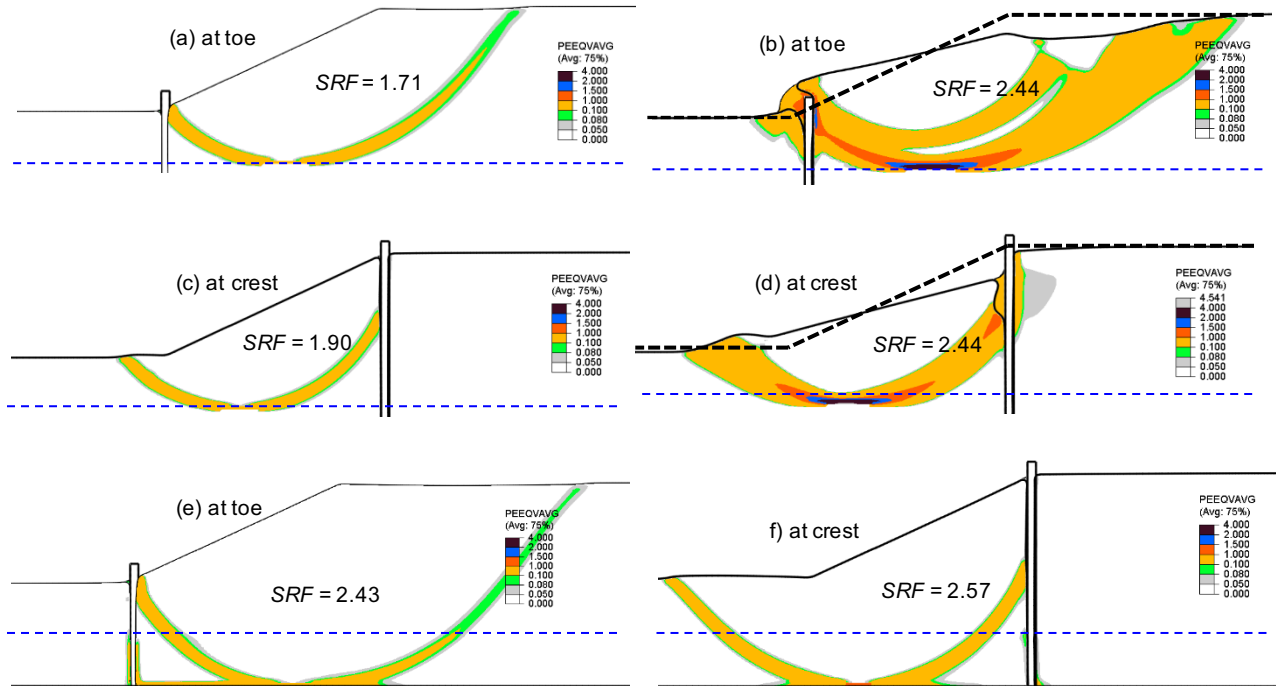
Fig. 6.8. Formation of failure planes: (a–d) Case-A piles at the toe; (e–f) Case-B piles at the crest

Increase in Factor of Safety

The success of using piles for slope stabilization is generally checked by the increase in the factor of safety. Figure 6.9 shows the stability improvement ratio, $N_{ps} = FS/FS_s$, with pile spacing for the two cases analyzed in the present study. Here, FS is the factor of safety for pile stabilized slope; FS_s is the factor of safety without pile. Also, FS represents the value of SRF at which a global failure plane develops in FE analysis, as discussed above. To calculate N_{ps}, the value of FS_s obtained from FE results without pile is used, which is also similar to the value of FS in limit equilibrium analysis.

Figure 6.9 shows that a row of piles could significantly increase the FS; for example, at $s = 3$, the FS is increased by ~80%. Moreover, N_{ps} decreases with increasing pile spacing; however, even

at $s = 5$, the piles could increase the FS by 40% of the F_s without piles. It is to be noted here that, for a c–ϕ soil, Wei and Cheng (2009) found the effect of pile on FS is negligible after, $s = 10–14$.
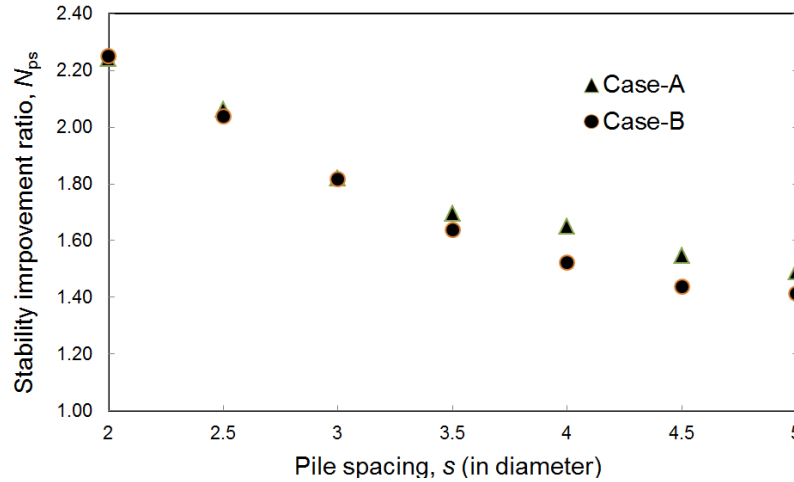
Fig. 6.9. Effects of pile spacing on the increase in factor of safety

6.5.2 Results of sliding clay layer movements around a pile

Force–displacement behaviour

Figure 6.10 shows the variation of average normalized force ($N_{av} = F_x/(s_{u(in)}D_eL)$) with free-field displacement ($u_{x(ff)} = v_{x(ff)} \times t$, where t is the time during which the lateral velocity boundary conditions are applied). Here, D_e is the effective diameter, and L is the total length of the pile (= 5 m). The total force on the pile (F_x) is twice the sum of the horizontal force on each rigid segment of the pile, as shown in Fig. 6.2(b). Note that the maximum force on a pile segment is smaller near the ground surface, increases with depth, and is almost constant after ~ 3 m. An effective diameter (D_e), instead of the outer diameter D (= 0.8 m), is used to calculate the normalized force because a fully bonded condition is used. In this case, the failure occurs in the soil instead of sliding of soil at the pile–soil interface. Assuming that the failure occurs at the middle of the soil element next to

the pile surface, $D_e = D + t_{FE} = 0.8 + 0.1 = 0.9$ m is calculated. Moreover, $s_{uN} = 2/\sqrt{3} s_{u(in)}$, (please see Hawlader et al. (2015) for further discussion).

Figure 6.10 shows that N_{av} reaches the maximum value at a free-field displacement of approximately 40 to 80 mm; a larger displacement is required for a larger spacing. The maximum normalized force increases with pile spacing. The difference between the force–displacement curves for $s = 5D$ and $8D$ is negligible, which indicates that the pile behaves as a single pile for this range of pile spacing. The maximum normalized forces are lower in the smaller spacing cases (i.e., $s = 2D$), which indicates that the ultimate pressure on a single pile will be higher than the closely spaced or group piles. Pan et al. (2002) and Bauer et al. (2014) reported similar results by conducting physical modeling for piles subjected to lateral soil movements. Note that as the pile spacing decreases, the group effects of pile increase.

For spacing, $s \geq 5D$, the maximum normalized force is approximately 10.5, which remains almost similar for single pile cases. As mentioned above, Randoloph & Houlsby (1984) calculated the maximum normalized forces of 11.94 and 9.14 for the rough and smooth pile–soil interface conditions, respectively.

Effects of pile spacing

The effects of pile spacing on the force–displacement behaviour are examined further, based on arching effects. Figure 6.11 shows the contour of the horizontal component of the instantaneous velocity of soil elements (v_h) on a horizontal plane at a depth of 4.0 m below the original ground surface for a free-field displacement of 100 mm. For the soil elements far from the pile, v_h is approximately equal to the free-field velocity applied at the boundary (i.e., $v_h = v_{x(ff)} = 0.01$ m/s) for all four pile spacing cases. As expected, v_h is very small near the pile. For the $s = 2D$ case, a

large zone near the pile has a negligible velocity. Moreover, v_h is very small up to the mid-distance between two piles because of arching effects (e.g., point A in Fig. 6.11(a)). Therefore, in this case, a considerable soil heave occurs in the left side of the pile for a large free-field displacement as the soil moves from the left to the right.
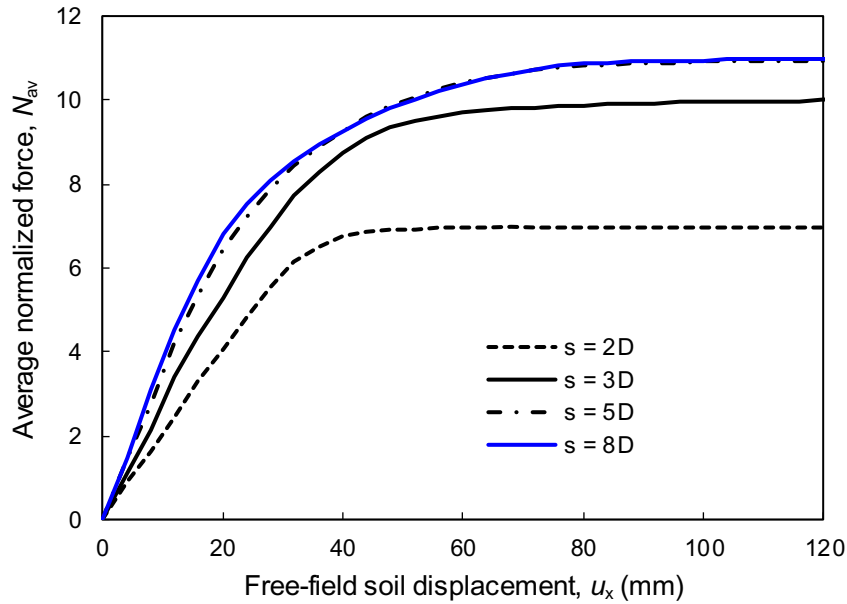
Fig. 6.10. Variation of normalized force with free-field displacement

For $s = 3D$, the tendency of soil to flow around the pile is higher than in $s = 2D$. Therefore, a higher v_1 is calculated near the pile (e.g., point B in Fig. 6.11(b)) than in $s = 2D$ (e.g., point A). For $s = 5$ and $s = 8$, the arching effect is not sufficient to stop the soil flow between the piles. Therefore, a higher velocity of soil elements near the pile (e.g., at points C and D in Figs. 6.11(c) and 6.11(d), respectively) is obtained because the same amount of soil displaced in the free-field zone is passed through the narrower space between the piles.
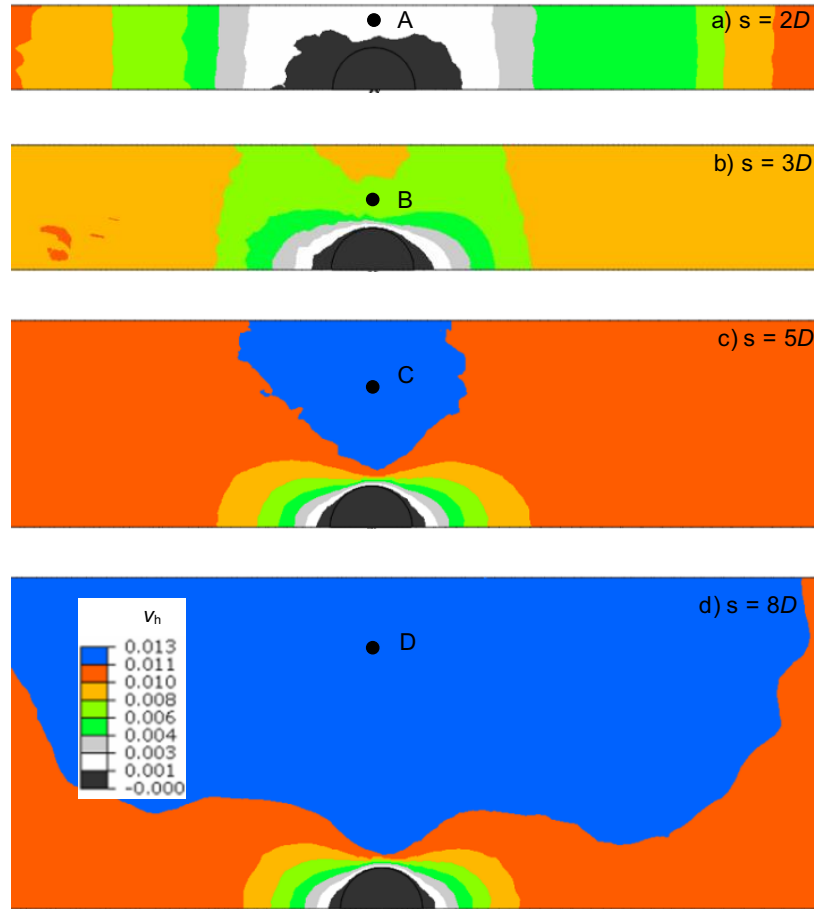
Fig. 6.11. Instantaneous soil velocity at 4-m depth for 100-mm free field displacement

The arching effects can also be explained using equivalent plastic shear strain distributions. Figure 6.12 shows the distribution of plastic shear strain for various pile spacing due to the free-field soil displacement of 100 mm from the left boundary. For $2D$ pile spacing, as shown in Fig. 6.12(a), plastic strain is observed at both sides of the pile, although the distribution is not symmetrical. As the free-field soil velocity is placed in the left and right boundaries of the model, soil tends to displace from both sides of the pile. On the left side of the pile, the soil is observed to be piled up, generating plastic strain around the pile. However, soil can move rightward on the right side of the pile, and higher plastic strain is observed on that side.

Higher plastic strain is also observed around the pile surface in all cases, as shown in Figs. 6.12(a–d). In Figs. 6.12(b–d), a small strain is observed at the centre of the pile spacing, as the soil can pass through that zone without any obstructions. However, arching effects are still found in the $s = 5D$ case, as the strain distributions are found to be overlapped along the centre line of the pile spacing. In the $s = 8D$ case, the pile is actually acting as a single pile. No plastic shear strain is observed around the centre line of the pile spacing as the soil can pass through it without any interruptions.

Effects of undrained shear strength and Young's modulus

The effects of undrained shear strength on force–displacement behaviour is examined by varying $s_{u(in)}$ between 10 and 40 kPa for $s = 3D$. In these analyses, $E_u = 250s_{u(in)}$ is used, which implies varying E_u. Analyses are also performed for a constant $E_u = 10$ MPa but with varying $s_{u(in)}$.

Figure 6.13(a) shows the total lateral forces (i.e., the sum of all the reaction forces in each pile segment in Fig. 6.2(b)) with free-field displacement. The maximum lateral force for a given $s_{u(in)}$ is the same for both E_u ($E_u = 10$ MPa and $250s_{u(in)}$). However, the force-displacement curve prior to the mobilization of the maximum force is different; the higher the E_u, the faster the mobilization of reaction force.

The normalized force-displacement curves (N_{av} vs. $u_{x(ff)}$) for these analyses are shown in Fig. 6.13(b). As shown, a single N_{av}–$u_{x(ff)}$ relationship is found when $E_u = 250s_{u(in)}$ is used; however, N_{av}–$u_{x(ff)}$ curves are different before the maximum N_{av} for the constant E_u. At a large free-field displacement, N_{av} is independent of $s_{u(in)}$ and E_u. Note that the maximum N_{av} will be smaller for closely spaced piles (e.g., $s = 2D$) that are shown in Fig. 6.13(b) (see also Fig. 6.10).
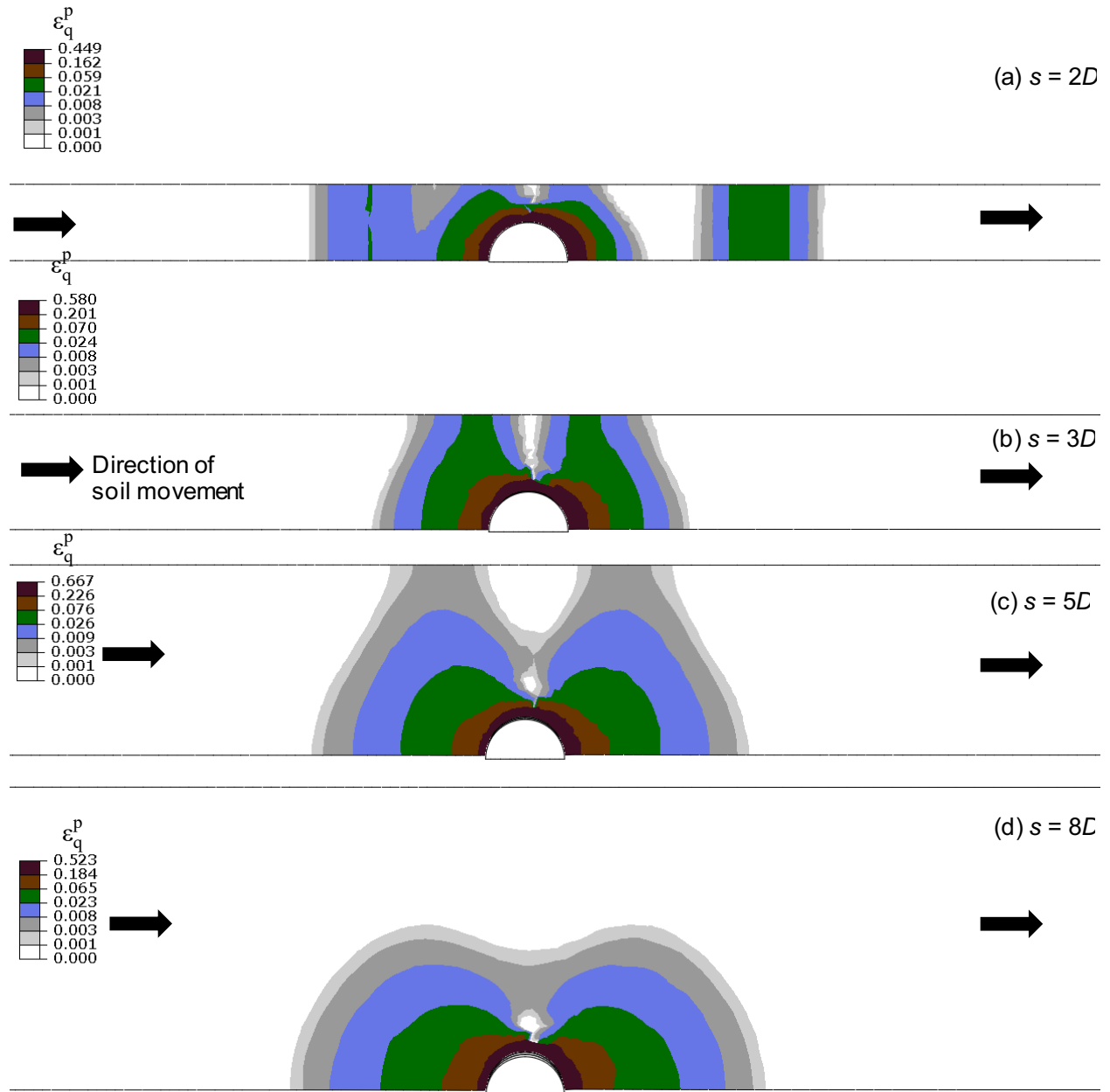
Fig. 6.12. Equivalent plastic shear strain distribution on various spacing distances
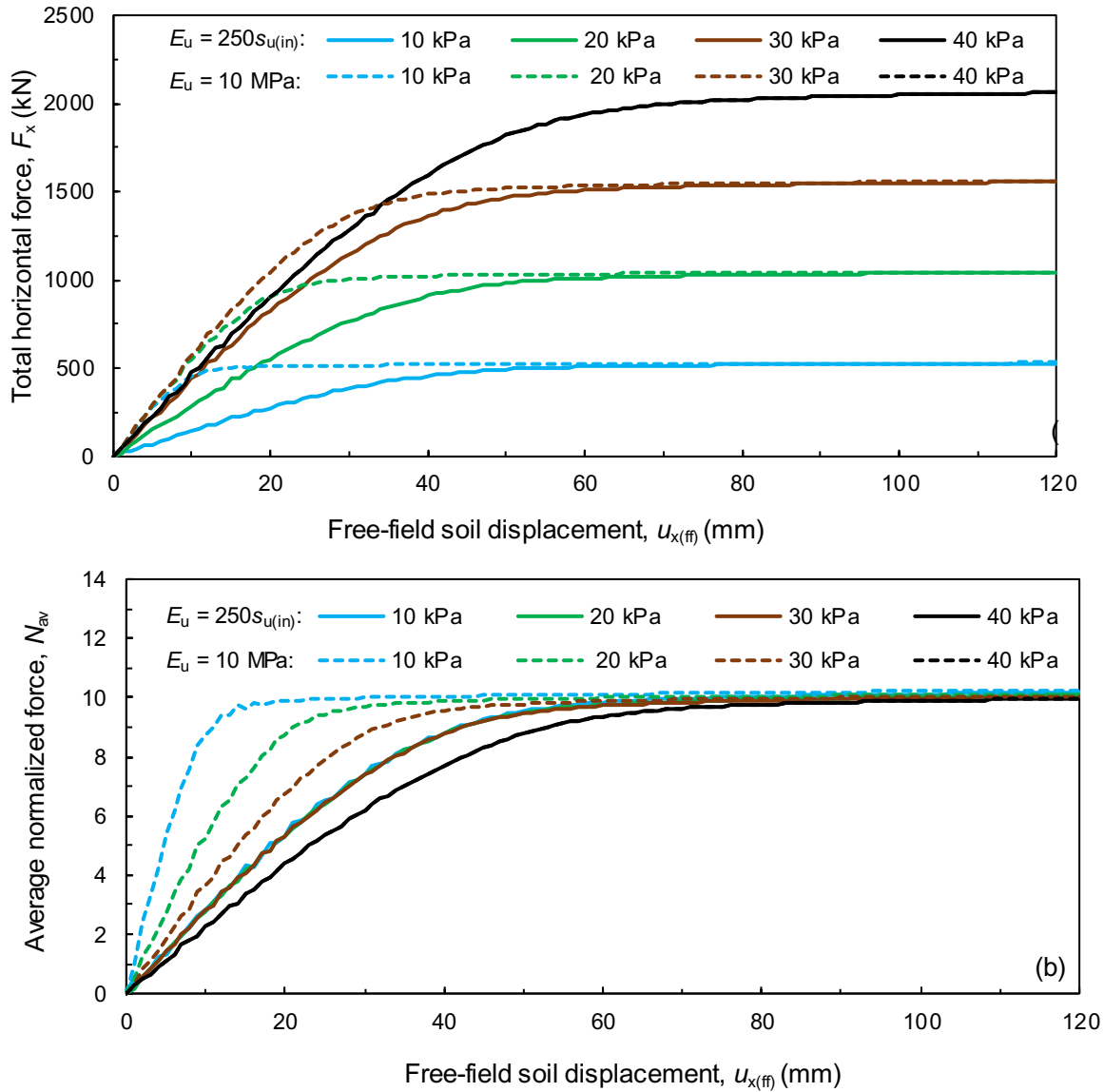
Fig. 6.13. Effects of undrained shear strength and Young's modulus: (a) variation of

horizontal force, (b) variation of average normalized force

Modeling of structural response– an example

Consider a row of a 25-m long steel pipe pile of 0.8-m outer diameter and 45-mm wall thickness, which is installed in a three-layered soil, with a mild slope as shown in Fig. 6.1(b). The upper sliding clay layer has a thickness (H_c) of 5 m and undrained shear strength ($s_{u(in)}$) of 20 kPa. The thickness of the unstable loose sand layer (H_u) is 5 m. The shear strength of this soil layer is

226

decreased due to an earthquake that caused sliding of the upper clay layer and permanent ground deformation. The groundwater table is assumed at the ground surface.

The structural response of the pile is calculated using LPILE Version 8.03 software. For simplicity, only the bottom part of the pile (20 m) below the interface between the sliding clay layer and liquefied layer is modelled. The authors understand that a fully coupled pile–soil interaction analysis could be performed using the FE technique presented above. However, this type of three-dimensional modeling with a flexible pile is computationally expensive, especially for a long pile and large centre-to-centre spacing. Moreover, the force from the sliding soil layer could be presented in the normalized form, as described above, and LPILE is a widely used software in the industry; therefore, a decoupled analysis is performed for this study.

The estimation of the lateral resistance of a liquefied soil layer is more difficult than for non-liquefied soils. As loose sand liquefies in an undrained condition, some studies modelled its behaviour as soft clay (Wang et al., 2008). The residual shear strength, a constant or linear function of the initial vertical effective stress, is also used to estimate the maximum lateral resistance (Cubrinovski et al., 2009). The reduction of resistance using a "p-multiplier" of 0.1–0.3 was suggested in some studies (Liu & Dobry 1995; Wilson 1998). A conservative assumption of zero lateral resistance of liquefied soil is also available. Based on full-scale test results, Rollins et al. (2005) proposed a power function for the p–y curve, where p is the soil resistance, and y is the lateral displacement, that varies with depth, effective unit weight and pile diameter. In the present study, the recommendation provided by Rollins et al. (2005) is used in LPILE analyses. Effective unit weight of 7 kN/m^3 is used for the loose liquefied sand layer. The soil below the liquefied layer is a dense sand, which is modelled based on the recommendation of Reese et al. (1974), with the

following parameters: an effective unit weight of $10.19\,\text{kN/m}^3$, the initial modulus of subgrade reaction of 34 MPa/m, and an angle of internal friction of $45°$.

The following properties are used for the steel pile: the modulus of elasticity of 210 GPa, yield strength of 315 MPa, and Poisson's ratio of 0.23. The nominal moment capacity of the pile is 8,031 kN-m.

The pile is modelled as for a free-head condition. The force exerted by the sliding soil layer on the pile is calculated based on the FE analysis for the two pile spacing presented above. The total maximum lateral reaction force $F_0 = 1,030$ kN and moment $M_0 = 2,417$ kN-m are obtained at the base of the 5-m rigid pile segment in the sliding clay layer (i.e. at point B in Fig. 6.2(b)) for $3D$ pile spacing. Similarly, $F_0 = 713$ kN and $M_0 = 1,892$ kN-m are obtained for $2D$ pile spacing. In the LPile analysis, F_0 and M_0 are applied at the free-head.

Figure 6.14 shows the deflection, bending moment, and shear force in a pile for $s = 2D$ and $3D$. With an increase in pile spacing, the force on the pile due to sliding soil layer movement increases, which results in a larger deflection of the pile. The magnitude of deflection decreases with depth and is negligible ~10 m below the interface between the sliding clay layer and liquefied layer (Fig. 6.14(a)). The maximum bending moment develops ~ 1.5 m below the interface between the liquefied loose sand and non-liquefied dense sand layers. Therefore, this section of the pile would have the largest possibility of damage. Note that, based on field observation, Cubrinovski et al. (2009) reported that the largest damage of piles due to the 1995 Kobe earthquake occurred slightly below the liquefied layer.
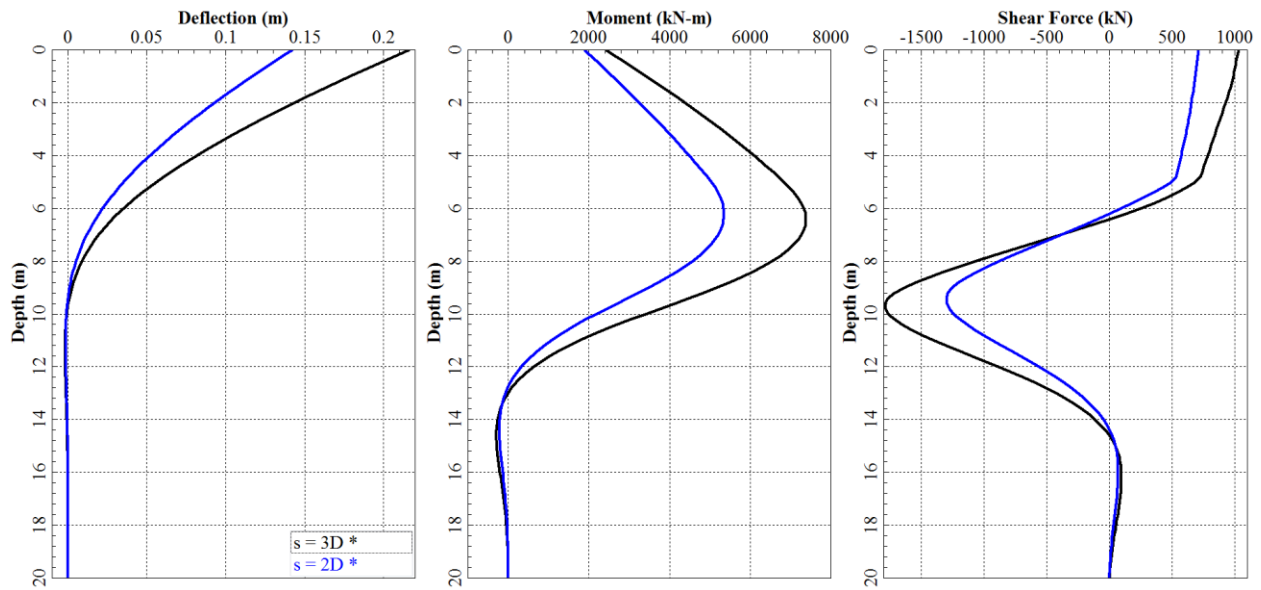
Fig. 6.14. Structural response of pile for varying spacing

6.6 Conclusions

Finite element analysis of pile-reinforced clay slopes is presented in this first part of the chapter. The slope has two layers of clay, which has been modelled using the undrained shear strength of the soil. The numerical modeling is performed using the Coupled Eulerian-Lagrangian approach in Abaqus FE software, where the soil is modelled as an Eulerian material and pile as a Lagrangian body. The following conclusions can be drawn from this study:

a) The global failure plane passes through the bottom of the weaker clay layer in both conditions (overlain or underlain by a strong layer).

b) The existence of piles slightly increases the size of the failure wedge, as compared to that of the slope without pile; however, the depth of the failure plane at the pile location (mid-slope) is the same.

c) For the cases analyzed, the factor of safety increases even for centre-to-centre spacing of 5.

In the second part of the chapter, numerical analyses are performed to investigate the response of piles subjected to passive loading resulting from lateral spreading due to an earthquake. First, three-dimensional finite-element (FE) analyses are performed for the displacement of a clay layer over a liquefied (weak) loose sand layer, which exerts a large lateral load on a row of piles. The analysis is performed using Abaqus/Explicit FE software. The calculated lateral force increases with pile spacing; however, for a pile spacing greater than five diameters ($s \geq 5D$), the spacing does not significantly influence lateral resistance, and the pile behaves as a single pile. For a given pile spacing, the lateral force increases with the undrained shear strength of clay ($s_{u(in)}$); however, the normalized maximum lateral resistance is independent of $s_{u(in)}$. The arching effect is significant for a pile spacing less than $2D$. The soil flows between the piles for $s \geq 5D$. The LPILE analyses show that the maximum bending moment is generated at a location below the interface between the liquefied and stable layer, representing a segment of possible damage.

Finally, although the present analyses show the success of the CEL approach for modeling pile–slope interaction, even for large deformations, it has some limitations. The analyses have been performed using rigid piles installed at the mid-slope. Further studies considering the flexibility of the pile for different locations along the slope need to be investigated.

Notations

γ	total unit weight
ν_u	undrained Poisson's ratio
ϕ	angle of internal friction
c	cohesion
D	pile outer diameter
D_e	effective diameter of pile
E_u	undrained Young's modulus
F_0	total reaction force
F_x	total lateral force
FS	factor of safety with pile
FS_s	factor of safety without pile
H_c	thickness of sliding clay layer
H_s	thickness of liquified or weakened layer
H_u	thickness of stable layer
L	length of the pile
M_0	bending moment
N_{av}	average normalized force
N_p	lateral bearing capacity factor
N_{ps}	ratio of factor of safety with pile to without pile
p	lateral load per unit length
p_u	ultimate resistance per unit length
SRF	strength reduction factor

s	pile spacing
s_u	mobilized undrained shear strength
$s_{u(in)}$	initial (peak) undrained shear strength
s_{uN}	undrained shear strength used for normalization
t_{FE}	thickness of the FE element
t	time
$u_{x(ff)}$	lateral free-field displacement
v_h	instantaneous lateral velocity of the soil element
v_x	the component of velocity in x-direction
$v_{x(ff)}$	lateral free-field velocity
v_y	the component of velocity in y-direction
v_z	the component of velocity in z-direction
y	displacement
z	horizontal distance from the centre of the pile

References

ABAQUS 6.14 [Computer software]. D. S. Simulia, *Dassault Systémes*.

Ashour, M., Norris, G. M. & Pilling, P. (1998). Lateral loading of a pile in layered soil using the strain wedge model. *Journal of Geotechnical and Geoenvironmental Engineering* **124**, No. 4, 303–315.

Bauer, J., Kempfert, H. G. & Reul, O. (2014). Lateral Pressure on Piles due to Horizontal Soil movement – 1g Model Tests on Single Piles and Pile Rows. *8th International Conference on Physical Modeling in Geotechnics*, Perth, Australia **2**, 839–846.

Cai, F. & Ugai, K. (2000). Numerical analysis of the stability of a slope reinforced with piles. *Soils and Foundations* **40**, No. 1, 73–84.

Cubrinovski, M., Ishihara, K. & Poulos, H. (2009). Pseudo-Static Analysis of Piles Subjected to Lateral Spreading. *Bulletin of the New Zealand Society for Earthquake Engineering* **42**, No. 1, 28–38.

Chow, Y. K. (1996). Analysis of piles used for slope stabilization. *International Journal for Numerical and Analytical Methods in Geomechanics*, 20(9): 635–646.

Day, R. A. & Potts, D. M. (1994). Zero thickness interface elements-numerical stability and application. *International Journal for Numerical and Analytical Methods in Geomechanics* **18**, No. 10, 689–708.

Griffiths, D. V. & Lane, P. A. (1999). Slope stability analysis by finite elements. *Géotechnique* **49**, No. 3, 387–403.

Hawlader, B., Dutta, S., Fouzder, A. & Zakeri, A. 2015. Penetration of Steel Catenary Riser in Soft Clay Seabed: Finite-Element and Finite-Volume Methods. *International Journal of Geomechanics, ASCE* **15**, No. 6, 04015008.

Ho, I. H. (2015). Numerical study of slope-stabilizing piles in undrained clayey slopes with a weak thin layer. *International Journal of Geomechanics* **15**, No. 5.

Ito, T. & Matsui, T. (1975). Methods to estimate lateral force acting on stabilizing piles. *Soils and Foundations* **15**, No. 4, 43–59.

Kokusho, T. (1999). Water Film in Liquefied Sand and Its Effect on Lateral Spread. *Journal of Geotechnical and Geoenvironmental Engineering* **125**, No. 10, 817–826.

Kourkoulis, R., Gelagoti, F., Anastasopoulos, I. & Gazetas, G. (2012). Hybrid method for analysis and design of slope stabilizing piles. *Journal of Geotechnical and Geoenvironmental Engineering* **137**, No. 1, 1–14.

Liu, L. & Dobry, R. (1995). Effect of Liquefaction on Lateral Response of Piles by Centrifuge Model Tests. *NCEER Bulletin* **9**, No. 1, 7–11.

Matlock, H. (1970). Correlation for design of laterally loaded piles in soft clays. *2nd Annual Offshore Technology Conference*, Houston, Texas **1**, 577–588.

Matsui, T. & San, K. (1992). Finite element slope stability analysis by shear strength reduction technique. *Soils and Foundations* **32**, No. 1, 59–70.

McVay, M., Zhang, L., Molnit, T. & Lai, P. (1998). Centrifuge Testing of Large Laterally Loaded Pile Groups in Sands. *Journal of Geotechnical and Geoenvironmental Engineering* **124**, No. 10, 1026–1026.

Oakland, M. W. & Chameau, J. (1986). Drilled pilers used for slope stabilization, *Joint Highway Research Project,* Indiana Department of Transportation and Purdue University, West Lafayette, Indiana, FHWA/IN/JHRP-86/07.

Pan, J. L., Goh, A. T. C., Wong, K. S. & Teh, D. I. (2002). Ultimate soil pressures for piles subjected to lateral soil movements. *Journal of Geotechnical and Geoenvironmental Engineering* **128**, No. 6, 530–535.

Poulos, H. G. (1995). Design of reinforcing piles to increase slope stability. *Canadian Geotechnical Journal* **32**, No. 5, 808–818.

Randolph, M. F. & Houlsby, G. T. (1984). The Limiting Pressure on a Circular Pile Loaded Laterally in Cohesive Soil. *Géotechnique* **34**, No. 4, 613–623.

Reese, L. C., Cox, W. R., & Koop, F. D. (1974). Analysis of Laterally Loaded Piles in Sand. *6th Offshore Technology Conference, Houston, Texas* **2**: 473–484.

Rollins, K. M., Gerber, T. M., Lane, J. D. & Ashford, S. A. (2005). Lateral Resistance of a Full-Scale Pile Group in Liquefied Sand. *Journal of the Geotechnical and Geoenvironmental Engineering Division, ASCE* **131**, 115–125.

Rowe, R. K. & Poulos, H. G. (1979). A method for predicting the effect of piles on slope behaviour. *3rd International Conference on Numerical Methods in Geomechanics*, Achen **3**, 1073–1085.

SLOPE/W. (2018). 4th ed., *GEO- SLOPE International Ltd.*, Calgary, AB, Canada.

Taghavi, A., Muraleetharan, K. K., Miller, G. A. & Cerato, A. B. (2016). Centrifuge Modeling of Laterally Loaded Pile Groups in Improved Soft Clay. *Journal of Geotechnical and Geoenvironmental Engineering, ASCE* **142**, No. 4, 04015099.

Tan, D. & Sarma, S. K. (2008). Finite element verification of an enhanced limit equilibrium method for slope analysis. *Géotechnique* **58**, No. 6, 481–487.

Wang, S. T., Vasquez, L. & Reese, L. C. (2008). Study of the Behavior of Pile Groups in Liquefied Soils, *14th World Conference on Earthquake Engineering,* Beijing, China.

Wei, W. B. & Cheng, Y. M. (2009). Strength reduction analysis for slope reinforced with one row of pile. *Computers and Geotechnics* **36**, 1176–1185.

Welch, R. C., & Reese, L. C. (1972). Laterally Loaded Behavior of Drilled Shafts. *Center for Highway Research Report, the University of Texas at Austin* **3**, No. 5, 65–89.

Wilson, D. W. (1998). Soil-pile-Superstructure interaction in Liquefying Sand and Soft Clay, *Ph.D. Dissertation*, Department of Civil and Environmental Engineering, University of California, Davis.

Won, J., You, K., Jeong, S. & Kim, S. (2005). Coupled effect in stability analysis of pile-slope systems. *Computers and Geotechnics* **32**, No. 4, 304–315.

Zienkiewicz, O. C., Humpheson, C. & Lewis, R. W. (1975). Associated and non-associated viscoplasticity and plasticity in soil mechanics. *Géotechnique* **25**, No. 4, 671–689.

Chapter 7

Conclusions and Future Work

7.1 Conclusions

Pile–soil interaction during the installation of displacement piles and those near the sloping ground is investigated in this thesis. The main focus of this study is to examine the response when large soil deformation occurs, especially in sensitive clays. As the traditional finite element (FE) program cannot handle such a large deformation, an Eulerian-based FE modeling technique available in Abaqus FE software is used for numerical analysis, which can handle extremely large deformation without any numerical issues related to mesh distortion. The undrained shear strength of sensitive clays degrades rapidly after the peak and is highly strain-rate dependent, especially after remoulding. Therefore, the analyses are performed implementing strain-softening and strain-rate dependent undrained shear strength models for sensitive clays. The software allows the simulation of only single-phase materials; therefore, a method to estimate the excess pore water pressure during pile installation is proposed. FE simulations are performed for the installation of vertical piles by jacking and driving in the level ground and also for inclined piles in the sloping ground. Finally, pile–soil interaction under lateral loading is studied.

The following sections provide a general overview of the entire thesis. The problem-specific conclusions have been presented at the end of each chapter (Chapters 3–6) and appendices.

The effects of pile installation on soil can be evaluated using simplified analytical solutions, such as cavity expansion theories and stain path methods. The spherical cavity expansion theory better resembles the response near the pile tip, while the cylindrical cavity expansion theory could be used for soil further above the pile tip. Although simple, these methods have a number of limitations and cannot explain the soil flow mechanisms properly during pile installation. Small-

strain and large deformation FE modeling techniques have also been used to model pile penetration; however, most of these analyses are limited to non-sensitive to low sensitive clays. In Chapter 3, large deformation FE analyses are performed for pile jacking in sensitive clays. It is shown that the response in sensitive clays is significantly different from that in non-sensitive clays because of the remoulding of sensitive clay near the pile.

Displacement piles are also installed by impact driving. A comprehensive numerical simulation of impact driving is presented in Chapter 4. The impact loading in a short period penetrates the pile rapidly; however, a rebound occurs when the load on the pile head is ceased. The strain-rate effects on undrained shear strength play a considerable role in impact driving. As the loading patterns are different, some different soil response is observed in impact driving from jacking.

Inclined pile installation in sensitive clay near the sloping ground could trigger the failure of a slope. In Chapter 5, the Rigaud landslide in Québec is reexamined considering the updated geotechnical investigation results and from large deformation finite element simulations. It is found that the presence of a thin sand/silt layer around the horizontal failure plane may not be the cause of failure, as hypothesized by the 1979 Expert Committee. Numerical simulations show that the presence of a stronger soil layer below the horizontal failure plane might be a cause of the progressive formation of a failure plane. A comparison with the Daniel's Harbour landslide in Newfoundland shows some similarities in failure patterns, although this landslide involved different strain-softening materials and was triggered by toe erosion and soil weakening near the toe.

Finally, in Chapter 6, the lateral pile–soil interaction is analyzed for two passive loading scenarios. Firstly, the effectiveness of piles for slope stabilization is shown. The soil flows through the space between the piles if the pile spacing is large. Piles at the mid-slope are the most effective

location to increase the factor of safety. Secondly, the impact load on a vertical pile caused by the sliding of a clay layer is modelled. A simplified approach is provided to calculate the structural response based on finite element calculated impact load. A large deformation FE method is useful to simulate the response for both cases.

7.2 Recommendations for Future Research

Although many important features involved in pile–soil interaction for sensitive clays could be successfully examined, the present study has some limitations. Some of the limitations are discussed in Chapters 3–6. In addition, some of the following issues could be addressed in future research:

i) The excess pore water pressure is calculated by developing a simplified approach because the current version of Abaqus CEL does not allow the simulation of two-phase materials. Also, the dissipation of excess pore water pressure could be studied in future.

ii) Further studies are required on the selection of model parameters, more specifically, the modeling of strain softening and strain rate effects on undrained shear strength.

iii) Taking advantage of symmetry, the three-dimensional effects are properly modelled for vertical penetration of piles in level ground. However, the inclined pile installation in the sloping ground and resulting slope failure could not be modelled in the three-dimensional conditions. It could be studied in future, although computationally very expensive.

iv) In general, the numerical simulation results are expected to be mesh-size dependent when the strain-softening behaviour of the soil is considered. In the present study, the element size scaling rule, as a function of the characteristic length of the element, is used. This issue could be examined further.

v)   For impact driving, additional analyses could be performed for varying forcing functions and effects of driving on ground vibration.

REFERENCES

Afshin, A. & Rayhani, M. T. (2015). Evaluation of bearing capacity with time for small-scale piles driven into Leda clay. *International Journal of Geotechnical Engineering* **9**, No. 3, 307–315.

Alves, A. M. L., Lopes, F. R., Randolph, M. F. & Danziger, B. R. (2009). Investigations on the dynamic behaviour of a small-diameter pile driven into soft clay. *Canadian Geotechnical Journal* **46**, 1418–1430.

Azzouz, A. S. & Lutz, D. G. (1986). Shaft behaviour of a model pile in plastic empire clays. *Journal of Geotechnical Engineering* **112,** No. 4, 389–406.

Azzouz, A. S. & Morrison, M. J. (1988). Field measurements on model pile in two clay deposits. *Journal of Geotechnical Engineering* **114,** No. 1, 104–121.

Bakroon, M., Daryaei, R., Aubram, D. & Rackwitz, F. (2018). Multi-material arbitrary Lagrangian-Eulerian and coupled Eulerian-Lagrangian methods for large deformation geotechnical problems. In *Numerical Methods in Geotechnical Engineering* **9**, 673–681.

Baligh, M. M. (1976). Cavity expansion in sands with curved envelopes. *Journal of the Geotechnical Engineering Division* **102**, No. 11, 1131–1146.

Baligh, M. M. (1985). Strain path method. *Journal of Geotechnical Engineering*, ASCE **111**, No. 9, 1108–1136.

Basu, P., Prezzi, M., Salgado, R. & Chakraborty, T. (2014). Shaft resistance and setup factors for piles jacked in clay. *Journal of Geotechnical and Geoenvironmental Engineering* **140**, No 3, 04013026.

Benson, D. J. (1992). Computational methods in Lagrangian and Eulerian hydrocodes. *Computer methods in Applied mechanics and Engineering* **99,** No. (2-3), 235–394.

Bernander, S. (1978). Brittle Failures in Normally Consilidated Soils. *Väg-och Vattenbyggaren* **49,** 8–9.

Bernander, S. (2000). Progressive landslides in long natural slopes: potential extension and configuration of finished slides in strain-softening soils (*Doctoral dissertation*, Luleå tekniska universitet).

Bishop, R. F., Hill, R. & Mott, N. F. (1945). The theory of indentation and hardness tests. *Proceedings of the Physical Society (1926-1948)* **57**, No. 3, 147.

Bjerrum, L., Hansen, B. J. & Sevaldson, R. (1958). Geotechnical investigations for quay structure in Horten, *Norwegian Geotechnical Institute, Publications* **28**, 1–18.

Bjerrum, L. (1961). The effective shear strength parameters of sensitive clays. In: *Proceedings of the 5th international conference soil mechanics foundation engineering*, Paris, 23–28.

Bjerrun, L. and Lo, K. Y. (1963). Effect of aging on the shear strength properties of a normally consolidated clay. *Géotechnique* **13**, 147–157.

Bjerrum, L. & Landva, A. (1966). Direct simple-shear tests on a Norwegian quick clay. *Norwegian Geotechnical Institute*, Oslo, 1–22.

Blanchet, R., Tavenas, F. & Garneau, R. (1980). Behavior of Friction Piles in Soft Sensitive Clay. *Canadian Geotechnical Journal* **17**, No. 2, 203–224.

Bond, A. J. & Jardine, R. J. (1991) Effects of installing displacement piles in a high OCR clay. *Géotechnique* **41,** No. 3, 341–363.

Borja, R. I. (1988). Dynamic of pile driving by the finite element method. *Computer and Geotechnics* **5**, 39–49.

Bozozuk, M., Fellenius, B. H. & Samson, L. (1978). Soil disturbance from pile driving in sensitive clay. *Canadian Geotechnical Journal* **15**, 346–361.

Brand, E. W. & Krasaesin, P. (1970). Investigation of an embankment failure in soft clay. *Bulletin of the International Association of Engineering Geology-Bulletin de l'Association Internationale de Géologie de l'Ingénieur*, **1**, No. 1, 53–64.

Burland, J. B., Rampello, S. & Georgiannou, V. N. (1997). A laboratory study of the strength of four stiff clays. *Géotechnique* **47**, No. 3, 491–514.

Butterfield, R. & Banerjee, P. K. (1971). The problem of pile group–pile capinteraction. *Géotechnique* **21**, No. 2, 135–142.

Cai, F. & Ugai, K. (2000). Numerical analysis of the stability of a slope reinforced with piles. *Soils & Foundations* **40**, No. 1, 73–84.

Canadian Geotechnical Society (CGS). (2006) Canadian foundation engineering manual, *4th edn.c/o BiTech Publisher Ltd, Richmond*, page 506.

Canadian Geotechnical Society (CGS). (2013) Errata – *Canadian foundation engineering manual* **4**.

Carson, M. A. (1977). On the retrogression of landslides in sensitive muddy sediments. *Canadian Geotechnical Journal* **14**, No. 4, 582–602.

Carson, M.A. (1979a). On the retrogression of landslides in sensitive muddy sediments: Reply. *Canadian Geotechnical Journal* **16**, 431–444.

Carson, M. A. (1979b). Le glissement de Rigaud (Québec) du 3 mai 1978: une interprétation du mode de rupture d'après la morphologie de la cicatrice. Géographie physique et Quaternaire **33**, No. 1, 63–92.

Carter, J. P., Randolph, M. F. & Wroth, C. P. (1979). Stress and pore pressure changes in clay during and after the expansion of a cylindrical cavity. *International Journal for Numerical and Analytical Methods in Geomechanics* **3**, No. 4, 305–322.

Carter, J. P. & Yeung, S. K. (1985). Analysis of cylindrical cavity expansion in a strain weakening material. *Computers and Geotechnics* **1**, No. 3, 161–180.

Carter, J. P., Booker, J. R. & Yeung, S. K. (1986). Cavity expansion in cohesive frictional soils. *Géotechnique* **36**, No. 3, 349–358.

Casagrande, A. (1932). The structure of clay and its importance in foundation engineering. *Boston Society Civil Engineers Journal*.

Chen, R. H. & Chameau, J. L. (1985). Discussion: Three-dimensional limit equilibrium analysis of slopes. *Géotechnique* **35**, No. 2, 215–216.

Chow, Y. K. & Teh, C. I. (1990). A theoretical study of pile heave. *Géotechnique* **40**, No. 1, 1–14.

Chow, Y. K. (1996). Analysis of piles used for slope stabilization. *International Journal for Numerical and Analytical Methods in Geomechanics* **20**, No. 9, 635–646.

Cooke, R. W., Price, G. & Tarr, K. (1979). Jacked piles in London Clay: a study of load transfer and settlement under working conditions. *Géotechnique* **29**, No. 2, 113–147.

Crawford, C. B. (1963). Cohesion in an undisturbed sensitive clay. *Géotechnique* **13**, No. 2, 132–146.

Cruden, D. M. & Varnes, D. J. (1996). Landslides: investigation and mitigation. Chapter 3-Landslide types and processes. *Transportation research board special report* **247**.

Cubrinovski, M., Ishihara, K. & Poulos, H. (2009). Pseudo-static analysis of piles subjected to lateral spreading. *Bulletin of the New Zealand Society for Earthquake Engineering* **42**, No.1, 28–38.

Cummings, A. E., Kerkhoff, G. O. & Peck, R. B. (1950). Effect of driving piles into soft clay. *Transactions of the American Society of Civil Engineers* **115**, No. 1, 275–285.

Davis, R. O. & Phelan, P. J. (1978). Numerical approximations in pile-driving analysis. *International Journal for Numerical and Analytical Methods in Geomechanics* **2**, No. 3, 303–310.

Davidson, J., Castelletti, M., Torres, I., Terente, V. & Irvine, J. (2019). Pile driving prediction for monopile foundations in London clay.

de Chaunac, H. & Holeyman, A. (2018). Numerical analysis of the set-up around the shaft of a closed-ended pile driven in clay. *Géotechnique* **68**, No. 4, 332–344.

Dey, R., Hawlader, B., Phillips, R. & Soga, K. (2015). Large deformation finite-element modeling of progressive failure leading to spread in sensitive clay slopes. *Géotechnique* **65**, No. 8, 657–668.

Demers, D., Robitaille, D., Locat, P. & Potvin, J. (2014). Inventory of large landslides in sensitive clay in the province of Québec, Canada: preliminary analysis. In *Landslides in sensitive clays* (pp. 77-89). Springer, Dordrecht.

Doherty, P. & Gavin, K. (2011). Shaft capacity of open-ended piles in clay. *Journal of Geotechnical and Geoenvironmental Engineering* **137**, No. 11, 1090–1102.

Einav, I. & Randolph, M. F. (2005). Combining upper bound and strain path methods for evaluating penetration resistance. *International Journal for Numerical Methods in Engineering* **63**, No. 14, 1991–2016.

Fan, S., Bienen, B. & Randolph, M. F. (2021). Effects of Monopile Installation on Subsequent Lateral Response in Sand. I: Pile Installation. *Journal of Geotechnical and Geoenvironmental Engineering* **147**, No. 5, 04021021.

Fellenius, B. & Broms, B. (1969). Negative skin friction acting on steel pipe pile in clay. In *Proc. 7th Int. Conf. on Soil Mech*, **2**.

Fellenius, B. H. & Samson, L. (1976). Testing drivability of concrete piles and disturbance to sensitive clay. *Canadian Geotechnical Journal* **13**, 139–160.

Flaate, K. (1972). Effects of pile driving in clays. *Canadian Geotechnical Journal* **9**, 81–88.

Gavin, K. G. & Lehane, B. M. (2003). The shaft capacity of pipe piles in sand. *Canadian geotechnical journal* **40**, No. 1, 36–45.

Gibson, R. E. & Anderson, W. F. (1961). In-situ measurement of soil properties with pressuremeter, *Civil Engineering and Public Works review* **56**, 658.

Gill, D. R. & Lehane, B. M. (2000). Extending the strain path method analogy for modeling penetrometer installation. *International journal for numerical and analytical methods in geomechanics* **24**, No. 5, 477–489.

Goble, G. G. & Rausche, F. (1980). Pile drivability predictions by CAPWAP. In *Numerical methods in offshore piling*, Thomas Telford Publishing, 29–36.

Graham, J., Crooks, J. H. A. & Bell, A. L. (1983). Time effects on the stress-strain behaviour of natural soft clays. *Géotechnique* **33**, No. 3, 327–340.

Griffiths, D. V. & Lane, P. A. (1999). Slope stability analysis by finite elements. *Géotechnique* **49**, No. 3, 387–403.

Gylland, A., Jostad, H. P. & Nordal, S. (2012). Failure geometry around a shear vane in sensitive clays. In: *Proceedings of the 16th Nordic geotechnical meeting*, Copenhagen **1**, 103–110.

Hill, R. (1950). A comparative study of some variational principles in the theory of plasticity.

Ho, I. H. (2015). Numerical study of slope-stabilizing piles in undrained clayey slopes with a weak thin layer. *International Journal of Geomechanics* **15**, No. 5, 06014025.

Hu, Y. & Randolph, M. F. (1998). A practical numerical approach for large deformation problems in soil. *International Journal for Numerical and Analytical Methods in Geomechanics* **22**, No. 5, 327–350.

Hwang, J. H., Liang, N. & Chen, C. H. (2001). Ground response during pile driving. *Journal of Geotechnical and Geoenvironmental Engineering* **127***, No.* 11, 939–949.

Ito, T. & Matsui, T. (1975). Methods to estimate lateral force acting on stabilizing piles. *Soils and Foundations* **15**, No. 4, 43–59.

Ito, T., Matsui, T. & Hong, W. P. 1981. Design method for stabilizing piles against landslide-one row of piles. *Soils and Foundations* **21**, No. 1, 21–37.

Jostad, H. P., Andresen, L. & Thakur, V. (2006). Calculation of shear band thickness in sensitive clays. In: *6th numerical methods in geotechnical engineering* **1**, 27–32.

Kallstenius, T. (1963). *Studies on clay samples taken with standard piston sampler*.

Karlsrud, K., Aas, G. & Gregersen, O. (1985). Can we predict landslide hazards in soft sensitive clays? Summary of Norwegian practice and experiences. *Publikasjon-Norges Geotekniske Institutt*, 158.

Karlsson, R. & Hansbo, S. (1989). Soil classification and identification. Byggforskningsrådet. Dokument D8:1989. Stockholm.

Karmaker, R. & Hawlader, B. (2018). Modeling of Pile Stabilized Clay Slopes Using a Large Deformation Finite-Element Method, *7th Canadian Geohazards Conference*, Canmore, Canada, Paper No-155.

Karmaker, R., Hawlader, B. & Dutta, S. (2018). Modeling of vertical piles subjected to a clay crust movement over a liquefied soil. *GeoEdmonton 2018*, AB, Canada. Paper No-488.

Karmaker, R., Hawlader, B. & Chen, W. (2019). Finite element modeling of jacked piles in clay and loose sand. *72nd Canadian Geotechnical Conference, GeoSt.John's 2019*, St. John's, NL, Canada. Paper No-436.

Karmaker, R., Hawlader, B., Dey, R. & Deering, P. 2021. A landslide case study in Lacustrine/Marine clay deposits in western Newfoundland–field observation and numerical analysis. *GeoNiagara 2021*, Niagara, ON, Canada. Paper No. 350.

Karmaker, R. and Hawlader, B. 2022. Large deformation finite-element modeling of pile jacking in sensitive clay. In *Proc. of 20th Int. Conf. on SMGE*, Sydney, Australia.

Ko, J., Jeong, S. & Lee, J. K. (2016). Large Deformation FE Analysis of Driven Steel Pipe Piles with Soil Plugging. *Computers and Geotechnics* **71**, 82–97.

Koizumi, Y. & Ito, K. (1967). Field tests with regard to pile driving and bearing capacity of piled foundations. *Soils and Foundations* **7**, No. 3, 30–53.

Konkol, J. (2015). Numerical estimation of the pile toe and shaft unit resistances during the installation process in sands. *Studia Geotechnica et Mechanica* **37**, No. 1, 37–44.

Konrad, J. M. & Roy, M. (1987). Bearing capacity of friction piles in marine clay. *Geotechnique* **37**, No. 2, 163–175.

Kou, H., Zhang, M. & Yu, F. (2015). Shear zone around jacked piles in clay. *Journal of Performance of Constructed Facilities* **29**, No. 6, 04014169-6.

Lacasse, S., Berre, T. & Lefebvre, G. (1985). Block sampling of sensitive clays. In *Proceedings of the eleventh international conference on soil mechanics and foundation engineering*, san francisco, 12–16.

Ladanyi, B. (1963). Expansion of a cavity in a saturated clay medium. *Journal of the Soil Mechanics and Foundations Division* **89**, No. 4, 127–161.

LaGatta, D. P. & Whiteside, S. L. (1984). Failure of a dredged slope in a sensitive clay.

Länsivaara, T. & Poutanen, T. (2014). Safety concepts for slope stability. In *Landslides in Sensitive Clays,* Springer, Dordrecht, 395–407.

Lee, S. L., Chow, Y. K., Karunaratne, G. P. & Wong, K. Y. (1988). Rational wave equation model for pile-driving analysis. *Journal of geotechnical engineering* **114**, No. 3, 306–325.

Lee, C. Y., Hull, T. S. & Poulos, H. G. (1995). Simplified pile-slope stability analysis. *Computers and Geotechnics* **17**, No. 1, 1–16.

Lefebvre, G. & LeBoeuf, D. (1987). Rate effects and cyclic loading of sensitive clays. *Journal of Geotechnical Engineering* **113**, No.5, 476–489.

Lefebvre, G. & Pfendler, P. (1996). Strain rate and preshear effects in cyclic resistance of soft clay. *Journal of geotechnical engineering* **122**, No. 1, 21–26.

Lefebvre, G. (2017). Sensitive clays of Eastern Canada: from geology to slope stability. In *Landslides in Sensitive Clays*, Springer, Cham. 15–34.

Lehane, B. M. & Gavin, K. G. (2001). Base resistance of jacked pipe piles in sand. *Journal of Geotechnical and Geoenvironmental Engineering* **127**, No. 6, 473–480.

Leroueil, S., Vaunat, J. & Picarelli, L. (1996). Geotechnical characterisation of slope movements. In *proceedings of the 7th International Symposium on Landslides* **1**, 53–74.

Lo, K. Y. (1961). Stress-strain relationship and pore water pressure characteristics of a normally-consolidated clay. In *Proc. 5th Int. Conf. Mech. Found. Eng* **1**, 219–224.

Lo, K. Y. & Stermac, A. G. (1965). Induced pore pressures during pile-driving operations. In Proceeding of *Soil Mechanics & Foundation Engineering Conference,* Canada.

Lo, K. Y. & Morin, J. P. (1972). Strength anisotropy and time effects of two sensitive clays. *Canadian Geotechnical Journal* **9**, No. 3, 261–277.

Locat, A., Leroueil, S., Bernander, S., Demers, D., Jostad, H. P. & Ouehb, L. (2011). Progressive failures in eastern Canadian and Scandinavian sensitive clays. *Canadian Geotechnical Journal* **48**, No. 11, 1696–1712.

Locat, A., Jostad, H. P. & Leroueil, S. (2013). Numerical modeling of progressive failure and its implications for spreads in sensitive clays. *Canadian Geotechnical Journal* **50**, No. 9, 961–978.

Locat, A., Leroueil, S., Fortin, A., Demers, D. & Jostad, H. P. (2015). The 1994 landslide at Sainte-Monique, Quebec: geotechnical investigation and application of progressive failure analysis. *Canadian Geotechnical Journal* **52**, No. 4, 490–504.

Locat, A., Locat, P., Demers, D., Leroueil, S., Robitaille, D. & Lefebvre, G. (2017). The Saint-Jude landslide of 10 May 2010, Quebec, Canada: Investigation and characterization of the landslide and its failure mechanism. *Canadian geotechnical journal* **54**, No. 10, 1357–1374.

Lunne, T., Berre, T. & Strandvik, S. (1999). Sample disturbance effects in soft low plastic Norwegian clay. *Publication 204*. Norwegian Geotechnical Institute, Oslo.

Mabsout, E. M. & Tassoulas, J. L. (1994). A finite element model for the simulation of pile driving, *International journal for numerical methods in Engineering* **37**, 257–278.

Mabsout, E. M., Reese, L. C. & Tassoulas, J. L. (1995). Study of pile driving by finite-element method. *Journal of Geotechnical Engineering* **121**, No. 7, 535–543.

Mabsout, E. M., Sadek, S. M. & Smayra, T. E. (1999). Pile Driving by Numerical Cavity Expansion, *International journal for numerical and analytical methods* **23**, No. 11, 1121–1140.

Mayne, P. W., Cargill, E. & Miller, B. (2019). Geotechnical characteristics of sensitive Leda clay at Canada test site in Gloucester, Ontario. *AIMS Geoscience* **5**, 390–411.

Nian, T. K., Huang, R. Q., Wan, S. S. & Chen, G. Q. (2012). Three-dimensional strength-reduction finite element analysis of slopes: geometric effects. *Canadian Geotechnical Journal* **49**, No. 5, 574–588.

Odenstad, S. (1951). The landslide at Sköttorp on the Lidan River, February 2, 1946. *Royal Swedish Geotechnical Institute Proceedings* **4**, 1–3.

Orrje, O. & Broms, B. B. (1967). Effects of pile driving on soil properties. *Journal of the Soil Mechanics and Foundations Division* **93**, No. 5, 59–73.

Perret, D., Mompin, R., Demers, D., Lefebvre, G. & Pugin, A. J. M. (2013, October). Two large sensitive clay landslides triggered by the 2010 Val-des-bois earthquake, Quebec (Canada)–implications for risk management. In *Workshop on Landslides in Sensitive Clays (IWLSC), Québec, Canada*, 28–30.

Poulos, H. G. (1995). Design of reinforcing piles to increase slope stability. *Canadian Geotechnical Journal* **32**, No. 5, 808–818.

Qiu, G., Henke, S. & Grabe, J. (2011). Application of a Coupled Eulerian–Lagrangian approach on geomechanical problems involving large deformations. *Computers and Geotechnics* **38**, No. 1, 30–39.

Quinn, P. E. (2009). Large landslides in sensitive clay in eastern Canada and the associated hazard and risk to linear infrastructure **71**, No. 11.

Quinn, P. E., Diederichs, M. S., Rowe, R. K. & Hutchinson, D. J. (2012). Development of progressive failure in sensitive clay slopes. *Canadian Geotechnical Journal* **49**, No. 7, 782–795.

Randolph, M. F., Carter, J. P. & Wroth, C. P. (1979). Driven piles in clay-the effects of installation and subsequent consolidation. *Géotechnique* **29**, No. 4, 361–393.

Randolph, M. F., Leong, E. C. & Houlsby, G. T. (1991). One-dimensional analysis of soil plugs in pipe piles. *Géotechnique* **41**, No. 4, 587–598.

Randolph, M. F. (2003). Science and empiricism in pile foundation design. *Géotechnique* **53**, No. 10, 847–875.

Rooz, A. F. H. & Hamidi, A. (2019). A numerical model for continuous pile driving using ALE adaptive mesh method. *Soil Dynamics and Earthquake Engineering* **118**, 134–143.

Rosenqvist, I. T. (1953). Considerations on the sensitivity of Norwegian quick-clays. *Géotechnique* **3**, No. 5, 195–200.

Roy, M., Blanchet, R., Tavenas, F. & Rochelle, P. L. (1981). Behaviour of a sensitive clay during pile driving. *Canadian Geotechnical Jounal* **18**, No. 1, 67–85.

Roy, M., Tremblay, M., Tavenas, F. & La Rochelle, P. (1982). Development of pore water pressures in quasi-static penetration tests in sensitive clay. *Canadian Geotechnical Journal* **19**, 124–138.

Roy, M. & Leblanc, A. (1988). Factors affecting the measurements and interpretation of the vane strength in soft sensitive clays. In *Vane shear strength testing in soils: Field and laboratory studies*. ASTM International.

Sagaseta, C. (1987). Analysis of undrained soil deformation due to ground loss. *Géotechnique* 37, No. 3, 301–320.

Sagaseta, C., Whittle, A. J. & Santagata, M. (1997). Deformation analysis of shallow penetration in clay. *International journal for numerical and analytical methods in geomechanics* **21**, No. 10, 687–719.

Sagaseta, C. & Whittle, J. (2001). Prediction of ground movements due to pile driving in clay. *Journal of Geotechnical and Geoenvironmental Engineering* **127**, No. 1, 55–66.

Schofield, A. N. & Wroth, P. (1968). Critical state soil mechanics. London: *McGraw-hill* **310**.

Sandven, R., Ørbech, T., & Lunne, T. (2004). Sample disturbance in highly sensitive clay. In: *Proceedings of the 2nd international conference on geotechnical and geophysical site characterization*, 1861–1868.

Shen, S. L., Han, J., Zhu, H. H. & Hong, Z. S. (2005). Evaluation of a dike damaged by pile driving in soft clay. *Journal of performance of constructed facilities* **19**, No. 4, 300–307.

Sheng, D., Eigenbrod, K. D. & Wriggers, P. (2005). Finite element analysis of pile installation using large-slip frictional contact. *Computers and Geotechnics* **32**, 17–26.

Smith, E. A. L. (1960). Pile driving analysis by the wave equation. *Journal of the Soil Mechanics and Foundations Division,* ASCE **86**, No. 4, 35–61.

Smith, I. M. & Chow, Y. K. (1982). Three-dimensional analysis of pile driveability. In *proc. of 2nd International conference of numerical methods on offshore piling, university of Texas, Austin* **2**, 1–19.

Smith, I. M. & To, P. (1988). Numerical studies of vibratory pile driving. *International Journal for numerical and analytical methods in geomechanics* **12**, No. 5, 513–531.

Stark, T. D. & Contreas, I. A. (1996). Constant volume ring shear apparatus. *Geotechnical Testing Journal* **19**, No. 1, 3–11.

Take, W. A., Valsangkar, A. J. & Randolph, M. F. (1999). Analytical solution for pile hammer impact. *Computers and Geotechnics* **25**, No. 2, 57–74.

Tavenas, F., Flon, P., Leroueil, S. & Lebuis, J. (1983). Remolding energy and risk of slide retrogression in sensitive clays. In *Proceedings of the Symposium on Slopes on Soft Clays,* SGI Report, Linköping, Sweden, No. 17, 423–454.

Tavenas, F. (1984). Landslides in Canadian sensitive clays–a state-of-the-art. In *Proceedings of the 4th International Symposium on Landslides, Toronto, Ont.*, 16–21.

Teh, C. I. & Houlsby, G. T. (1991). An Analytical Study of the Cone Penetration Test in Clay. *Géotechnique* **41**, No. 1, 17–34.

Tian, Y., Wang, D. & Cassidy, M. (2011). Large deformation finite element analysis of offshore geotechnical penetration tests. *In proceeding of the second International Symposium on Computational Geomechanics, USA* **1**, 925–933.

Thakur, V., Nordal, S., Jostad, H. P. & Andresen, L. (2005). Study on pore water pressure dissipation during shear banding in sensitive clays. In *11th international conference on computer methods and advances in geomechanics, IACMAG,* Turino, Italy 4, 289–296.

Thakur, V. (2007). Strain localization in sensitive soft clays. *Ph.D. thesis*, Norwegian University of Science and Technology.

Thakur, V. (2011). Numerically observed shear bands in soft sensitive clays. *International Journal of Geomechanics and Geoengineering* **6**, No. 2.

Thakur, V. & Degago, S. (2012). Quickness of sensitive clays, *Géotechnique Letter* **2**, 81–88.

Thakur, V., Degago, S. A., Oset, F., Aabøe, R., Dolva, B. K., Aunaas, K., ... & L'Heureux, J. S. (2014a). Characterization of post-failure movements of landslides in soft sensitive clays. In *Landslides in sensitive clays,* Springer, Dordrecht, 91–103.

Thakur, V., Jostad, H. P., Kornbrekke, H. A. & Degago, S. A. (2014b). How well do we understand the undrained strain softening response in soft sensitive clays?. In *Landslides in Sensitive Clays*, Springer, Dordrecht, 291–303.

Tho, K. K., Leung, C. F., Chow, Y. K. & Swaddiwudhipong, S. (2012). Eulerian finite-element technique for analysis of jack up spudcan penetration. *International Journal Geomechanics* **12**, No. 1, 64–73.

Tomlinson, M. J. (1957). The Adhesion of Piles Driven in Clay Soils. *4th International Conference of Soil Mechanics and Foundation Engineering,* London **2**, 66–71.

Torstensson, B. A. (1973). Kohesionspalar I lös lera. En Fältstudie. *Ph.D. thesis*, Chalmers Institute of Technology, Gothenburg.

Vaid, Y., Robertson, P. & Campanella, R. (1979). Strain rate behaviour of Saint-Jean-Vianney clay. *Canadian Geotechnical Journal* **16**, No. 1, 34–42.

Vesić, A. S. (1972). Expansion of cavities in infinite soil mass. *Journal of the Soil mechanics and Foundations Division* **98**, No. 3, 265–290.

Viggiani, C. (1981). Ultimate lateral load on piles used to stabilize landslides. *10th International Conference on Soil Mechanics and Foundation Engineering*, A. A. Balkema, Rotterdam, Netherlands **3**, 555–560.

Wang, J. & Gadala, M. S. (1997). Formulation and survey of ALE method in nonlinear solid mechanics. *Finite Elements in Analysis and Design* **24**, No. 4, 253–269.

Wang, D., Hu, Y. & Randolph, M. F. (2010). Three-dimensional large deformation finite-element analysis of plate anchors in uniform clay. *Journal of geotechnical and geoenvironmental engineering* **136**, No. 2, 355–365.

Wang, D., Hu, Y. & Randolph, M. F. (2011). Keying of rectangular plate anchors in normally consolidated clays. *Journal of Geotechnical and Geoenvironmental Engineering* **137**, No. 12, 1244–1253.

Wang, D., Bienen, B., Nazem, M., Tian, Y., Zheng, J., Pucker, T. & Randolph, M. F. (2015). Large deformation finite element analyses in geotechnical engineering. *Computers and Geotechnics* **65**, 104–114.

Wang, C., Hawlader, B., Perret, D. & Soga, K. (2020). Effects of Geometry and Soil Properties on Type and Retrogression of Landslides in Sensitive Clays, *Géotechnique*, 1–15.

Wei, W. B. & Cheng, Y. M. (2009). Strength reduction analysis for slope reinforced with one row of pile. *Computers and Geotechnics* **36**, 1176–1185.

White, D., Finlay, T., Bolton, M. & Bearss, G. (2002). Press-in piling: ground vibration and noise during pile installation. *Deep Foundations 2020*, 363–371.

Won, J., You, K., Jeong, S. & Kim, S. (2005). Coupled effect in stability analysis of pile-slope systems. *Computers and Geotechnics* **32**, No. 4, 304–315.

Yang, J., Tham, L. G., Lee, P. K. K., Chan, S. T. & Yu, F. (2006). Behaviour of jacked and driven piles in sandy soil. *Géotechnique* **56**, No. 4, 245–259.

Yu, H. S. & Houlsby, G. T. (1991). Finite cavity expansion in dilatant soils: loading analysis. *Géotechnique* **41**, No. 2, 173–183.

Zhou, H., Liu, H., Yuan, J. & Chu J. (2019). Numerical simulation of XCC pile penetration in undrained clay. *Computers and Geotechnics* **106**, 18–41.

Zhu, H. & Randolph, M. F. (2011). Numerical analysis of a cylinder moving through rate dependent undrained soil. *Ocean Eng.* **38**, No. 7, 943–953.

Appendix-I

Finite element modeling of jacked piles in clay and loose sand

This paper has been published in the 72nd Canadian Geotechnical Conference (GeoSt.John's 2019), St. John's, NL, Canada. Most of the research work presented in this paper was conducted by the first author. He also prepared the draft manuscript. The other authors supervised the research and reviewed the manuscript.

Finite element modeling of jacked piles in clay and loose sand

Ripon Karmaker, Bipul Hawlader & Chen Wang
Memorial University of Newfoundland, St. John's, NL, Canada

ABSTRACT

Pile jacking is one of the alternative pile installation methods to conventional dynamic installations. Jacking does not cause significant vibration or disturbance of the surrounding soil. The present study uses a Coupled Eulerian-Lagrangian (CEL) approach of finite element analysis to simulate the pile jacking process. Quasi-static penetration of a rigid pile in clay and loose sand is simulated. The simulations are performed for an undrained condition for clay and a drained condition for sand. The penetration resistance, penetration-induced radial stress, ground surface heave, and plastic shear strain resulting from pile jacking in clay and sand are compared.

RÉSUMÉ

Le levage de pieux est l'une des méthodes alternatives d'installation des pieux aux installations dynamiques conventionnelles. Le fonçage ne provoque pas de vibrations importantes ni de perturbation du sol environnant. La présente étude utilise une approche d'analyse par éléments finis Coupled Eulerian-Lagrangian (CEL) pour simuler le processus de levage de pieux. La pénétration quasi statique d'un pieu rigide en argile et en sable meuble est simulée. Les simulations sont effectuées pour une condition non drainée pour l'argile et une condition drainée pour le sable. La résistance à la pénétration, la contrainte radiale induite par la pénétration, le soulèvement de la surface du sol et la contrainte de cisaillement du plastique résultant du fonçage de pieux dans l'argile et le sable sont comparés.

1. INTRODUCTION

Dynamic pile driving techniques using hammers or vibrators are commonly used to drive piles. However, the dynamic installation could cause noise, vibration, and even slope failure (e.g., of sensitive clay slopes). The jacking of the pile is an alternative approach to avoid these issues, where a pile is pushed into the soil using a jacking machine up to the jack stroke length, usually at a constant rate.

A large volume of soil displaces when displacement piles (e.g., concrete, closed-ended pipe and plugged open-ended pipe piles) are penetrated into the soil. The displacement of soil could create a number of issues. If the soil has a low hydraulic conductivity (clay), significant excess pore water pressure generates, which cannot dissipate during the period of installation as commonly practiced. This type of penetration could be considered as an undrained loading case. However, for the highly permeable soils (sand), the generated excess pore water pressure would be dissipated; therefore, the drained soil behaviour governs the installations.

The installation of a pile causes a large radial stress increase. At small penetrations, the soil flows outward and upwards, which causes ground surface heave. However, at greater depths, the soil primarily displaces radially; therefore, the cavity expansion theory can be used for modeling the response (Randolph et al. 1979). Using the modified Cam-clay model and assuming the process as an undrained expansion of a cylindrical cavity, Randolph et al. (1979) calculated the radial stress, excess pore water pressure generation, and subsequent consolidation. The concept of cavity expansion has also been used by other researchers (e.g., Basu et al. 2014).

The strain path method (SPM) has also been used to simulate the penetration of piles. Sagaseta and Whittle (2001) modeled the ground movement caused by the installation of piles in clay. They have shown large plastic shear strains around the pile, and their developed SPM could handle such large strains.

The installation of a pile involves a significantly large deformation of soil. The typical finite element (FE) modeling cannot handle such large deformations; therefore, advanced large deformation FE modeling techniques have been used to simulate this process (Qiu et al. 2011; Ko et al. 2016). Note that the penetration of a pile is similar to cone penetration on a small scale. Some studies focused on analytical and numerical modeling of cone penetration in clay and sand (Teh and Houlsby 1991; Wang et al. 2015). Also, field and small-scale laboratory tests were conducted to understand the mechanisms involved in pile installations (Deeks et al. 2005; Yang et al. 2006). The plastic shear strains generated around the pile could reduce the shear strength of the soil. Moreover, the soil displacement could cause ground heave which could be another design issue.

The main objective of the present study to investigate pile installation in clay and loose sand using a large deformation FE modeling technique.

2. PROBLEM STATEMENT

A solid pile of 0.4-m diameter (D) is penetrated into the soil at a constant velocity (v_p) along the z-axis, as shown in Fig. 1. The bottom of the pile is modeled as a half sphere. At any instant, the depth of the pile tip (point T in the inset of Fig. 1) from the ground surface is denoted as w_{tip}. The pile is penetrated to a maximum depth of 10D. The pile penetration in both clay and loose sand is simulated.

Initially, the tip of the pile is placed slightly above the ground surface (w_{tip} = 0.01 mm) to avoid any interaction of the pile with the soil when the soil layer is brought to the in-situ stress condition through a gravity loading step, as discussed later. The groundwater table is considered at the ground surface.
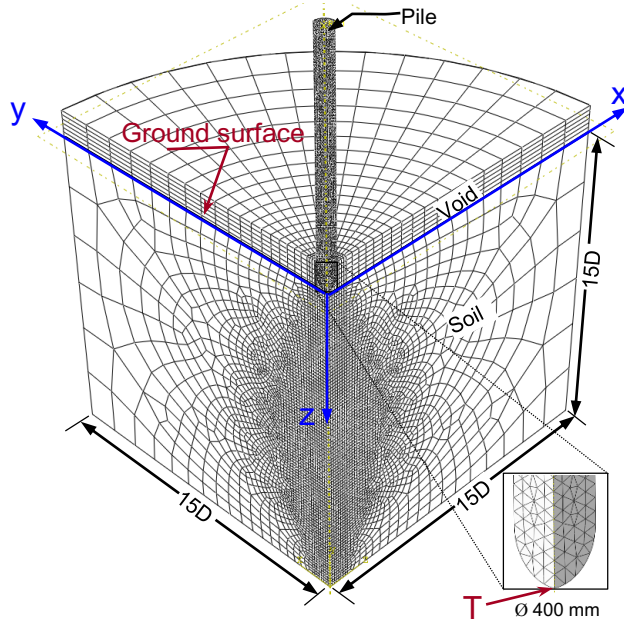
Figure 1: Finite-element mesh

3. FINITE ELEMENT MODELING

The Coupled Eulerian-Lagrangian (CEL) approach available in Abaqus 6.14-2 FE software is used for numerical modeling. One of the main advantages of the CEL is that an extremely large deformation can be simulated without any numerical issues related to mesh distortion, which cannot be performed using a traditional Lagrangian-based FE modeling technique.

Three-dimensional FE analysis is performed by modeling a quarter of the whole domain. The FE mesh used in the analysis is shown in Fig. 1. A dense mesh is used in the zone near the pile where significant soil deformation is expected due to the penetration of the pile. The mesh size is increased with radial distance to reduce the computational time.

The cylindrical boundary is placed at a radial distance of $15D$ from the center of the pile. The height of the soil is $15D$, which represents that at the maximum penetration depth ($w_{tip} = 10D$), the bottom boundary will be $5D$ far from the tip of the pile. Analyses are also performed with a larger soil domain by placing the boundaries at larger distances and also using finer mesh than that of Fig. 1; however, no significant changes in the result is found. Therefore, the FE mesh shown in Fig. 1 is used.

The soil is modeled as a Eulerian material such that it can flow through the mesh without causing any numerical issue related to mesh distortion (Qui et al. 2011, Karmaker and Hawlader 2018). The pile is modeled as a Lagrangian rigid body. The FE model consists of three parts: soil, pile, and a void. The soil and void for the initial condition are defined by using the Eulerian Volume Fraction (EVF) tool in the software. For a soil element, EVF = 1 means that the element is filled with soil. On the other hand, EVF = 0 represents no soil in the void elements. Note that, during

the penetration of the pile, the soil might displace in the void and fill the void element partially (i.e., 0 < EVF < 1.0).

Soil is modeled using the EC3D8R elements, which are 8-node linear multi-material Eulerian brick elements. The pile is first discretized using C3D10M elements, which are 10-node modified quadratic tetrahedrons. The pile is then defined as a rigid body using rigid constraints.

Zero-velocity boundary conditions are used normal to all the vertical faces. In the curved cylindrical outer surface, the soil is allowed to move only in the vertical direction. At the bottom of the domain, zero-velocity boundary conditions are applied in all three directions (i.e. $v_x = v_y = v_z = 0$), meaning that the soil elements next to this boundary are restrained from any movement. No boundary condition is applied at the soil–void interface so that the soil can displace into the void during the penetration of the pile when needed (e.g., ground surface heaving near the pile).

For clay, the analysis is performed for an undrained condition. The soil is modeled as an elastic-perfectly plastic material. Based on the Tresca yield criterion, the yield strength ($\sigma_y = \sqrt{3}s_u$, where s_u is the undrained shear strength of clay) is given as an input. The undrained Young's modulus (E_u) of $500s_u$ is used. The analysis is performed for $s_u = 30$ kPa; however, two more analyses are carried out for $s_u = 10$ and 20 kPa. The undrained Poisson's ratio (ν_u) of 0.49 and submerged unit weight (γ') of 10 kN/m^3 are used. The parameters used in the FE analysis are listed in Table 1.

For sand, the Mohr–Coulomb failure criterion is used to simulate the drained behaviour of loose sand. The angle of internal friction (ϕ') of 32°, which is equal to the critical state friction angle, and the zero dilation angle (ψ) are used (Bolton 1986). The drained Young's modulus (E) of 13.5 MPa and the drained Poisson's ratio of 0.25 are used. A small value of cohesion (c') is used in the FE analysis in order to avoid numerical issues. The other parameters used in the analysis are listed in Table 1.

Table 1: Geotechnical properties used in FE analysis

	Soil Parameter	Value
Clay	Submerged unit weight, γ' (kN/m^3)	10
	Undrained shear strength, s_u (kPa)	30 (20, 10)
	Undrained Young's modulus E_u	$500s_u$
	Undrained Poisson's ratio, ν_u	0.49
Sand	Submerged unit weight, γ' (kN/m^3)	7.8
	Drained friction angle, ϕ' (°)	32
	Dilation angle, ψ (°)	0
	Young's modulus E (MPa)	13.5
	Drained Poisson's ratio, ν'	0.25
	Drained cohesion, c' (kPa)	0.1

The pile-soil interface frictional resistance depends on a number of factors, such as surface roughness of the pile, friction angle for the drained condition, and the undrained shear strength for an undrained loading condition. In the present study, the pile–soil interface for clay is modeled as a smooth condition. For sand, an interface friction coefficient μ of 0.3 is taken. Further studies are required to investigate the effects of interface behaviour on pile penetration.

The present FE modeling consists of two loading steps. First, the gravity loading is applied gradually to bring the soil to the in-situ state. At the end of the gravity loading step, the ratio between the horizontal (radial in this case) and vertical stress (K) is $\nu/(1-\nu)$, where ν is the Poisson's ratio. In the second step, the pile is displaced downward at a constant velocity (v_p).

4. RESULTS

In the following sections, the discussion is focused primarily on the force–displacement relation and associated soil failure mechanisms during penetration.

For the undrained penetration in clay, the penetration resistance has two components: (i) the resistance from the shear strength of soil (F_s), and (ii) self-weight, which is similar to buoyancy (F_b). A detailed discussion on interpreting the effects of buoyancy on undrained penetration of an object in soft clay is available in the work of Merifield et al. (2009).

In the present FE analysis, the total resistance (F) for a given pile tip depth (w_{tip}) is obtained from the reaction force at the reference point of the rigid pile. For clay, subtracting F_b from F, the soil resistance is obtained as $F_s = F - F_b$. The soil resistance is then presented as a normalized penetration resistance (N) as $N = F_s/s_u A_p$, where A_p is the cross-sectional area of the pile. The F_b is calculated as $\gamma' A_p w_{tip}$, where $A_p w_{tip}$ represents the volume of the displaced soil.

4.1 Effects of penetration rate

In the field, the pile is jacked at a range of velocities. For example, Yang et al. (2006) jacked the test piles at v_p = 0.017–0.03 m/s. In the present study, the penetration rate effects on soil behaviour, for example, excess pore water pressure generation/dissipation or strain-rate effects on undrained shear strength, are not modeled. However, as the analyses are performed for a quasi-static condition, the penetration velocity should be sufficiently small to minimize the inertia effect.
Figure 2 shows the normalized penetration resistance in clay for three penetration velocities. The lowest penetration velocity (v_p = 0.01 m/s) gives a slightly lower N than that for v_p = 0.1 m/s. Therefore, recognizing a significant increase in computational time with the reduction of v_p, the analyses presented in the following sections are conducted with v_p = 0.1 m/s.

4.2 Comparison with previous numerical and analytical solutions

Figure 3 shows the comparison of the normalized force versus tip depth curves obtained from the present FE analysis and two previous large deformation FE analyses. The calculated resistance shown in Fig. 3 is only due to the tip resistance, because a smooth condition is used for the pipe–soil interface.

Using the implicit remeshing and interpolation technique by small strain (RITSS), Wang et al. (2015) simulated the penetration of a cone in weightless soil (i.e., buoyancy force $F_b = 0$; therefore, the calculated force is

only due to soil resistance). They also simulated cone penetration using CEL. Figure 3 shows that the present CEL results closely match with the CEL results of Wang et al. (2015). The small difference, especially near the ground surface, is potentially due to higher E_u and the shape of the pile tip, a half-sphere in this study, while it is a cone in Wang et al. (2015). Moreover, CEL modeling gives slightly higher N than that of RITSS.
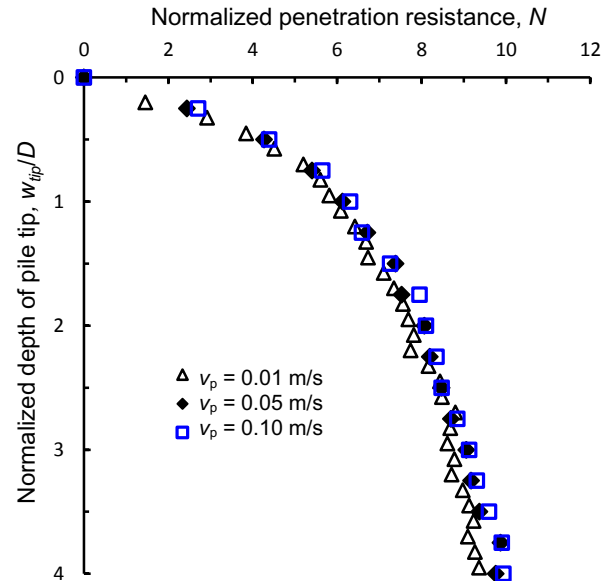
Figure 2: Influence of penetration velocities in CEL analysis

Teh and Houlsby (1991) showed that the normalized cone penetration resistance depends on the rigidity index, I_r (= G/s_u). Some of the smooth cases they analyzed show that $N \sim 10$–13 for $I_r = 100 - 300$. In the present study, $I_r = 167$ is used. Based on theoretical modeling, without simulating a large deformation of the pile, Meyerhof (1951) calculated the normalized ultimate bearing capacity of 9.34 for a deep circular foundation.

While there are some similarities in calculated penetration resistance in different studies, the differences might result from the modeling technique, soil properties and shape of the tip of the penetrating object. These factors influence the soil failure mechanisms during penetration and thereby the penetration resistance.

4.3 Effects of undrained shear strength

In addition to the simulation for s_u = 30 kPa, as discussed above, two more simulations are performed for s_u = 10 kPa and 20 kPa. The Young's modulus is also changed accordingly, maintaining the same rigidity index (= 167). Figure 4(a) shows the penetration resistance (F) with the depth of the pile tip. As expected, F increases with s_u but F is not directly proportional to s_u. However, if the buoyancy component (F_b) is subtracted and normalized (N), the normalized penetration resistance follows an almost single line, as shown in Fig. 4(b). In other words, the penetration resistance only due to undrained shear strength is a

function of N. The maximum N at a deep condition (e.g., $w_{tip} > 7D$) is ~ 10.3.
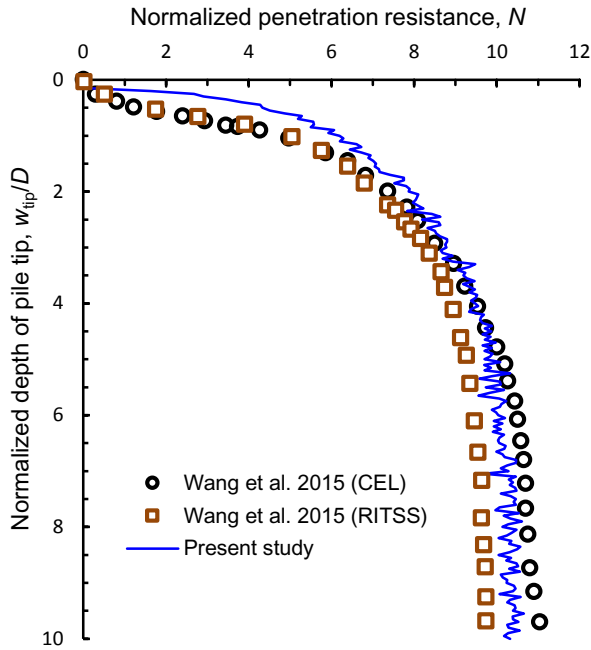
Figure 3: Variation of normalized penetration resistance with a normalized depth of pile tip for clay

4.4 Penetration resistance for sand

Figure 5 shows the penetration resistance (F) in loose sand. In this case, F increases rapidly up to w_{tip} ~ 4.5D and then the rate of increase of F decreases. At $w_{tip} > 4.5D$, the slope of the curve remains constant. A close examination of soil flow around the pile shows that, at $w_{tip} > 4.5D$, the soil failure mechanism is a deep flow mechanism, where the soil flow mainly occurs around the tip of the pile instead of there being any change in flow mechanism. Therefore, the linear increase of F with penetration is due to the increase in vertical stress at the tip and length of the shaft, which increases both tip and shaft resistances.

An analysis is also performed for a smooth pile–soil interface condition. A maximum value of F = 177 kN is found at w_{tip} = 10D, which is 108 kN (= 285 − 177) smaller than the value shown in Fig. 5 at the same tip depth. This difference is the contribution of the shaft resistance.
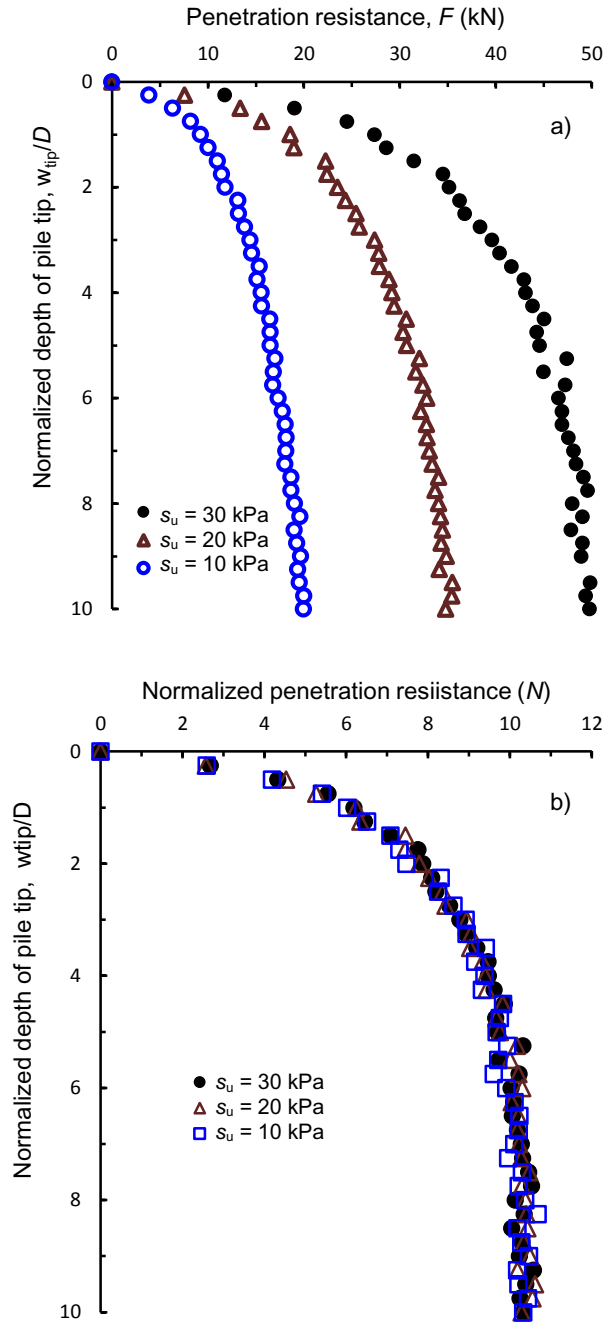
Figure 4: Effects of undrained shear strength of clay on: (a) penetration resistance, (b) normalized penetration resistance

4.5 Radial stresses

The change in radial stress (σ_r) plays a major role in soil failure mechanisms, development of shear strain and pile–soil interface resistance. The variation of radial stress during pile penetration at four depths measured from the initial ground surface (z in Fig. 1) is shown in Fig. 6. The radial distance from the pile surface is plotted in a normalized form ((r-R)/R), where r is the radial distance from the center of the pile and R is the radius of the pile.

Figure 6 shows that the penetration-induced radial stress reaches the maximum when the tip of the pile passes that level. However, the generated radial stress decreases with further penetration. For example, at z = 2.0 m for the pile penetration in clay, the maximum σ_r is 280 kPa (near the pile surface) when the pile tip is at this location (w_{tip} = 2.0 m) (Fig. 6(a)); however, σ_r = 76 kPa when w_{tip} = 3.0 m (Fig. 6(b)). The reduction of σ_r occurs due to stress redistribution during further penetration. Similar behavior has also been observed in sand (Figs. 6(d)–6(f)).

The penetration causes a higher radial stress increase in sand than that in clay, especially at greater depths. Figure 6 also shows that σ_r decreases with radial distance in both sand and clay. However, σ_r decreases faster in sand than in clay. For sand, the penetration-induced radial stress increase is not significant after 5R–10R distance from the pile surface (Figs. 6(d)–6(f)).
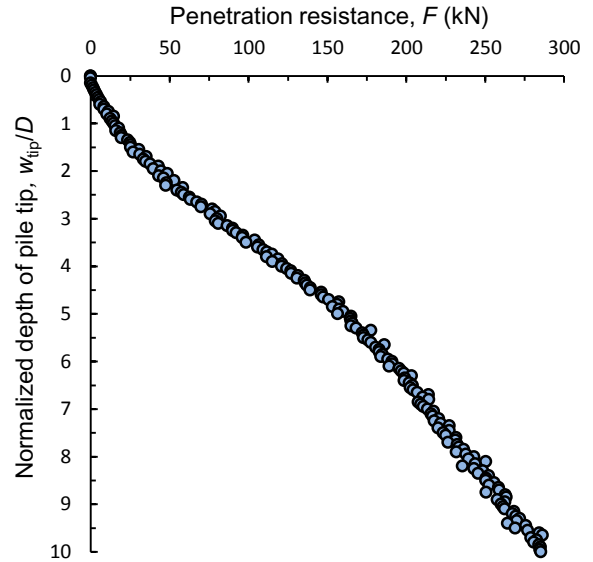
Figure 5: Penetration resistance in loose sand
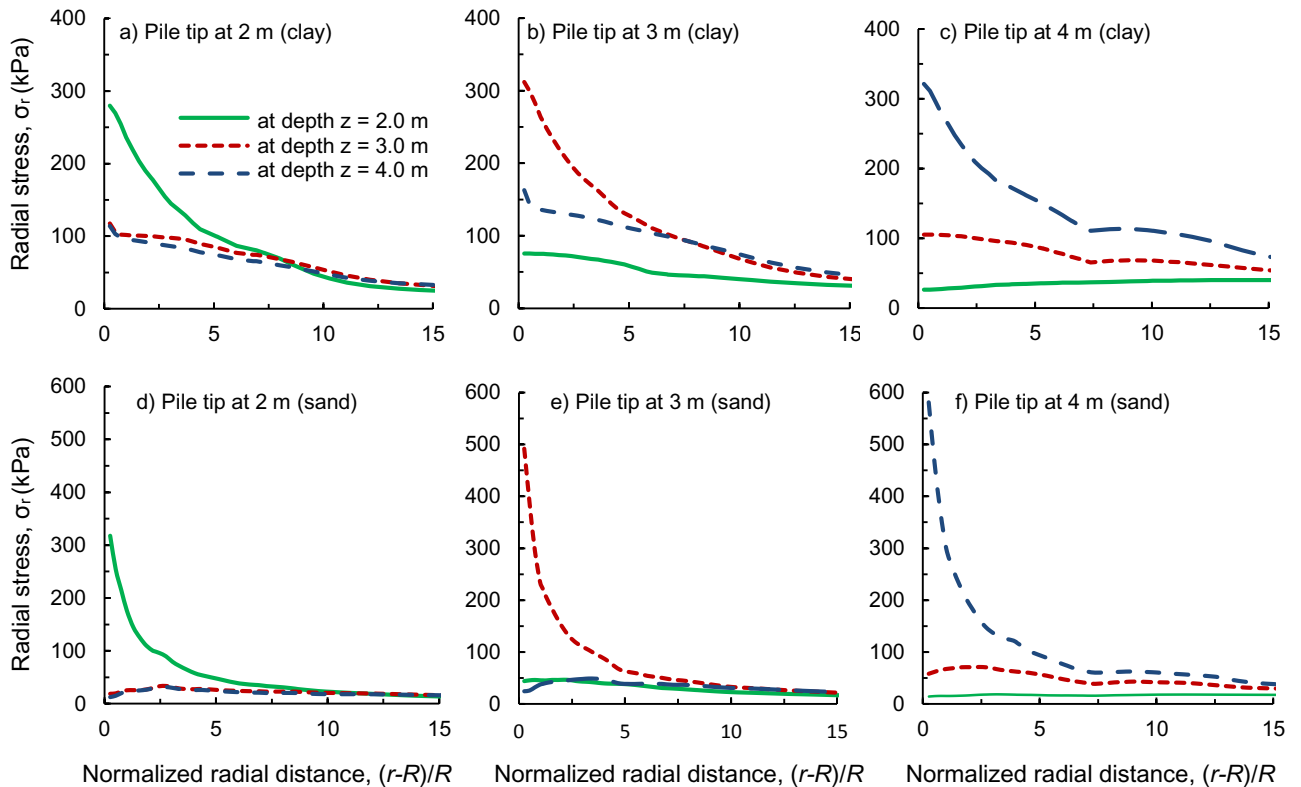
Figure 6: Radial stresses at 2.0, 3.0, 4.0 m depths for different pile tips position: a–c for clay; d–f for sand

4.6 Ground surface heave

Ground heave occurs when a pile is driven into the soil. For example, ~ 400 mm of vertical soil movement was observed at 1.5 m depth when a group of concrete piles was installed in a sensitive marine clay in Quebec (Bozozuk et al. 1978). The heave was negligible further than~ 12 m from the pile group. The occurrence of ground heave has also been reported from many pile installations in clays (e.g., Blanchet et al. 1980; Tomlinson 1957). Ground heave was also observed during the installation of piles in sands (L'Herminier 1953), although the shape and size of the heave in the sand could be different from that observed in clay.

In the present study, the ground surface heave (w_h) is obtained from the deformed ground surface profile of the FE analysis. Figure 7 shows the ground surface heave with the normalized radial distance from the pile ((r-R)/R) for six pile tip depths. For clay, the heave is maximum at ~ 0.5R from the pile surface and then decreases rapidly with radial distance and after ~ 3R the heave is negligible (Fig. 7a).

For sand, the maximum heave is smaller and occurs at a larger radial distance than that of clay (compare Figs. 7(a) and 7(b)). Moreover, the heave spreads over a larger radial distance in the case of sand.

The magnitude of ground heave increases with penetration depth. For clay, the heave increases until the tip penetration depth of 1.0 m (= 2.5D) and no significant change in ground heave occurs during further penetration (Fig. 7(a)).However, the increase of ground heave continues up to 4.0 m penetration of the pile tip in the sand (Fig. 7(b)).

The negative value of w_h close to the pile surface represents a gap between the soil and pile. This gap forms due to soil flow mechanisms during penetration, and the size and shape of the gap depend on soil properties. Note that during the installation of a pile using a hammer, the transverse vibration also helps to form a gap. The separated segment of the pile by the gap does not provide any shaft resistance in the calculated total resistance (F), as presented in Fig. 5.

4.7 Plastic shear strain

Figure 8 shows the equivalent plastic shear strain ϵ_q^p (= PEEQVAVG in Abaqus) with penetration. The plastic shear zone increases with the depth of penetration at shallow depths (e.g., w_{tip} = 1.0 m). However, the width of the plastic shear zone does not increase after a certain depth of penetration. Comparing Figs. 8(a–d) and 8(e–f) for the clay and sand cases, respectively, shows a wider plastic shear zone in the case of clay, especially for deeper penetration, than that of sand.

Based on monotonic expansion of a cylindrical cavity, Randolph and Wroth (1979) suggested that the width of the plastic shear zone (r_p) for undrained penetration in clay can be estimated as $r_p = R\sqrt{G/s_u}$. For the soil parameters listed in Table 1, r_p of 2.58 m (= 12.9R) is calculated. The inset of Fig. 8 shows the plastic shear strain at depth z = 3.53 m when the pile penetrates to 4.0 m. The plastic shear strain generates up to r ~ 12R, although it is negligible after r ~ 4R.
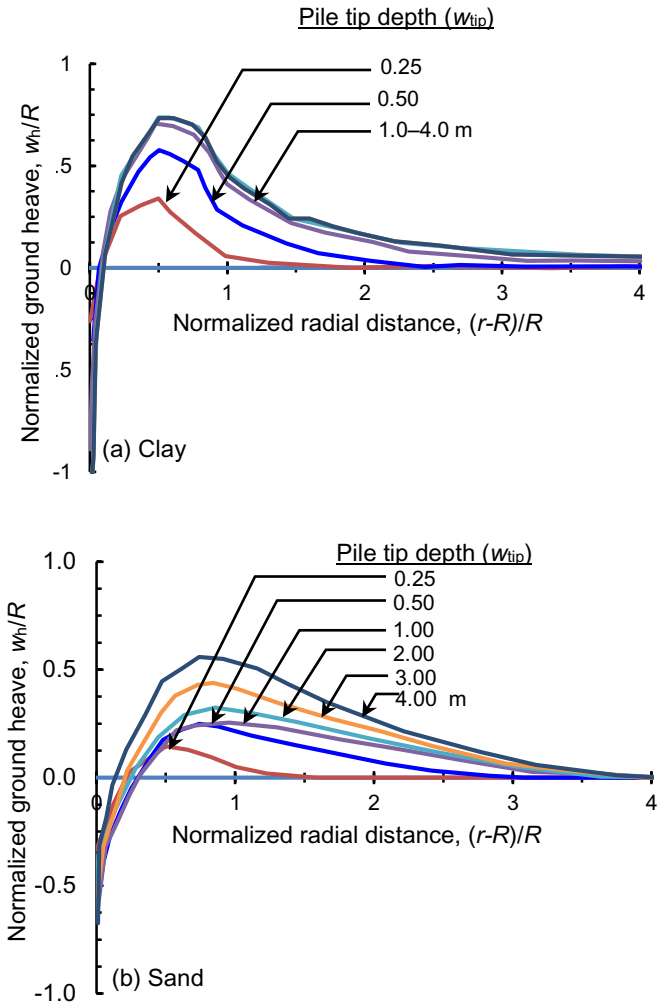
Figure 7: Ground heaves in different soil profiles for various pile tip locations

5. CONCLUSIONS

This paper presents a comparative numerical study of solid pile penetration in clay and loose sand. Considering the hydraulic conductivity of the soils, the clay is modeled in undrained and sand in drained conditions. The pile is penetrated up to ten diameters. The penetration resistance in clay increases with depth and becomes constant. In the case of sand, the penetration resistance continues to increase because of the effective stress increase with depth, which increases the drained shear strength. The normalized penetration resistance obtained from the present FE analysis compares well with previous studies.

A significant increase in radial stress occurs due to the penetration of the pile. The maximum penetration-induced radial stress develops near the pile surface when the pile tip passes that depth. The radial stress decreases with further penetration of the pile. The radial stress decreases faster with radial distance in sand than in clay. The ground surface heave is larger in clay than in sand; however, a wider heave is obtained for sand.
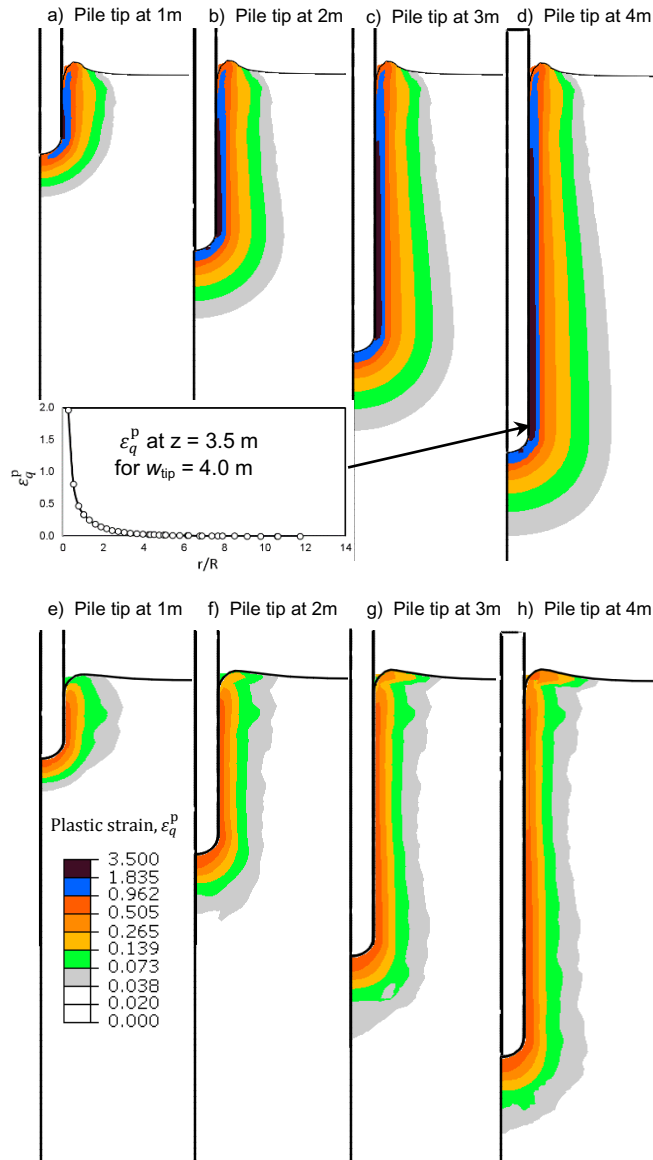
Figure 8: Plastic shear strain with penetration: a–d for clay; e–h for sand

REFERENCES

ABAQUS 6.14 [Computer software]. D. S. Simulia, *Dassault Systémes*.

Basu, P., Pressi, M. and Salgado, R. 2014. Shaft Resistance and Setup Factors for Piles Jacked in Clay, *Journal of Geotechnical and Geoenvironmental Engineering*, ASCE, 140(3): 04013026.

Blanchet, R., Tavenas, F. and Garneau, R. 1980. Behaviour of Friction Piles in Soft Sensitive Clay, *Canadian Geotechnical Journal*, 17(2): 203–224.

Bolton, M. D. 1986. The Strength and Dilatancy of Sands, *Géotechnique*, 36(1): 65-78.

Bozozuk, M., Fellenius, B. H. and Samson, L. 1978. Soil Disturbance from Pile Driving in Sensitive Clay, *Canadian Geotechnical Journal*, 15: 346–361.

Deeks, A. and White, D. J. 2006. Centrifuge Modelling of Jacked Piles, *6th International Conference on Physical Modelling in Geotechnics*, Hong Kong, 6: 821–826.

Karmaker, R. and Hawlader, B. 2018. Modeling of Pile Stabilized Clay Slopes Using a Large Deformation Finite-Element Method, *7th Canadian Geohazards Conference,* paper no-155.

Ko, J., Jeong, S. and Lee, J.K. 2016. Large Deformation FE Analysis of Driven Steel Pipe Piles with Soil Plugging, *Computers and Geotechnics*, 71: 82–97.

L'Herminier, R. 1953. Remarques sur le Poinçonnement Continue des Sables et Graviers, *Annales de l'Institut Technique du Bfitiment et des Travaux Publics*, 63–64: 377–386.

Merifield, R. S., White, D. J. and Randolph, M. F. 2009. Effect of Surface Heave on Response of Partially Embedded Pipelines on Clay, *Journal of Geotechnical and Geoenvironmental Engineering*, ASCE, 135(6): 819–829.

Meyerhof, G. G. 1951. The Ultimate Bearing Capacity of Foundations, *Géotechnique*, 2(4): 301–332.

Qui, G., Henke, S. and Grabe, J. 2011. Application of a Coupled Eulerian-Lagrangian Approach on Geomechanical Problems Involving Large Deformations, *Computers and Geotechnics*, 38: 30–39.

Randolph, M. F., Carter, J. P. and Wroth, C. P. 1979. Driven Piles in Clay–the Effects of Installation and Subsequent Consolidation, *Géotechnique*, 29(4): 361–393.

Randolph, M. F. and Wroth, C. P. 1979. An Analytical Solution for the Consolidation around a Driven pile, *International Journal for Numerical and Analytical Methods in Geomechanics*, 3: 217–229.

Sagaseta, C. and Whittle, A. J. 2001. Prediction of Ground Movement Due to Pile Driving in Clay, *Journal of Geotechnical and Geoenvironmental Engineering*, ASCE, 127(1): 55–66.

Teh, C. I. and Houlsby, G. T. 1991. An Analytical Study of the Cone Penetration Test in Clay, *Géotechnique,* 41(1): 17–34.

Tomlinson, M. J. 1957. The Adhesion of Piles Driven in Clay Soils, *4th International Conference of Soil Mechanics and Foundation Engineering*, London, 2: 66–71.

Wang, D., Bienen, B., Nazem, M., Tian, Y., Zheng, J., Pucker, T. and Randolph, M. F. 2015. Large Deformation Finite Element Analysis in Geotechnical Engineering, *Computers and Geotechnics*, 65: 104–114.

Yang, J., Tham, L. G., Lee, P. K. K., Chan, S. T. and Yu, F. Behaviour of Jacked and Driven Piles in Sandy Soil, *Géotechnique*, 56(4): 245–259.

Appendix-II

Large deformation finite-element modeling of pile jacking in sensitive clay

The paper has been published in 20th International Conference on soil mechanics and Geotechnical Engineering, Sydney 2022. Most of the research work presented in this paper was conducted by the first author. He also prepared the draft manuscript. The other authors supervised the research and reviewed the manuscript.

Large deformation finite-element modeling of pile jacking in sensitive clay

Modélisation par éléments finis de grandes déformations du fonçage de pieux dans l'argile sensible

Ripon Karmaker & Bipul Hawlader

Memorial University of Newfoundland, St. John's, NL, Canada, [rkarmaker@mun.ca]

ABSTRACT: This study presents Coupled Eulerian-Lagrangian (CEL) finite element (FE) analyses of pile jacking in sensitive clays. Implementing the effects of strain rate and strain softening on undrained shear strength of sensitive clay, the process is simulated over a large penetration distance for varying sensitivities and rate of shear strength degradation with plastic shear strain. The simulation results show that the soil flow mechanisms and development of plastic shear strains in the soil around the pile are significantly influenced by the sensitivity; therefore, the modelling with idealized soil conditions (i.e., without strain-rate and softening effects) cannot simulate the installation process properly for highly sensitive clays. For high sensitivity, large plastic shear strains develop in a narrow zone near the pile, which could reduce the shaft friction to a very low value; however, the plastic shear strains distributed over a larger area for the soil of lower sensitivity and a lower rate of shear strength degradation.

RÉSUMÉ : Cette étude présente des analyses par éléments finis (EF) couplés eulérien-lagrangien (CEL) du fonçage de pieux dans des argiles sensibles. En mettant en œuvre les effets de la vitesse de déformation et de l'adoucissement de la déformation sur la résistance au cisaillement non drainée de l'argile sensible, le processus est simulé sur une grande distance de pénétration pour différentes sensibilités et taux de dégradation de la résistance au cisaillement avec la déformation de cisaillement plastique. Les résultats de la simulation montrent que les mécanismes d'écoulement du sol et le développement des déformations plastiques de cisaillement dans le sol autour du pieu sont significativement influencés par la sensibilité ; par conséquent, la modélisation avec des conditions de sol idéalisées (c'est-à-dire sans effets de vitesse de déformation et de ramollissement) ne peut pas simuler correctement le processus d'installation pour les argiles très sensibles. Pour une sensibilité élevée, de grandes déformations de cisaillement plastique se développent dans une zone étroite près du pieu, ce qui pourrait réduire le frottement de l'arbre à une valeur très faible ; cependant, les déformations de cisaillement plastique se sont réparties sur une plus grande surface pour le sol de sensibilité inférieure et un taux de dégradation de la résistance au cisaillement plus faible.

KEYWORDS: pile jacking; large deformation; finite element analysis; sensitive clay.

1 INTRODUCTION

Pile jacking is one of the pile installation processes that create less ground vibration and disturbances than traditional pile installation methods. This method of pile installation has gained popularity in urban environments to avoid/reduce disturbance on pre-existing infrastructures due to pile installation (White et al. 2002). However, pile jacking causes a large volume of soil displacements, and the displaced soils predominantly cause ground heave during the shallow depth of penetration and local radial displacement for the higher depth of penetration. Several theoretical (Baligh 1976, Sagaseta 1987, Teh & Houlsby 1991, Sagaseta & Whittle 2001), experimental (Flaate 1972, Bozozuk et al. 1978, Blanchet et al. 1980, Roy et al. 1981) and numerical (Qui et al. 2011, Tian et al. 2011, Tho et al. 2012, Karmaker et al. 2019, Zhou et al. 2019) investigations were carried out to find the ground responses during and after pile installation.

The installation of piles in sensitivity clay shows some unique features. For example, Roy et al. (1981) presented the results of a field test program where six instrumented piles of 219-mm diameter (D) were jacked into a highly sensitive clay layer. During continuous penetration (e.g., #5 of their study), no significant increase in shaft friction contribution to the total load was found. This implies that the shaft friction of sensitive clay may not be significant during continuous penetration. They also conducted vane shear tests around the pile before and after pile installation and showed that the installation reduced the undrained shear strength up to ~3D from the pile surface. The disturbance of soil is high near the pile, although the strength could not be measured very close to the pile surface, which governs the shaft friction. Azzouz & Morrison (1988) presented field test results from two sites where the soils were lightly overconsolidated ($OCR = 1.2–1.5$) but different sensitivities: (a) Lower Boston Blue Clay ($S_t = 7 \pm 2$), and (b) Lower Empire Clay ($S_t = 2 \pm 1$). They used piezo-lateral stress cells for continuous measurement of total horizontal stress and pore water pressure. A very different response was observed during pile installation:

the effective horizontal stress near the pile surface is almost zero for sensitive Boston Blue Clay while it is considerably high for the low sensitive Lower Empire Clay. This again implies that the remoulding of soil during penetration increases with the sensitivity that might have increased the pore water pressure. Unfortunately, the remoulding process cannot be measured directly in the field. Therefore, numerical simulations might provide some further insights.

Pile jacking is a large deformation process, which cannot be simulated using typical Lagrangian-based FE modelling techniques. The authors of the present study developed CEL models to analyze the installation of piles in clay and sand considering idealized soil behaviour (Karmaker et al. 2019). The main objective of this study is to present the simulations of pile jacking in sensitive clay to investigate the effects of strain rate and strain softening on penetration resistance and soil disturbance.

2 PROBLEM STATEMENT

A solid pile of 0.4-m diameter is penetrated in a sensitive clay layer at a constant velocity along the z-axis, as shown in Fig. 1. The position of the pile tip at a given instant, measured from the ground surface prior to installation, is w_{tip}. The penetration is continued up to 10 pile diameter. In the beginning, the pile tip is kept slightly above the ground level to avoid any interaction between pile and soil during the application of gravity load, as discussed in the following sections.

The analysis is performed for an undrained condition. A linearly increasing initial undrained shear strength (s_{u0}) profile is considered.

$$s_{u0} = s_{ug} + kz \tag{1}$$

Where s_{u0} is the initial undrained shear strength before any softening and at the reference strain rate, as discussed below; s_{ug} is the shear strength at the ground surface in kPa; k is the strength

gradient in kPa/m, and z is the depth of soil element below the ground surface in meters. The groundwater table is considered at the ground surface. The pile is considered a rigid body.
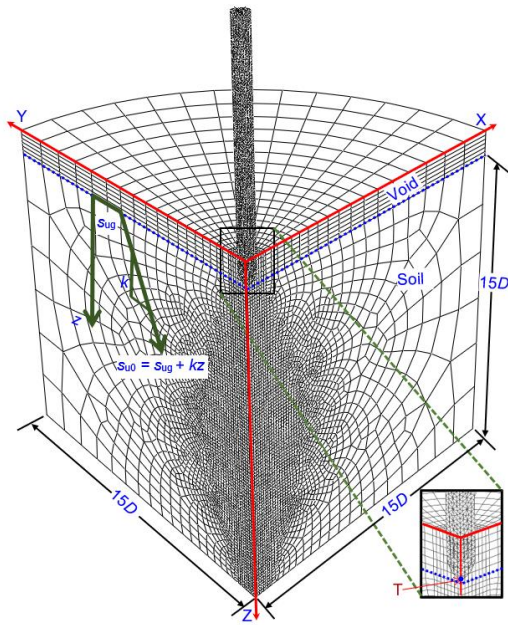
Figure 1. Finite element mesh used in analysis

3 FINITE ELEMENT MODELING

The Coupled Eulerian-Lagrangian (CEL) approach available in Abaqus 2019 is used. The CEL can model large deformation problems without any numerical issues related to mesh distortion. The simulation process can be viewed as the flowing of soil, as an Eulerian material, through a fixed mesh.

Taking the advantages of symmetry, only a quarter of the whole domain is modelled. A dense mesh is used in the zone around the pile where significant deformation of soil is expected. A cylindrical boundary is placed at a radial distance of $15D$ from the pile center. The total height of the soil model is $15D$. Analyses are also performed with a larger soil domain than that described above; however, no significant change in the result is found.

The soil and the pile are modelled as an Eulerian material and Lagrangian rigid body, respectively. The model has three parts: soil, pile, and void. The soil and void are defined using the Eulerian Volume Fraction (EVF) tool available in the software, where EVF = 1 means the element is filled with soil and EVF = 0 means no soil in the element (void). During the analysis, some elements might be partially filled with soil ($0 < EVF < 1$). The soil elements are modelled using the EC3D8R element in the software, which are linear multi-material Eulerian brick elements. The clay is modelled as an elastic-perfectly plastic material using the von Mises yield criteria incorporating strain-softening and the strain-rate effects, as discussed later. Zero-velocity boundary conditions are used normal to all the vertical faces. In the curved cylindrical outer surface, the soil is allowed to move only in the vertical direction. At the bottom of the domain, zero-velocity boundary conditions are applied in all three directions (i.e. $v_x = v_y = v_z = 0$), meaning that the soil elements next to this boundary are restrained from any movement. No boundary condition is applied at the soil–void interface so that the soil can displace into the void during the penetration of the pile when needed (e.g., ground surface heaving near the pile). The parameters used in the analysis are listed in Table 1. A detailed discussion on the selection of the soil parameters is available in Dey et al. (2015, 2016) and Wang et al. (2020).

The pile–soil interface is modelled as a frictional contact using the default general contact formulation in the software. In the present undrained total stress analysis, the Coulomb friction law is implemented by limiting the maximum shear stress at the soil–pile interface (τ_{max}) to αs_{u0}, where $0 \leq \alpha \leq 1.0$. Previous studies also suggested that α could be estimated as the inverse of the sensitivity (Einav & Randolph 2005, Hossain & Randolph 2009). A large value of Coulomb friction coefficient (= 50) is taken to ensure quick mobilization of τ_{max}. Although s_{u0} increases with depth, a constant value of τ_{max} is used.

Table 1: Geotechnical properties used in EF analysis

Parameters	Value
Total unit weight, γ (kN/m³)	17
Undrained Young's modulus, E_u (MPa)	10
Undrained Poison's ratio, ν_u	0.49
Shear strength at the ground surface, $s_{u,g}$ (kPa)	20
Strength gradient, k (kPa/m)	1.67
Reference shear strain rate, $\dot{\gamma}_{ref}$	5.0
Viscous property, η	0.5
Shear-thinning index, β	0.1
$\delta_{95\ u}$ (m)	0.1, 0.4
S_t ($= s_{u0}/s_{uR}$)	2, 5, 10, 20

The FE analysis consists of two steps of loading. First, gravity is applied to the soil to bring it to the *in-situ* stress condition. Using a predefined field, the expected geostatic stress distribution is assigned first to the soil elements, and then the gravity load is applied using body force. Predefined stresses reduce excessive deformation of soil during gravity loading. Earth pressure coefficient of 0.96 is used. Note that the earth pressure coefficient at rest for Canadian sensitive clays is significantly higher than that obtained from Jaky's formula and is also higher than many Norwegian sensitive clays. A detailed discussion is available in previous studies (Hamouche et al. 1995, L'Heureux et al. 1917, Wang et al. 2020).

In the second step, the pile is penetrated at a constant velocity of 0.1 m/s. Several field investigations were carried out at jacking velocity of $0.01-0.001$ m/s (e.g., Roy et al. 1981, Yang et al. 2006, Kou et al. 2015), which are 10 to 100 times slower than the adopted velocity in the present study. In numerical analysis, such a slow rate of penetration is not required because it unnecessarily increases the computational time (Tho et al. 2006, Wang et al. 2015). Rather the simulations should be performed maintaining the quasi-static condition, which generally occurs if the kinetic energy of the model does not exceed 5%–10% of its internal energy and the external work done is nearly equal to the internal energy throughout the analysis (Robert et al. 2020).

3.1 S*train-softening and strain-rate effects*

The mobilized undrained shear strength (s_u) of sensitive clay is modelled using Eq. (2), incorporating a strain-softening factor, f_1 (≤ 1.0), and strain-rate factor, f_2.

$$s_u = f_1 f_2 s_{uy} \tag{2}$$

Where, s_{uy} is the undrained shear strength at a very low strain rate. Linear and exponential functions have been used in previous studies to define the reduction of shear strength as a function of accumulated plastic shear strain (ξ) or plastic shear displacement (δ) (Locat et al. 2013, Dey et al. 2015, Wang et al. 2020). In the present study, the following equations are used to define the post-peak degradation undrained shear strength (Dey et al. 2016, Wang et al. 2020):

$$
f_1 = \begin{cases} \dfrac{s_{uR}}{s_{u0}} + \left(1 - \dfrac{s_{uR}}{s_{u0}}\right) e^{-3\delta/\delta_{95}} & \text{if } 0 \le \delta < 2\delta_{95} \\[2ex] \dfrac{s_{uR}}{s_{u0}} - \dfrac{s_{uR}\text{-}s_{uld}}{s_{u0}} \dfrac{\delta\text{-}2\delta_{95}}{\delta_{ld}\text{-}2\delta_{95}} + c & \text{if } 2\delta_{95} \le \delta < \delta_{ld} \\[2ex] \dfrac{s_{uld}}{s_{u0}} + c & \text{if } \delta \ge \delta_{ld} \end{cases} \quad (3)
$$

where s_{u0} is the peak undrained shear strength at the reference shear strain rate ($\dot{\gamma}_{ref}$) before softening; s_{uR} is the value of s_u at sufficiently large δ; δ_{95} is the value of δ at which 95% reduction of (s_{u0} - s_{uR}) occurs; $c = (1 - s_{uR}/s_{u0})e^{-6} \approx 0$; and δ_{ld} is a very large value of δ (> δ_{95}) when the soil becomes completely remoulded to $s_u = s_{uld}$. The rate of post-peak shear strength degradation primarily depends on S_t and δ_{95}. Further details on the above strain-softening equations, including the selection of the model parameters, are available in Dey et al. (2015) and Wang et al. (2020).

For strain-softening materials, the solution is generally mesh-size dependent. Various mesh regularization techniques have been proposed in the past to reduce mesh dependency, as discussed in previous studies (e.g., Gylland 2012). For a given δ in Eq. (3), the finer mesh in Fig. 1 would give higher shear strain. In the present study, an element size scaling rule, similar to that presented in Dey et al. (2015), is used. Table 1 shows the value of δ_{95_u} for a unit shear band thickness. The value of δ_{95} of a soil element is calculated as δ_{95_u}/t_{FE} where t_{FE} represents the size of the element. In this study, the characteristic length is used as t_{FE}. In the subroutine, t_{FE} is called, which is then used to calculate the element-size dependent δ_{95}, which is then used to calculate the post-peak strength degradation factor f_1 using Eq. (3).

For strain-rate effects, a geotechnical approach could be used for low strain levels; however, a fluid mechanics approach would be more appropriate for the remoulded condition. An "additive power-law model" proposed by Zhu & Randolph (2011), which combines the Herschel-Bulkley (fluid mechanics approach) and power-law model (geotechnical approach), is used in this study:

$$
f_2 = \left[1 + \eta(\dot{\gamma}/\dot{\gamma}_{ref})^\beta\right] \quad (4)
$$

where η and β are the soil parameters. The value of η depends on the reference shear strain rate. The typical range of β is 0.05–0.15, which increases with the plasticity index. The selection of these soil parameters has been discussed in Randolph et al. (2012) in general and Wang et al. (2020) for sensitive clays. Using $\dot{\gamma} = \dot{\gamma}_{ref}$ in Eq. (4) and then inserting f_2 in Eq. (2) with $f_1 = 1.0$ (no softening) and $s_u = s_{u0}$, the undrained shear strength at a very low strain rate can be calculated as $s_{uy} = s_{u0}/(1 + \eta)$. However, in the field, the process becomes partially drained or drained at a low rate of shearing. For example, vane shear tests in low plastic sensitive clays show that the shear strength does not decrease at a very slow rate of rotations rather increases because of excess pore water pressure dissipation (Roy & Leblanc 1988). Therefore, in the present study, $s_u = s_{u0}$ is used when $\dot{\gamma} \le \dot{\gamma}_{ref}$. Also, as the numerical simulation is performed with a higher penetration rate than the typical field jacking rate (discussed above), a higher value of $\dot{\gamma}_{ref}$ is used to model comparable rate effects on s_u.

User subroutines are used to implement the variation of s_u with depth and the effects of strain rate and strain-softening. Further details are available in Dutta et al. (2015) and Wang et al. (2020).

4 RESULTS

In the following sections, the discussion is mainly focused on force-displacement behaviour and the development of plastic

shear strains around the pile. The latter one has a profound effect on the disturbance of sensitive clay and subsequent load-carrying capacity.

The reaction force at the reference point of the rigid pile in FE analysis gives the total penetration resistance (F) at a given pile tip depth (w_{tip}). Subtracting the buoyancy contribution (F_b), as discussed in Karmaker et al. (2019), the normalized penetration resistance (N) is calculated as $N = (F - F_b)/\left(\frac{2}{\sqrt{3}} s_{u0} A_p\right)$, where A_p is the cross-sectional area of the pile tip (see Hawlader et al. 2016 for further details on normalization). The equivalent plastic shear strain, ε_q^p (PEEQVAVG in the software), is used to define the plastic zone and soil disturbance.

4.1 Effects of pile–soil interface resistance

Pile–soil interface resistance for sensitive clays might vary significantly, depending upon the degree of remoulding and pore pressure generation (e.g., Azzouz & Morrison 1988). The parameter δ_{95} in Eq. (3) is related to the rate of remoulding—the lower the value of δ_{95} the faster the remoulding. To investigate the effects of skin friction, analyses are performed for five interface conditions: smooth, $\tau_{max} = 6$ kPa, $\tau_{max} = 10$ kPa, $\tau_{max} = 15$ kPa and rough. One more analysis is performed for the smooth condition without considering the effects of softening and strain rate (ideal soil, where $f_1 = f_2 = 1$).

Figure 2(a) shows that, for the smooth condition, the penetration resistance (N) is higher for the ideal soil than that with strain-rate and strain-softening ($\delta_{95\_u} = 0.1$ m) effects. This implies that the mobilized s_u (Eq. (2)) is smaller than s_{u0} of the ideal soil. A similar analysis for the smooth condition but with $\delta_{95\_u} = 0.4$ m also gives smaller N than that of the ideal soil; however, the difference is smaller than that shown in Fig. 2(a). These two sets of analyses show that strain-softening could have a significant effect on the penetration resistance of a pile in highly sensitive clays.

For the ideal soil case, N increases with the depth of penetration; however, the rate of increase of N decreases at larger depths. The value of N is 10.5 at $w_{tip}/D = 9.5$. Teh & Houlsby (1991) showed that the normalized cone penetration resistance also depends on the rigidity index, I_r (= G/s_u). For a smooth interface condition and uniform s_u profile, they found $N \sim 10$ and $N \sim 13$ for $I_r = 100$ and $I_r = 300$, respectively. In the present study, $I_r = 167$ and s_{u0} increases with depth. Also, based on theoretical modelling, Meyerhof (1951) calculated $N = 9.34$ for deep circular foundations.

Figures 2(a) and 2(b) show that the rate of penetration resistance increase with depth increases with τ_{max}. The rough interface condition gives a rapid increase in N at a shallower depth; however, at larger depths, the N increases slowly. Below $w_{tip}/D = 8$, the calculated N for $\tau_{max} = 15$ kPa is similar to that of the rough condition.

4.2 Effects of sensitivity

Figure 3 shows the effects of sensitivity, S_t (= s_{u0}/s_{uR}), on penetration resistance for two values of δ_{95_u} (= 0.1 & 0.4 m) and smooth interface condition. For $\delta_{95\_u} = 0.1$ m, N decreases significantly with an increase in S_t (Fig. 3(a))—for example, at $w_{tip}/D = 9.5$, N is ~8.8 and ~5.8 for $S_t = 2$ and $S_t = 20$, respectively. For $\delta_{95\_u} = 0.4$ m, no significant difference in N is observed for $S_t = 5$ to 20 because of the slower rate of remoulding. Note that, for idealized weightless soil with uniform undrained shear strength, the N becomes constant after ~$8D$ penetration for smooth pile–soil interface condition, as discussed in Karmaker et al. (2019).
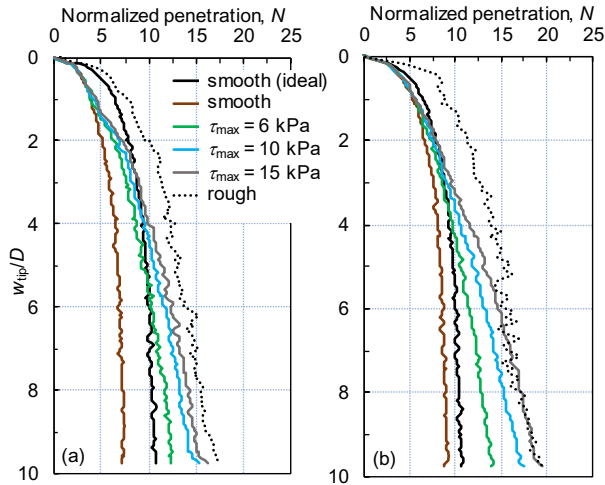
Figure 2. Effects of shaft friction on penetration resistance: (*a*) $\delta_{95\_u} = 0.1$ m, (*b*) $\delta_{95\_u} = 0.4$ m
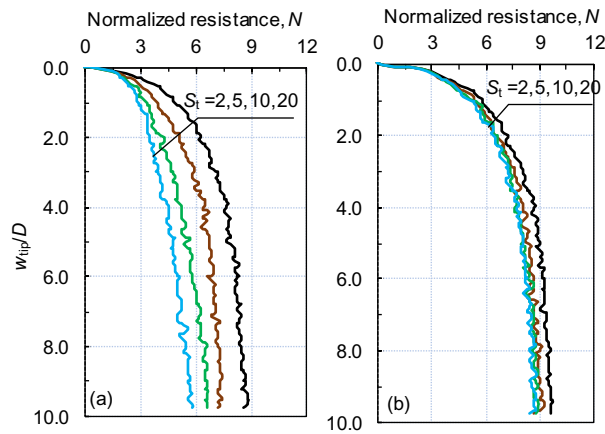
Figure 3. Effects of sensitivity on penetration resistance: (*a*) $\delta_{95\_u} = 0.1$ m, (*b*) $\delta_{95\_u} = 0.4$ m

4.3 *Reduction of undrained shear strength around piles*

When a pile is jacked into the sensitive clay, the disturbance could reduce the undrained shear strength of soil within a radial distance of several pile diameters. Figure 4 shows the mobilized s_u normalized by s_u far from the pile at the same depth. The results are shown for six different radial distances (*r*) measured from the centerline of the pile and at 4 m penetration depth. The mobilized s_u is small near the pile, and it increases with radial distance. One interesting observation is that, for a given radial distance of 0.875*D*–2.0*D*, the mobilized s_u is higher near the ground surface (e.g., z < 2 m for r = 0.825*D*) and then decreases to smaller values at larger depth. When the pile tip is at a shallower depth (z < 2 m), the soil can move outward because of the free boundary at the ground surface. However, when the pile tip moves sufficiently deep, the displaced soil around the pile tip tries to move through the weak remoulded soil near the pile, which increases the plastic shear strains and causes further reduction of mobilized shear strength. This type of soil movement does not occur in non-sensitive clays. Significant remoulding of soil near the pile and possible pore pressure generation could mobilize a very small shaft friction during installation, as observed in field tests (e.g., Roy et al. 1981)

Figure 4 shows that, with an increase in radial distance, the mobilized s_u increases, which means less remoulding of soil at a larger distance. Almost no reduction of s_u occurs in the soil elements at a radial distance larger than 4.0*D*. The maximum reduction of strength is ~80% for r = 0.625*D* while it is ~10% for r = 2.0*D*. This indicates that a highly remoulded zone formed within ~2 pile diameters. Based on field test results, some studies showed a similar extend of disturbed zone (Flaate 1972, Bozozuk et al. 1978).
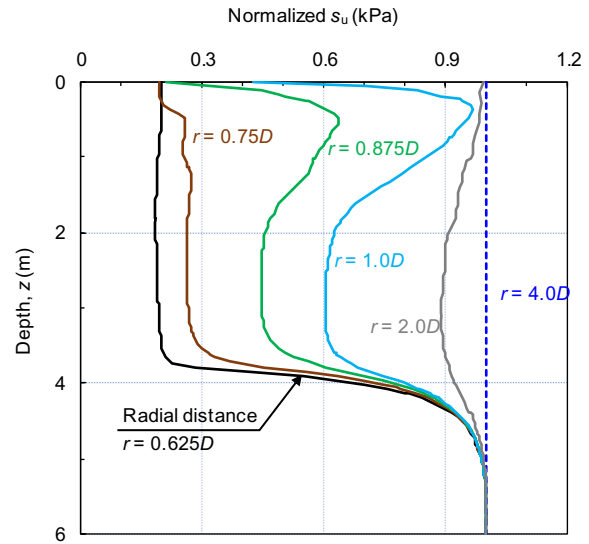
Figure 4. Mobilized undrained shear strength at different radial distances from pile center for 4-m penetration depth

4.4 *Effects of strain rate and softening*

Equation (2) shows that the mobilized s_u depends on strain softening (f_1) and strain rate (f_2). The mobilized s_u finally governs the penetration resistance and soil flow mechanisms. Figure 5 shows the contours of f_1 when the pile is penetrated to 4 m depth. The results are shown for four different sensitivities ($S_t = 2, 5, 10$ & 20). In these analyses, smooth interface condition and $\delta_{95\_u} = 0.1$ m are used. The other parameters are the same as Table 1. Very different strength softening zones are found depending upon sensitivity. The strength degradation occurs over a larger area for low S_t. For high sensitivity ($S_t = 20.0$), the soil in a narrow zone around the pile becomes completely remoulded and flows up like a fluid.

As a high value of reference shear strain rate is used, the rate effect is not significant for the penetration rate considered in this study.

To explain the mechanisms further, the development of plastic shear strains in the soil around the pile when it is penetrated to 4.0 m depth is shown in Fig. 6. Analyses are performed for three different sensitivities ($S_t = 2, 5, 10$), again with $\delta_{95\_u} = 0.1$ m and $\delta_{95\_u} = 0.4$ m. Figure 6(a) shows that, for low sensitivity ($S_t = 2$), the plastic shear strains distribute over a large area. On the other hand, the plastic shear strains accumulated in a narrower zone for higher sensitivity (e.g., Fig. 6(c)). Moreover, in the highly sensitive clay, large plastic shear strains develop near the pile (Fig. 6(c)), as compared to those in the low sensitive clay (Fig. 6(a)). Recall that strength degradation depends on plastic shear strain (Eq. (3)). Therefore, the shaft friction in highly sensitive clays is expected to be less than that of low sensitive clays.
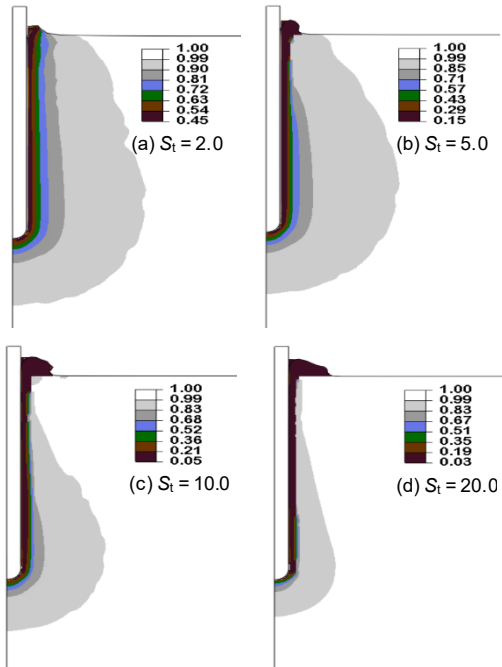
Figure 5. Strain-softening effects on soil deformation for 4-m penetration depth

5 CONCLUSIONS

Analytical methods (e.g., cavity expansion and strain path methods) are available to model the response of soil around the pile during installation. Numerical studies are also available, primarily for idealized soil conditions. The present study examines the effects of pile installation in sensitive clays. Large deformation finite element analyses are performed incorporating the effects of strain rate and strain softening on undrained shear strength.

The disturbance of soil around the pile is significantly influenced by the sensitivity of the soil and the rate of remoulding. The size of the plastic zone around the pile is smaller for higher sensitive clays. However, the magnitude of plastic shear strain is higher in high sensitive clays. More importantly, a narrow zone near the pile surface might be significantly remoulded due to the development of high plastic shear strains that could reduce the pile–soil interface resistance to a very low value, as observed in some field tests where the contributions of shaft friction to the total penetration resistance do not increase with penetration in sensitive clays. A slower rate of post-peak softening with plastic shear strain does not degrade the shear strength significantly and shows less effect on penetration resistance. In summary, the rate of shear strength degradation, which is a combined effect of S_t and δ_{95_u}, is a key factor that changes the response during penetration of a pile in sensitive clays.

6 ACKNOWLEDGEMENTS
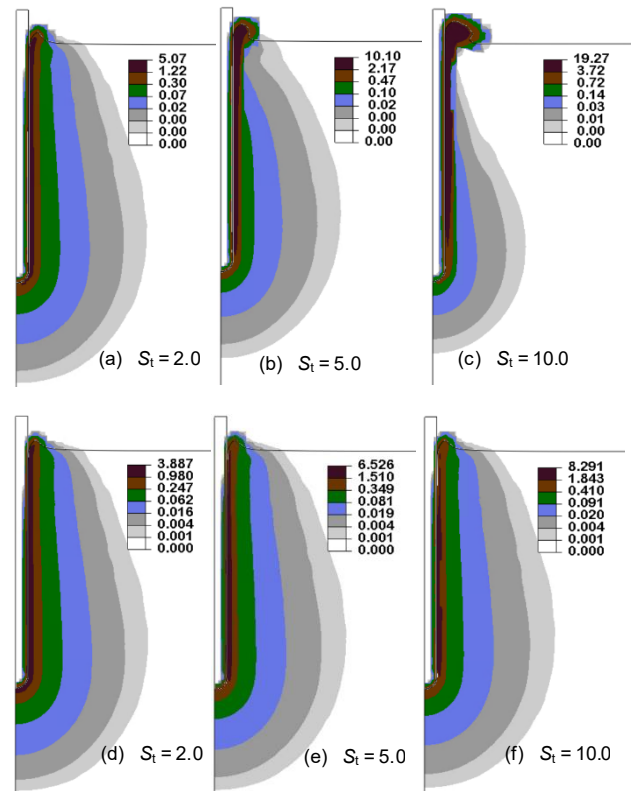
Figure 6. Plastic shear strains for different sensitivities for 4 m pile penetration depth: (*a*)–(c) δ_{95_u} = 0.1 m, (d)–(f) δ_{95_u} = 0.4 m

7 REFERENCES

Azzouz A.S. and Morrison M. 1988. Field measurements on model pile in two clay deposits. *J. Geot. Eng*, 114(1), 104–121.

Baligh M.M. 1976. Cavity expansion in sand with curved envelopes. *J. Geot. Eng. Div.,* 102(11), 1131–1146.

Blanchet R., Tavenas F. and Garneau R. 1980. Behaviour of friction piles in soft sensitive clay. *Can. Geotech. J.*, 17(2), 203–224.

Bozozuk M., Fellenius B.H. and Samson L. 1978. Soil disturbance from pile driving in sensitive clay. *Can. Geotech. J.*, 15, 346–361.

Dey R., Hawlader B., Phillips R. and Soga K. 2015. Large deformation finite-element modeling of progressive failure leading to spread in sensitive clay slopes. *Géotechnique,* 65(8), 657–668.

Dey R., Hawlader B., Phillips R., and Soga K. 2016. Modeling of large-deformation behaviour of marine sensitive clays and its application to submarine slope stability analysis. *Can. Geotech. J.*, 53(7), 1138–1155.

Dutta S., Hawlader B., and Phillips R. 2015. Finite element modeling of partially embedded pipelines in clay seabed using Coupled Eulerian-Lagrangian method. *Can. Geotech. J.*, 52, 52–72.

Einav I. and Randolph M.F. 2005. Combining upper bound and strain path methods for evaluating penetration resistance. *Int. J. Num. Meth. Eng.*, 63(14), 1991–2016.

Flaate K. 1972. Effects of pile driving in clays. *Can. Geotech. J.*, 9, 81–88.

Gylland A.S. 2012. Material and slope failure in sensitive clays. *Ph.D. thesis*. Norwegian University of Science and Technology.

Hamouche K.K., Leroueil S., Roy M., and Lutenegger A. J. 1995. In situ evaluation of K0 in eastern Canada clays. *Can. Geotech. J.*, 32(4), 677–688.

Hawlader, B., Fouzder, A., and Dutta, S. 2016. Numerical modeling of suction and trench formation at the touchdown zone of steel catenary riser. *Int. J. Geomech.*, 16 (1), 04015033.

Hossain M.S. and Randolph M.F. 2009. Effect of strain rate and strain softening on the penetration resistance of spudcan foundations on

clay. *Int. J. Geomech.*, 9, 122–132.

Karmaker R., Hawlader B., and Chen W. 2019. Finite element modeling of jacked piles in clay and loose sand. *72nd Can. Geotech. Conf., GeoSt.John's 2019,* St. John's, NL, Canada. Paper No-436.

Kou H., Zhang M. and Yu F. 2015 Shear zone around jacked piles in clay, *J. Perform. Const. Facilities.*, 29(6), 04014169.

L'Heureux J. S., Ozkul Z., Lacasse S., D'Ignazio M. and Lunne T. 2017. A revised look at the coefficient of earth pressure at rest for Norwegian clays. *In Fjellsprengningsteknikk, Bergmekanikk/ Geoteknikk (eds K. K. Dunham, Ø. Dammyr, M. Rømoen and S. Engen)*, 35.1-35.11.

Locat A., Jostad H.P. and Leroueil S. 2013. Numerical modeling of progressive failure and its implications for spreads in sensitive clays. *Can. Geotech. J.*, 50(9), 961–978.

Meyerhof G. G. 1951. The ultimate bearing capacity of foundations. *Géotechnique*, 2(4), 301–332.

Qiu G., Henke S. and Grabe J. 2011. Application of a Coupled Eulerian–Lagrangian approach on geomechanical problems involving large deformations. *Comp. and Geotech.*, 38, 30–39.

Randolph M.F., White D.J. and Yan Y. 2012. Modelling the axial soil resistance on deep-water pipelines. *Géotechnique*, 62(9), 837-846.

Robert D.J., Britto A. and Setunge S. 2020. Efficient approach to simulate soil-pipeline interaction. *J. Pipeline. Syst. Eng. Pract.*, 11(1), 04019046.

Roy M., Blanchet R., Tavenas F. and Rochelle P.L. 1981. Behaviour of a sensitive clay during pile driving. *Can. Geotech. J.*, 18(1), 67–85.

Roy M. and Leblanc A. 1988. Factors affecting the measurements and interpretation of the vane strength in soft sensitive clays, *Vane shear strength testing in soils: field and laboratory studies*, ed. A. Richards, West Conshohocken, PA, 117–128.

Sagaseta C. 1987. Analysis of undrained soil deformation due to ground loss. *Géotechnique*, 37(3), 301–320.

Sagaseta C. and Whittle J. 2001. Prediction of ground movements due to pile driving in clay. *J. Geotech. Geoenviron. Eng.*, 127(1), 55–66.

Teh C.I. and Houlsby G.T. 1991. An analytical study of the cone penetration test in clay. *Géotechnique*, 41(1), 17–34.

Tho K.K., Leung C.F., Chow Y.K., and Swaddiwudhipong S. 2012. Eulerian finite-element technique for analysis of jack up spudcan penetration. *Int. J. Geomech.*, 12(1), 64–73.

Tian Y., Wang D. and Cassidy M. 2011. Large deformation finite element analysis of offshore geotechnical penetration tests. *Proc. 2nd Int. Symp. Comp. Geomech., USA*, 1, 925-933.

Wang C., Hawlader B., Perret D. and Soga K. 2020. Effects of geometry and soil properties on type and retrogression of landslides in sensitive clays. *Géotechnique*, doi.org/10.1680/jgeot.20.P.046.

Wang D., Bienen B., Nazem M., Tian Y., Zheng J., Pucker T. and Randolph M. F. 2015. Large deformation finite element analysis in geotechnical engineering. *Comp. and Geotech.*, 65, 104–114.

White D., Finlay T., Bolton M., and Bearss G. 2002. Press-in piling: ground vibration and noise during pile installation. *Deep Foundations 2002*, 363–371.

Yang J., Tham L.G., Lee P.K., Chan S. T. and Yu F. 2006. Behaviour of jacked and driven piles in sandy soil. *Géotechnique*, 56(4), 245–259.

Zhou H., Liu H., Yuan J. and Chu J. 2019. Numerical simulation of XCC pile penetration in undrained clay. *Comp. and Geotech.*, 106, 18–41.

Zhu H. and Randolph M.F. 2011. Numerical analysis of a cylinder moving through rate dependent undrained soil. *Ocean Eng.* 38(7), 943–953.